

# **Accessibility, Structure and Reactivity of Individual Catalyst Particles Studied by Fluorescence Microscopy**

*Toegankelijkheid, Structuur en Reactiviteit van Individuele Katalysatordeeltjes, Bestudeerd met Behulp van Fluorescentiemicroscopie*

*(met een samenvatting in het Nederlands)*

## **Proefschrift**

ter verkrijging van de graad van doctor aan de Universiteit Utrecht op gezag van de rector magnificus, prof. dr. G. J. van der Zwaan, ingevolge het besluit van het college van promoties in het openbaar te verdedigen op woensdag 20 december 2017 des ochtends te 10.30 uur

door

**Frank Christiaan Hendriks**

geboren op 30 oktober 1985 te Waalre

Promotor: Prof. dr. ir. B. M. Weckhuysen

Copromotoren: Dr. P. C. A. Bruijnincx

Dr. F. Meirer

Dit proefschrift werd mede mogelijk gemaakt met financiële steun van NWO.

*Voor mijn ouders*

Hendriks, Frank Christiaan

Title: Accessibility, Structure and Reactivity of Individual Catalyst Particles Studied by Fluorescence Microscopy

Cover design by the author, with special thanks to Pablo Picasso and [www.deepart.io](http://www.deepart.io)

Printed by Gildeprint

ISBN: 978-94-6233-828-9

The work described in this thesis was carried out at the Inorganic Chemistry and Catalysis group, Debye institute of Nanomaterials Science, Faculty of Science, Utrecht University, The Netherlands.



**Universiteit Utrecht**



# Contents

|   |            |
|---|------------|
| <i>Chapter 1</i><br><b>Introduction</b>   | <b>6</b>   |
| <br>  |            |
| <u>Part 1</u>   |            |
| <i>Chapter 2</i><br><b>Zeolite Molecular Accessibility and Host-Guest Interactions Studied<br/>by Adsorption of Organic Probes of Tunable Size</b>  | <b>28</b>  |
| <i>Chapter 3</i><br><b>Probing Zeolite Crystal Architecture and Structural Imperfections<br/>Using Differently Sized Fluorescent Organic Probe Molecules</b>  | <b>54</b>  |
| <i>Chapter 4</i><br><b>Unravelling the Internal Architecture of Zeolite Ferrierite Crystals</b>   | <b>76</b>  |
| <br>  |            |
| <u>Part 2</u>   |            |
| <i>Chapter 5</i><br><b>Single-Molecule Fluorescence Microscopy Reveals Local Diffusion<br/>Coefficients in the Pore Network of an Individual Fluid Catalytic<br/>Cracking Catalyst Particle</b>         | <b>94</b>  |
| <i>Chapter 6</i><br><b>Developing Correlative Single Molecule Fluorescence, Electron<br/>and X-ray Microscopy as a Tool to Study Structure, Reactivity and<br/>Ageing of a Single Catalyst Particle</b> | <b>120</b> |
| <i>Chapter 7</i><br><b>Integrated Transmission Electron and Single Molecule Fluorescence<br/>Microscopy Correlates Reactivity with Ultrastructure in a Single<br/>Catalyst Particle</b>                 | <b>138</b> |
| <i>Chapter 8</i>  |            |
| <b>A      Summary, Conclusions and Future Perspectives</b>  | <b>154</b> |
| <b>B      Nederlandse samenvatting</b>  | <b>164</b> |
| <br>  |            |
| <b>Back Matter</b>  | <b>170</b> |



# Chapter 1

## Introduction

Catalysts are known by most people only for the fact that there is one installed in their car, converting exhaust fumes into more benign gases. Although that is a major application, it is less well-known that catalysts are also used extensively in almost every area of modern chemical industry. It is estimated that the production of virtually all transportation fuels and over 85% of all chemical processes involve a catalyst.<sup>[1]</sup> In this thesis, a specific class of highly industrially relevant materials, zeolites, and their use in catalysis is studied. In this chapter, some general concepts for catalysis are introduced, such as catalyst structure, accessibility and reactivity, and zeolites are introduced as important materials in catalysis. Finally, the aim and structure of this thesis are laid out.

## 1.1 General introduction

The research described in this thesis concerns the accessibility, mass transfer and reactivity of zeolite-based heterogeneous catalysts. The aim of this introduction is to familiarize the reader with the scientific concepts most relevant to this subject. The following questions are addressed: i) what is catalysis?, ii) what are zeolites?, iii) how are zeolites applied in heterogeneous catalysis?, and finally, iv) how are accessibility, mass transfer and reactivity studied in heterogeneous catalysts? This is followed by a definition of the scope of the thesis.

## 1.2 Catalysis

A catalyst is a material added to a chemical reaction to increase the rate of that reaction. Catalysts make chemical reactions happen that would otherwise require much more energy and/or time or would not happen at all. This is achieved by providing an alternative pathway for the reaction on the energy landscape, with a lower activation energy (Figure 1). Furthermore, by increasing the rate of only one specific reaction pathway, a catalyst can also selectively produce desired products. The ability of catalysts to selectively convert reactants to products in an energy- and atom-efficient way makes catalysis a key, enabling technology and is an important driver for making chemical production processes more sustainable.

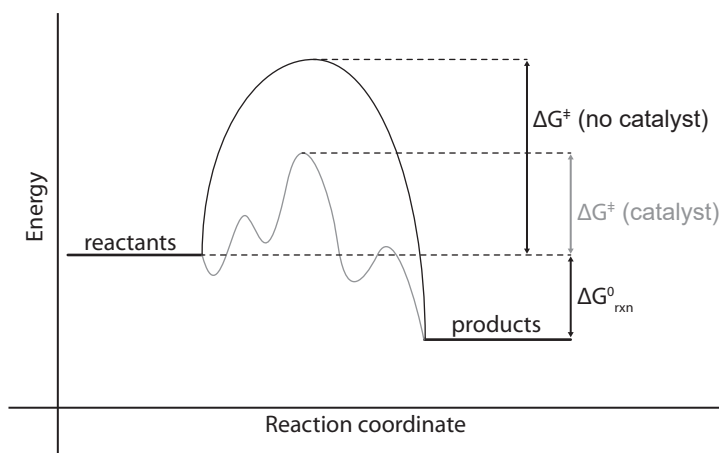


Figure 1.1. A plot of energy versus reaction progress, showing the effect of adding a catalyst to a reaction. By providing an alternative, low activation energy ( $\Delta G^\ddagger$ ) route for the reaction, the catalyst increases the rate of the reaction.

One way to classify catalysts is to distinguish between heterogeneous catalysis, in which the catalyst and reactants are part of different state of matter; and homogeneous catalysis, in which the catalyst is in the same phase as the reactants. In the case of heterogeneous catalysts, the catalyst is a solid, while the reactant can be either a

gas or a liquid. This makes product separation straightforward, which is one of the main reasons heterogeneous catalysts are predominantly used in industrial processes (in homogeneous catalysis, with both the catalyst and the reactants in solution, this is more difficult). Furthermore, heterogeneous catalysts are usually more stable than their homogeneous counterparts.<sup>[2]</sup>

The actual reaction (Figure 1.1) takes place on the active sites on the surface of the catalyst. Reactants must reach the active site and are then converted into products. The reaction rate is directly related to the availability and number of active sites; heterogeneous catalysts are therefore preferably based on porous materials with high surface areas, ensuring maximum accessibility of the active sites. These porous materials can either have the active sites incorporated in the material (e.g. solid acid catalysts) or, in the case of supported metal catalysis, a metal deposited on the surface, which acts as the active site. It is important to make a distinction of different types of porosity that can be present in catalytic materials. Usually, three types of pore sizes are considered: with a diameter larger than 50 nm (macropores), between 2 and 50 nm (mesopores) and smaller than 2 nm (micropores).<sup>[3]</sup> Smaller pores are usually associated with a larger surface area; microporous materials can reach surface areas of thousands of square meters per gram. Zeolites are a prime example of a class of microporous materials and will be discussed in the next section.

## 1.3 Materials of interest

The materials studied in this thesis are zeolites and materials based on zeolites. In section 1.3.1, a brief overview of the structure and most important properties of zeolites is given. In 1.3.2, fluid catalytic cracking catalysts, a catalyst material used in oil refining containing zeolite as the active phase will be discussed. Finally, a description of zeolite crystals, model systems often used in the study of zeolite materials, is given in 1.3.3.

### 1.3.1 Zeolites

Zeolites are crystalline aluminosilicate materials consisting of silica and alumina tetrahedra connected to each other by shared oxygen atoms. These tetrahedra can combine to form secondary building blocks, which can be connected in different ways to form many different crystalline, ordered porous frameworks.<sup>[4]</sup> Zeolites were discovered over 250 years ago by Alex Fredrik Cronstedt. He observed that upon heating, the natural mineral he was studying appeared to bubble and dance, and therefore called the material zeolite (“boiling stone”).<sup>[5]</sup> It turns out that what Cronstedt had observed was the loss of water, in the form of steam, from the micropores of the zeolite. These pores are a key property of zeolite materials and are the result of the zeolite’s crystalline framework. They are highly regular in dimension and orientation and have dimensions similar to those of organic molecules. Depending on the framework type, the pores can run in 1, 2 or 3 dimensions within the material (Table 1.1). Zeolites can occur naturally, like the

material Cronstedt was studying, but most zeolites used industrially today are synthesized. The synthesis of zeolites involves a silica and alumina source, a mineralizing agent, usually an alkali metal hydroxide, and optionally a structure directing agent.<sup>[6]</sup> To date, over 230 types of synthetic zeolite structures have been synthesized, with the potential for much more in the future: it has been calculated that over 250.000 feasible structures can be made from the tetrahedral silica and alumina building blocks.<sup>[7,8]</sup>

While  $[\text{SiO}_4]$  tetrahedra are neutral,  $[\text{AlO}_4]$  tetrahedra are negatively charged; their inclusion in the zeolite framework thus introduces a negative charge in the framework. The extra framework cation required for compensating this positive charge is typically an alkali metal ion or a proton. The latter (which can be introduced by ion exchange with  $\text{NH}_4^+$  and subsequent calcination, removing  $\text{NH}_3$ ) introduces a Brønsted acid site to the zeolite framework, turning the zeolite into a solid acid. Depending on the number of incorporated aluminium atoms, the acid strength of the zeolite material can be varied, with acid strength being related to the isolation of the acid site. Low aluminium content leads to strong, but few acid sites, while high aluminium content leads to numerous weaker acid sites. Depending on the zeolite structure, the aluminium content, usually expressed as the silicium to aluminium ratio, can be varied to a large extent to tune the acidity of zeolite materials. Furthermore, compared to other heterogeneous catalysts, the acid sites within zeolites are relatively well-defined because of their crystalline structure.

This variety in acid functionality, combined with their well-defined, porous structure and the fact that zeolites are chemically and hydrothermally stable materials,

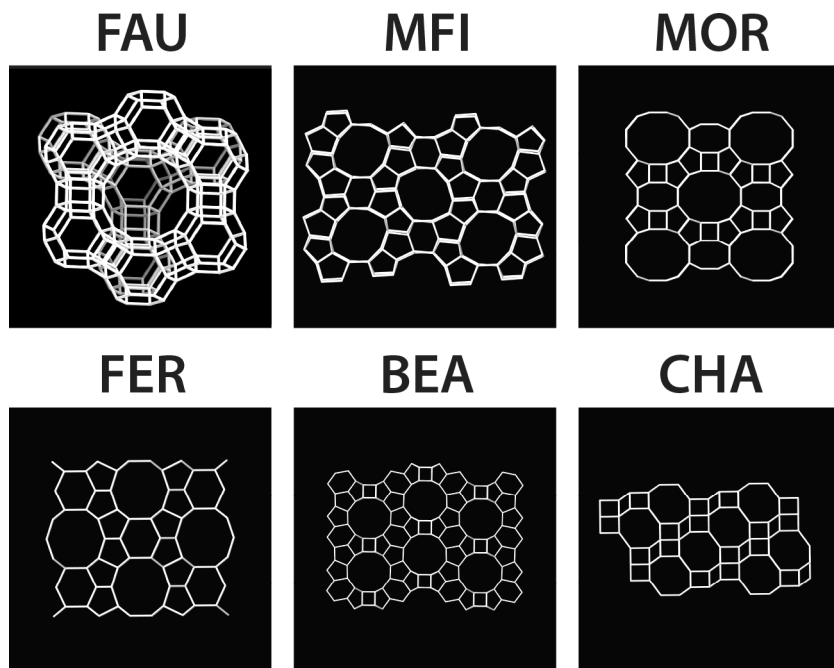


Figure 1.2. Structure models of important zeolites used in industrial applications.<sup>[7]</sup>

make them interesting materials for use in industrial applications. The application of zeolites as catalytic materials found its origin in the petrochemical industry in the 1960s. The beneficial properties of zeolites as solid acid catalysts were exploited in refinery processes, such as hydrocracking and catalytic cracking.<sup>[9,10]</sup> Apart from refinery processes, zeolites are applied in three main areas: adsorption (for example in product separation and water treatment), ion exchange (in detergents and the treatment of nuclear waste), and (non-refinery) catalysis.<sup>[11-13]</sup>

From the large number of synthesized zeolite structure, one group of industrially relevant zeolite frameworks stands out and receives the most attention in terms of research efforts. These are called the “big five”: Faujasite (FAU), MFI (ZSM-5), Mordenite (MOR), Ferrierite (FER) and Beta (BEA) (Table 1.1 and Figure 1.2).<sup>[9]</sup> Chabazite (CHA) has also attracted considerable interest due to its applicability in the methanol-to-hydrocarbons process, in which methanol is converted into fuels and chemical building blocks.<sup>[14-16]</sup> The scale of (potential) applications motivates research into a proper understanding of the structure and behavior of these materials. Any improvements made based on the fundamental understanding of zeolites would have a large impact given the scale at which they are applied: the synthetic zeolite market is valued at over \$ 13 billion.<sup>[16-18]</sup>

Table 1.1. Characteristics of some industrially important zeolite systems and their related applications. <sup>a</sup> the size of the largest pore is given.

| Framework type | Pore diameter (Å) <sup>a</sup> | Pore system | Applications <sup>[10]</sup> |
|----------------|--------------------------------|-------------|------------------------------|
| <b>FAU</b>     | 7.4                            | 3-D         | FCC, acylation               |
| <b>MFI</b>     | 5.6                            | 3-D         | FCC, isomerization, MTH      |
| <b>MOR</b>     | 6.5                            | 2-D         | Trans-alkylation             |
| <b>FER</b>     | 4.7                            | 2-D         | Olefin isomerization         |
| <b>BEA</b>     | 6.0                            | 3-D         | Cumene production, acylation |
| <b>CHA</b>     | 3.7                            | 3-D         | MTH, DeNO <sub>x</sub>       |

The micropores of zeolites allow separation and reactivity based on molecular size. Most zeolites have pore sizes of 4-10 Å, allowing for separation and size selection of organic molecules, which often have dimensions in the same size range. This match in size gives rise to an interesting phenomenon called shape selectivity; the catalytic activity of zeolites is influenced by the accessibility of the zeolite material for the molecules.<sup>[19,20]</sup> Three main types of shape selectivity can be distinguished:

reactant shape selectivity, in which more bulky reactants can be excluded from entering the catalyst: this is used in e.g. the dewaxing of paraffins using zeolite ZSM-5. Conversely, product shape selectivity precludes certain products to exit the zeolite, limiting the amount of these products in the final product composition. For example, the largest product that can be formed in the MTH reaction, catalyzed by SAPO-34 and ZSM-5, is tetramethylbenzene.<sup>[16]</sup> Finally, transition-state selectivity puts a restraint on the formation of certain transition states or reaction intermediates, for example, in the prevention of coke formation in ZSM-5 in catalytic cracking.<sup>[21]</sup>

### 1.3.2 Zeolites in catalysis: fluid catalytic cracking

One of the most important catalytic applications of zeolites is in fluid catalytic cracking (FCC) which was also the first reaction in which zeolites were applied industrially.<sup>[10]</sup> FCC is the most important refinery process converting heavy crude oil fractions, into lighter, more valuable hydrocarbons. Crude oil is a mixture of chemicals with a large variation in molecular weight, of which these lighter products, such as gasoline, diesel and light olefins, are a fraction. However, the

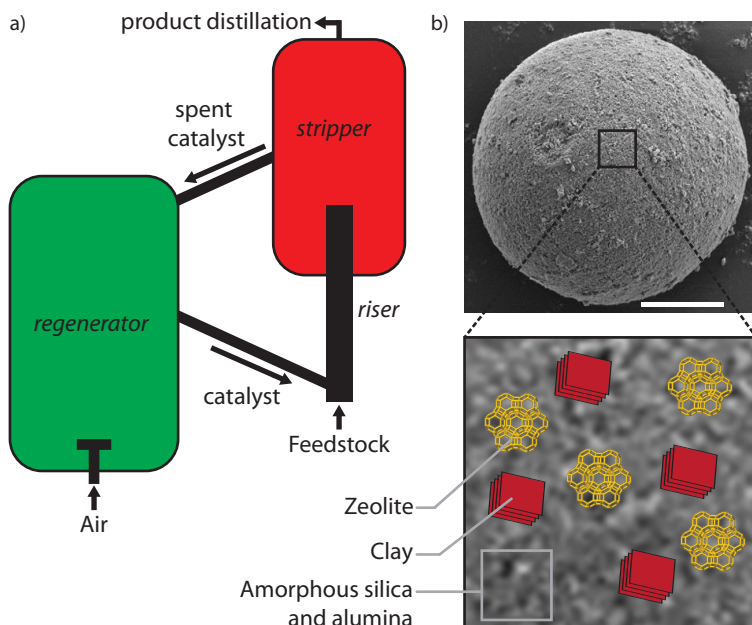


Figure 1.3. Overview of the FCC process and the catalyst used. a) The FCC reactor setup. Feedstock and catalyst are mixed in the riser in which the cracking reaction takes place. The products are then separated from the catalyst using cyclones, with the products exiting the reactor to be distilled. Remaining products are stripped from the catalyst in the stripper, after which the catalyst is regenerated by burning off the coke and reused. b) The FCC catalyst consists of small spherical particles with zeolite crystals as the active phase within a matrix of clay and amorphous silica and alumina. The scale bar represents 20  $\mu\text{m}$ .

demand for this fraction far exceeds the amount found in oil naturally. Therefore, the heavier hydrocarbons in the crude oil, which are less commercially interesting, are converted into these lighter products.<sup>[2,22]</sup> The cracking reaction takes place in a circulating fluidized bed reactor (Figure 1.3a). The feedstock and catalyst are mixed and move upwards in the riser, in which also the cracking reaction takes place. Catalyst and feedstock are in contact for only a short time (i.e. in the order of seconds), after which the products are separated using cyclones. Remaining products are stripped from the catalyst using steam followed by a catalyst regeneration step. Fast deactivation by coke formation requires regeneration of the catalyst by burning off the coke, supplying energy to the endothermic cracking process.

The harsh conditions of the process (high temperatures, steam) require a robust catalyst. Catalytic cracking is acid-catalyzed, and the acidity is provided by zeolite crystals. These crystals are embedded within a matrix of silica, alumina and clay, which provide protection, accessibility to the zeolite's acid sites, and act as a heat sink.<sup>[22,23]</sup> To protect the catalyst against attrition, it has a spherical shape with a diameter of 50–100 µm. Zeolite Y is used as the active phase, although ZSM-5 can alternatively be added to increase gasoline yield.<sup>[10,21]</sup> Usually, so-called ultra-stable Y (USY) is used, which has been treated with steam to create mesopores in the zeolite crystals. This improves their accessibility and makes the zeolite more resistant towards the reaction conditions (i.e. steam).<sup>[24]</sup>

In addition to the micro- and mesopores present in the zeolite, the silica and alumina components in the catalyst particle also contain meso- and macropores and have varying particle sizes.<sup>[22]</sup> The combination of these components results in a large pore size range. Together, these pores form a hierarchical network of pores, facilitating access to the zeolites inside the catalyst.<sup>[25]</sup> Large feedstock molecules cannot enter the zeolites because of their size and must first be pre-cracked inside the larger pores; the matrix possesses some acid functionality to facilitate this. The smaller cracking products can then diffuse into increasingly smaller pores to form the desired products (Figure 1.3b). In the FCC process the contact time between the feedstock and the catalyst is very short (in the order of seconds), mainly to limit the amount of coke produced.<sup>[23]</sup> The ability of molecules to reach the active sites is thus of paramount importance. In addition, the desired product should rapidly be able to leave the catalyst to prevent unwanted side reactions leading to overcracked products and coke formation.

The catalyst deteriorates quickly under the harsh conditions of the FCC process. Contaminant metals present in the feedstock deposit on and inside the catalyst pore network, for example. These contaminant metals catalyze unwanted side-reactions, producing more coke. Furthermore, contaminant metals can block pores and are not removed during regeneration of the catalyst by coke burn-off.<sup>[26,27]</sup> Steam used in the FCC process causes dealumination of the zeolite phase.<sup>[24,28,29]</sup> In aged FCC particles, the decrease detected in the number of tetrahedral versus octahedral aluminium sites in the active zeolite phase provides proof of the destruction of the zeolite structure.<sup>[24]</sup> These deactivation mechanisms occur simultaneously, bringing about structural as well as chemical changes within the catalyst material during operation.

From the above, it is evident that the FCC catalyst is a complex mixture of materials that requires careful design. The structure of the catalyst greatly influences the accessibility of the active zeolite sites and the mass transfer characteristics within the catalyst. Therefore, intimate knowledge of the hierarchical pore network and the location of the active sites within the FCC catalyst can aid in understanding how the catalyst functions and can be improved.

### 1.3.3 Zeolite model systems

Zeolites are usually synthesized as crystals with a grain size of less than 1  $\mu\text{m}$ , i.e. as microcrystalline powders, and these materials are often polycrystalline rather than single crystals.<sup>[30]</sup> In other words, the regular crystalline nature of zeolites cannot easily be studied, and this complicates gaining fundamental insight into their properties. Thus, most studies are conducted on zeolite powders and such results reflect macroscopic properties, making it harder to draw conclusions on local phenomena, e.g. if a reaction takes place within the pores of the zeolite or rather on its outer surface.<sup>[31]</sup> One method to overcome this barrier has been the synthesis of large, single zeolite crystals to allow single particles to be studied using various optical microscopy techniques. Crystals of up to 1 mm have been synthesized, but crystals larger than 10  $\mu\text{m}$  can already be studied using optical microscopy. The regular three-dimensional structure of these model zeolite crystals allows for a more precise evaluation of the location of guest molecules<sup>[32,33]</sup> and active sites<sup>[34]</sup> in discrete areas of the zeolite crystal. Apart from their size and specific substructure, large zeolite crystals have an identical microporous structure to zeolite powders. Therefore, knowledge on structure-activity relationships gained from studying zeolite crystals can be extrapolated to zeolite-containing catalysts and aid in gaining a detailed understanding of their properties.<sup>[35,36]</sup>

Ideally, large zeolite crystals have the same crystallographic orientation throughout the complete crystal, meaning that the pores run in the same direction in any location in the crystal. Unfortunately, many large zeolite crystals exhibit considerable internal structural heterogeneity, and exist as complex crystalline intergrowths rather than single crystals.<sup>[37]</sup> In addition, zeolite crystals can have structural defects<sup>[38]</sup> or intentionally created mesopores, influencing both the accessibility as well as the rate and extent of adsorption of molecules. These heterogeneities and changes in internal architecture complicate the structure, can create internal diffusion barriers and can give rise to gradients of catalytically active heteroatoms.<sup>[39]</sup> Such defects and heterogeneities will also be present in industrially applied zeolite materials and can be hotspots of catalytic activity, making studying them indispensable in improving our understanding of zeolite catalysis.<sup>[40]</sup>

Studies of zeolite crystals are driven by both the relevance of the zeolite involved and the availability of sufficiently large crystals. Of the FAU framework (zeolite Y), for example, although it is one of the most important zeolites, only a limited number of studies is available due to the difficulty in synthesizing large crystals of this framework type.<sup>[41–43]</sup> Perhaps the most investigated system is that of large zeolite MFI (ZSM-5) crystals.<sup>[44–48]</sup> Microspectroscopic investigations have given insight into

their substructure,<sup>[37,39,49]</sup> changes in reactivity and structure due to steaming<sup>[34,50,51]</sup> and elemental composition.<sup>[52,53]</sup> Another zeolite from the big five, FER (ferrierite), has also been studied extensively, thereby aided by the relatively facile synthesis of very large (up to 1 mm) crystals.<sup>[54,55]</sup> Fortunately, the emergence of high resolution analysis techniques have gradually enabled studying zeolites for which only smaller crystals are available.<sup>[56–58]</sup>

## 1.4 Zeolite-based catalyst materials under investigation

A large analytical toolbox has been developed to investigate catalytic materials, broadly falling into two main categories. Bulk techniques, i.e. those probing ensemble properties, are relatively easy to perform and can quickly give an overview of the macroscopic, sample-averaged characteristics of a catalyst sample. These techniques include physisorption, IR and UV-Vis spectroscopy, X-ray diffraction and NMR spectroscopy.<sup>[59]</sup> Many of these techniques can also be applied under difficult conditions, i.e. in operando or *in situ* measurements, which is an added advantage.<sup>[31]</sup> Conversely, catalytic materials can also be studied at the single particle level, in studies designed to probe the intra- and interparticle differences of catalysts. The latter studies require techniques with high spatial resolution, such as those offered by vibrational, X-ray, electronic spectroscopy and electron microscopy techniques.<sup>[60–62]</sup> These microscopic techniques often require more complex equipment, however, and they are more difficult to perform under reaction conditions. However, the application of these techniques to zeolite systems has shown that many catalysts show heterogeneity across different length scales, emphasizing the need to study catalysts in a spatiotemporal fashion with the highest possible resolution.

Fluorescence microscopy, in particular, has taken a prominent role as a versatile tool to study catalytic materials.<sup>[63–66]</sup> Its use originates in the life sciences and the application of fluorescence microscopy relies on using visible light to excite probe molecules, of which the fluorescence is then recorded. Because mostly organic probe molecules possess fluorescence properties, their use is intimately connected to this type of microscopy. As catalysts are often designed for the conversion of organic molecules, they are good candidates to be studied using fluorescence microscopy. Furthermore, zeolite-based catalysts contain micropores with molecular dimensions; studying the accessibility and diffusion of organic probe molecules can thus provide a wealth of information on the pore network of these catalytic materials. Advantageously, the absorption of light is often influenced by the environment in which a molecule is confined, allowing the interaction between the probe molecule and its host material to be evaluated.<sup>[47,67]</sup> Furthermore, the regular pore system of zeolite crystals can be exploited using polarization-dependent measurements; the alignment of the probe molecules or probe reaction products within the pore system can then be used to gain more insight in the pore orientation within the zeolite.<sup>[34,68,69]</sup>

While conventional fluorescence microscopy still regards an ensemble of molecules, novel fluorescence microscopy techniques, by virtue of improvements

in sensitivity and resolution, now allow the detection of single molecules within solid materials.<sup>[70]</sup> Employing extremely low concentrations effectively separates molecules spatiotemporally, allowing them to be observed as individual diffraction-limited fluorescent spots. By fitting such a spot with a 2D Gaussian, the location of the emitting molecule can be determined with a resolution down to 10 nm. This method is called single molecule fluorescence (SMF) microscopy, and has been applied successfully to a wide range of materials. Examples of the application of this technique are discussed in detail below.

#### 1.4.1 Accessibility and diffusion

The accessibility of and mass transport into porous catalysts influences the overall catalytic activity and final product composition.<sup>[71]</sup> Therefore, various bulk methods have been developed to determine which molecules can enter the pores of the catalyst and how fast these molecules can reach the interior. These bulk methods are usually based on the extent and rate of adsorption of various probe species into the catalyst particles, and include water titration<sup>[72]</sup>, physisorption<sup>[26,73,74]</sup> and the determination of the so-called accessibility index.<sup>[75,76]</sup> The latter method evaluates the adsorption of Vacuum Gas Oil (VGO, i.e. the fraction of crude oil with a boiling point range of 340–540 °C)<sup>[77]</sup> dissolved in toluene into the FCC catalyst, providing an indirect measure of its mass transfer characteristics. Furthermore, methods have been developed to determine the accessibility of (modified) zeolites and other microporous materials based on the reactivity of probe molecules in test reactions.<sup>[78–82]</sup> For example, the reactivity of isomers of hexane and decane in cracking reactions has been used to study the effective diameter of zeolite pores.<sup>[78,83]</sup> In addition, gas adsorption of molecules of increasing size (e.g. N<sub>2</sub> < propane < isobutene < neopentane) is often applied to assess reactant and product shape selectivity.<sup>[84]</sup> These studies can give valuable insight in the effective pore diameter as well as the accessibility of pore entrances for reactant molecules. However, what all these analysis methods have in common, is that they provide a macroscopic description of the properties for a bulk system, without giving any information about intra- or interparticle heterogeneity.

Conversely, spatial information on accessibility and diffusion in single catalyst particles can be obtained from studying large zeolite crystals. For example, interference microscopy allows for the evaluation of concentration of small organic molecules inside crystals with micrometer spatial resolution and high temporal resolution.<sup>[85]</sup> This technique has been successfully applied to MFI and FER crystals and has demonstrated the existence of internal and external diffusion barriers.<sup>[61,86,87]</sup> Furthermore, it was found that transport of molecules through a zeolite is strongly influenced by the degree of crystal intergrowth.<sup>[36,88]</sup> Using SMF microscopy, diffusion of single molecules through nanoporous materials can be monitored. Movement of fluorescent probe molecules has thus been mapped in mesoporous materials,<sup>[89,90]</sup> gels,<sup>[91]</sup> membranes<sup>[92]</sup> and polymers.<sup>[93]</sup> However, these studies are almost exclusively carried out on model materials, and have so far been applied very limited to, for example, real catalysts.<sup>[94]</sup>

### 1.4.2 Reactivity

While the accessibility and mass transfer characteristics of a zeolite determine which molecules can reach the active sites as well as how quickly, the nature of the active sites determines for a large part what kind of molecules can be formed. Much attention has therefore been devoted to studying the acidity of zeolite materials.<sup>[95,96]</sup> Although the acid sites within a zeolite are relatively well defined compared to other porous acidic materials, the local environment of the site as well as neighboring atoms play a large role in the strength of the site and hence, in the type of reaction it catalyzes.<sup>[97]</sup> In zeolite-based catalysts, not only the acidity of the zeolite itself plays a role, but also its location in the catalyst particle, as the active sites of the zeolite should be accessible to reactants.

For fluorescence microscopy, several probe reactions are available to stain acid sites within zeolite crystals.<sup>[98]</sup> Well-known examples include oligomerization of styrene derivatives<sup>[34,99]</sup>, thiophenes<sup>[100]</sup> or furfuryl alcohol.<sup>[101]</sup> Catalytic reactions that form fluorescent species, mainly coke, have also been used to visualize acid sites.<sup>[46,102,103]</sup> Furthermore, during template removal of zeolite crystals by calcination, fluorescent species are formed that can be used to visualize the intergrowth structure of the crystals.<sup>[104]</sup> These reactions have also been successfully carried out on zeolite-based catalysts, providing proof for the heterogeneity of these materials.<sup>[105,106]</sup>

Reactivity maps of catalytic materials using single-molecule fluorescence microscopy have been obtained, relying on similar probe reactions as conventional fluorescence microscopy, such as styrene<sup>[107]</sup> or furfuryl alcohol<sup>[56,105,108,109]</sup> oligomerization reactions.<sup>[64,65]</sup> A fluorogenic reaction produces fluorescent product molecules, which are subsequently excited by laser light. To prevent a buildup of fluorescent molecules, which would prevent the localization of single molecule events, the molecule is photobleached by the strong laser light or diffuses out of the focal plane.<sup>[110]</sup> This method allows for the localization of active sites within the catalyst with high resolution,<sup>[105]</sup> but it can also shed light on any differences in reactivity of the individual active sites,<sup>[51,107,108]</sup> as well as intraparticle diffusion.<sup>[94]</sup>

### 1.4.3 Structure-activity relationships

Because of the high level of complexity of catalytic materials, such as an FCC catalyst, it is beneficial to study them using multiple, complementary techniques to gain the desired insights. For example, complementary information is provided by the combination of optical and electron microscopy. Such an approach is relatively well-known in the life sciences,<sup>[111,112]</sup> and has also recently found its way into material science. Indeed, fluorescence microscopy is an effective tool to study reactivity and diffusion in catalytic materials,<sup>[70,110,113,114]</sup> while electron microscopy can visualize the different ultrastructures present. For example, the oligomerization of styrene as well as thiophene were used as fluorogenic probe reactions to stain the Brønsted acid sites of whole FCC catalyst particles.<sup>[115,116]</sup> Follow-up work demonstrated that wide-field fluorescence microscopy could be correlated with Transmission Electron Microscopy (TEM) to study structural degradation and loss of reactivity in FCC.<sup>[117,118]</sup>

While the resolution of TEM is orders of magnitude higher than that of fluorescence microscopy, SMF microscopy has bridged this gap by bringing the resolution down to the nanometer level, i.e. on par with electron microscopy. This was first applied to study the diffusion of a probe molecule into a mesoporous material, with the movement of molecules being linked to pore direction using TEM.<sup>[119]</sup> Furthermore, SMF has been used to study the catalytic turnovers of single molecule on the active sites of catalyst particles.<sup>[105,120]</sup> Very recently, SMF in combination with scanning electron microscopy (SEM) has been used to study photocatalysis with ZnO crystals, photoluminescence of perovskite nanorods as well as the acidity of single mordenite crystals.<sup>[121–123]</sup>

## 1.5 Aim and outline of this thesis

Clearly, zeolite model systems and zeolite-based catalysts have been the subject of extensive research. Research into their accessibility, reactivity, ageing and structure has also revealed, however, that there are still many things we do not yet fully understand. For example, the emergence of various high-resolution techniques has shown that intra- and interparticle heterogeneity exists in zeolite crystals as well as catalyst particles. Therefore, it is important to study these differences and determine their influence on the properties of these materials.

This thesis is aimed at using fluorescence microscopy to study accessibility, structure and reactivity of two types of systems: zeolite model systems, i.e. powders and crystals; and zeolite-based industrial catalytic materials, in this case FCC catalyst particles. Accessibility studies will include both the ability of molecule to enter the micropores of zeolite materials, as well as the mass transfer of probe molecules into the pore network of a catalyst particle. The structure includes both the pore network and defects in zeolite crystals, as well the distribution of the active phase in catalyst particles. These will be studied at two levels of detail: at the bulk or ensemble level, applying adsorption and confocal fluorescence microscopy; and at the single molecule level, using super-resolution microscopy methods, complemented with other high-resolution techniques such as TEM.

Part 1 of this thesis is focused on model zeolite crystals, which are studied using organic probe molecules and a variety of techniques, including adsorption experiments, confocal fluorescence microscopy and X-ray diffraction. Fundamental insights into the accessibility and internal structure of zeolite powders and crystals are gained.

In Chapter 2, the aim was to study shape selectivity in zeolite catalysis from an *in situ*, molecular viewpoint. To this end, four fluorescent organic probe molecules were synthesized, which we systematically varied in size by adding bulky substituents. The ability of these probe molecules to enter zeolite powders with different pore sizes was studied; the results show a clear correlation between the size of the molecule versus the total amount of molecules are taken up. Furthermore, UV-Vis absorption spectroscopy showed that the electronic properties of these molecules are influenced by the highly polar interior of the zeolite and that this effect is strongest

when there is a tight fit between the molecule and the host zeolite.

This series of molecules of different size provided the possibility to study their accessibility in zeolite micropores while their fluorescence allowed for a determination of their location using fluorescence microscopy. In Chapter 3, we used this series to probe the large zeolite crystals MFI and BEA, giving insight into the accessibility of these important zeolite model systems. Because the probe molecules fluoresce without the need for external activation (e.g. via reaction at the acid site of a zeolite), their distribution inside a zeolite crystal can be studied using confocal fluorescence microscopy. In this way, we showed that certain subunits in MFI and BEA crystals are prone to defects. Furthermore, for BEA, the pore orientation proposed in earlier studies was confirmed.

In Chapter 4, a combination of analysis techniques is employed to unravel the internal architecture of another industrially-relevant zeolite: ferrierite (FER). Crystals of this zeolite are platelet-shaped with a 2-dimensional pore system with different pore sizes in each direction. Previously, the pore orientation of this system had to be determined using technically demanding single-crystal X-ray diffraction studies. Several alternative techniques, based on optical and confocal fluorescence microscopy, are offered that can be used to provide this information in a more facile way.

In Part 2, focus is shifted from zeolite model systems to real industrial FCC catalysts, which add a layer of complexity because the catalyst particles consist of zeolites embedded within a matrix of multiple types of materials, so-called binders (e.g. clay, silica and alumina). To study this material and uncover the heterogeneity at the microscopic single-particle scale, a push is made towards higher-resolution techniques, such as single-molecule fluorescence microscopy.

Using single-molecule fluorescence microscopy, the diffusion of individual feedstock-like organic probe molecules in the pore system of a single FCC particle was studied in Chapter 5. Two states were detected for the probe molecules: immobile (i.e. trapped or adsorbed to the pore wall) and mobile, moving through the catalyst pore network. The obtained information is highly localized and can be used to evaluate and map heterogeneities in diffusion properties within hierarchically structured catalysts. At the same time, the results shine light on the macroscopic properties of the catalyst particles such as the diffusion coefficient and the catalyst efficiency under reaction conditions.

In Chapter 6, a multimodal approach to study thin sections of industrially used fresh and aged FCC particles was developed. A novel sample preparation method allowed a combination of scanning electron microscopy (SEM), to distinguish structural features; single-molecule fluorescence microscopy (SMF), to map the reactivity; and X-ray fluorescence (XRF) microscopy, to map the elemental composition to be used to obtain correlated high-resolution information. Cross-correlation of these three techniques is shown to be feasible without the need for fiducial markers in the sample. A measurement protocol is developed, describing the preparation and treatment of thin slices of single catalyst particles for use in such combined SEM-

SMF-XRF measurements. This laid the foundations for the results described in Chapter 7.

In Chapter 7, structure–activity relationships within thin sections of FCC catalyst particles are studied, using a combination of transmission electron microscopy (TEM) to determine structure of the catalyst materials, correlated with single-molecule fluorescence (SMF) microscopy, to map the reactivity. Ultrastructure components of zeolitic and non-zeolitic material could be distinguished and showed differences in reactivity in the thiophene oligomerization reaction. It was found that seemingly identical zeolite crystals can exhibit large differences in reactivity. The approach allowed structure–activity relationships to be visualized, for the first time with nanometer precision.

Finally, in Chapter 8, the results of this thesis are summarized. A look ahead to where the employed (combinations of) techniques can take us is presented in the outlook.

## 1.6 References

- [1] American Chemical Society, American Institute of Chemical Engineers, Chemical Manufacturers Association, Council for Chemical Research, Synthetic Organic Chemical Manufacturers Association, in *Technology Vision 2020*, 1996.
- [2] J. A. Dumesic, G. W. Huber, M. Boudart, in *Handbook of Heterogeneous Catalysis* (Eds.: G. Ertl, H. Knözinger, F. Schüth, J. Weitkamp), Wiley-VCH, Weinheim, 2008, p. 2741.
- [3] K. S. W. Sing, *Pure Appl. Chem.* **1985**, *57*, 2201–2218.
- [4] J. Weitkamp, *Solid State Ionics* **2000**, *131*, 175–188.
- [5] A. F. Masters, T. Maschmeyer, *Microporous Mesoporous Mater.* **2011**, *142*, 423–438.
- [6] C. S. Cundy, P. A. Cox, *Microporous Mesoporous Mater.* **2005**, *82*, 1–78.
- [7] C. Baerlocher, L. B. McCusker, [www.iza-structure.org/databases](http://www.iza-structure.org/databases), 2017, retrieved: 1 August.
- [8] R. Pophale, P. A. Cheeseman, M. W. Deem, *Phys. Chem. Chem. Phys.* **2011**, *13*, 12407.
- [9] E. T. C. Vogt, G. T. Whiting, A. Dutta Chowdhury, B. M. Weckhuysen, *Adv. Catal.* **2015**, *58*, 143–314.
- [10] W. Vermeiren, J.-P. Gilson, *Top. Catal.* **2009**, *52*, 1131–1161.
- [11] J. Coronas, *Chem. Eng. J.* **2010**, *156*, 236–242.
- [12] C. Martínez, A. Corma, *Coord. Chem. Rev.* **2011**, *255*, 1558–1580.
- [13] J. N. Armor, *Catal. Today* **2011**, *163*, 3–9.
- [14] Q. Qian, C. Vogt, M. Mokhtar, A. M. Asiri, S. A. Al-Thabaiti, S. N. Basahel, J. Ruiz-Martínez, B. M. Weckhuysen, *ChemCatChem* **2014**, *6*, 3396–3408.
- [15] D. Verboekend, M. Milina, J. Pérez-Ramírez, *Chem. Mater.* **2014**, *26*, 4552–4562.
- [16] U. Olsbye, S. Svelle, M. Bjørøgen, P. Beato, T. V. W. Janssens, F. Joensen, S. Bordiga, K. P. Lillerud, *Angew. Chem. Int. Ed.* **2012**, *51*, 5810–5831.
- [17] B. Smit, T. L. M. Maesen, *Chem. Rev.* **2008**, *108*, 4125–4184.

- [18] Synthetic Zeolites Market – Global Forecast to 2022, <http://www.marketsandmarkets.com/PressReleases/synthetic-Zeolite.asp>, 2017.
- [19] T. F. Degnan, *J. Catal.* **2003**, *216*, 32–46.
- [20] C. Marcilly, *Top. Catal.* **2000**, *13*, 357–366.
- [21] J. S. Buchanan, *Catal. Today* **2000**, *55*, 207–212.
- [22] E. T. C. Vogt, B. M. Weckhuysen, *Chem. Soc. Rev.* **2015**, *44*, 7342–7370.
- [23] K. Folmar, M. Willis, *Thermochemical Structuring of Matrix Components for FCC Catalysts*, 2015, US Patent US8940156.
- [24] S. Kalirai, P. P. Paalanen, J. Wang, F. Meirer, B. M. Weckhuysen, *Angew. Chem. Int. Ed.* **2016**, *55*, 11134–11138.
- [25] C. Perego, R. Millini, *Chem. Soc. Rev.* **2013**, *42*, 3956–3976.
- [26] F. Meirer, S. Kalirai, D. Morris, S. Soparawalla, Y. Liu, G. Mesu, J. C. Andrews, B. M. Weckhuysen, *Sci. Adv.* **2015**, *1*, e1400199.
- [27] J. C. da Silva, K. Mader, M. Holler, D. Haberthür, A. Diaz, M. Guizar-Sicairos, W.-C. Cheng, Y. Shu, J. Raabe, A. Menzel, J. A. van Bokhoven, *ChemCatChem* **2015**, *7*, 413–416.
- [28] G. Agostini, C. Lamberti, L. Palin, M. Milanesio, N. Danilina, B. Xu, M. Janousch, J. A. van Bokhoven, *J. Am. Chem. Soc.* **2010**, *132*, 667–678.
- [29] A. C. Psarras, E. F. Iliopoulos, K. Kostaras, A. A. Lappas, C. Pouwels, *Microporous Mesoporous Mater.* **2009**, *120*, 141–146.
- [30] O. Ugurlu, J. Haus, A. A. Gunawan, M. G. Thomas, S. Maheshwari, M. Tsapatsis, K. A. Mkhoyan, *Phys. Rev. B* **2011**, *83*, 113408.
- [31] B. M. Weckhuysen, *Angew. Chem. Int. Ed.* **2009**, *48*, 4910–4943.
- [32] G. Calzaferri, *Langmuir* **2012**, *28*, 6216–6231.
- [33] G. Tabacchi, E. Fois, G. Calzaferri, *Angew. Chem. Int. Ed.* **2015**, *54*, 11112–11116.
- [34] C. Sprung, B. M. Weckhuysen, *J. Am. Chem. Soc.* **2015**, *137*, 1916–1928.
- [35] J. P. Hofmann, D. Mores, L. R. Aramburo, S. Teketel, M. Rohnke, J. Janek, U. Olsbye, B. M. Weckhuysen, *Chem. Eur. J.* **2013**, *19*, 8533–8542.
- [36] G. Muller, T. Narbeshuber, G. Mirth, J. A. Lercher, *J. Phys. Chem.* **1994**, *98*, 7436–7439.
- [37] M. B. J. Roeffaers, R. Ameloot, M. Baruah, H. Uji-i, M. Bulut, G. De Cremer, U. Müller, P. A. Jacobs, J. Hofkens, B. F. Sels, D. E. De Vos, *J. Am. Chem. Soc.* **2008**, *130*, 5763–5772.
- [38] P. Kortunov, S. Vasenkov, C. Chmelik, J. Kärger, D. M. Ruthven, J. Wloch, *Chem. Mater.* **2004**, *16*, 3552–3558.
- [39] L. Karwacki, M. H. F. Kox, D. A. M. de Winter, M. R. Drury, J. D. Meeldijk, E. Stavitski, W. Schmidt, M. Mertens, P. Cubillas, N. John, A. Chan, N. Kahn, S. R. Bare, M. Anderson, J. Kornatowski, B. M. Weckhuysen, *Nat. Mater.* **2009**, *8*, 959–965.
- [40] C.-Y. Wu, W. J. Wolf, Y. Levartovsky, H. A. Bechtel, M. C. Martin, F. D. Toste, E. Gross, *Nature* **2017**, *541*, 511–515.
- [41] S. Hashimoto, H. R. Moon, K. B. Yoon, *Microporous Mesoporous Mater.* **2007**, *101*, 10–18.
- [42] N. S. John, S. M. Stevens, O. Terasaki, M. W. Anderson, *Chem. Eur. J.* **2010**, *16*, 2220–2230.

- [43] S. Mintova, V. de Waele, U. Schmidhammer, E. Riedle, T. Bein, *Angew. Chem. Int. Ed.* 2003, 42, 1611–1614.
- [44] I. L. C. Buurmans, E. A. Pidko, J. M. de Groot, E. Stavitski, R. A. van Santen, B. M. Weckhuysen, *Phys. Chem. Chem. Phys.* 2010, 12, 7032.
- [45] D. Mores, E. Stavitski, M. H. F. Kox, J. Kornatowski, U. Olsbye, B. M. Weckhuysen, *Chem. Eur. J.* 2008, 14, 11320–11327.
- [46] D. Mores, J. Kornatowski, U. Olsbye, B. M. Weckhuysen, *Chemistry* 2011, 17, 2874–84.
- [47] E. Stavitski, M. H. F. Kox, B. M. Weckhuysen, *Chem. Eur. J.* 2007, 13, 7057–7065.
- [48] L. R. Aramburo, L. Karwacki, P. Cubillas, S. Asahina, D. A. M. de Winter, M. R. Drury, I. L. C. Buurmans, E. Stavitski, D. Mores, M. Daturi, P. Bazin, P. Dumas, F. Thibault-Starzyk, J. A. Post, M. W. Anderson, O. Terasaki, B. M. Weckhuysen, *Chem. Eur. J.* 2011, 17, 13773–13781.
- [49] J. Lu, E. Bartholomeeusen, B. F. Sels, D. Schrijvers, *J. Microsc.* 2016, 264, 370–377.
- [50] L. R. Aramburo, J. Ruiz-Martínez, J. P. Hofmann, B. M. Weckhuysen, *Catal. Sci. Technol.* 2013, 3, 1208–1214.
- [51] Z. Ristanović, J. P. Hofmann, G. De Cremer, A. V. Kubarev, M. Rohnke, F. Meirer, J. Hofkens, M. B. J. Roeffaers, B. M. Weckhuysen, *J. Am. Chem. Soc.* 2015, 137, 6559–6568.
- [52] D. E. Perea, I. Arslan, J. Liu, Z. Ristanović, L. Kovarik, B. W. Arey, J. A. Lercher, S. R. Bare, B. M. Weckhuysen, *Nat. Commun.* 2015, 6, 7589.
- [53] Z. Ristanović, J. P. Hofmann, U. Deka, T. U. Schülli, M. Rohnke, A. M. Beale, B. M. Weckhuysen, *Angew. Chem. Int. Ed.* 2013, 52, 13382–13386.
- [54] C. Berger, R. Gläser, R. A. Rakoczy, J. Weitkamp, *Microporous Mesoporous Mater.* 2005, 83, 333–344.
- [55] A. Kuperman, S. Nadimi, S. Oliver, G. A. Ozin, J. M. Garcés, M. M. Olken, *Nature* 1993, 365, 239–242.
- [56] K. Liu, A. V. Kubarev, J. Van Loon, H. Uji-i, D. E. De Vos, J. Hofkens, M. B. J. Roeffaers, *ACS Nano* 2014, 8, 12650–12659.
- [57] E. Fois, G. Tabacchi, G. Calzaferri, *J. Phys. Chem. C* 2012, 116, 16784–16799.
- [58] K. F. Domke, T. A. Riemer, G. Rago, A. N. Parvulescu, P. C. A. Bruijnincx, A. Enejder, B. M. Weckhuysen, M. Bonn, *J. Am. Chem. Soc.* 2012, 134, 1124–1129.
- [59] G. Leofanti, G. Tozzola, M. Padovan, G. Petrini, S. Bordiga, A. Zecchina, *Catal. Today* 1997, 34, 307–327.
- [60] C. Lamberti, A. Zecchina, E. Groppo, S. Bordiga, *Chem. Soc. Rev.* 2010, 39, 4951–5001.
- [61] J. Kärger, P. Kortunov, S. Vasenkov, L. Heinke, D. B. Shah, R. A. Rakoczy, Y. Traa, J. Weitkamp, *Angew. Chem. Int. Ed.* 2006, 45, 7846–7849.
- [62] I. L. C. Buurmans, B. M. Weckhuysen, *Nat. Chem.* 2012, 4, 873–886.
- [63] Q. Qian, J. Ruiz-Martínez, M. Mokhtar, A. M. Asiri, S. A. Al-Thabaiti, S. N. Basahel, B. M. Weckhuysen, *Catal. Today* 2014, 226, 14–24.
- [64] P. Chen, X. Zhou, H. Shen, N. M. Andoy, E. Choudhary, K.-S. Han, G. Liu, W. Meng, *Chem. Soc. Rev.* 2010, 39, 4560–4570.
- [65] G. De Cremer, B. F. Sels, D. E. De Vos, J. Hofkens, M. B. J. Roeffaers, *Chem. Soc. Rev.* 2010, 39, 4703–4717.

- [66] A. V. Kubarev, E. Breynaert, J. Van Loon, A. Layek, G. Fleury, S. Radhakrishnan, J. Martens, M. B. J. Roeffaers, *ACS Catal.* **2017**, *7*, 4248–4252.
- [67] A. Devaux, C. Minkowski, G. Calzaferri, *Chem. Eur. J.* **2004**, *10*, 2391–2408.
- [68] E. Stavitski, M. R. Drury, D. A. M. De Winter, M. H. F. Kox, B. M. Weckhuysen, *Angew. Chem. Int. Ed.* **2008**, *47*, 5637–5640.
- [69] M. H. F. Kox, E. Stavitski, B. M. Weckhuysen, *Angew. Chem. Int. Ed.* **2007**, *46*, 3652–3655.
- [70] J. Michaelis, C. Bräuchle, *Chem. Soc. Rev.* **2010**, *39*, 4731–4740.
- [71] C. Chmelik, J. Kärger, *Chem. Soc. Rev.* **2010**, *39*, 4864–4884.
- [72] C. Liu, Z. Tan, W. Ding, S. Zheng, X. Pang, S. Sun, D. Wang, Q. Teng, T. Lu, *Method to Raise the Solid Content of Catalytic Cracking Catalyst Slurry*, 2010, US Patent 7,727,924 B2.
- [73] D. A. M. De Winter, F. Meirer, B. M. Weckhuysen, *ACS Catal.* **2016**, *6*, 3158–3167.
- [74] S. Mitchell, N.-L. Michels, K. Kunze, J. Pérez-Ramírez, *Nat. Chem.* **2012**, *4*, 825–831.
- [75] S. M. Babitz, *Catalyst, a Process for Its Preparation, and Its Use*, 2017, US Patent 9534177 B2.
- [76] D. Stamires, P. O'Connor, E. J. Laheij, C. Vadovic, *FCC Catalyst, Its Preparation and Use*, 2016, US Patent 9381502 B2.
- [77] K. H. Altgelt, M. M. Boduszynski, in *Composition and Analysis of Heavy Petroleum Fractions*, CRC Press, New York, 1993.
- [78] J. A. Martens, M. Tielen, P. A. Jacobs, J. Weitkamp, *Zeolites* **1984**, *4*, 98–107.
- [79] J. A. Martens, M. Tielen, P. A. Jacobs, *Catal. Today* **1987**, *1*, 435–453.
- [80] S. I. Zones, T. V. Harris, *Microporous Mesoporous Mater.* **2000**, *35–36*, 31–46.
- [81] J. Weitkamp, S. Ernst, R. Kumar, *Appl. Catal.* **1986**, *27*, 207–210.
- [82] L. I. Devriese, L. Cools, A. Aerts, J. A. Martens, G. V. Baron, J. F. M. Denayer, *Adv. Funct. Mater.* **2007**, *17*, 3911–3917.
- [83] V. J. Frillette, W. O. Haag, R. M. Lago, *J. Catal.* **1981**, *67*, 218–222.
- [84] K. S. W. Sing, R. T. Williams, *Part. Part. Syst. Charact.* **2004**, *21*, 71–79.
- [85] U. Schemmert, J. Kärger, J. Weitkamp, *Microporous Mesoporous Mater.* **1999**, *32*, 101–110.
- [86] O. Geier, S. Vasenkov, E. Lehmann, J. Kärger, U. Schemmert, R. A. Rakoczy, J. Weitkamp, *J. Phys. Chem. B* **2001**, *105*, 10217–10222.
- [87] D. Tzoulaki, L. Heinke, W. Schmidt, U. Wilczok, J. Kärger, *Angew. Chem. Int. Ed.* **2008**, *47*, 3954–3957.
- [88] Y. S. Lin, N. Yamamoto, Y. Choi, T. Yamaguchi, T. Okubo, S.-I. Nakao, *Microporous Mesoporous Mater.* **2000**, *38*, 207–220.
- [89] B. Rühle, M. Davies, T. Lebold, C. Bräuchle, T. Bein, *ACS Nano* **2012**, *6*, 1948–1960.
- [90] F. Feil, C. Jung, J. Kirstein, J. Michaelis, C. Li, F. Nolde, K. Müllen, C. Bräuchle, *Microporous Mesoporous Mater.* **2009**, *125*, 70–78.
- [91] C. H. Lee, A. J. Crosby, T. Emrick, R. C. Hayward, *Macromolecules* **2014**, *47*, 741–749.

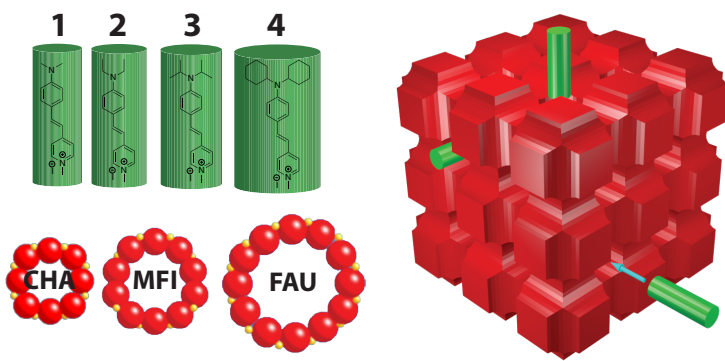
- [92] M. J. Skaug, D. K. Schwartz, *Ind. Eng. Chem. Res.* **2015**, *54*, 4414–4419.
- [93] B. Araoz, D. Täuber, C. von Borczyskowski, P. F. Aramendía, *J. Phys. Chem. C* **2012**, *116*, 7573–7580.
- [94] G. De Cremer, M. B. J. Roeffaers, E. Bartholomeeusen, K. Lin, P. Dedecker, P. P. Pescarmona, P. A. Jacobs, D. E. De Vos, J. Hofkens, B. F. Sels, *Angew. Chem. Int. Ed.* **2010**, *49*, 908–911.
- [95] E. G. Derouane, J. C. Védrine, R. R. Pinto, P. M. Borges, L. Costa, M. A. N. D. A. Lemos, F. Lemos, F. R. Ribeiro, *Catal. Rev.* **2013**, *55*, 454–515.
- [96] W. E. Farneth, R. J. Gorte, *Chem. Rev.* **1995**, *95*, 615–635.
- [97] A. Corma, *J. Catal.* **2003**, *216*, 298–312.
- [98] M. M. Kerssens, C. Sprung, G. T. Whiting, B. M. Weckhuysen, *Microporous Mesoporous Mater.* **2014**, *189*, 136–143.
- [99] Z. Ristanović, J. P. Hofmann, M.-I. Richard, T. Jiang, G. A. Chahine, T. U. Schülli, F. Meirer, B. M. Weckhuysen, *Angew. Chem. Int. Ed.* **2016**, *55*, 7496–7500.
- [100] M. H. F. Kox, K. F. Domke, J. P. R. Day, G. Rago, E. Stavitski, M. Bonn, B. M. Weckhuysen, *Angew. Chem. Int. Ed.* **2009**, *48*, 8990–8994.
- [101] M. B. J. Roeffaers, R. Ameloot, A.-J. Bons, W. Mortier, G. De Cremer, R. de Kloe, J. Hofkens, D. E. De Vos, B. F. Sels, *J. Am. Chem. Soc.* **2008**, *130*, 13516–13517.
- [102] A. N. Parvulescu, D. Mores, E. Stavitski, C. M. Teodorescu, P. C. A. Bruijnincx, R. J. M. K. Gebbink, B. M. Weckhuysen, *J. Am. Chem. Soc.* **2010**, *132*, 10429–10439.
- [103] S. C. C. Wiedemann, Z. Ristanović, G. T. Whiting, V. R. Reddy Marthala, J. Kärger, J. Weitkamp, B. Wels, P. C. A. Bruijnincx, B. M. Weckhuysen, *Chem. Eur. J.* **2016**, *22*, 199–210.
- [104] L. Karwacki, E. Stavitski, M. H. F. Kox, J. Kornatowski, B. M. Weckhuysen, *Angew. Chem. Int. Ed.* **2007**, *46*, 7228–7231.
- [105] Z. Ristanović, M. M. Kerssens, A. V. Kubarev, F. C. Hendriks, P. Dedecker, J. Hofkens, M. B. J. Roeffaers, B. M. Weckhuysen, *Angew. Chem. Int. Ed.* **2015**, *54*, 1836–1840.
- [106] G. T. Whiting, A. D. Chowdhury, R. Oord, P. Paalanen, B. M. Weckhuysen, *Faraday Discuss.* **2016**, *188*, 369–386.
- [107] Z. Ristanović, A. V. Kubarev, J. Hofkens, M. B. J. Roeffaers, B. M. Weckhuysen, *J. Am. Chem. Soc.* **2016**, *138*, 13586–13596.
- [108] X. Zhu, N. Kosinov, A. V Kubarev, A. Bolshakov, B. Mezari, I. Valastyan, J. P. Hofmann, M. B. J. Roeffaers, E. Sarkadi-Pribóczki, E. J. M. Hensen, *ChemCatChem* **2017**, DOI: 10.1002/cctc.201700567.
- [109] K. Kennes, C. Demaret, J. Van Loon, A. V. Kubarev, G. Fleury, M. Sliwa, O. Delpoux, S. Maury, B. Harbuzaru, M. B. J. Roeffaers, *ChemCatChem* **2017**, DOI: 10.1002/cctc.201700696.
- [110] K. P. F. Janssen, G. De Cremer, R. K. Neely, A. V. Kubarev, J. Van Loon, J. A. Martens, D. E. De Vos, M. B. J. Roeffaers, J. Hofkens, *Chem. Soc. Rev.* **2014**, *43*, 990–1006.
- [111] P. de Boer, J. P. Hoogenboom, B. N. G. Giepmans, *Nat. Methods* **2015**, *12*, 503–513.
- [112] M. Hauser, M. Wojcik, D. Kim, M. Mahmoudi, W. Li, K. Xu, *Chem. Rev.* **2017**, *117*, 7428–7456.

- [113] P. Chen, X. Zhou, N. M. Andoy, K.-S. Han, E. Choudhary, N. Zou, G. Chen, H. Shen, *Chem. Soc. Rev.* **2014**, *43*, 1107–17.
- [114] K. Kitagawa, S. A. Blum, *ACS Catal.* **2017**, *7*, 3786–3791.
- [115] I. L. C. Buurmans, J. Ruiz-Martínez, W. V. Knowles, D. van der Beek, J. A. Bergwerff, E. T. C. Vogt, B. M. Weckhuysen, *Nat. Chem.* **2011**, *3*, 862–867.
- [116] I. L. C. Buurmans, J. Ruiz-Martínez, S. L. van Leeuwen, D. van der Beek, J. A. Bergwerff, W. V. Knowles, E. T. C. Vogt, B. M. Weckhuysen, *Chem. Eur. J.* **2012**, *18*, 1094–1101.
- [117] M. A. Karreman, I. L. C. Buurmans, J. W. Geus, A. V. Agronskaia, J. Ruiz-Martínez, H. C. Gerritsen, B. M. Weckhuysen, *Angew. Chem. Int. Ed.* **2012**, *51*, 1428–1431.
- [118] M. A. Karreman, I. L. C. Buurmans, A. V. Agronskaia, J. W. Geus, H. C. Gerritsen, B. M. Weckhuysen, *Chem. Eur. J.* **2013**, *19*, 3846–3859.
- [119] A. Zürner, J. Kirstein, M. Döblinger, C. Bräuchle, T. Bein, *Nature* **2007**, *450*, 705–708.
- [120] N. M. Andoy, X. Zhou, E. Choudhary, H. Shen, G. Liu, P. Chen, *J. Am. Chem. Soc.* **2013**, *135*, 1845–1852.
- [121] E. Debroye, J. Van Loon, X. Gu, T. Franklin, J. Hofkens, K. P. F. Janssen, M. B. J. Roeffaers, *Part. Part. Syst. Charact.* **2016**, *33*, 412–418.
- [122] H. Yuan, E. Debroye, G. Caliandro, K. P. F. Janssen, J. van Loon, C. E. A. Kirschhock, J. A. Martens, J. Hofkens, M. B. J. Roeffaers, *ACS Omega* **2016**, *1*, 148–159.
- [123] J. Van Loon, K. P. F. Janssen, T. Franklin, A. V. Kubarev, J. A. Steele, E. Debroye, E. Breynaert, J. A. Martens, M. B. J. Roeffaers, *ACS Catal.* **2017**, *7*, 5234–5242.



# **Part I**

## **Zeolite model systems**



# Chapter 2

## Zeolite Molecular Accessibility and Host-Guest Interactions Studied by Adsorption of Organic Probes of Tunable Size

A series of fluorescent probe molecules based on the commercially available *trans*-4-(4'-(*N,N*-diethylamino)styryl)-*N*-methylpyridinium iodide (DAMPI) scaffold has been synthesized. The dynamic radii of these DAMPI-type probes covered a range of 5.8 to 10.1 Å allowing for the direct evaluation of the micropore architecture of zeolite materials. Evaluation of industrially relevant zeolite materials with 8- (CHA), 10- (MFI) and 12-membered ring (FAU) pores show that adding steric bulk to the probe molecule influences the rate of adsorption and the amount of probe molecule taken up by the zeolite. Furthermore, it alters the interaction of the probe molecule with the zeolite material. The approach developed in this Chapter shows the general principle of determining size-accessibility relationships in microporous solids with a series of fluorescent probe molecules of systematically tunable size.

**Based on:** “Zeolite Molecular Accessibility and Host-Guest Interactions Studied by Adsorption of Organic Probes of Tunable Size”, Frank C. Hendriks, Diego Valencia, Pieter C. A. Bruijnincx and Bert M. Weckhuysen, *Physical Chemistry Chemical Physics*, 2016, 19, 1857–1867.

## 2.1 Introduction

The ability of zeolites to influence the outcome of a catalytic reaction arises from geometric constraints imposed by their topology and pore dimension; an effect which is better known as shape selectivity.<sup>[1]</sup> Shape selectivity can influence which specific product molecules are formed within the zeolite pores (transition state shape selectivity) or whether molecules can enter or exit the zeolite (reactant and product shape selectivity).<sup>[2,3]</sup> Well-known examples include the catalytic cracking of oil feedstock, dewaxing of petroleum products and methanol-to-hydrocarbon conversion.<sup>[4–6]</sup> To study shape selectivity, knowledge about the effective pore diameter of a microporous material is of paramount importance.

In this Chapter, the micropore accessibility in zeolites of varying topology is studied making use of a series of differently sized fluorescent probe molecules **1–4**, based on the *trans*-4-(4'-(*N,N*-diethylamino)styryl)-*N*-methylpyridinium iodide (DAMPI) scaffold. Their synthesis and structure is described in Scheme 2.1 and Scheme 2.2. The commercially available diethyl analogue **2** of this series of fluorescent probes has been used before to stain zeolite crystals<sup>[7]</sup> and, more specifically, to visualize the straight pores of MFI crystals<sup>[8]</sup> as well as mesopores in zeolites formed by steaming.<sup>[9]</sup> The alkylamino moiety of this molecule offers a convenient synthetic handle for a systematic size modification of the probe molecule by variation of the alkyl substituents. This results in a series of T-shaped molecular probes of different size that can be used to study changes in zeolite pore accessibility. Variation of only the alkyl groups should not change the electronic properties of the probes much, allowing observed differences in adsorption to be attributed to pore size-dependence. Furthermore, the anisotropy of rod-shaped, conjugated molecules, such as DAMPI, also offers other distinct advantages. The polarization-dependent light absorption that such probes display, for example, can be used to elucidate the specific orientation of the probe molecule in a three-dimensional micropore system, such as those found in zeolites.<sup>[10]</sup>

The probe series is tested on three industrially relevant zeolites, namely CHA (i.e., SAPO-34), MFI (i.e., ZSM-5) and FAU (i.e., zeolite Y).<sup>‡</sup> These frameworks are representative for zeolite materials with 8-, 10- and 12-membered ring pores (MRPs), respectively. Probe molecules **1–4**, bearing methyl-, ethyl-, isopropyl- and cyclohexyl-substituents, were subjected to two types of experiments. First, adsorption experiments were carried out to determine if the probe is taken up by the zeolite material. In this way, the relationship between probe molecule and zeolite pore size can be studied and serves as a benchmark for zeolite accessibility. We show that the zeolite frameworks studied allow molecules to enter with a diameter slightly larger than the reported effective pore diameter. Kinetic experiments furthermore showed that internal mass transfer limitations influence the extent of probe adsorption. UV-Vis absorption spectroscopy experiments on the probe-loaded zeolite samples demonstrated the influence of confinement in and interaction with the zeolite on the spectroscopic properties of the probe molecule. Indeed, based on observed changes in the electronic properties of the probe, the

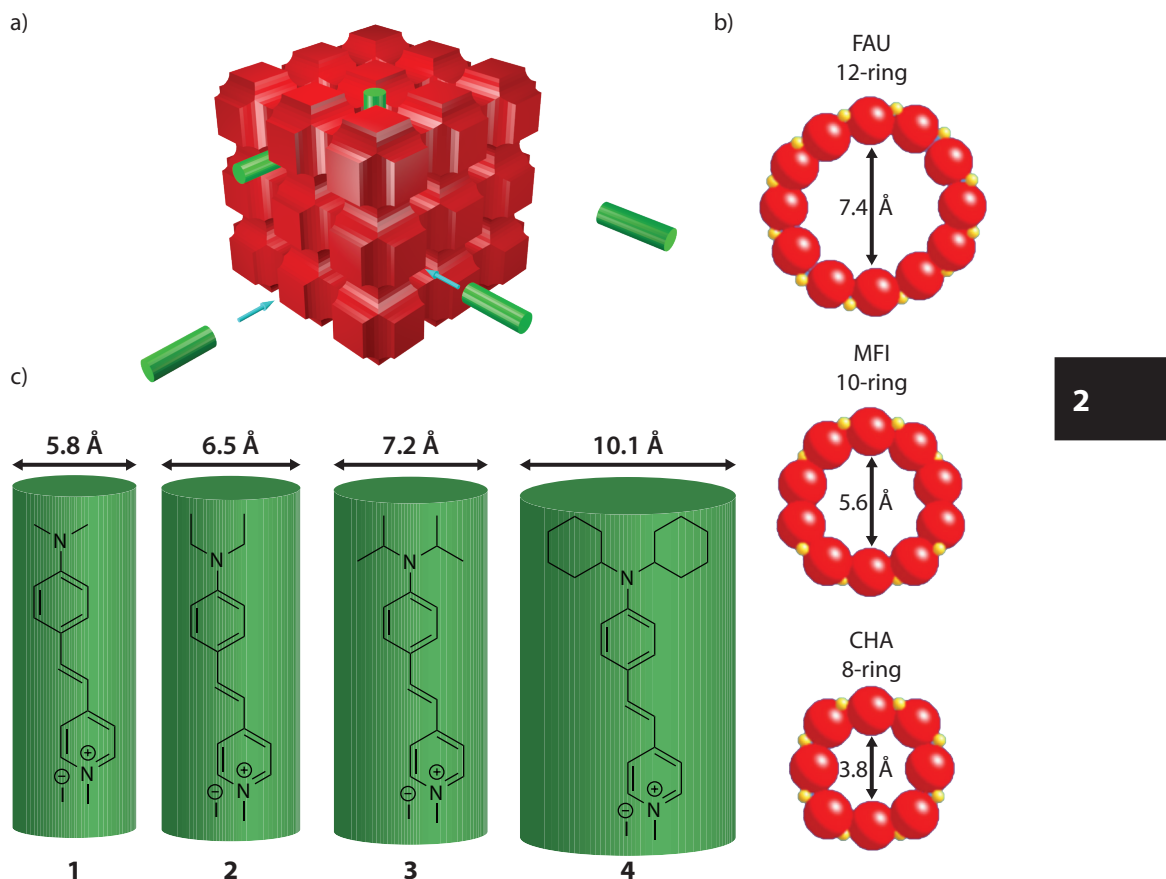


Figure 2.1. a) Schematic representation of the experiments showing a generalized zeolite structure (red) and the probe molecules (green). b) Pore openings and sizes of selected zeolites used in the adsorption experiments. Zeolite Y (FAU) is used as a model for 12-ring pores, ZSM-5 (MFI) for 10-ring pores and SAPO-34 (CHA) for 8-ring pores.<sup>[11]</sup> MFI has two types of pores, straight pores with a diameter of 5.6 Å, and sinusoidal pores with a diameter of 5.3 Å (not shown) c) The four synthesized molecular probes 1–4 with their sizes based on DFT calculations.

molecules were found to chemically interact with the zeolite Brønsted acid sites.

## 2.2 Experimental

### 2.2.1 Materials

*Trans*-4-(4'-(*N,N*-diethylamino)styryl)-*N*-methylpyridinium iodide **2** (98%) was purchased from Fluka; *N,N*-diisopropylaniline (97%), phosphorus oxychloride (99%), dimethylformamide (99.8%) and *N,N*-dicyclohexylamine (99%) from

Aldrich; 4-dimethylaminobenzaldehyde (99%), 4-picoline (99%) and iodomethane (99%) from Acros; iodobenzene (98%) from ABCR; ethanol (99.5%) from Merck; H-SAPO-34 from ACS Chemicals and NH<sub>4</sub>-ZSM-5 and NH<sub>4</sub>-Y from Zeolyst. The zeolite powders were calcined in a static oven at 773 K for 24 h in air to convert them into their proton form and remove any impurities. All other chemicals were used as received.

N-methylpicolinium iodide was synthesized according to a literature procedure.<sup>[12]</sup> The product was obtained as a brown solid (3.45 g, 74%). <sup>1</sup>H NMR (CDCl<sub>3</sub>, 400 MHz): δ 8.79 (d, J = 6.6 Hz, Ar-H, 2H), 7.92 (d, J = 6.3 Hz, Ar-H, 2H), 4.24 (s, N-CH<sub>3</sub>, 3H), 2.56 (s, CCH<sub>3</sub>, 3H) ppm.

N,N-dicyclohexylaniline was synthesized based on a literature procedure.<sup>[13]</sup> Iodobenzene (1.08 g, 5.29 mmol), dicyclohexylamine (1.89 g, 10.4 mmol), potassium *tert*-butoxide (1.03 g, 9.14 mmol) and 10 mL of DMSO were combined in a microwave reactor (20 mL). This mixture was heated in a microwave operating at 200 W to 413 K and then kept at this temperature for 7 min. The mixture was cooled down and poured into ice. N.B.: it is advisable to do this in a properly functioning fume hood because the reaction mixture has a penetrating odor. A saturated NH<sub>4</sub>Cl solution (25 mL) was added after which the product was extracted 3 times with Et<sub>2</sub>O. The solution was filtered and washed with NH<sub>4</sub>Cl, brine and then concentrated. The product was purified using column chromatography using silica gel (pore size 60 Å) and a pentane/triethylamine/ethanol (90/7/3) mixture as eluent (*R*<sub>f</sub> = 0.5). The product was obtained as a yellow oil (286 mg, 21 %). <sup>1</sup>H NMR (CDCl<sub>3</sub>, 400 MHz): δ 7.16 (dd, J = 8.6, 7.2 Hz, Ar-H, 2H), 6.92 (dd, J = 8.7, 1.1 Hz, Ar-H, 2H), 6.78 (tt, J = 7.3, 1.1 Hz, Ar-H, 1H), 3.22 (tt, J = 11.5, 3.3 Hz, Cy-H, 2H), 1.82–1.72 (m, Cy-H, 8H), 1.61 (ddtd, J = 12.9, 4.6, 3.2, 1.5 Hz, Cy-H, 2H), 1.58 – 1.42 (m, Cy-H, 4H), 1.38 – 1.21 (m, Cy-H, 4H), 1.10 (qt, J = 12.9, 3.4 Hz, Cy-H, 2H) ppm.

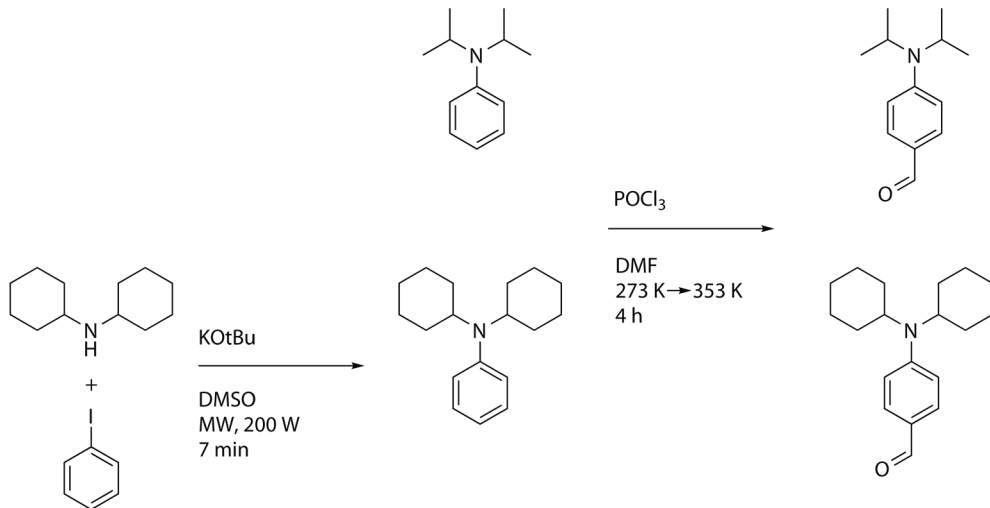
4-(N,N-diisopropylamino)-benzaldehyde was synthesized according to a literature procedure.<sup>[14]</sup> Phosphorus oxychloride (658 mg, 4.29 mmol) was added dropwise to a solution of N,N-diisopropylaniline (622 mg, 3.51 mmol) in DMF (0.95 g, 13.0 mmol) at 273 K and stirred at this temperature for 0.5 h. The resulting mixture was stirred at 353 K for 2 h. Ice and NaOH solution (1 M) were added to the mixture until the pH was above 6. The product was extracted with 3 times 20 mL of Et<sub>2</sub>O. The organic layer is washed with KHCO<sub>3</sub>, dried with Na<sub>2</sub>SO<sub>4</sub>, concentrated in vacuo and dried on an oil pump for 1 h. The product was purified by column chromatography using silica gel (pore size 60 Å) using hexanes/ethyl acetate (5/1) as eluent (*R*<sub>f</sub> = 0.6). The product is a white oil (360 mg, 50%). <sup>1</sup>H NMR (CDCl<sub>3</sub>, 400 MHz): δ 9.71 (s, OCH, 1H), 7.68 (d, J = 9.0 Hz, Ar-H, 2H), 6.84 (d, J = 9.0 Hz, Ar-H, 2H), 4.00 (hept, J = 7.0 Hz, CH(CH<sub>3</sub>)<sub>2</sub>, 2H), 1.34 (d, J = 6.9 Hz, CH(CH<sub>3</sub>)<sub>2</sub>, 12H) ppm.

4-(N,N-dicyclohexylamino)-benzaldehyde was synthesized based on a literature procedure.<sup>[14]</sup> Phosphorus oxychloride (200 mg, 1.30 mmol) was added dropwise to a solution of N,N-dicyclohexylaniline (286 mg, 1.11 mmol) in DMF (1.90 g, 25.9 mmol) at 273 K and stirred at this temperature for 0.5 h. The resulting mixture

was stirred at 353 K for 2 h. Ice and NaOH solution (1 M) were added to the mixture until the pH was above 6. The product was extracted with 5 times 10 mL of Et<sub>2</sub>O. The organic layer is washed with KHCO<sub>3</sub>, H<sub>2</sub>O and brine. The organic layer was dried with Na<sub>2</sub>SO<sub>4</sub>, concentrated in vacuo and dried on an oil pump for 1 h. The product was purified by column chromatography using silica gel (pore size 60 Å). Impurities were removed by the eluent (DCM) and the product was eluted afterwards using DCM/MeOH (1/1). The product was obtained as a black oil (161 mg, 51%). <sup>1</sup>H NMR (CDCl<sub>3</sub>, 400 MHz): δ 9.69 (s, OCH, 1H), 7.64 (d, *J* = 8.1 Hz, Ar-H, 2H), 6.87 (d, *J* = 8.7 Hz, Ar-H, 2H) 3.48–3.41 (m, Cy-H, 2H), 1.87–1.08 (m, Cy-H, 20H) ppm.

*Trans*-4-(4'-(*N,N*-dimethylamino)styryl)-*N*-methylpyridinium iodide (1) was synthesized based on a literature procedure.<sup>[15]</sup> *N,N*-Dimethylaminobenzaldehyde (747 mg, 5.01 mmol), *N*-methylpicolinium iodide (1.19 g, 5.05 mmol) and piperidine (a few drops) were added to absolute ethanol (50 mL) in a round bottom flask, heated to 373 K and refluxed at this temperature for 2 h. The product was purified by crystallization from ethanol. The product was obtained as a red, microcrystalline powder (1.94 g, 95%). <sup>1</sup>H NMR (DMSO-d<sub>6</sub>, 400 MHz): δ 8.65 (d, *J* = 7.0 Hz, pyr-H, 2H), 8.01 (d, *J* = 7.0 Hz, pyr-H, 2H), 7.87 (d, *J* = 16.1 Hz, C=CH, 1H), 7.56 (d, *J* = 8.9 Hz, Ar-H 2H), 7.14 (d, *J* = 16.1 Hz, Ar-H, 2H), 6.75 (d, *J* = 8.9 Hz, Ar-H, 2H), 4.14 (s, N-CH<sub>3</sub>, 3H), 2.99 (s, N(CH<sub>3</sub>)<sub>2</sub>, 6H) ppm. <sup>13</sup>C NMR (DMSO-d<sub>6</sub>, 100 MHz): δ 153.8 (pyr, 1C), 152.3 (C-N(CH<sub>3</sub>)<sub>2</sub>, 1C), 144.8 (pyr, 2C), 142.3 (C=C, 1C), 130.6 (Ar, 2C), 122.9 (C=C, 1C), 122.6 (pyr, 2C), 117.6 (Ar, 1C), 112.4 (Ar, 2C), 46.8 (NCH<sub>3</sub>, 1C) ppm. MS (ESI-TOF, in acetonitrile) m/z [M<sup>+</sup>]: calcd. for C<sub>16</sub>H<sub>19</sub>N<sub>2</sub> 239.1548; found 239.1558.

*Trans*-4-(4'-(*N,N*-diisopropylamino)styryl)-*N*-methylpyridinium iodide (3) was synthesized based on a literature procedure.<sup>[15]</sup> *N,N*-diisopropylaminobenzaldehyde (220 mg,



Scheme 2.1. Synthesis of the precursors for probe molecule 3 (top) and 4 (bottom).

1.07 mmol), *N*-methylpicolinium iodide (252 mg, 1.07 mmol) and piperidine (a few drops) were added to absolute ethanol (10 mL) in a round bottom flask. This mixture was refluxed overnight, after which the solvent was evaporated. The product dried using vacuum and was obtained as dark green crystals (456 mg, 100%). <sup>1</sup>H NMR (CDCl<sub>3</sub>, 400 MHz): δ 8.74 (d, J = 6.9 Hz, pyr-H, 2H), 7.82 (d, J = 7.0 Hz, pyr-H, 2H), 7.59 (d, J = 15.9 Hz, C=CH, 1H), 7.47 (d, J = 9.1 Hz, Ar-H, 2H), 6.84 (d, J = 15.9 Hz, C=CH, 1H), 6.80 (d, J = 9.1 Hz, Ar-H, 2H), 3.94 (p, J = 6.9 Hz, CH(CH<sub>3</sub>)<sub>2</sub>, 2H), 1.30 (d, J = 6.9 Hz, CH(CH<sub>3</sub>)<sub>2</sub>, 12H) ppm. <sup>13</sup>C NMR (CDCl<sub>3</sub>, 100 MHz): δ 154.2 (pyr, 1C), 150.1 (C-N(CH<sub>3</sub>)<sub>2</sub>, 1C), 143.8 (pyr, 2C), 143.1 (C=C, 1C), 130.4 (Ar, 2C), 122.5 (C=C, 1C), 122.0 (pyr, 2C), 115.9 (Ar, 1C), 115.0 (Ar, 2C), 47.7 (NCH<sub>3</sub>, 1C), 21.0 (CH(CH<sub>3</sub>)<sub>2</sub>, 4C) ppm. MS (ESI-TOF, in acetonitrile) m/z [M<sup>+</sup>]: calcd for C<sub>20</sub>H<sub>27</sub>N<sub>2</sub> 295.2174; found 295.2183.

*Trans*-4-(4'-(*N,N*-dicyclohexylamino)styryl)-*N*-methylpyridinium iodide (4) was synthesized based on a literature procedure.<sup>[15]</sup> *N,N*-dicyclohexylaminobenzaldehyde (75 mg, 0.26 mmol), *N*-methylpicolinium iodide (61 g, 0.26 mmol) and piperidine (a few drops) were added to absolute ethanol (5 mL) in a round bottom flask. This mixture was refluxed overnight. The product was purified by crystallization using ethanol. The product was obtained as a red powder (33 mg, 25%). <sup>1</sup>H NMR (CDCl<sub>3</sub>, 400 MHz): δ 8.73 (d, J = 6.7 Hz, pyr-H, 2H), 7.79 (d, J = 6.7 Hz, pyr-H, 1H), 7.57 (d, J = 15.8 Hz, C=CH, 1H), 7.44 (d, J = 9.0 Hz, Ar-H, 2H), 6.85 (d, J = 9.0 Hz, Ar-H, 2H), 6.81 (d, J = 15.8 Hz, C=CH, 1H), 3.42 (ddd, J = 15.1, 11.4, 3.4 Hz, Cy-H, 2H), 1.87-1.12 (m, Cy-H, 20H) ppm. <sup>13</sup>C NMR (CDCl<sub>3</sub>, 100 MHz): δ 154.3 (pyr, 1C), 151.8 (C-N(CH<sub>3</sub>)<sub>2</sub>, 1C), 143.7 (pyr, 2C), 143.2 (C=C, 1C), 130.2 (Ar, 2C), 122.4 (C=C, 1C), 122.0 (pyr, 2C), 115.7 (Ar, 1C), 115.6 (Ar, 2C), 58.3 (Cy, 2C), 47.5 (NCH<sub>3</sub>, 1C), 31.3 (Cy, 4C), 26.4 (Cy, 4C), 25.6 (Cy, 2C) ppm. MS (ESI-TOF, in acetonitrile) m/z [M<sup>+</sup>]: calcd. for C<sub>26</sub>H<sub>35</sub>N<sub>2</sub> 375.2800; found 375.2771.

## 2.2.2 Equipment

UV-Vis spectroscopy studies on solids were carried out with an Avantes Avalight DH-S-BAL with deuterium and halogen lamps used as the light source. An Avantes Avaspec 2048L is used as the detector. Both are connected through a fiber optic cable. For the UV-Vis spectroscopic studies of the probe molecules in solution, a Cary 50 spectrophotometer from Varian was used. NMR spectra were recorded at 298 K using a Varian 400 MHz NMR spectrometer. Chemical shifts are reported in ppm and referenced against the residual solvent signal. Mass spectra were obtained using an LCT Premier XE mass spectrometer from Waters Micromass using electron spray injection (ESI) as the ionization method. Scanning electron microscope (SEM) images were acquired on a Phenom SEM (Phenom World) equipped with a CsB6 filament at 5 kV in backscatter electron (BSE) mode. Ar physisorption isotherms were recorded using a Micromeritics Tristar 3000 setup operating at 77 K. Prior to the physisorption measurements, zeolite MFI and FAU were sieved using only the fraction 75≤x≤90 μm. The samples were dried in vacuum at 673 K overnight. X-ray diffractograms were recorded on a Bruker D2 Phaser. Before X-ray measurements, the zeolite powders were calcined at 773 K. Temperature programmed desorption

of ammonia ( $\text{NH}_3$ -TPD) was performed on a Micromeritics ASAP-2020 equipped with a TCD detector. Prior to  $\text{NH}_3$ -TPD, 0.1 g of catalyst was outgassed in He for 1 h at 873 K with a heating ramp of  $10 \text{ K min}^{-1}$ . For zeolite Y, a heating ramp of  $2 \text{ K min}^{-1}$  was used, pausing at 353 K and 423 K for 2 h. Ammonia was adsorbed at 373 K until saturated, followed by flushing with He for 120 min at 373 K. The ammonia desorption was monitored using the TCD detector until 873 K (ZSM-5: 973 K) with a ramp of  $5 \text{ K min}^{-1}$ , using a flow of  $25 \text{ mL min}^{-1}$ . The number of acid sites was calculated by taking the area under the TPD curve.

### 2.2.3 Methods

The amount of probe molecule adsorption on the zeolite powders versus time was studied by stirring a suspension of the zeolite powder in an ethanol solution containing one of the probes. Before the adsorption experiments, zeolite powders were calcined in vials at 773 K for 6 h. The vials containing the zeolite powders were sealed at 373 K to minimize adsorption of water and cooled down to room temperature. 20 or 50 mg of zeolite powder was stirred with one of the probes **1–4** in ethanol in various concentrations; the resulting suspension was 50 mL. Samples were taken every hour for up to 8 h and then daily for 5 days, taking care to take samples only from a properly homogenized suspension. Samples were immediately filtered using a  $0.45 \mu\text{m}$  PTFE filter. At the end of the experiment the zeolite powders were washed with ethanol and dried in air. Some probe degradation was observed in acidic environments, likely caused by hydrolysis, the reverse of the reaction illustrated in Scheme 2.2. Indicative of such probe degradation is the emergence of a band in the UV-Vis spectra at  $\sim 270 \text{ nm}$  corresponding to a less conjugated system. To minimize degradation dry solvents were used in the zeolite adsorption experiments, and zeolites were calcined before each experiment.

The probe concentration in each sample was measured from the absorption of the solution at the  $\lambda_{\max}$  of the probe molecule (**1** 481 nm; **2** 492 nm; **3** 495 nm; **4** 501 nm). The amount of probe adsorbed by the zeolite  $q_t$  ( $\text{mol}\cdot\text{g}^{-1}$ ) at time  $t$  was calculated using the following formula:

$$q_t = \frac{(c_0 - c_t)V}{m} \quad 2.1.$$

where  $c_0$  and  $c_t$  are the initial concentration and the concentration at time  $t$  ( $\text{mol L}^{-1}$ ),  $V$  is the volume of the solution (L) and  $m$  is the mass of the zeolite (g).

**Zeolite-probe materials** were made by suspending the zeolite powder in ethanol containing an excess of one of the probe molecules **1–4**. For experiments with  $\text{NEt}_3$ , an excess of  $\text{NEt}_3$  was added to the solution before addition of the zeolite. UV-Vis spectroscopy was used to determine the absorption spectra of the zeolite-probe combination.

The adsorption capacity and mechanism were studied by fitting three adsorption models to the data, which are described below.

a) the Pseudo First Order Equation (PFOE) as proposed by Lagergren.<sup>[16]</sup> The linearized PFOE is described by the equation

$$\ln(q_e - q_t) = \ln q_e - k_1 \cdot t \quad 2.2.$$

where  $q_e$  and  $q_t$  are the amount of probe adsorbed ( $\mu\text{mol g}^{-1}$ ) at equilibrium and time  $t$  (h), respectively and  $k_1$  is the rate constant ( $\text{h}^{-1}$ ).<sup>[17]</sup> This equation can be applied to the results by plotting  $\ln(q_e - q_t)$  versus  $t$ , which should give a straight line, while the intersect with the y-axis should correspond to  $\ln(q_e)$ .

b) the Pseudo Second Order Equation (PSOE) by Ho,<sup>[18]</sup> which is described by

$$\frac{dq_t}{dt} = k_2 (q_e - q_t)^2 \quad 2.3.$$

where  $k_2$  ( $\text{g mol}^{-1} \text{ min}^{-1}$ ) is the rate constant for pseudo second order sorption. The data was fitted to the PSOE using the linear form of this model, which is given by

$$\frac{t}{q_t} = \frac{1}{k_2 q_e^2} + \frac{1}{q_e} t \quad 2.4.$$

The initial adsorption rate  $h$  ( $\text{mmol g}^{-1} \text{ h}^{-1}$ ) can be derived from the PSOE and is given by

$$h = k_2 q_e^2 \quad 2.5.$$

derived from equation 2.3 as  $q_t$  approaches 0.

c) The intraparticle diffusion model (IDM) as described by Weber and Morris.<sup>[19]</sup> This model can provide more insight in the adsorption into microporous materials such as zeolites. It can be evaluated by the following expression

$$q_t = k_{id} \sqrt{t} \quad 2.6.$$

with  $k_{id}$  the intraparticle diffusion rate constant.

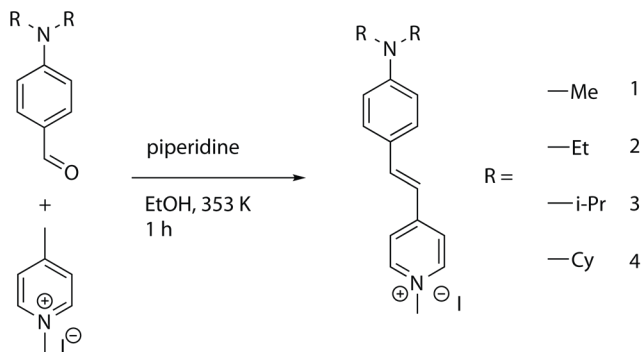
#### 2.2.4 Computational details

The ground states for probe molecules **1–4** were obtained by means of Density Functional Theory (DFT) calculations using the well-known B3LYP<sup>[20,21]</sup> functional with the 6-31+G(d,p) basis set. With all harmonic vibrational frequencies being real, all structures are minima on the potential energy surface. The optimized geometry in the ground state was used for the calculation of the dimensions of the molecule. The dimensions were determined by the smallest cylinder that fully enclosed the

entire molecule using the RADI software.<sup>[22,23]</sup> Van der Waals radii were taken as the minimum distance between the calculated atom positions and the walls of the cylinder. The diameter of this cylinder is used below as the diameter of the probe molecule.

Solvation energies were computed at the same level of theory for each probe molecule in ethanol with the Solvation Model based on Density (SMD).<sup>[24]</sup> The UV-Vis spectra were calculated for the molecules in this solvent environment by TD-DFT. The ground state geometries were employed throughout all excited state calculations. Thus, the theoretical excitation energies correspond to vertical transitions, which can be approximately identified as band maxima in experimental absorption spectra. All calculations were performed with the Gaussian 09 software.<sup>[25]</sup>

The simulations of movement of the probe molecules through straight pores of MFI zeolite were carried out with the Gaussian and plane waves (GPW) method implemented within the CP2K package.<sup>[26]</sup> The DFT-D3 dispersion-corrected Perdew, Burke and Ernzerhof (PBE) functional with the DZVP basis set and a plane waves density cut-off of 1000 Ry was used. The initial zeolite structure was taken from the IZA database<sup>[27]</sup> and further optimized using ab initio molecular dynamics simulations performing 10 ps isothermal-isobaric (NPT) simulations at 1 bar and 400 K followed by a canonical ensemble (NVT) simulation at 400 K with a time step of 2 fs. After initial equilibration, the structures from the snapshots with the minimal potential energy were taken and optimized. The structure with the minimal potential energy was used for all further calculations. A probe molecule was placed into the zeolite at the intersection of a sinusoidal and straight channel and systematically moved along the straight pore (step size 1 Å). To prevent movement of the zeolite and probe molecules during geometry optimizations, 5 atoms in the probe molecule and zeolite were fixed in the direction of the pore. The energies are given as the difference between the energy of the optimized geometry of the probe inside the pore versus the sum of the probe and zeolite in vacuum (not in contact with each other). The activation energy for movement from one intersection to the



Scheme 2.2. Synthesis of DAMPI derivatives 1 (methyl, Me), 2 (Ethyl, Et), 3 (isopropyl, i-Pr) and 4 (cyclohexyl, Cy). Synthesis of the precursors can be found in Scheme 2.1.

next was calculated from the difference of energies corresponding to the most and the least stable positions within the zeolite pore.

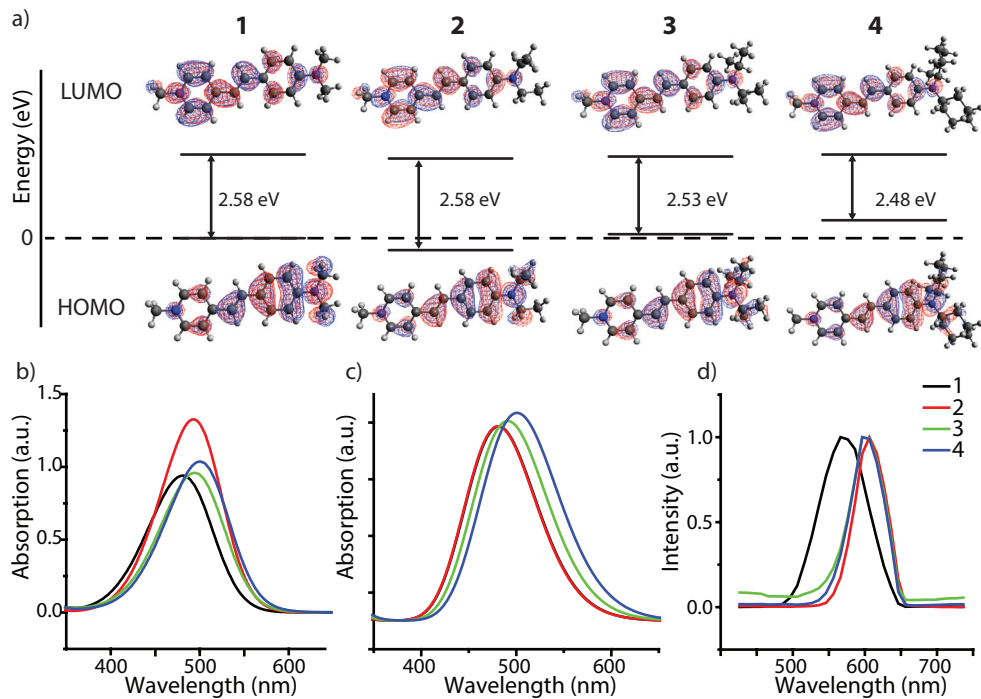
## 2.3 Results and discussion

### 2.3.1 Probe molecule synthesis and characterization

As illustrated in Scheme 2.2, Three derivatives of the commercially available DAMPI molecule were synthesized by changing the alkyl substituents on the aniline group from ethyl groups (2) to methyl (1), isopropyl (3) and cyclohexyl (4) groups, with the latter two compounds being new. These probe molecules are synthesized by a base-catalyzed reaction from a common picoline precursor and a modular benzaldehyde component. The benzaldehyde component is synthesized by a Vilsmeier reaction from the corresponding aniline (Scheme 2.1).<sup>[14]</sup> While diisopropylaniline is commercially available, the dicyclohexylaniline must be synthesized. This proved to be the most difficult step in the synthesis, because the amine moiety in this molecule is surrounded by extremely bulky substituents. A successful synthesis was effected using a microwave-assisted method, albeit with low yield, in sharp contrast to what has been reported for this reaction.<sup>[15]</sup>

Variation of the alkyl substituents provided a convenient handle to control the effective diameter of the probe molecule. The substituents on the benzaldehyde component can be systematically varied, in principle providing access to a broad range of DAMPI-type molecules. Powdered samples of the four probes show various shades of red, in line with the assumption that variation of the alkyl substituent has little effect on the electronic properties of these dyes. Notably, crystallization of probe molecule 3 yields dark green crystals (which give a red powder upon crushing), highlighting the large effect of intermolecular interactions. The color shift to green in the crystal could be due to intermolecular donor-acceptor interactions, if those parts of the molecule are in close proximity due to specific stacking within the crystal.<sup>[28]</sup>

As probe molecules 1–4 were designed to probe zeolite pore accessibility and diffusivity, a proper estimate of their molecular size is of prime importance. To this end, the molecular structure of the four probe molecules was determined by DFT calculations. The optimized geometry was enveloped with the smallest possible cylinder taking into account the Van der Waals radii, resulting in a typical length and diameter for each probe molecule. While the length of the cylinders showed only minor differences, the effect of the alkyl substituent is clearly reflected in the diameter (Figure 2.1c). Probe sizes thus range from 5.8 Å, which is approximately the size of a 10-ring zeolite micropore, to 10.1 Å, the size of a 14-ring zeolite pore.<sup>[29]</sup>



2

Figure 2.2. a) Molecular orbital plots of the probe molecules 1–4, showing the electron density at the amine moiety for the HOMO and electron density at the pyridine moiety for the LUMO. The energy level of the HOMO of probe 1 is taken as a reference point for the other HOMO and LUMO energy levels. b) UV-Vis absorption spectra (in ethanol) of probes 1–4 at a 25 mM concentration. c) UV-Vis absorption spectra of probes 1–4 as calculated by TD-DFT based on the optimized geometry of each probe molecule. d) Normalized emission spectra of probes 1–4 in solid state (probe molecules do not fluoresce in solution, *vide infra*) using a 488 nm laser as the excitation source.

Table 2.1. Properties of the probe molecules 1–4 used in this study. <sup>a</sup> in ethanol. <sup>b</sup> in the solid state (probes are non-fluorescent in solution). <sup>c</sup> calculated by DFT from the optimized geometry of the probe molecule, see section 2.2.3 for details.

| Probe molecule | $\lambda_{\text{max,abs}}^{\text{a}}$ (nm) | $\lambda_{\text{max,emi}}^{\text{b}}$ (nm) | $\epsilon$ ( $10^3 \text{ mol}^{-1} \text{ L}^{-1} \text{ cm}^{-1}$ ) | diameter <sup>c</sup> (Å) |
|----------------|--|--|---|---------------------------|
| 1              | 481  | 571  | 37.6  | 5.8                       |
| 2              | 493  | 606  | 53.1  | 6.5                       |
| 3              | 495  | 601  | 38.3  | 7.2                       |
| 4              | 501  | 601  | 41.5  | 10.1                      |

The UV-Vis spectra of the dilute, reddish solutions of probe molecules 1–4 (Figure

2.2b) show one main absorption band for all probes with a  $\lambda_{\max}$  ranging from 482 to 501 nm. Larger alkyl substituents cause a red shift in the absorption maximum (i.e. to longer wavelengths). This is likely caused by an increase in electron donation of the larger alkyl groups, rendering the amine moiety with stronger donor character. Indeed, DFT calculations show an increased electron density on the amine moiety for larger alkyl substituents (Figure 2.2a). The energy levels for the highest occupied molecular orbital (HOMO) also increase in energy with increased alkyl substitution, which is in line with previous results.<sup>[30]</sup> On the other hand, the lowest unoccupied molecular orbital (LUMO) does not change much throughout the probe series; the electron density for the LUMO is mostly located on the pyridine moiety, which remains unchanged in the series. As a result, the increased energy level for the HOMO thus leads to a smaller HOMO-LUMO gap and the associated red shift.<sup>‡‡</sup> The calculated UV-Vis spectra (Figure 2.2c) of these probe molecules correspond very well to those measured experimentally in ethanol. The relatively small shift in absorption maximum within the series again shows that modification of the probe

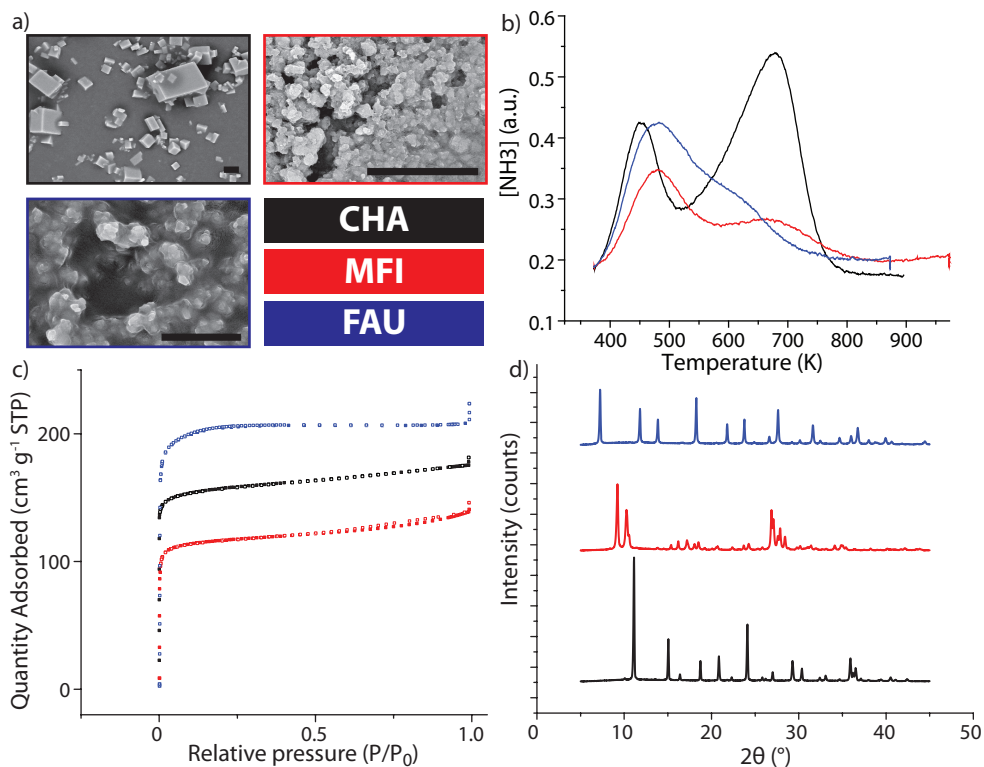


Figure 2.3. Details on the zeolite powders used in this work and the related physicochemical characterization. In each of these images and graphs, black represents CHA, red represents MFI and blue represents FAU. a) SEM images of the three zeolite materials under study. The scale bars represent 10  $\mu\text{m}$ . b) Ammonia TPD used to determine the number of acid sites of each zeolite. c) Ar physisorption isotherms for each zeolite. d) X-ray diffractograms of each zeolite material.

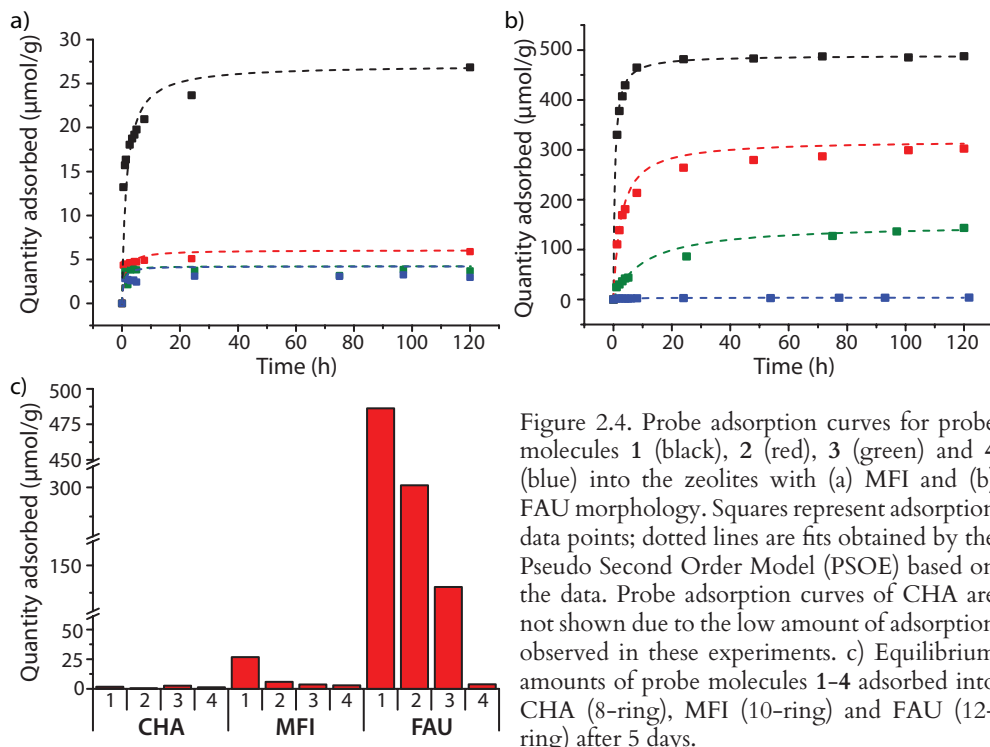


Figure 2.4. Probe adsorption curves for probe molecules 1 (black), 2 (red), 3 (green) and 4 (blue) into the zeolites with (a) MFI and (b) FAU morphology. Squares represent adsorption data points; dotted lines are fits obtained by the Pseudo Second Order Model (PSOE) based on the data. Probe adsorption curves of CHA are not shown due to the low amount of adsorption observed in these experiments. c) Equilibrium amounts of probe molecules 1–4 adsorbed into CHA (8-ring), MFI (10-ring) and FAU (12-ring) after 5 days.

molecule by substitution of the alkyl groups on the amine moiety does not lead to a large change in the electronic properties of the molecule.<sup>[9]</sup> Emission spectra of the four probe molecules were recorded for the powders using a 488 nm laser as the excitation source (Figure 2.2d); in solution, fluorescence is quenched by *cis-trans* isomerization.<sup>[8,31]</sup> The emission maxima of the probe molecules range from 571–606 nm; such a large Stokes shift is beneficial for probes that are used for imaging purposes.<sup>[32]</sup>

### 2.3.2 Adsorption of DAMPI-type molecules into zeolites

An overview of the three zeolite framework structures selected for the adsorption experiments (i.e. CHA with 8-ring pores, MFI with 10-ring pores and FAU with 12-ring pores) is given in Figure 2.3 and Table 2.2. While these zeolites appear as white powders, SEM images show that while CHA forms small crystals, MFI and FAU consist of small polycrystalline particles that form larger aggregated structures (Figure 2.3a). All zeolites have a 3-dimensional pore system, with the CHA and FAU frameworks having the same pores in all directions, while MFI has straight pores in one direction while the sinusoidal ones are oriented perpendicularly. The MFI pore system of large ZSM-5 crystals has previously been subject of a study by Roeffaers et al.<sup>[8]</sup> using probe molecule 2, arguing that this probe enters the pore mouths of the straight pores only in an end-on, stop-cock kind of fashion (i.e. pyridinium-side

first). Ar physisorption was performed to show the accessibility of the pore network and the micropore volume of each zeolite. Some mesoporosity is detected, but this is expected to be derived from the area between aggregates of zeolite particles, and therefore will have no substantial influence on probe adsorption (see Figure 2.3c).

Table 2.2. Properties of the zeolite materials used in this study. <sup>a</sup> This is an approximate value as in SAPO materials, the acidity is highly dependent on Si distribution in the framework.<sup>[37]</sup> <sup>b</sup> t-plot method. <sup>c</sup> All acid sites, as determined by ammonia TPD. <sup>d</sup> based on the largest pore diameter of relevant pores as stated in the International Zeolite Database. <sup>e</sup> Sinusoidal pores of MFI are slightly smaller but are not considered to be relevant for this research.<sup>[27]</sup>

| Pore system | Topology      | Si/Al ratio      | Micropore volume <sup>b</sup><br>(cm <sup>3</sup> g <sup>-1</sup> ) | Acid site density <sup>c</sup><br>(mmol g <sup>-1</sup> ) | Micropore size <sup>d</sup><br>(Å) |
|-------------|---------------|------------------|---|---|------------------------------------|
| 8-ring      | CHA (SAPO-34) | 0.2 <sup>a</sup> | 0.18  | 1.68  | 3.8                                |
| 10-ring     | MFI (ZSM-5)   | 15               | 0.13  | 0.74  | 5.6 <sup>e</sup>                   |
| 12-ring     | FAU (Y)       | 2.6              | 0.23  | 1.02  | 7.4                                |

The zeolite powders were contacted with solutions of the probe molecules, and samples were taken at regular intervals to investigate the rate of adsorption of the DAMPI-type molecules. The results are summarized in Figure 2.4 and Table 2.3.

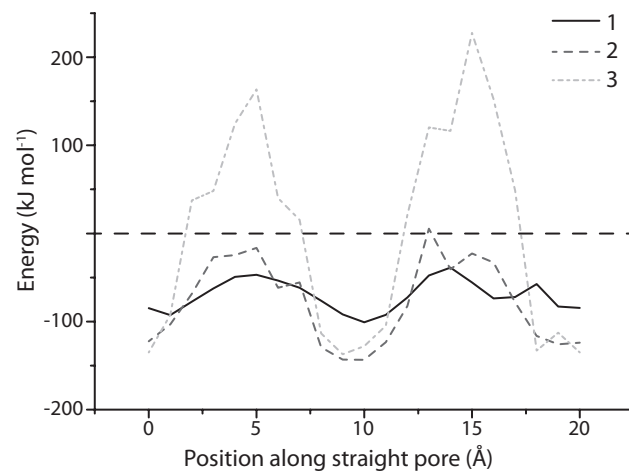


Figure 2.5. The structure of probe molecules 1–3 was optimized by DFT with intervals of 1 Å along the straight pore of a 10-ring zeolite (MFI). The corresponding energy level of each position is plotted here against position. The molecule and zeolite not in contact in vacuum is taken as a reference. The probe molecule was first placed at an intersection of a straight pore with a (perpendicular) sinusoidal pore and was then moved approximately two intersections further.

As expected, the zeolite with 8-ring pores shows no adsorption of any of the probes, confirming that probe molecules 1–4 are too large to enter these pores, which are only 3.8 Å in diameter. For the other zeolite materials under study, it was found that the quantity of probe molecule adsorbed usually plateaus in 1 or 2 days, (Figure 2.4 for FAU and MFI). Experiments were stopped after 5 days, as in some cases partial degradation of

the probe was observed if the contact time was longer than that. The total probe uptake after 5 days is shown for each zeolite in Figure 2.4c. There is significant uptake of probe molecule 1 ( $5.8 \text{ \AA}$ ) into the 10-MRPs of zeolite MFI ( $5.6 \text{ \AA}$ ), even though these pores were expected to be too small for probe inclusion, based on our

Table 2.3. Adsorption of probe molecules 1-4 into selected zeolite powders with increasing pore size.

| Zeolite type | Amount of probe adsorbed ( $\mu\text{mol g}^{-1}$ ) |       |       |     |
|--------------|---|-------|-------|-----|
|              | 1   | 2     | 3     | 4   |
| CHA          | 1.8   | 0.5   | 2.6   | 1.3 |
| MFI          | 26.5  | 5.9   | 3.7   | 3.0 |
| FAU          | 484.6   | 303.8 | 143.7 | 3.9 |

2

calculations. It is known that the similarly-sized *trans*-stilbene ( $5.7 \text{ \AA}$ ) also readily enters zeolite MFI.<sup>[33]</sup> Evidently, there is some degree of flexibility in either the probe molecule or the zeolite structure; the latter is indeed known to exhibit some flexibility in case of tight fits.<sup>[34,35]</sup> In addition, van der Waals radii, due to their statistical nature, can vary by few tenths of an Ångström depending on the system.<sup>[36]</sup> In contrast to probe molecule 1, probe 2 shows adsorption just above the detection limit while probes 3 and 4 do not show any adsorption.

To study these differences of adsorption into the MFI framework in more detail, DFT calculations were performed on probe molecules 1-3 within an MFI straight

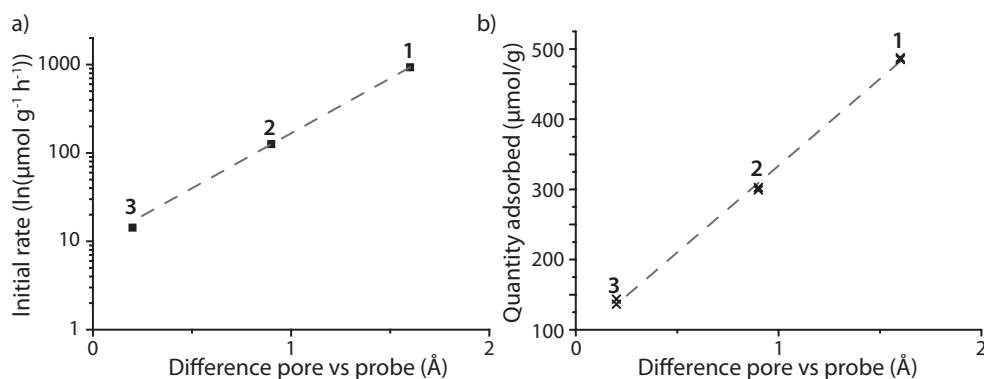


Figure 2.6. The initial rate (a) and the equilibrium amount (b) of the different probe molecules 1-3 adsorbed in FAU in comparison to the tightness of fit between probe and the zeolite pore. a) The initial rate is calculated from the Pseudo Second Order Equation and plotted on a logarithmic scale. The sizes of the probes 1-3 and zeolites can be found in Tables 2.1 and 2.2. The  $R^2$  value of the fit is 0.9997. b) Adsorbed amounts were recorded from adsorption experiments when the adsorption had reached a plateau, after 4 and 5 days. The  $R^2$  value of the fit is 0.9983.

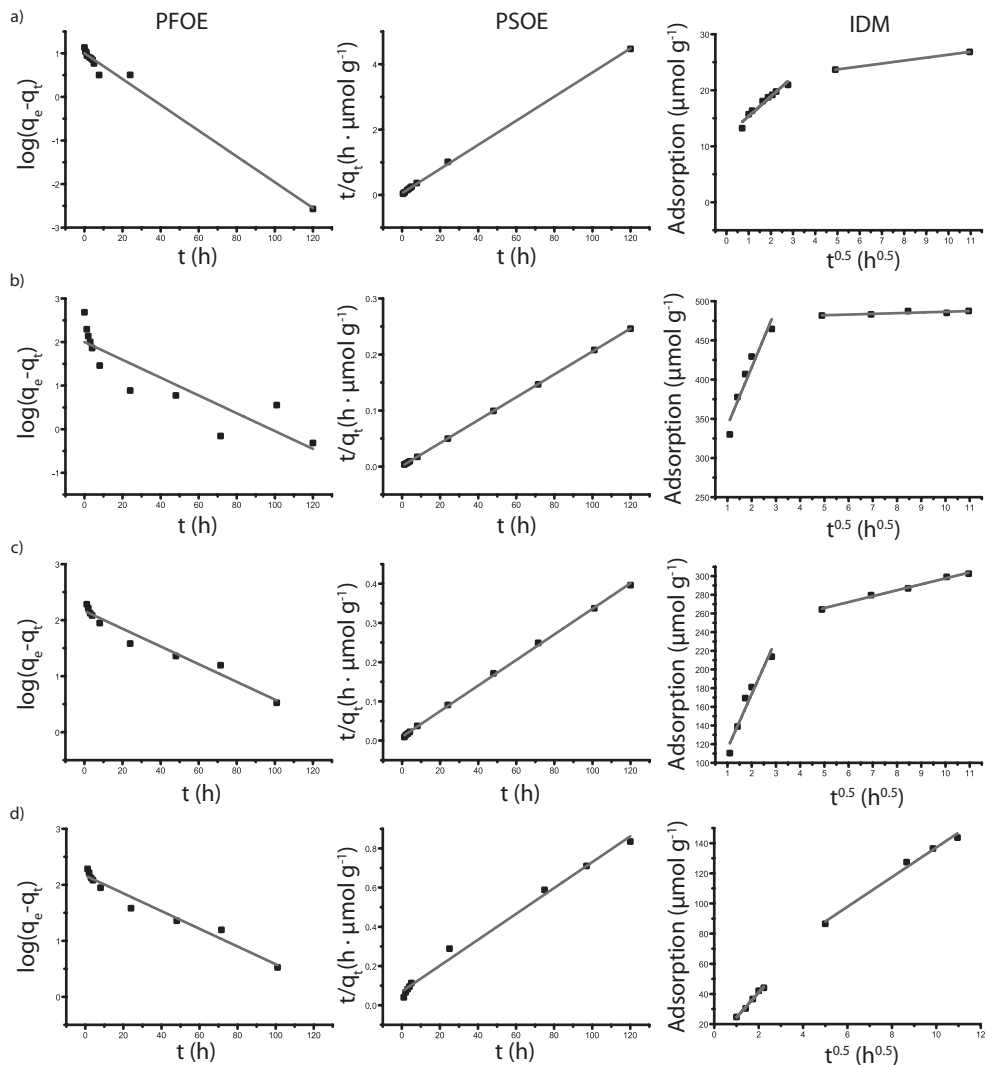


Figure 2.7. The application of the three models (PFOE, PSOE, IDM, see section 2.2.2.2) to the probe-zeolite combinations showing significant probe uptake: Probe molecule 1 in 10-ring pores (MFI) (a) as well as probe 1 (b), probe 2 (c) and probe 3 (d) in 12-ring pores (FAU). The linear variant of the PSOE is shown (see also Figure 2.4). In the IDM plot, two different linear regions can be observed, which apply to two different stages of adsorption.

pore. The molecule was moved along a straight pore stepwise from one intersection (with a sinusoidal pore) to the next intersection. The energy landscape obtained this way is shown in Figure 2.5. For probe molecule 1, the activation energy associated with this translocation is just  $50 \text{ kJ mol}^{-1}$ , which can be easily overcome at room temperature. Movement of probe molecule 2, however, should be very slow or negligible given the calculated activation energy of  $125 \text{ kJ mol}^{-1}$ , while probe 3

is unlikely to move through the pore ( $> 300 \text{ kJ mol}^{-1}$ ). These results are in line with the experimental adsorption results. For zeolite FAU, adsorption of varying amounts of probe molecules 1–3 is seen, while no significant amount of probe 4 is adsorbed: this is in line with what is calculated based on probe size. The initial rate of the adsorption is influenced by the size of the pore, showing that, as expected, the steric bulk of the molecule influences the speed at which the molecules move into or through the zeolite pores. The plot between the probe versus pore size difference (PPSD) and the natural logarithm of the initial rate of adsorption shows the relationship is exponential as a straight line is obtained from this plot (Figure 2.6a). This implies that the activation energy  $E_a$  of the adsorption of the probe into the zeolite is linearly related to the size of the probe.

Interestingly, the total amount of probe adsorbed is also influenced by probe size: the equilibrium adsorption amounts versus the PPSD also give a linear relationship (Figure 2.6b). The relatively small increase in volume between the probe molecules (due to steric bulk) cannot explain this large change in adsorption.<sup>§</sup> The equilibrium amount adsorbed is a thermodynamic parameter and must therefore be governed by physical (i.e. van der Waals or dipole interactions) or chemical (i.e. protonation) interactions of the probe molecule with the zeolite. These interactions become weaker with distance; it is therefore likely that the steric bulk surrounding the molecule limits the probe from effectively binding to the zeolite.

To gain more insight in the kinetics and mode of adsorption, three adsorption models were tested on the data. A comparison was first made between the Pseudo First Order Equation (PFOE)<sup>[16]</sup> and the Pseudo Second Order Equation (PSOE) models, two models applied extensively to adsorption of molecules into microporous materials.<sup>[38,39]</sup> These models are both empirical, but can be derived from the Langmuir adsorption model. The applicability of these models depends on the concentration of the probe with respect to the zeolite, with the PFOE giving better fits at higher probe/zeolite ratio and PSOE at a lower ratio.<sup>[39]</sup> However, as this ratio is not constant over the course of the experiment, the applicability of the model may differ over time.<sup>[38]</sup> It was found that a good fit could be obtained with the PFOE for the first 24 h of the experiment only (Figure 2.7). Moreover, the model was unable to predict the adsorbed amount at equilibrium. Because of

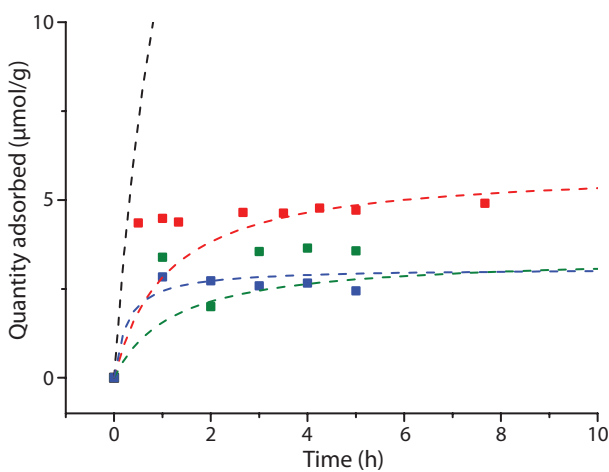


Figure 2.8. A close up of the first 10 h for the adsorption of probe molecules 1 (black), 2 (red), 3 (green) and 4 (blue) into a 10-ring zeolite (MFI), showing that for low adsorption of dyes, the model deviates from the experimental results.

this, the PFOE was discarded as model for the adsorption process. Conversely, the PSOE was found to fit well the adsorption of probe molecules 1–4 into zeolites over the complete time range. The application of the linear form of this model is shown in Figure 2.7, while Figure 2.4 shows how the model fits the adsorption curves. If the total adsorption is low, the experimental error hampers an accurate fit (Figure 2.8); therefore, only probes that were adsorbed in significant amounts (more than 10  $\mu\text{mol g}^{-1}$ ) were analyzed.

The PSOE can be applied to systems where the adsorption is dependent on the amount of available adsorption sites in the material and when desorption is not contributing to the overall rate.<sup>[18]</sup> The first condition is applicable to zeolites where a finite number of probes fit into the pores. The second condition was verified by experiment; probes adsorbed into zeolites do not desorb when stirred in a solution with ethanol. Apparently, the equilibrium is completely on the adsorbed side, so there must be a significant energy gain. A good fit obtained with the PSOE is usually indicative of a chemical interaction between adsorbent and adsorbate, as it is associated with the Langmuir adsorption model.<sup>[40]</sup> The probe molecules used contain several functional groups, most notably an amine group which can be protonated. The good fit with the model therefore again suggests that the molecules are chemically bound to the acid sites of the zeolite. Protonation of the probe molecule by an acid site is also supported by the linear relationship between PPSD and the equilibrium amount adsorbed for probe 1–3 in FAU (Figure 2.6b): increased steric bulk will negatively influence the ability of the zeolite to protonate the probe molecule because of the increase in probe–zeolite proton distance.

Table 2.4. Quality of fits of kinetic models for probe/zeolite combinations with sufficient adsorption and initial rate of reaction for the PSOE. <sup>a</sup>  $R^2_2$  is unity as only two data points fell within this region.

| Zeolite | Probe | PFOE   | PSOE   | IDM  |         |                |
|---------|-------|--------|--------|--|---------|----------------|
|         |       | $R^2$  | $R^2$  | initial rate<br>$\mu\text{mol g}^{-1} \text{h}^{-1}$ | $R^2_1$ | $R^2_2$        |
| MFI     | 1     | 0.8848 | 0.9994 | 17.5   | 0.9484  | 1 <sup>a</sup> |
| FAU     | 1     | 0.6971 | 1      | 932.1  | 0.9194  | 0.7062         |
| FAU     | 2     | 0.9623 | 0.9994 | 126.0  | 0.9246  | 0.9865         |
| FAU     | 3     | 0.9539 | 0.9914 | 14.3   | 0.9893  | 0.9883         |

The Intraparticle Diffusion Model (IDM)<sup>[19]</sup> is a model closely related to the PSOE and can yield additional insight in the diffusional behavior of a system.<sup>[40]</sup> This model assumes that (slow) diffusion of molecules within pores influences the overall adsorption rate.<sup>[40]</sup> The rate limiting step in this type of adsorption studies is usually film diffusion or intraparticle diffusion.<sup>[41,42]</sup> The Weber plot of  $t^{0.5}$  versus  $q_t$  used in this model shows two separate linear regions (Figure 2.7). The timeframe of the

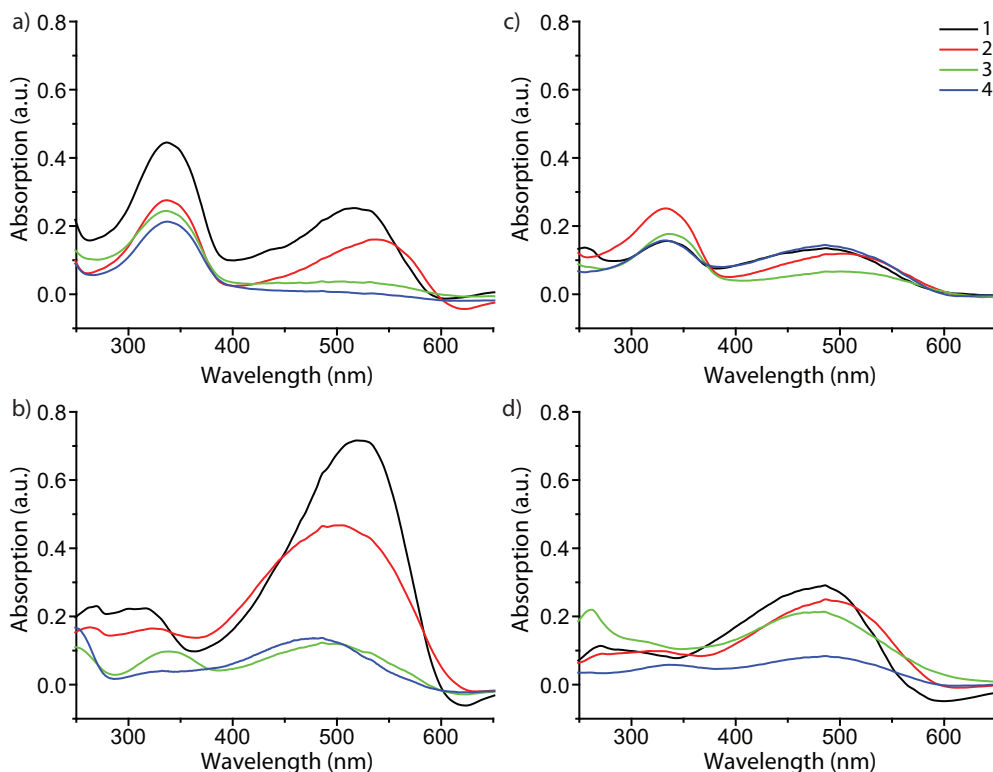


Figure 2.9. UV-Vis absorption spectra of probe molecules 1-4 adsorbed in MFI and FAU. Left: Probe molecules 1-4 in MFI (a) without and (b) with  $\text{NEt}_3$  present. Right: Probe molecules 1-4 in FAU (c) without and (d) with  $\text{NEt}_3$  present. Experiments on 8-ring pore zeolites are excluded as no significant UV-Vis absorption was observed.

first region is longer than the typical time attributed to film diffusion in adsorption experiments<sup>[43]</sup>; it is therefore likely that film diffusion has already taken place before the first data point. The first linear region of the plot, representing the first 24 h, is therefore likely to be due to internal mass transfer limitations i.e. intraparticle diffusion.<sup>[44]</sup> The slope of this region shows that intraparticle diffusion is dependent on the PPSD, with a larger PPSD leading to faster diffusion. The second linear region of the plot, representing the experiment from 24 h till the end is almost flat for most probe-zeolite combinations, showing that equilibrium has been reached. However, for probe molecule 1 in MFI and probes 2 and 3 in FAU, this region of the plot shows a slight slope, indicating equilibrium has not yet been reached. Possibly, the first region signifies diffusion through the aggregates of zeolite particles, while the second region corresponds to diffusion into the zeolite pores (see Figure 2.3a).

As pointed out above, processes governing diffusion on time scales relevant to catalysis are mostly not taken into account in our results.<sup>[45]</sup> Because of the tight fit between probe molecule and zeolite and the resulting slow diffusion processes, the adsorption process of the DAMPI-type molecules goes well beyond this time scale.

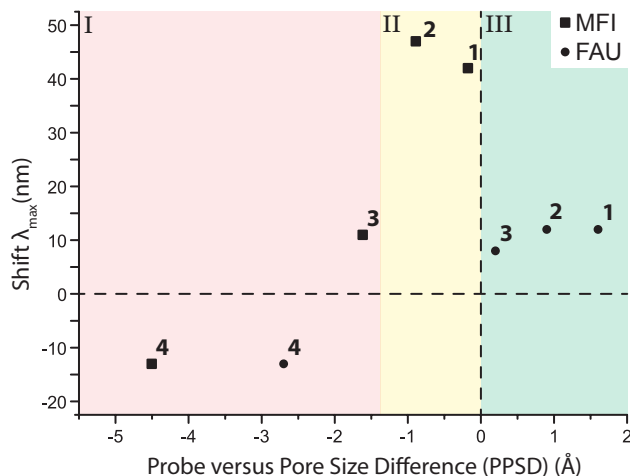


Figure 2.10. The observed spectral shift  $\Delta \lambda_{\max}$  of the probe molecule adsorbed onto MFI (■) and FAU (●) with respect to the  $\lambda_{\max}$  in ethanol solution, plotted against the size difference between the probe molecule and the zeolite pore. The diameters of probe molecules and zeolite pores can be found in Table 2.1 and 2.2.

It is therefore clear DAMPI-type molecules are most suitable to study uptake and accessibility on longer timescales.

### 2.3.3 Spectroscopic study of adsorbed probe molecules on zeolites

Although the uptake of some probes was low due to their inability to access the zeolite pore network, UV-Vis absorption spectra could be measured for each probe taken up by MFI and FAU. This allowed us to study the influence of the framework environment on the probes' spectroscopic properties. The results are summarized in Figure 2.9. Invariably, the absorption spectra of the probes show an intense band at 330 nm. As absorption at this wavelength was also reported for probe molecule 2 in aqueous HCl, it is postulated that the 330 nm band can be attributed to protonation of the amine moiety of the probe by the Brønsted acid sites in the zeolite.<sup>[46,47]</sup> To verify this hypothesis, the adsorption experiments of probe molecules 1–4 on the zeolite materials under study were repeated, but now in the presence of triethylamine, in order to neutralize the acid sites of the zeolites.<sup>[8]</sup>

For the quenched zeolites that were stained this way (without available protons to react with the probe molecules), the band at 330 nm is (almost entirely) absent, confirming the interaction of the probes with the acid sites of the zeolite. Additionally, an MFI sample stained with probe molecule 1 was contacted with both pure ethanol and ethanol containing NEt<sub>3</sub>. It was found that the solution containing base is able to leach the probe molecule from the zeolite, while the one without the addition of the base is not. Additionally, the amount of probe adsorbed never exceeds the amount of available acid sites in these experiments.<sup>§§</sup> Figure 2.10

shows that the main absorption bands of probe molecule 1 ( $\Delta = 42$  nm), probe 2 ( $\Delta = 47$  nm) and probe 3 ( $\Delta = 11$  nm) are red-shifted within MFI with respect to the dilute probe solutions. On the other hand, probe molecule 4 is blue-shifted ( $\Delta = -13$  nm). A similar trend for the four probes is observed in FAU (1:  $\Delta = 12$  nm, 2:  $\Delta = 12$  nm, 3:  $\Delta = 8$  nm, 4:  $\Delta = -13$  nm). One reason for these spectral shifts is the interaction of the zeolite with the push-pull conjugated system of DAMPI; the absorption properties of these probe molecules are known to be dependent on solvent polarity.<sup>[48–50]</sup> The zeolite is in this case evidently comparable to a highly polar solvent.<sup>[51,52]</sup>

The differences in the shifts of the probes are related to the PPSD, although the relationship is not straightforward, as is shown in Figure 2.10. In this figure, region I includes probe molecules that are too large to enter the pores, which have a small or even negative shift. The other regions both contain probe molecules within pores. Region II is a narrow band within the PPSD that can be associated with a tight fit between the probe and the zeolite, with a corresponding large influence on the absorption maximum. Region III represents a loose fit, leading again only to a small change in absorption properties. Interestingly, the effect of confinement is seen with all probe-zeolite combinations, even the probes that do not fit into the pore network. Possibly, the T-shaped probe molecule is inserted end-on into a zeolite pore, thus allowing the molecule to behave as if it was completely adsorbed.<sup>[8]</sup> The sensitivity of the spectroscopic properties of this probe series for the microscopic environment can be thus be used to gain more insight in the interaction of the probe with its surroundings.

2

## 2.4 Conclusions

Distinct fluorescent DAMPI-type molecules of sizes comparable to zeolite pore diameters were successfully synthesized by changing the steric bulk substituents using alkyl groups, while the electronic properties of this series of molecular probes were kept almost constant. The accessibility of these probe molecules into different zeolite framework structures, namely CHA (8-MRPs), MFI (10-MRPs) and FAU (12-MRPs), was evaluated and a correlation was found between the calculated size of a molecule and its ability to enter the zeolite pores. An increase in steric bulk leads to a decrease in the initial adsorption rate, because bulky molecules move slower through the zeolite pores. Additionally, steric bulk influences the equilibrium amount of probe adsorbed into FAU, presumably by increasing the distance between the probe molecule and the zeolite pore wall. Kinetic experiments show that while internal mass transfer limitations play a role when there is a tight fit between the probe and the zeolite, this effect is less pronounced when the probe easily fits in the pores.

The probe molecules are protonated upon adsorption into the zeolite by a Brønsted acid site, which causes irreversible adsorption of the probe molecules. Adsorption into the pores of the zeolite is accompanied by the emergence of a second band in

the UV-Vis spectrum, caused by protonation. Additionally, the main absorption band is shifted, with a large spectral shift indicating a tight fit of the DAMPI-type molecule and the zeolite pore. In this way, probe molecules give valuable information about the interaction with the zeolite that goes beyond information on pore accessibility.

The approach presented here shows that steric hindrance can be systematically added to probe molecules to modify their size and accessibility. These probe molecules can be used to study physicochemical properties of a wide range of materials and possibly predict effective pore sizes based on the adsorption of a series of probe molecules differing in size.

## Acknowledgements

Dr. Javier Ruiz-Martínez (Utrecht University, UU) is acknowledged for useful discussions, Katarina Stančiaková (UU) and Dr. Rosa Bulo (UU) for help with calculating the probe movement inside MFI pores, Henk Klein (UU) for recording mass spectra of **1–4** and Ramon Oord (UU) and Pasi Paalanen (UU) for zeolite characterization.

## 2.5 Notes and references

‡ According to the original definition, SAPO-34 is not a zeolite, as it is not an aluminosilicate material. However, within the scope of this PhD work there is no distinction between these so-called zeotype materials and zeolite materials as this research only deals with the relative size of the micropores.

## The HOMO-LUMO gap does not coincide with the absorption maximum of the probes; this is because the Kohn-Sham DFT model was used.<sup>[53]</sup>

§ The enclosing cylinder used in the probes' size determination is only 1.5 times larger for probe molecule **3** than for probe **1**.

§§ For probe molecule **1** in FAU 0.5 mmol g<sup>-1</sup> is adsorbed (Figure 2.4), while the amount of available acid sites is 1 mmol g<sup>-1</sup> (Table 2.3).

- [1] B. Smit, T. L. M. Maesen, *Nature* **2008**, *451*, 671–678.
- [2] T. F. Degnan, *J. Catal.* **2003**, *216*, 32–46.
- [3] S. M. Csicsery, *Zeolites* **1984**, *4*, 202–213.
- [4] E. T. C. Vogt, G. T. Whiting, A. Dutta Chowdhury, B. M. Weckhuysen, *Adv. Catal.* **2015**, *58*, 143–314.
- [5] U. Olsbye, S. Svelle, M. Bjørgen, P. Beato, T. V. W. Janssens, F. Joensen, S. Bordiga, K. P. Lillerud, *Angew. Chem. Int. Ed.* **2012**, *51*, 5810–5831.
- [6] J. A. Martens, D. Verboekend, K. Thomas, G. Vanbutsele, J. Pérez-Ramírez, J.-P. Gilson, *Catal. Today* **2013**, *218–219*, 135–142.
- [7] C. Seebacher, J. Rau, F.-W. Deeg, C. Bräuchle, S. Altmaier, R. Jäger, P. Behrens, *Adv.*

- Mater.* 2001, **13**, 1374–1377.
- [8] M. B. J. Roeffaers, R. Ameloot, M. Baruah, H. Uji-i, M. Bulut, G. De Cremer, U. Müller, P. A. Jacobs, J. Hofkens, B. F. Sels, D. E. De Vos, *J. Am. Chem. Soc.* 2008, **130**, 5763–5772.
- [9] L. R. Aramburo, J. Ruiz-Martínez, J. P. Hofmann, B. M. Weckhuysen, *Catal. Sci. Technol.* 2013, **3**, 1208–1214.
- [10] M. H. F. Kox, E. Stavitski, B. M. Weckhuysen, *Angew. Chem. Int. Ed.* 2007, **46**, 3652–3655.
- [11] C. Baerlocher, L. B. McCusker, [www.iza-structure.org/databases](http://www.iza-structure.org/databases), 2017, retrieved: 1 August.
- [12] S. Long, L. Chen, Y. Xiang, M. Song, Y. Zheng, Q. Zhu, *Chem. Commun.* 2012, **48**, 7164–7166.
- [13] L. Shi, M. Wang, C. A. Fan, F.-M. M. Zhang, Y. Q. Tu, *Org. Lett.* 2003, **5**, 3–8.
- [14] C. Wink, H. Detert, *J. Phys. Org. Chem.* 2013, **26**, 137–143.
- [15] G. Clemo, G. Swan, *J. Chem. Soc.* 1938, 1454–1455.
- [16] S. Lagergren, *K. Svenska Vetenskapsakad. Handl.* 1898, **24**, 1–39.
- [17] Y. S. Ho, G. McKay, *Chem. Eng. J.* 1998, **70**, 115–124.
- [18] Y. S. Ho, *J. Hazard. Mater.* 2006, **136**, 681–689.
- [19] W. J. Weber Jr., J. C. Morris, *J. Sanit. Div. Am. Soc. Civ. Eng.* 1963, **89**, 31–59.
- [20] A. D. Becke, *J. Chem. Phys.* 1993, **98**, 5648–5652.
- [21] C. Lee, W. Yang, R. G. Parr, *Phys. Rev. B* 1988, **37**, 785–789.
- [22] M. Petitjean, *J. Chem. Inf. Model.* 1992, **32**, 331–337.
- [23] M. Petitjean, *Appl. Algebr. Eng. Commun. Comput.* 2012, **23**, 151–164.
- [24] A. V. Marenich, A. Majumdar, M. Lenz, C. J. Cramer, D. G. Truhlar, *Angew. Chem. Int. Ed.* 2012, **51**, 12810–12814.
- [25] M. J. Frisch, G. W. Trucks, H. B. Schlegel, G. E. Scuseria, M. A. Robb, J. R. Cheeseman, G. Scalmani, V. Barone, B. Mennucci, G. A. Petersson, H. Nakatsuji, M. Caricato, X. Li, H. P. Hratchian, A. F. Izmaylov, J. Bloino, G. Zheng, J. L. Sonnenberg, M. Hada, M. Ehara, K. Toyota, R. Fukuda, J. Hasegawa, M. Ishida, T. Nakajima, Y. Honda, O. Kitao, H. Nakai, T. Vreven, J. J. A. Montgomery, J. E. Peralta, F. Ogliaro, M. Bearpark, J. J. Heyd, E. Brothers, K. N. Kudin, V. N. Staroverov, R. Kobayashi, J. Normand, K. Raghavachari, A. Rendell, J. C. Burant, S. S. Iyengar, J. Tomasi, M. Cossi, N. Rega, J. M. Millam, M. Klene, J. E. Knox, J. B. Cross, V. Bakken, C. Adamo, J. Jaramillo, R. Gomperts, R. E. Stratmann, O. Yazyev, A. J. Austin, R. Cammi, C. Pomelli, J. W. Ochterski, R. L. Martin, K. Morokuma, V. G. Zakrzewski, G. A. Voth, P. Salvador, J. J. Dannenberg, S. Dapprich, A. D. Daniels, Ö. Farkas, J. B. Foresman, J. V. Ortiz, J. Cioslowski, D. J. Fox, *Gaussian 09 (revision B.01)*, Gaussian Inc. 2009.
- [26] J. Vandevondele, M. Krack, F. Mohamed, M. Parrinello, T. Chassaing, J. J. J. Hutter, *Comput. Phys. Commun.* 2005, **167**, 103–128.
- [27] IZA, in *Database of Zeolite Structures*, Retrieved: 2 August, 2016.
- [28] E. H. A. Beckers, S. C. J. Meskers, A. P. H. J. Schenning, Z. Chen, F. Würthner, P. Marsal, D. Beljonne, J. Cornil, R. A. J. Janssen, *J. Am. Chem. Soc.* 2006, **128**, 649–657.
- [29] J. Martinez-Triguero, M. J. Diaz-Cabanas, M. A. Cambor, V. Fornes, T. L. M. Maesen, A. Corma, *J. Catal.* 1999, **182**, 463–469.
- [30] Y. Huang, T. Cheng, F. Li, C.-H. Huang, T. Hou, A. Yu, X. Zhao, X. Xu, *J. Phys. Chem. B* 2002, **106**, 10020–10030.
- [31] S. Cicchi, P. Fabbrizzi, G. Ghini, A. Brandi, P. Foggi, A. Marcelli, R. Righini, C. Botta, *Chem. Eur. J.* 2009, **15**, 754–764.
- [32] T. Beppu, K. Tomiguchi, A. Masuhara, Y.-J. Pu, H. Katagiri, *Angew. Chem. Int. Ed.* 2015, **54**, 7332–7335.
- [33] F. Gessner, A. Olea, J. H. Lobaugh, L. J. Johnston, J. C. Scaiano, *J. Org. Chem.* 1989, **54**, 259–261.
- [34] T. R. Forester, W. Smith, *J. Chem. Soc. Faraday Trans.* 1997, **93**, 3249–3257.

- [35] J. Kärger, T. Binder, C. Chmelik, F. Hibbe, H. Krautscheid, R. Krishna, J. Weitkamp, *Nat. Mater.* **2014**, *13*, 333–343.
- [36] S. S. Batsanov, *Inorg. Mater.* **2001**, *37*, 871–885.
- [37] D. Verboekend, M. Milina, J. Pérez-Ramírez, *Chem. Mater.* **2014**, *26*, 4552–4562.
- [38] Y. Liu, L. Shen, *Langmuir* **2008**, *24*, 11625–11630.
- [39] S. Azizian, *J. Colloid Interface Sci.* **2004**, *276*, 47–52.
- [40] W. Plazinski, J. Dziuba, W. Rudzinski, *Adsorption* **2013**, *19*, 1055–1064.
- [41] D. Borah, S. Satokawa, S. Kato, T. Kojima, *J. Hazard. Mater.* **2009**, *162*, 1269–1277.
- [42] K. Gupta, U. C. Ghosh, *J. Hazard. Mater.* **2009**, *161*, 884–892.
- [43] J. Chen, Y. Cai, M. Clark, Y. Yu, *PLoS One* **2013**, *8*, e60243.
- [44] V. Fierro, V. Torné-Fernández, D. Montané, A. Celzard, *Microporous Mesoporous Mater.* **2008**, *111*, 276–284.
- [45] J. van den Bergh, J. Gascon, F. Kapteijn, in *Zeolites and Catalysis, Synthesis, Reactions and Applications* (Eds.: J. Čejka, A. Corma, S. Zones), Wiley-VCH, Weinheim, 2010, pp. 361–387.
- [46] A. P. Phillips, *J. Org. Chem.* **1949**, *14*, 302–305.
- [47] S. T. Abdel-Halim, *J. Lumin.* **2011**, *131*, 30–35.
- [48] F. Laeri, in *Host-Guest-Systems Based on Nanoporous Crystals* (Eds.: F. Laeri, F. Schüth, U. Simon, M. Wark), Wiley-VCH, Weinheim, 2003, p. 506.
- [49] K. Hoffmann, PhD Thesis, Technischen Universität Berlin, 2002, pp. 62–63.
- [50] X. Wang, Y. Zhou, G. Zhou, W. Jiang, M. Jiang, *Bull. Chem. Soc. Jpn.* **2002**, *75*, 1847–1854.
- [51] S. Uppili, K. J. Thomas, E. M. Crompton, V. Ramamurthy, *Langmuir* **2000**, *16*, 265–274.
- [52] L. Gilbert, C. Mercier, C. Mercer, in *Heterogeneous Catalysis and Fine Chemicals III* (Eds.: J. Barbier, J. Barrault, C. Bouchoule, D. Duprez, C. Montassier, M. Guisnet, G. Pérot), Elsevier, Amsterdam, 1993, pp. 51–66.
- [53] E. J. Baerends, O. V. Gritsenko, R. van Meer, *Phys. Chem. Chem. Phys.* **2013**, *15*, 16408–16425.



# CHEMISTRY

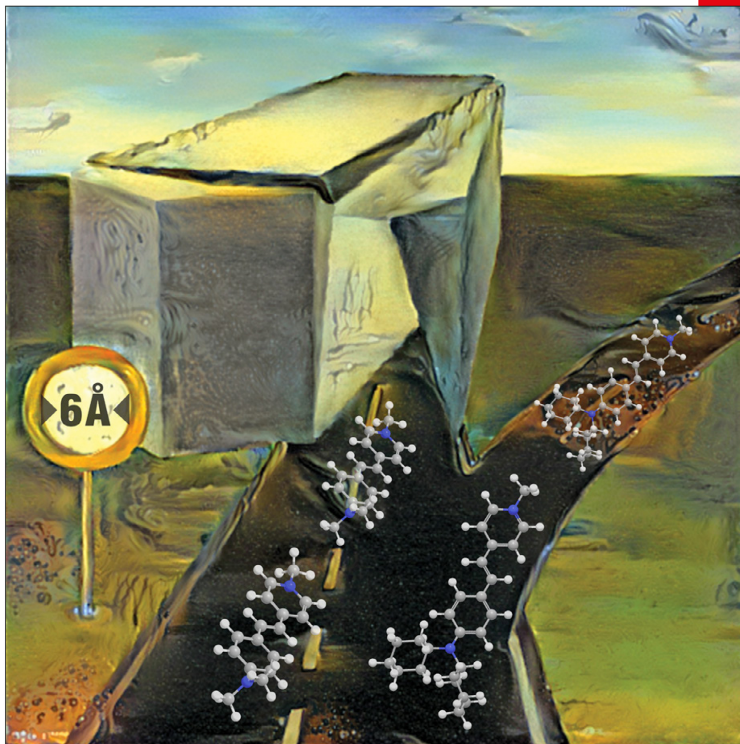
## A European Journal

[www.chemeurj.org](http://www.chemeurj.org)

A Journal of



2017-23/00



**Front Cover Picture:**

B. M. Weckhuysen et al.  
Probing Zeolite Crystal Architecture and Structural Imperfections  
using Differently Sized Fluorescent Organic Probe Molecules

**Supported by**

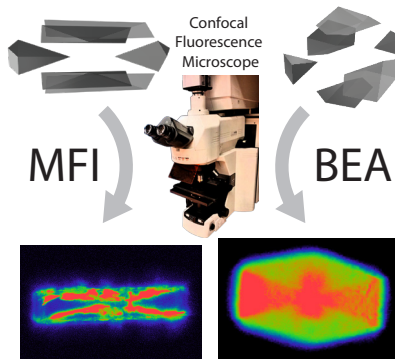


**WILEY-VCH**

# Chapter 3

## Probing Zeolite Crystal Architecture and Structural Imperfections Using Differently Sized Fluorescent Organic Probe Molecules

A micro-spectroscopic method is described to probe the accessibility of large zeolite crystals using the series of DAMPI-type fluorescent probes described in Chapter 2. The probes are used to stain large zeolite crystals with MFI topology and allow 3D mapping of the resulting fluorescence using confocal fluorescence microscopy. The 90° intergrowth sections of MFI crystals are prone to develop structural imperfections, which act as entrance routes for the probes into the zeolite crystal. The developed method was extended to BEA crystals, showing that the previously observed hourglass pattern is a general feature of BEA crystals with this morphology. Polarization-dependent measurements could spatially resolve the architecture-dependent internal pore structure of microporous materials, which is difficult to assess using other characterization techniques, such as X-ray diffraction.



**Based on:** "Probing Zeolite Crystal Architecture and Structural Imperfections using Differently Sized Fluorescent Organic Probe Molecules", Frank C. Hendriks, Joel E. Schmidt, Jeroen A. Rombouts, Koop Lammertsma, Pieter C. A. Bruijnincx, and Bert M. Weckhuysen, *Chemistry: A European Journal*, 2017, 23, 6305–6314.

### 3.1 Introduction

In the previous Chapter, the synthesis of a series of rod-shaped probe molecules of tunable size, based on the *trans*-4-(4-(diethylamino)styryl)-*N*-methylpyridinium iodide (DAMPI) scaffold was described.<sup>[1]</sup> This series was then used to probe the accessibility of zeolite powders, namely CHA with 8-membered ring pores (MRPs), MFI with 10-MRPs and FAU with 12-MRPs. The diameter of the probes was found to correlate with both the accessibility of and the rate of adsorption into the zeolite pore network. Furthermore, the UV-Vis absorption spectra of the probe molecules were indicative of the interaction with the zeolite framework.

Advantageously, the DAMPI probe molecules only exhibit fluorescence if positioned in a confined environment, such as a zeolite pore, with fluorescence in solution being fully quenched by *cis-trans* isomerization.<sup>[2]</sup> Furthermore, it is one of the smallest fluorescent probe molecules available that does not require external activation (i.e., a reaction that produces a fluorescent species). DAMPI-type probes have therefore also been employed to study internal diffusion barriers arising from intergrowths in zeolite crystals,<sup>[3]</sup> as well as the change in accessibility of steamed zeolites due to mesopore formation.<sup>[4]</sup>

In this Chapter, we use this series of fluorescent DAMPI-derived probe molecules to test the accessibility of micropores, structural imperfections, as well as the micropore orientation of large zeolite crystals. We focus on two industrially relevant zeolite materials, namely MFI (ZSM-5, with 10-membered ring pores (MRPs)) and BEA (Beta, with 12-MRPs). The method provided allows one to study complete crystals and non-destructively probe their interior. Moreover, the fact that no reaction is needed to create fluorescent species means that silicalite and other non-reactive microporous material compositions can be probed as well. The anisotropy of the rod-shaped probe molecules is exploited in polarization-dependent confocal fluorescence microscopy (CFM) experiments showing the alignment of probe molecules in the zeolite pore network, thus revealing the pore orientation of the two distinct zeolite crystals under study.

### 3.2 Experimental

#### 3.2.1 Materials

Ludox AS-40 (40 wt% in H<sub>2</sub>O), zinc fluoride (99.999%) and pyridine (>99%) were purchased from Aldrich. *trans*-4-(4-(diethylamino)styryl)-*N*-methylpyridinium iodide 2 (98%) and tetrapropylammonium bromide (>99%) were purchased from Fluka. Aluminium sulphate octadecahydrate (98%) and ammonium hydroxide (28–30%) were purchased from J.T. Baker. Tetraethylammonium fluoride hydrate (97%) was purchased from Alfa-Aesar, while Cabosil M-5 was purchased from Cabot Corporation. The synthesis of probe 1, 3 and 4 has been described in detail in Chapter 2.<sup>[1]</sup>

### 3.2.2 Equipment

Confocal Fluorescence Microscopy (CFM) measurements and mapping were performed on a Nikon Eclipse 90i upright microscope using a 100x/0.70 NA dry objective. The microscope is equipped with a Nikon-Eclipse A1R scan head. CFM images were recorded using excitation from a Melles Griot Argon ion 488 nm laser providing 40 mW. The extinction ratio of the polarization for this laser is >250:1. Fluorescence emitted from MFI crystals was detected by a single photomultiplier using a 525/50 band pass filter, while fluorescence emitted from BEA crystals was detected by a spectral detection unit equipped with a diffraction grating and a 32 photomultiplier tube array (detection in the range of 518–710 nm). Fluorescence microscopy images were processed using the Nikon NIS software; for Figure 3.2, the alpha blending algorithm of this software was used.

Scanning electron microscope (SEM) images of MFI crystals were acquired on a Phenom SEM (Phenom World) equipped with a CsB6 filament at 5 kV in backscatter electron (BSE) mode. SEM images of BEA crystals were acquired on a ZEISS 1550 VP FESEM, equipped with in-lens SE.

3

### 3.2.3 Zeolite crystals

The zeolite MFI crystals were provided by ExxonMobil and have a Si/Al ratio of 17. Details on these crystals have been reported in previous work from our group.<sup>[3,5]</sup> The synthesis gel had a molar composition of 6.65 (NH<sub>4</sub>)<sub>2</sub>O/0.67 TPA<sub>2</sub>O/0.025 Al<sub>2</sub>O<sub>3</sub>/10 SiO<sub>2</sub>/121 H<sub>2</sub>O. The gel was, without agitation, heated from RT to 453 K in 2 h. The crystals were kept at 453 K for 168 h. The MFI crystals were first calcined in air to remove the template. The temperature was increased at 1 K/min to 523 K and held for 2 h. The temperature was then increased at 1 K/min to 773 K and held for 12 h. Afterwards, temperature was decreased at 1 K/min to room temperature. Crystals were ion exchanged three times using a 10% solution of NH<sub>4</sub>NO<sub>3</sub> at 333 K for 24 h. A final calcination was carried out using the same program as for template removal. The zeolite BEA crystals used were synthesized in a non-aqueous system, similar to that used by Kuperman *et al.* to synthesize a number of large zeolite crystals, most notably large crystals of ferrierite.<sup>[6]</sup> First 6.55 g of pyridine was mixed with 1.05 g of tetraethylammonium fluoride dihydrate and 0.074 g of ZnF<sub>2</sub>·4H<sub>2</sub>O and 6.55 g of pyridine. Then 2 g of water was added to obtain a clear solution. Finally, 0.5 g of Cabosil was added and mixed by hand until a homogenous gel was obtained. Final molar ratios were 1 SiO<sub>2</sub>/0.03 ZnF<sub>2</sub>/0.65 TEAF/10 pyridine/15 H<sub>2</sub>O. The mixture was placed in a 23 mL Parr reactor and placed in a tumbling oven at 413 K for 24 days. The crystals were recovered by centrifugation and were rinsed with water several times followed by a final wash with acetone and then dried in air at 373 K. The BEA crystals were calcined in air. The temperature was increased at 1 K/min to 423 K and held at this temperature for 3 h, then heated to 853 K at 1 K/min and held at this temperature for 6 h.

### 3.2.4 Staining experiments

Immediately prior to staining experiments, the zeolite crystals were calcined in air. The temperature was increased at 1 K/min to 523 K and held at this temperature for 2 h. The temperature was then further increased at 1 K/min to 773 K and held at this temperature for 6 h. Afterwards, the temperature was decreased at 1 K/min to 373 K, at which the container containing the crystals was sealed to minimize adsorption

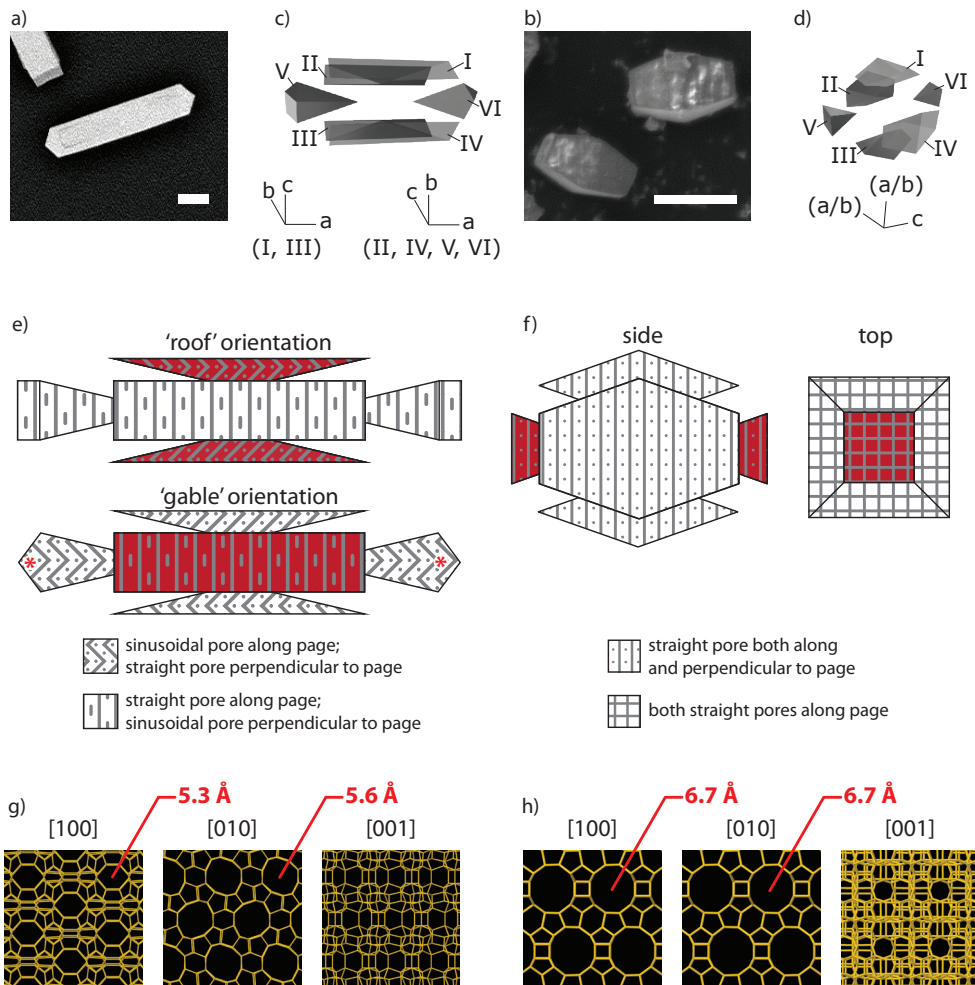


Figure 3.1. Overview of the two zeolite framework topologies used in this study. a,b) SEM images of zeolite MFI (a) and zeolite BEA (b) crystals; the scale bars represent 20 μm. c,d) Schematic representation of the zeolite crystals showing the different subunits the crystals consist of. The directions of the crystallographic edges for the subunits are shown below the model. e,f) Schematic representation of the both zeolite crystals showing the pore orientation in plane and parallel to the plane. Subunits with a high concentration of imperfections are shown in red for each zeolite crystal (vide infra). g,h) View of the zeolite framework along [100], [010] and [001], showing the pores that surface at those faces.<sup>[7]</sup>

of water before cooling to room temperature. Both MFI and BEA crystals were stained with a concentration of 1  $\mu\text{M}$  for all probes, unless otherwise indicated. These suspensions were allowed to stand for 1 week; if the crystal were left standing for a longer time, no additional fluorescence was observed. The suspensions were not stirred to avoid damaging the crystals. After staining the crystals were either filtered using a PTFE 0.45  $\mu\text{m}$  filter and, in the case of MFI, washed 3 times with ethanol, or washed by adding and siphoning off ethanol 3 times. Fluorescence of the zeolite crystals was evaluated by CFM. All crystals considered were of the same size. In quantification experiments, the ‘roof’ orientation was used for MFI crystals. Although the stained zeolite crystals were kept in a desiccator to minimize exposure to contaminants, MFI crystals that were kept for longer than one month after staining were often found to be contaminated with a fluorescent species accumulating at the edges of the crystal. Fortunately, this contamination could be detected by anomalies in the emission spectrum. In polarization-dependent CFM experiments, the intensities of the fluorescence of both type of crystals were evaluated at 15° (BEA) or 30° (MFI) intervals.

In fluorescence quantification experiments, CFM maps of the crystals were created by stacking 23 slices of the crystal with a Z increment of 1  $\mu\text{m}$ . The fluorescence intensity was summed over the whole stack and the background fluorescence, taken from the same image, was subtracted. The results for each probe were divided by the extinction coefficient to correct for differences in absorption efficiency between probes. The statistical significance of the differences in fluorescence intensity between crystals (of one type) stained using probes 1–4 was calculated by subjecting the (corrected) summed intensity data to a two-sample *t*-test. In this test, two samples (in this case, the summed fluorescence intensity of 8 crystals stained with one probe versus the intensity of 8 crystals stained with another probe) are compared to each other; the null hypothesis of this test is that the two samples have the same mean. At the  $p < 5\%$  significance level, the null hypothesis is rejected. The *p*-values of each test are given in Table 3.1.

3

### 3.2.5 DFT calculations

The anisotropy of light absorption by the probe molecules was investigated using real-time TD-DFT. For simplicity, probe 1 was used for these calculations, as the alkyl substituents have no substantial influence on the spectroscopic properties of the conjugated system. The molecular geometry was optimized on the ground state energy surface using DFT at the B3LYP/6-311G level of theory. Convergence of the geometry optimization was confirmed by frequency calculations. To properly assess long-range charge transfer interactions between the pyridinium and the aniline moieties, the cam-B3LYP hybrid functional was used in the TD-DFT calculations. The real-time TD-DFT simulation of absorption anisotropy was performed by evolving the density matrix in response to a polarized external electric field aligned to the molecular axes as described by Lopata *et al.*<sup>[8]</sup>

### 3.3 Results and discussion

#### 3.3.1 Zeolite crystals, molecular probes, and fluorescence microscopy

Large coffin-shaped ZSM-5 crystals with typical dimensions of  $100 \times 20 \times 20 \mu\text{m}$ , shown in Figure 3.1a, were used as a model system for zeolite MFI. These zeolite crystals have been the subject of many studies, resulting in detailed knowledge of their internal structure and composition.<sup>[2,3,9]</sup> It has been demonstrated that these materials are not single crystals, but rather consist of two types of subunits with distinct shapes (Figure 3.1c) and that intracrystalline voids are present between these subunits due to an imperfect match of the subunit's interface.<sup>[3,10]</sup> MFI has a 3D pore system with straight pores opening to the [010] face and sinusoidal pores opening to the [100] face, as shown in Figure 3.1g. The 10-MRPs have pore diameters between 5.3 and 5.6 Å. The growth mechanism of these zeolite crystals causes a 90° rotational intergrowth for subunit I and III, as evidenced by electron backscatter diffraction measurements.<sup>[3]</sup> This intergrowth has been shown to introduce structural weakness particularly to these subunits.<sup>[2]</sup> Thus, the direction of the sinusoidal and straight pores is switched in subunits I and III compared to the rest of the crystal. It is important to note that, regardless of the subunit, both the sinusoidal and straight pores of these large MFI crystals lie in the direction of the short axes of the crystal (i.e. never along the long axis).

The typical dimensions of the BEA crystals used in this work were  $20 \times 10 \times 10 \mu\text{m}$  (Figure 3.1b), which is similar to the BEA crystals typically used in sugar isomerization experiments, one of the promising applications of (Lewis acidic) BEA materials.<sup>[11]</sup> The crystals have a truncated bipyramidal morphology, typical for crystals synthesized in this way.<sup>[12]</sup> An hourglass pattern similar to that of MFI crystals has been reported for much larger crystals (ca.  $400 \mu\text{m}$ ) of this type, but has not yet been demonstrated in smaller crystals.<sup>[13]</sup> BEA has a 3D 12-membered ring pore system, with large 6.7 Å pores opening to the [100] and [010] face (Figure 3.1h). Sinusoidal pores open to the [001] face; these types of pores have a smaller effective diameter due to their zig-zag shape. Previous results from XRD measurements on the aforementioned  $400 \mu\text{m}$ -large BEA crystals showed that the [001] face is at the short, square end of the crystal.<sup>[13]</sup> Consequently, the straight pores open to all of the faces on the long sides of the crystal<sup>[14]</sup>. The structure of BEA is complicated by the fact that multiple, intergrown polymorphs, namely A and B, can be formed.<sup>[13,15–17]</sup> There is virtually no preference in growth of these polymorphs, which leads to layers of polymorphs on top of each other, making crystallographic analysis of zeolite BEA crystals rather difficult.<sup>[18]</sup> Moreover, these stacking faults also further restrict movement through the sinusoidal pores. The zeolite BEA crystals used in this study were synthesized using fluoride, which usually leads to highly crystalline, defect-free crystals. Contrary to MFI crystals in this study, to the best of our knowledge, the crystal morphology of BEA crystals has as of today not been investigated in such detail. Notably, and in contrast to the MFI crystals, the crystals used here are free of aluminium and thus contain no strong Brønsted acid sites.

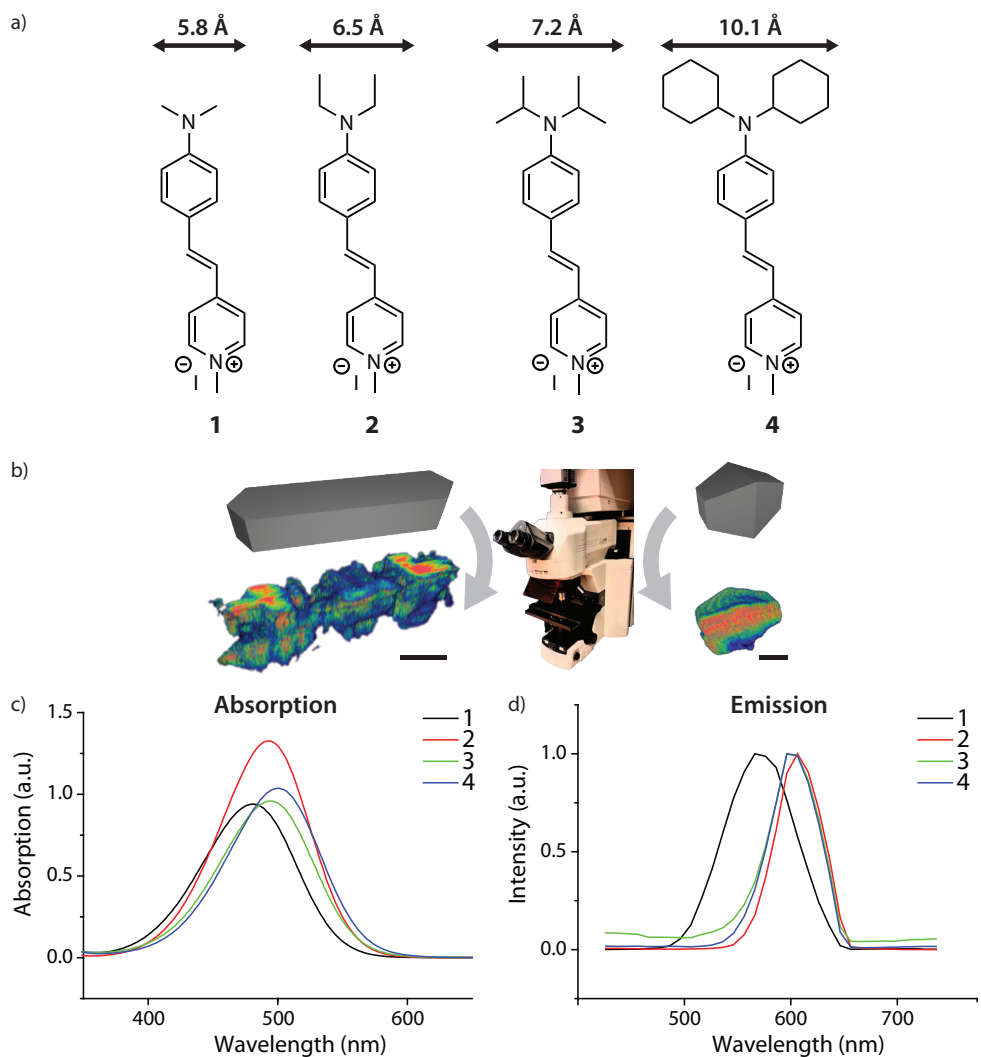


Figure 3.2. An overview of the experimental approach taken in this work. a) Molecular probes **1–4** developed in Chapter 2 and used here. The width of the probe molecule is calculated by fitting the smallest enclosing cylinder around the optimized structure as calculated by Density Functional Theory (DFT).<sup>[1]</sup> b) Schematic model of a zeolite MFI crystal (left) and a zeolite BEA crystal (right) with 3D confocal fluorescence microscopy maps for both zeolite crystals after staining with probe molecule **1**. The 3D images were obtained by stacking of individual fluorescence microscopy maps using alpha blending mode. Different settings were used for the zeolite MFI and BEA crystals so the absolute intensities cannot be compared. The scale bars represent 20  $\mu\text{m}$ . c) Absorption spectra of probe molecules **1–4** in equimolar solutions in ethanol. At the absorption maximum, the extinction coefficients of the probes are  $37.6 \times 10^3$ ,  $53.1 \times 10^3$ ,  $38.3 \times 10^3$  and  $41.5 \times 10^3 \text{ M}^{-1} \text{ cm}^{-1}$  for probe **1–4**, respectively. d) Normalized emission spectra of probe molecules **1–4**, recorded by confocal fluorescence microscopy on the pure compounds in solid form.

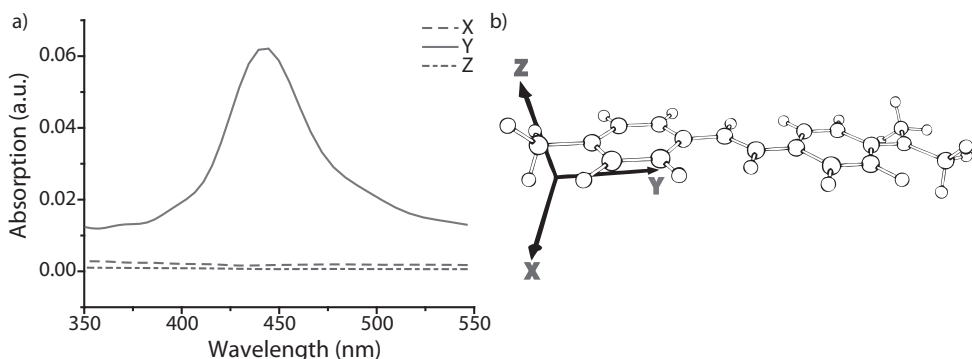


Figure 3.3. Polarization dependence of the absorption of probe molecule 1 with respect to laser light polarization. a) The absorption of light of probe molecule 1 if the angle of light polarization is parallel to the axis X, Y or Z; the propagation direction of light is then perpendicular to that axis. The absorption was calculated by TD-DFT. Maximum light absorption occurs when light polarization is parallel to the probe's long axis (Y) and thus propagates in any direction in the XZ plane. The  $\lambda_{\text{max}}$  of the absorption band is found at a lower wavelength compared to the experimental value, which is common for TD-DFT.<sup>[19]</sup> b) Scheme showing the axes used in the calculation of the polarization dependence.

The accessibility of probe molecules in the zeolite pore network and structural imperfections, such as cracks, of these two types of large zeolite crystals was evaluated using the series of fluorescent DAMPI-based probe molecules with increasingly bulky alkyl substituents developed in Chapter 2.<sup>[1]</sup> These probe molecules, denoted as 1–4, are depicted in Figure 3.2, together with their dimensions and spectroscopic properties. The steric bulk is increased by changing the *N*-alkyl substituents from methyl to cyclohexyl substituents, with the larger substituents giving the molecule a distinct T-shape. The amine substituents changes do not have a large influence on the spectroscopic properties of the probes, as they show very similar absorption properties (Figure 3.2c). Based on their sizes (varying from 5.8 Å for 1 to 10.1 Å for 4), probe molecule 1 is expected to be able to enter the pores of zeolite MFI, while probe molecules 1 and 2 are expected to be able to enter the pores of zeolite BEA.

The ability of the molecular probes to enter the zeolite pores was examined by evaluating probe uptake by the zeolite crystals from solution. Crystals of zeolites BEA and MFI were submersed in solutions of each of the probes until equilibrium was reached, after which they were collected, washed (in the case of MFI) and examined by CFM. The fluorescence of zeolite MFI crystals did not change after repeated washing with ethanol, suggesting that the probe is strongly bound, most likely to the Brønsted acid sites of the zeolite.<sup>[1]</sup> For zeolite BEA, however, washing of the crystals after staining lowered the fluorescence significantly, indicating that the probes are not strongly bound to the zeolite, as expected given the lack of Brønsted acid sites in this sample. Therefore, zeolite crystals with BEA morphology were not washed after staining. Visual inspection of the zeolite crystals after staining showed that for both types of crystals, probe molecule 1 caused the zeolite crystals to become bright pink, while probe molecules 2–4 did not induce a color

change. In the CFM experiments, only isolated single crystals were considered. It was confirmed visually that the zeolite crystals were undamaged, but no selection was performed based on the observed fluorescence.

The laser light source of CFM is intrinsically polarized, allowing for polarization-dependent measurements to be carried out on probe molecule 1 in both zeolite MFI and BEA crystals. Experimentally, the zeolite crystals were rotated with respect to the angle of polarization of the incoming laser light. The conjugated chromophore of the DAMPI scaffold runs along the long axis of the molecule, causing anisotropic light absorption. Therefore, the DAMPI-type probe molecules used in this work will absorb (and emit) light only when specifically oriented with respect to the incident laser light polarization. TD-DFT calculations showed that light absorption is maximized when the molecule's Y axis (Figure 3.3b) is oriented *perpendicular* to the incoming laser light (i.e. parallel to the microscope table) and *parallel* to the polarization axis of the light. If the molecule is rotated away from the orientation of maximum absorption, absorption gradually decreases. As is shown in Figure 3.3, light polarized along the X and Z axes is not absorbed by the molecule. Polarization-dependent CFM measurements thus directly give the orientation of the long axis of

3

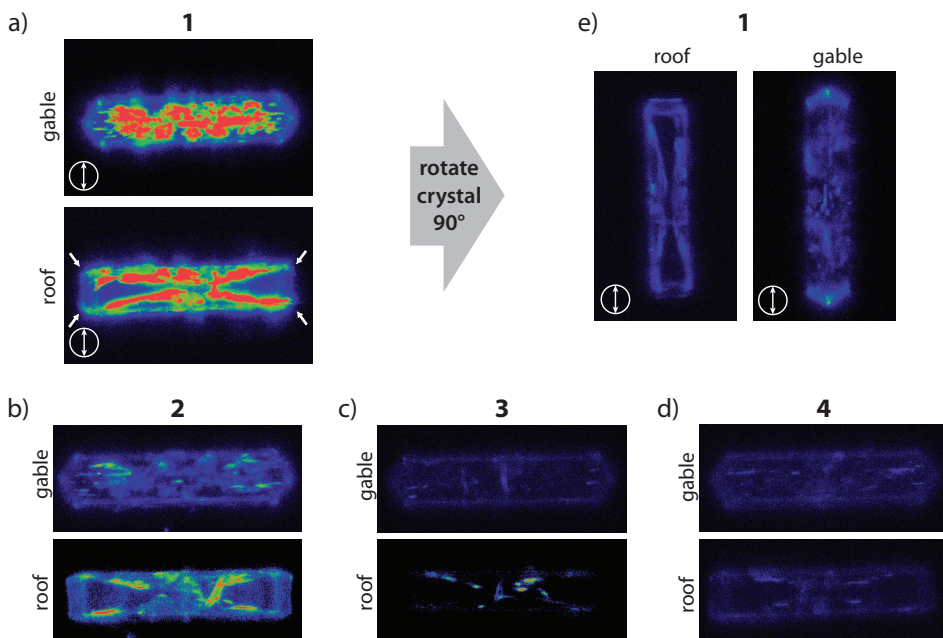


Figure 3.4. Fluorescence location in zeolite MFI crystals. The experimental settings were kept constant in all CFM images presented in this figure. a-d) Summed intensity over all layers of 3D maps of the zeolite crystals stained with probe molecules 1 (a), 2 (b), 3 (c) and 4 (d) in the two possible orientations of the zeolite crystals: 'gable' (top) and 'roof' (bottom) orientation. e) Image of zeolite MFI crystal after the crystal has been physically rotated by 90° i.e. with respect to the angle of polarization of the incoming laser light, showing diminished fluorescence intensity for both orientations.

the molecule. The observed polarization dependency, shown in Figures 3.4, 3.6 and 3.8, demonstrates that most of the molecules are aligned, indicating that the molecules have entered and are aligned in the micropores of the zeolite crystal; the angle of polarization is indicated by arrows in these figures.

### 3.3.2 Micro-spectroscopic investigation of zeolite MFI crystals

Figure 3.4a shows that the fluorescence of the zeolite MFI crystals stained with the probe molecules is not distributed homogeneously throughout the crystal. More specifically, an hourglass pattern is visible, similar to how the (unstained) crystal looks when examined under crossed polarizers.<sup>[20,21]</sup> The aforementioned space between the subunits of the zeolite crystals must therefore provide access to the interior of the crystal, which allows the probe molecules to enter. The hourglass pattern is a recurring feature in virtually all the studied crystals (see also Figure 3.5), but for each probe the intensity of the pattern differs. From the low amount of fluorescence observed in these areas for the larger probe molecules, it can be concluded that the limiting opening between the subunits is not much larger than the largest probe, i.e. approximately 1 nm.

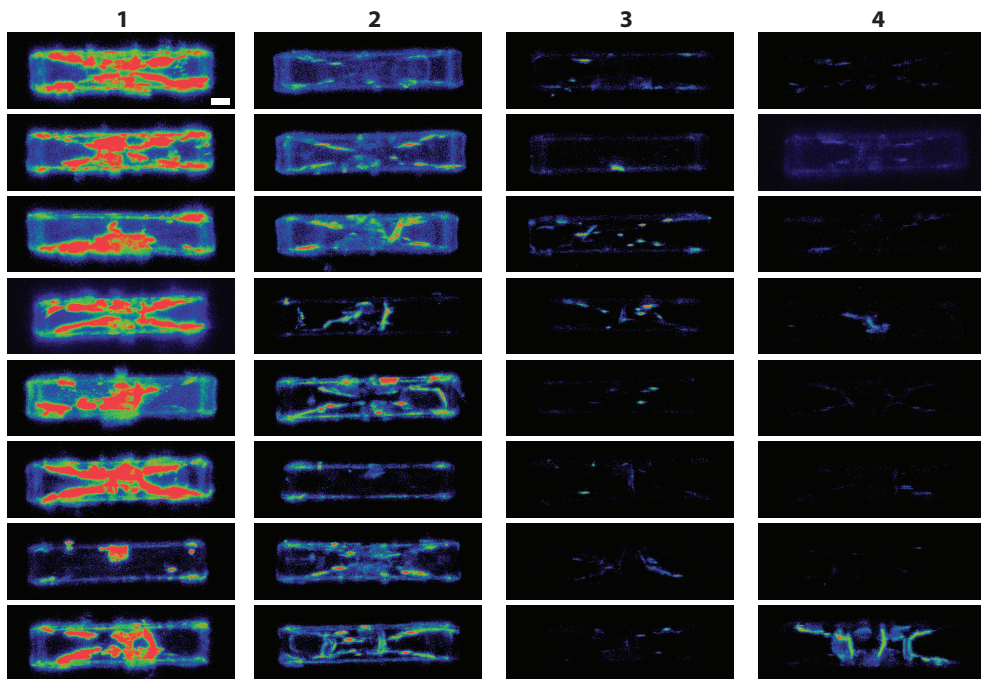


Figure 3.5. Confocal fluorescence microscopy maps of a representative set of MFI crystals, stained by each of the probes 1–4. The maximum intensity projections of each zeolite crystal are shown, which is the sum of all layers of a 3D stack. The intensity of these projections was used in calculating the total intensity of each zeolite crystal. The measurement settings for these images were kept constant. The scale bar is 10 µm.

When deposited on a flat surface (i.e. the microscope table), the zeolite crystals are encountered in two orientations in equal amounts: the ‘gable’ and ‘roof’ orientation.<sup>[9]</sup> Looking at the distribution of fluorescence for probe molecule 1 through 4 throughout the crystal, the two orientations of the crystal show distinct differences. In the roof orientation, the fluorescence observed has the shape of an hourglass, while in the gable orientation fluorescence is observed in a rectangular area (Figure 3.4). From these observations, it can be concluded that in both orientations the fluorescence is originating from the same subunits, namely subunits I and III (marked red in Figure 3.1e). The other subunits of the zeolite crystal only show a small amount of fluorescence on the edges.

Examining the size of each probe molecules with respect to the MFI pore size reveals that only 1 can enter the zeolite micropore system.<sup>[11]</sup> The bulky side groups of the other probes allow only partial, end-on entrance into pore mouths. The only area on the crystal exterior where straight pores open at the surface are the faces designated by a star in Figure 3.1e. To evaluate the penetration of probe molecules

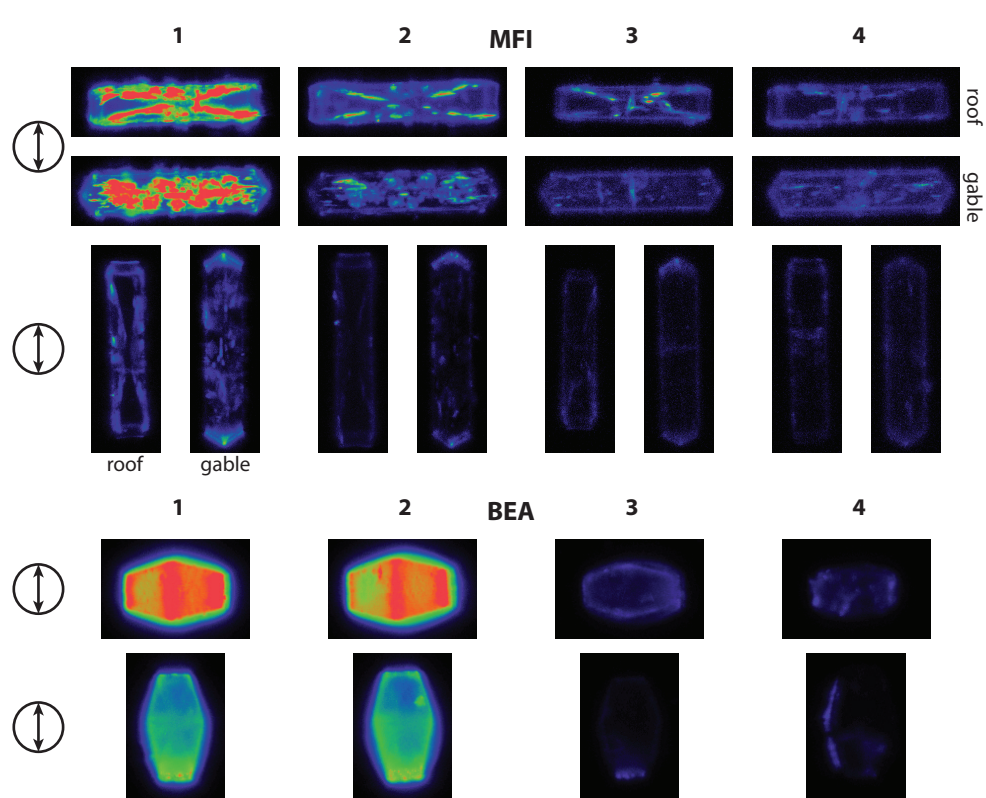


Figure 3.6. Fluorescence microscopy images of zeolite crystals MFI and BEA stained with probe 1–4 at 0° (parallel to polarization of laser light, vertical images in figure) and 90° (perpendicular to polarization of laser light, horizontal images in figure). Crystals were physically rotated on the microscopy stage. The image intensity of probes 3 and 4 in MFI crystals has been boosted by a factor 3 to increase visibility.

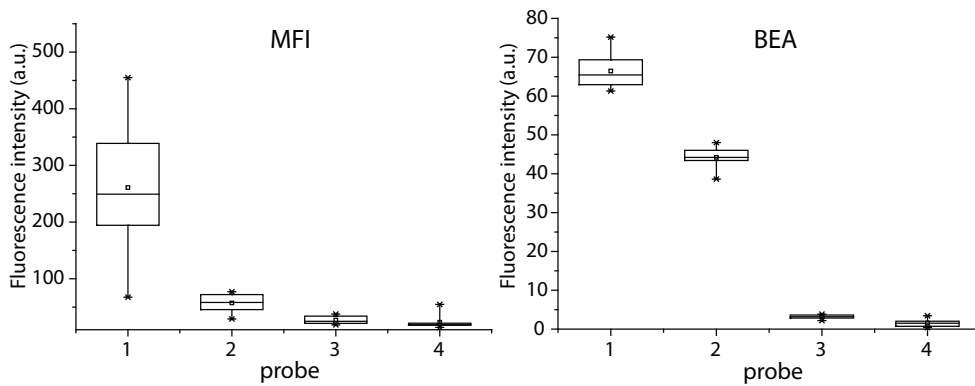


Figure 3.7. Overview of the summed fluorescence intensities of zeolite MFI and BEA crystals after staining with probe molecules 1–4. For each probe, background-corrected fluorescence was summed over all layers of a 3D map of the crystal and corrected for differences in extinction coefficient of the probe. Eight zeolite crystals were evaluated for each probe and each type of crystal to obtain statistically significant results. Intensities between the two types of zeolite crystals were taken using different measurement settings and should therefore not be compared. The box plot signifies all data for each probe. A “□” denotes the mean, the box the interquartile range and the whiskers the minimum and maximum of the data.

of 1 into straight pores of the crystal, this area was studied in the ‘roof’ orientation: molecules inside the straight pores will be oriented such that maximum absorption of laser light is expected (see Figure 3.3). From the fluorescence microscopy maps, it is clear that no additional fluorescence is observed in this area (see the arrows in Figure 3.4a). Thus, movement through straight pores is very slow, presumably because of the tight fit between probe and zeolite. From this result, it is clear that movement through straight pores cannot account for the fluorescence observed in crystals stained with 1.

The highly fluorescent nature of subunits I and III coincides with the different crystallographic orientation in these subunits with respect to the other units due to the 90° intergrowth in the crystal. In both orientations, fluorescence is distributed heterogeneously throughout these subunits and fluorescence intensity varies between subunits and between crystals (Figure 3.5). It is known that rotational intergrowths can induce structural weakness in zeolite crystals. Roeffaers *et al.*<sup>[2]</sup> have shown that intentionally damaging the crystal by sudden temperature changes allows probe molecule 2 to enter the subunits of the zeolite crystal. The crystals used in this study were calcined very gently according to methods used previously;<sup>[2]</sup> it is therefore unlikely that the calcination procedure damaged the crystals to a large extent. Therefore, the fluorescence results suggest that there must be many imperfections within subunits I and III, which allow the smaller probe molecule 1 to enter. A comparison of the fluorescence of zeolite MFI crystals stained with probe molecules 1–4 shows intense fluorescence for probe molecule 1 and only little fluorescence for probe molecules 2–4. This result is similar to what has been observed in experiments with the same probes in MFI zeolite powder in Chapter

2.<sup>[1]</sup> In the fluorescence maps of each probe molecule, outlines of fluorescence can be observed at the edges of the crystal, which suggests the probes are inserted end-on into the sinusoidal pore mouths at the surface in a “stopcock” fashion, as proposed before by Roeffaers *et al.*<sup>[2,22]</sup>

It should be noted that there is considerable heterogeneity in fluorescence intensity between the different MFI crystals stained with the same probe molecule (Figure 3.5). A warning against the assumption of homogeneity of crystal properties within a single batch has also been issued recently.<sup>[23]</sup> Therefore, to eliminate any experimenter’s bias, we evaluated the intensity for eight of these MFI crystals stained with probe molecules 1–4, to compare the amounts of each probe molecule the zeolite crystals could take up. The total fluorescence intensity for each zeolite crystal was summed over the entire crystal and evaluated for each type of probe molecule. Probe molecule concentrations for each type of probe molecule are compared in Figure 3.7. Significant differences (> 95% confidence, see Table 3.1) in average fluorescence intensity were found for the probe molecules, regardless of the differences in intensity seen for different crystals stained using the same probe.<sup>[24,25]</sup> The only exceptions to this for MFI crystals were probes 3 and 4, for which the differences in average intensity were too small. This approach shows the feasibility of using this series of fluorescent probe molecule experiments with consistent results on zeolite crystals, even though the fluorescence intensity observed seems heterogeneous. The clear differences in fluorescence intensity between crystals stained with differently sized probes offers a unique way to measure the accessibility of the crystal for molecules of discrete sizes. The polarization dependence of zeolite MFI crystals stained with probe molecule 1 is shown in Figure 3.4e. It was found that the fluorescence intensity is the highest when the light polarization is parallel to the short axis of the crystal, while a rotation of 90° leads to an almost complete disappearance of fluorescence. Both ‘roof’ and ‘gable’ orientations show this behavior. The large differences in fluorescence upon rotation of the crystal show that most of the probe molecules are aligned relative to each other, meaning they are aligned in identical micropores of the zeolite, shown in Figure 3.7. Interestingly, probe molecules 2–4 also exhibit polarization-dependent behavior, with a similar maximum and minimum upon rotation of the crystal (Figure 3.6). This implies that while the other probe molecules are unable to enter the pore system because of their size, they are still aligned to the pore system in a regular fashion. We therefore conclude that while the steric bulk of these probe molecules precludes full entry into the pores, part of the probe molecule may insert itself into the pore mouth of the zeolite end-on, in a “stopcock” fashion. This result suggests that probe molecules can be visualized selectively at the pore mouth of the zeolite crystal, a location of particular interest for catalysis.<sup>[22,26]</sup> For example, these probes may be used to detect pore blockage at the surface.<sup>[27]</sup> Rotating the zeolite crystal at 30° intervals, shown in Figure 3.8, demonstrates that the fluorescence intensity follows a  $\sin(2\Theta)$  curve.<sup>[28]</sup> The small overall decrease in fluorescence intensity upon multiple rotations is caused by photobleaching of the probe molecules upon prolonged exposure to laser light (i.e. after multiple measurements of the same zeolite crystal).

Table 3.1. Statistical T-tests carried out on intensity data for MFI and BEA. The summed

fluorescence intensity for the 8 crystals measured for each probe are compared against the summed intensities of each other probe. For each probe combination is indicated whether there is a significant difference (95% confidence interval) and what the accompanying p-value is (in brackets).

| MFI | 1 | 2                             | 3                              | 4                              |
|-----|---|-------------------------------|--------------------------------|--------------------------------|
| 1   | - | Yes ( $8.44 \times 10^{-4}$ ) | Yes ( $6.71 \times 10^{-5}$ )  | Yes ( $6.50 \times 10^{-5}$ )  |
| 2   | - | -                             | Yes ( $5.09 \times 10^{-5}$ )  | Yes ( $9.33 \times 10^{-5}$ )  |
| 3   | - | -                             | -                              | No ( $7.30 \times 10^{-1}$ )   |
| BEA | 1 | 2                             | 3                              | 4                              |
| 1   | - | Yes ( $4.26 \times 10^{-2}$ ) | Yes ( $5.81 \times 10^{-11}$ ) | Yes ( $9.18 \times 10^{-11}$ ) |
| 2   | - | -                             | Yes ( $5.42 \times 10^{-11}$ ) | Yes ( $1.00 \times 10^{-10}$ ) |
| 3   | - | -                             | -                              | Yes ( $6.60 \times 10^{-3}$ )  |

Interestingly, for both ‘gable’ and ‘roof’ orientations, fluorescence is observed almost exclusively in subunits I and III. The pore orientation of MFI crystals, as elucidated in previous studies,<sup>[3,29,30]</sup>

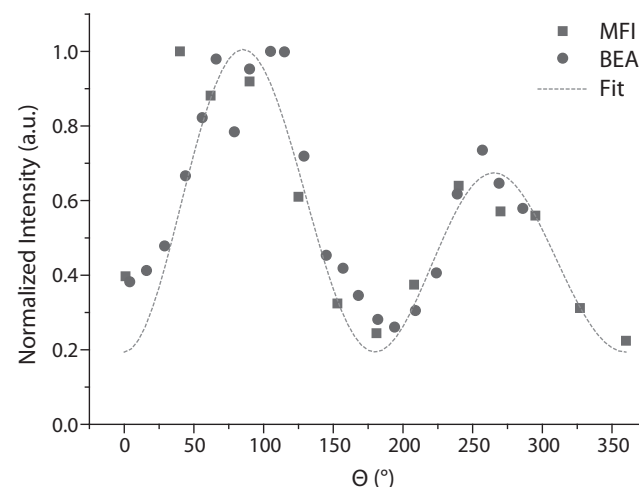


Figure 3.8. Intensity of fluorescence of probe molecule 1 within a zeolite MFI crystal (summed over the whole crystal) and a zeolite BEA crystal (intensity of middle plane) with respect to the angle of polarization. The angle was adjusted by physically rotating the crystal on the microscope table. The grey line represents a fit using the function  $f(\Theta) = a \cdot \exp(-\Theta \cdot c) \cdot \sin(2\Theta) + b$ . Fit parameters were determined empirically. A decay of the intensity at higher angles (i.e. after longer laser exposure) is observed due to photo-bleaching of the probe molecules within the zeolite crystal.

dictates that for subunits I-IV, straight pores run parallel to the crystal outer surface. The fluorescence originating from I and III in the ‘gable’ orientation therefore indicates that probe molecule 1 is aligned to the straight pores of these subunits. This is expected, as probe 1 fits into the straight pores of MFI.<sup>[1]</sup> In the ‘roof’ orientation, however, the same rationale leads to the conclusion that probe molecule 1 must be aligned to the sinusoidal pores of the crystal. This counterintuitive result can be explained by the many imperfections in these subunits. It is possible the deterioration in pore structure makes

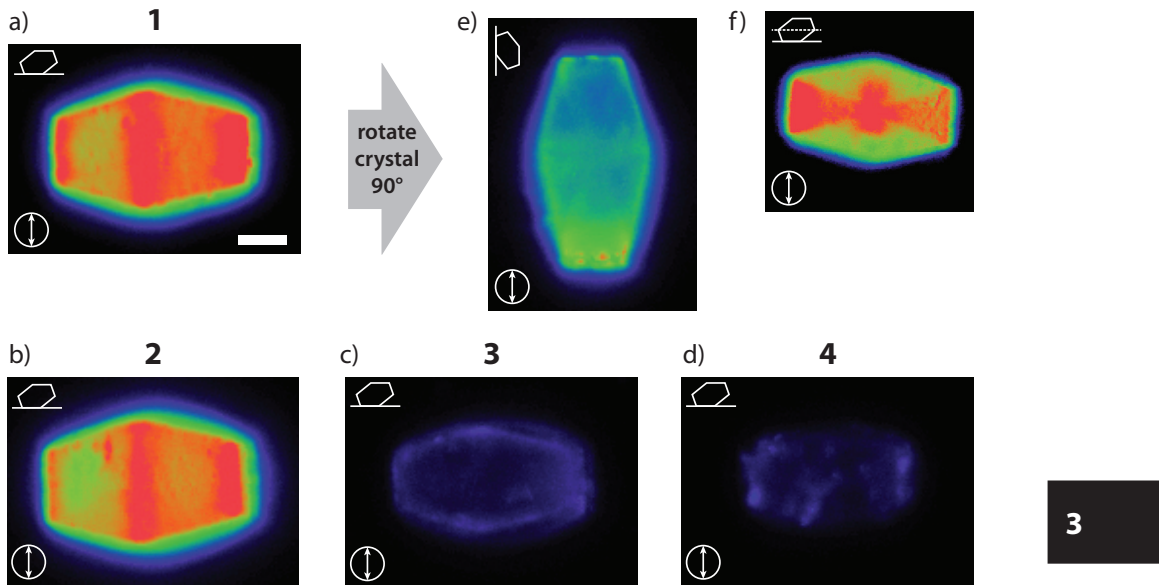


Figure 3.9: Fluorescence location in zeolite BEA crystals after staining with probes 1-4. The experimental settings were kept constant for all CFM images in this figure except f. a-d) Summed intensity over all layers of 3D maps of the crystals stained with 1 (a), 2 (b), 3 (c) and 4 (d). The scale bar is 5  $\mu\text{m}$ . e) Image of a zeolite BEA crystal after the crystal has been physically rotated by 90° i.e. with respect to the angle of polarization of the incoming laser light, showing diminished fluorescence intensity. f) Middle section of a zeolite BEA crystal showing the hourglass pattern observed after staining with a low amount of probe. The color scale of this CFM image was adjusted to show the hourglass pattern more clearly.

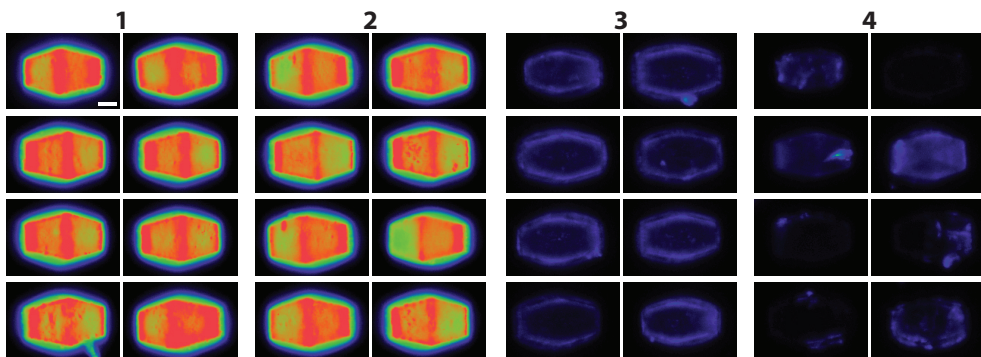


Figure 3.10. Confocal fluorescence microscopy maps of a representative set of BEA crystals, stained by each of the probes 1-4. The maximum intensity projections of each zeolite crystal is shown, which is the sum of all layers of a 3D stack. The intensity of these projections was used in calculating the total intensity of each zeolite crystal. Measurement settings for these images was kept constant. The scale bar is 5  $\mu\text{m}$ .

the sinusoidal pores wider and accessible to probe molecules. However, from the observed polarization dependence of the fluorescence, it follows that the probes are still aligned to the direction of the pore; there is thus no complete breakdown of pore structure. In this way, subunits I and III have probe molecule 1 in both types of pores. In the ‘gable’ orientation, the probes in the straight pores are visible, while in the ‘roof’ orientation, the probes in the sinusoidal pores are visible.

### 3.3.3 Micro-spectroscopic investigation of zeolite BEA crystals

BEA crystals stained with probe molecule 1 or 2 show fluorescence distributed throughout the complete crystal (Figure 3.9 and 3.10). Based on their size, both probes should be able to enter the zeolite pore system and be distributed throughout the crystal. In contrast, probe molecule 3 shows fluorescence mostly at the edges of the BEA crystal. Indeed, given its size probe molecule 3 is not expected to be able to enter the pores of the BEA crystal, and is present at the entrance of the pores. Some irregular fluorescence is observed for probe molecule 3; however, this is more pronounced for probe 4, for which randomly distributed areas within the crystal show fluorescence intensity. Probe molecule 4 is also present at the edges of the crystal, but the fluorescence is very weak. These results suggest that probe molecule 4 (and, less visible due to fluorescence at the edges, probe 3) can enter and stain imperfections of the crystal. In this way, probe molecule 4 can effectively be used to detect cracks and structural imperfections in the crystals that are accessible from the outside of the BEA crystal.

In analogy to MFI crystals, fluorescence intensity was evaluated for several BEA crystals to compare the difference in uptake of the probes. The results are summarized in Figure 3.7b. In BEA crystals, probe molecule 1 shows the highest concentration, followed by probe 2, while 3 and 4 are taken up in very minor amounts. This is in agreement with the sizes of the probe molecules with respect to the pore size of BEA. From the box plots it is apparent that there is considerably less spread in fluorescence intensity between zeolite BEA crystals stained with the same probe as is the case for MFI. The very consistent fluorescence intensity of these crystals per probe should be attributed to the low number of defects in these crystals, as a result of the fluoride-assisted synthesis method. For probe molecule 4, low fluorescence intensity is observed, but with relatively large differences in fluorescence intensity observed. Because probe molecule 4 can only enter imperfections in the crystal, the heterogeneity in fluorescence is caused by the variations in the amount of imperfections in each crystal, which can be seen in Figure 3.10. With higher fluorescence intensity, fluorescence from cracks does not play a role, as evidenced by the results of probe molecules 1–3. Furthermore, statistical analysis of the sets of fluorescence intensity showed that there were significant differences ( $> 95\%$  confidence) in intensity between sets of zeolite crystals stained with each of these probes (Table 3.1). Staining with a lower concentration of probe molecule 1 revealed an hourglass pattern for the BEA crystals (Figure 3.9f), similar to the one observed in MFI crystals (Figure 3.4). This phenomenon has been observed before in large BEA crystals with the same morphology using crossed polarizers

and is imaged here in small BEA crystals for the first time.<sup>[13]</sup> It is therefore likely that this is a general feature of BEA crystals with this morphology. Our results show that probe molecule 1, when supplied in low amounts, preferentially enters the pyramidal subunits of the crystal. This is an indication that these subunits are imperfect, as there are no straight pores opening to the square faces on the short edge of the crystal (see Figure 3.1f). Furthermore, the large difference in intensity shows that internal diffusion barriers exist between the two pyramidal and the other subunits of the BEA crystals.

Zeolite BEA crystals stained with these probes all show relatively high fluorescence intensity at the short edges of the crystal, i.e. the base of the two pyramidal subunits (see Figure 3.9). It has been observed before that this face of the BEA crystals has a “rugged” structure with terraces with a height of 100–200 nm covering the surface.<sup>[13]</sup> Therefore, it is possible that this rugged structure is an indication of imperfections in or damage to these faces of the crystal, which allow probes of any size to enter the edge of the crystal easily. Moreover, the surface area of these faces is expected to be high. Polarization-dependent CFM measurements of the BEA crystals, which are shown in Figure 3.6 and Figure 3.9e, allowed a deeper inquiry into the increased intensity at the short edges. Analogous to the MFI crystals, a 90° rotation of the zeolite crystals with respect to the polarization of the laser light leads to diminished fluorescence intensity throughout most of the zeolite crystal. However, the short edges of the crystal still show a significant amount of fluorescence after rotation. This is in line with the hypothesized damage to the crystal on these faces, which allows probes to orient themselves more freely because the normal pore structure has been disrupted.<sup>[13]</sup> Upon rotation of the BEA crystal with 15° intervals, the fluorescence intensity again gave a  $\sin(2\Theta)$  curve, consistent with the results for MFI crystals (Figure 3.8). These results confirm that probe molecules are aligned within the pore system of these crystals and that fluorescence intensity can therefore be used to elucidate the direction of the micropores in (subunits of) the BEA crystals.

It has been previously reported from XRD measurements of very large BEA crystals that the [100] and [010] faces are on the long sides of the crystal. Thus, the straight pores are open to the long edges, while the sinusoidal pores are open at the short edges (i.e. the square shaped faces).<sup>[13]</sup> The crystals can be observed lying on a surface in three different orientations: on the short-truncated end (rarely seen), or one of the four sides (with each side tilted in two possible directions), leading to two observable orientations: opposing sides (and tilts) result in the same orientation. Unlike MFI with its ‘roof’ and ‘gable’ position, the orientations of BEA lying on its side are indistinguishable (symmetrical). Because there are no significant differences in fluorescence intensity among the crystals stained with 1 (Figure 3.10), the two orientations must be equivalent. Therefore, the orientation of both straight pores of zeolite BEA is perpendicular to the long axis of the crystal and the sinusoidal pores run along the long axis of the crystal, which is in agreement with previous results.<sup>[13,14]</sup>

### 3.4 Conclusions

A new approach to assess the accessibility and orientation of the pore structure of zeolite crystals has been successfully applied to study large crystals of MFI and BEA. It was found that in MFI crystals with a 90° intergrowth structure, the rotated subunits were prone to develop imperfections during crystal growth. The probe series used in these experiments, based on the fluorescent *trans*-4-(4-(diethylamino)styryl)-*N*-methylpyridinium iodide (DAMPI) scaffold with increasing molecular dimensions, could stain these cracks and zeolite imperfections, showing the relative extent of imperfections and damage in the zeolite crystals under study. The results of the adsorption of the distinct DAMPI-type probes could be quantified by CFM and provided a quantitative measure of accessibility for these crystals based on the uptake of the fluorescent probe molecules. Polarization-dependent CFM measurements showed that although the cracks and imperfections are responsible for the macro-distribution, the probes were still aligned to the pore system of the crystal, with the larger probes presumably inserted end-on into the zeolite pore mouth, in a “stopcock” fashion.

Furthermore, the developed approach with DAMPI-type probes was applied successfully to the much less studied BEA zeolite crystals. The hourglass pattern, as observed in large BEA crystals, was observed for the first time in smaller BEA crystals, which suggests that this pattern is a general feature of BEA crystals of this morphology. Internal diffusion barriers between the subunits of a BEA crystal exist, which restrict probe movement. Polarization-dependent CFM measurements showed imperfections exist on the square short ends of the crystal, which accommodate probes with no preferential orientation. Furthermore, evidence is provided that the pore orientation proposed in previous studies is correct; i.e., the straight pores run perpendicular to the long axis of the BEA crystal.

In summary, investigating zeolite crystals using this series of DAMPI-type probes – which have discrete molecular dimensions and do not require external activation by light or an acidic site – offered a versatile and powerful tool to probe the accessibility of a wide variety of zeolite crystals. Furthermore, the methodology could visualize crystal imperfections, as well as internal diffusion barriers of zeolite crystals. The probes can therefore be used to evaluate how many imperfections are present within a specific crystal as function of the synthesis method or subsequent calcination steps. The current study suggests that BEA crystals have intrinsically less structural imperfections than MFI crystals, which is in line with what is expected based on the synthesis method. Furthermore, polarization-dependent CFM measurements could be used in combination with these probe molecules to elucidate pore network orientation within the zeolite crystals.

### Acknowledgments

Dr. Javier Ruiz-Martínez (UU) and Dr. Joost van der Lit (UU) are acknowledged for useful discussions and Özgün Attila (UU) for providing the MFI crystal SEM images. Dr. Machteld Mertens (ExxonMobil) and Prof. Mark E. Davis (California

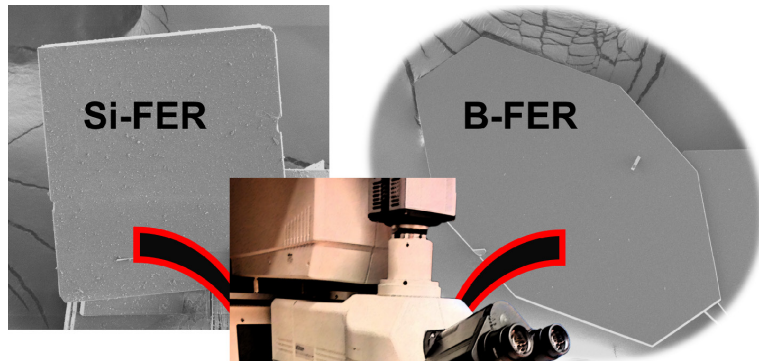
Institute of Technology) are acknowledged for providing respectively the MFI and BEA crystals.

### 3.5 References

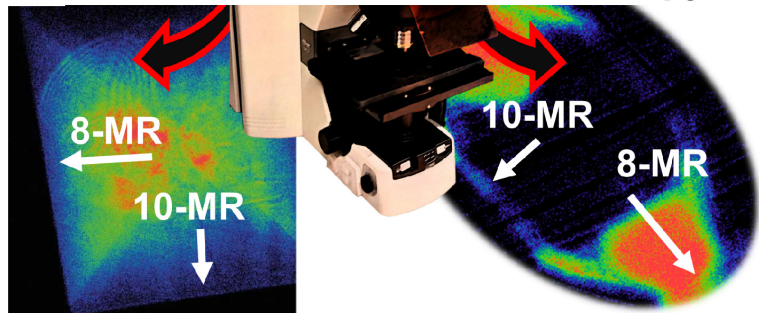
- [1] F. C. Hendriks, D. Valencia, P. C. A. Bruijnincx, B. M. Weckhuysen, *Phys. Chem. Chem. Phys.* 2017, 19, 1857–1867; Chapter 2 of this PhD thesis.
- [2] M. B. J. Roeffaers, R. Ameloot, M. Baruah, H. Uji-i, M. Bulut, G. De Cremer, U. Müller, P. A. Jacobs, J. Hofkens, B. F. Sels, D. E. De Vos, *J. Am. Chem. Soc.* 2008, 130, 5763–5772.
- [3] L. Karwacki, M. H. F. Kox, D. A. M. de Winter, M. R. Drury, J. D. Meeldijk, E. Stavitski, W. Schmidt, M. Mertens, P. Cubillas, N. John, A. Chan, N. Kahn, S. R. Bare, M. Anderson, J. Kornatowski, B. M. Weckhuysen, *Nat. Mater.* 2009, 8, 959–965.
- [4] L. R. Aramburo, L. Karwacki, P. Cubillas, S. Asahina, D. A. M. de Winter, M. R. Drury, I. L. C. Buurmans, E. Stavitski, D. Mores, M. Daturi, P. Bazin, P. Dumas, F. Thibault-Starzyk, J. A. Post, M. W. Anderson, O. Terasaki, B. M. Weckhuysen, *Chem. Eur. J.* 2011, 17, 13773–13781.
- [5] Z. Ristanović, J. P. Hofmann, M.-I. Richard, T. Jiang, G. A. Chahine, T. U. Schülli, F. Meirer, B. M. Weckhuysen, *Angew. Chem. Int. Ed.* 2016, 55, 7496–7500.
- [6] A. Kuperman, S. Nadimi, S. Oliver, G. A. Ozin, J. M. Garcés, M. M. Olken, *Nature* 1993, 365, 239–242.
- [7] C. Baerlocher, L. B. McCusker, [www.iza-structure.org/databases](http://www.iza-structure.org/databases), 2017, retrieved: 1 August.
- [8] K. Lopata, N. Govind, *J. Chem. Theory Comput.* 2011, 7, 1344–1355.
- [9] C. Sprung, B. M. Weckhuysen, *J. Am. Chem. Soc.* 2015, 137, 1916–1928.
- [10] Y. S. Lin, N. Yamamoto, Y. Choi, T. Yamaguchi, T. Okubo, S.-I. Nakao, *Microporous Mesoporous Mater.* 2000, 38, 207–220.
- [11] M. Moliner, Y. Roman-Leshkov, M. E. Davis, *Proc. Natl. Acad. Sci.* 2010, 107, 6164–6168.
- [12] R. Gounder, *Catal. Sci. Technol.* 2014, 4, 2877–2886.
- [13] J. Sun, G. Zhu, Y. Chen, J. Li, L. Wang, Y. Peng, H. Li, S. Qiu, *Microporous Mesoporous Mater.* 2007, 102, 242–248.
- [14] A. N. Parvulescu, D. Mores, E. Stavitski, C. M. Teodorescu, P. C. A. Bruijnincx, R. J. M. K. Gebbink, B. M. Weckhuysen, *J. Am. Chem. Soc.* 2010, 132, 10429–10439.
- [15] M. Tong, D. Zhang, W. Fan, J. Xu, L. Zhu, W. Guo, W. Yan, J. Yu, S. Qiu, J. Wang, F. Deng, R. Xu, *Sci. Rep.* 2015, 5, 1–10.
- [16] R. Szostak, M. Pan, K. P. Lillerud, *J. Phys. Chem.* 1995, 99, 2104–2109.
- [17] R. Szostak, K. P. Lillerud, M. Stocker, *J. Catal.* 1994, 148, 91–99.
- [18] J. M. Newsam, M. M. J. Treacy, W. T. Koetsier, C. B. D. Gruyter, *Proc. R. Soc. A* 1988, 420, 375–405.
- [19] D. Guillaumont, S. Nakamura, *Dyes Pigm.* 2000, 46, 85–92.
- [20] J. R. Agger, N. Hanif, C. S. Cundy, A. P. Wade, S. Dennison, P. A. Rawlinson, M. W. Anderson, *J. Am. Chem. Soc.* 2003, 125, 830–839.
- [21] J. Lu, E. Bartholomeeusen, B. F. Sels, D. Schrijvers, *J. Microsc.* 2016, 264, 370–377.
- [22] S. C. C. Wiedemann, Z. Ristanović, G. T. Whiting, V. R. Reddy Marthala, J. Kärger, J. Weitkamp, B. Wels, P. C. A. Bruijnincx, B. M. Weckhuysen, *Chem. Eur. J.* 2016, 22, 199–210.
- [23] J. C. Saint Remi, A. Lauerer, C. Chmelik, I. Vandendael, H. Terryn, G. V. Baron, J. F. M. Denayer, J. Kärger, *Nat. Mater.* 2015, 15, 401–406.
- [24] R. A. Fisher, *Metron* 1925, 5, 90–104.
- [25] Student, *Biometrika* 1908, 6, 1–25.
- [26] R. A. Ocakoglu, J. F. M. Denayer, G. B. Marin, J. A. Martens, G. V. Baron, *J. Phys. Chem.*

- B 2003, 107, 398–406.
- [27] A. R. Teixeira, C.-C. Chang, T. Coogan, R. Kendall, W. Fan, P. J. Dauenhauer, *J. Phys. Chem. C* 2013, 117, 25545–25555.
- [28] M. H. F. Kox, E. Stavitski, J. C. Groen, J. Pérez-Ramírez, F. Kapteijn, B. M. Weckhuysen, *Chem. Eur. J.* 2008, 14, 1718–1725.
- [29] C. Weidenthaler, R. X. Fischer, R. D. Shannon, O. Medenbach, *J. Phys. Chem.* 1994, 98, 12687–12694.
- [30] E. Stavitski, M. R. Drury, D. A. M. De Winter, M. H. F. Kox, B. M. Weckhuysen, *Angew. Chem. Int. Ed.* 2008, 47, 5637–5640.





### Confocal Fluorescence Microscopy



# Chapter 4

## Unravelling the Internal Architecture of Zeolite Ferrierite Crystals

Large crystals of zeolite ferrierite (FER) can serve as model systems for spatially resolved catalysis and diffusion studies. In this Chapter, a combination of complementary characterization techniques including single crystal X-ray diffraction, wide-field optical microscopy, high-temperature *in situ* confocal fluorescence microscopy, fluorescent probe molecule staining, and atomic force microscopy is applied to unravel the internal architecture of three distinct FER crystal types. Pyrolyzed template species can be used as markers for the 8-membered ring pore direction as they are trapped in the terraced roof of the FER crystals. This leads to a facile method to establish the material's pore system, which avoids the more difficult single crystal X-ray diffraction experiments.

**Based on:** „Diagnosing the Internal Architecture of Zeolite Ferrierite”, Joel E. Schmidt, Frank C. Hendriks, Martin Lutz, L. Christiaan Post, Donglong Fu, and Bert M. Weckhuysen, *ChemPhysChem*, 2017, DOI: 10.1002/cphc.201700583.

## 4.1 Introduction

Zeolite ferrierite (FER) can be synthesized as large, defect-free single crystals. Its structure contains a 2D system of intersecting perpendicular pores limited by 8- and 10-membered ring pores (MRPs), and is nonporous in the third direction. FER is used industrially, with olefin oligomerization as the largest reported catalytic application.<sup>[1]</sup> The synthesis of very large ( $> 100 \mu\text{m}$ ) single crystals of FER was first reported in the pioneering work of Kuperman *et al.*<sup>[2]</sup> Large FER crystals have a plate-like morphology and can be prepared as defect-free, purely siliceous materials, as well as catalytically active aluminosilicates and borosilicates. This has led to notable studies including diffusion through a single pore orientation,<sup>[3]</sup> spatiotemporal diffusion measurements<sup>[4–8]</sup> and pore-mouth catalysis.<sup>[9]</sup> The range of crystal habits and aspect ratios are dependent on the specific synthesis conditions

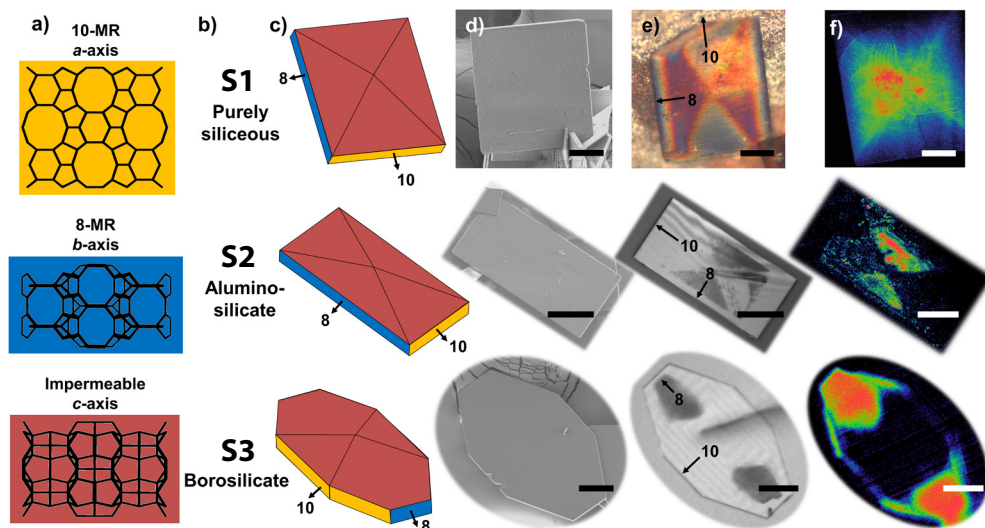


Figure 4.1. Overview of the different crystal morphologies as well as characterization techniques used in this study for the three different compositions of zeolite ferrierite (FER), shown across each row. a) Pore system down each of the three crystallographic directions. b) Composition of the crystal in each row for the three samples studied, as detailed in Table 4.1. c) Schematic representations of the morphologies of the three different samples used in this study, colors correspond to the different crystallographic directions in a. The crystal thickness and the height of the dome on top have been exaggerated for clarity. d) Scanning electron microscopy (SEM) images of the three different samples. e) Optical microscopy images of the three different samples showing triangular regions in each crystal containing pyrolyzed organic template, directions of the 8- and 10-membered rings are indicated. f) Confocal fluorescence microscopy (CFM) images of (top) template-containing large purely siliceous FER crystals recorded at 873 K in an *in situ* cell, with birefringence visible (concentric circles) caused by pressure buildup during fast calcination. (middle) Aluminosilicate FER that contains residual pyrolyzed organic template species after calcination, recorded at 773 K in an *in situ* cell in N<sub>2</sub> atmosphere. (bottom) Borosilicate FER that contained residual pyrolyzed organic template species after calcination, the image was recorded at room temperature. All scale bars represent 50  $\mu\text{m}$ .

and compositions.<sup>[2,10-12]</sup>

A key feature of these materials that has enabled many of the investigations is that the 8- and 10-MRPs run along the two longest dimensions of the crystal, and the top and bottom crystal faces are impermeable. However, the orientation of the 8- and 10-MRPs with respect to the length and width of the crystal is dependent on the exact synthesis composition and batch.<sup>[10,11,13,14]</sup> As conclusions are routinely drawn based on the size discrimination of 8- versus 10-MRPs, it is important that their orientation with respect to crystal habit can be readily established. Single crystal X-ray studies are the best method to determine this, but for the analysis, a large, single crystal is needed, and this can be difficult to obtain.

In this Chapter, investigations of a set of large FER crystals using a variety of techniques is reported to achieve a detailed view of these materials, including their pore orientation, growth mechanism and presence of defects. Patches of pyrolyzed template molecules, which remain in the zeolite crystal pore network after their synthesis, were found in the roof section of the crystals. These patches are leveraged as markers of pore orientation using optical and confocal fluorescence microscopy (CFM), in an approach similar to the study of template decomposition in zeolite crystals.<sup>[15]</sup> Complementary information can be obtained on calcined materials using fluorescent probe molecules, with the added benefit that they are an effective method of quickly screening for crystal accessibility and defects.<sup>[16,17]</sup> Using atomic force microscopy (AFM), it was found that the large crystals contain terraces with a half unit cell step, containing a single exposed layer of 8- and 10-MRPs per terrace. This terracing is consistent with a layer-by-layer growth mechanism that leads to trapped template molecules, and explains the correlation between trapped species and pore orientation that is used in this Chapter to easily diagnose the pore orientation of FER crystals.

4

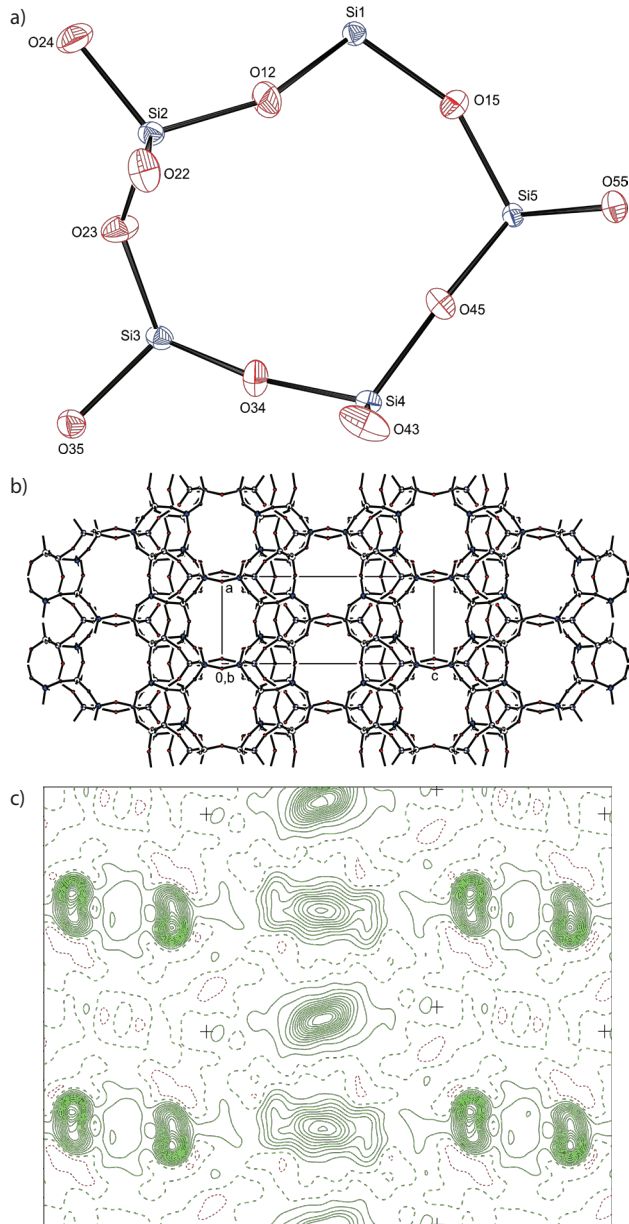
## 4.2 Experimental

Table 4.1. Description of the three large crystal FER samples under investigation.

| Sample number | Description                 | Composition      | Synthesis method     | Sample origin           |
|---------------|-----------------------------|------------------|----------------------|-------------------------|
| S1            | Uncalcined / with template  | Purely siliceous | Ref. <sup>[2]</sup>  | Caltech, Pasadena       |
| S2            | Calcined / template removed | Si/Al=23         | Ref. <sup>[10]</sup> | University of Stuttgart |
| S3            | Calcined / template removed | Si/B=108         | Ref. <sup>[10]</sup> | University of Stuttgart |

### 4.2.1 Single crystal diffraction

Unit cell determinations by X-ray diffraction have been performed on a Bruker Proteum diffractometer with rotating anode and Helios optics ( $\lambda = 1.54184 \text{ \AA}$ ).



**Analysis** procedure for sample 1.  $\text{Si}_9\text{O}_{18}$  + disordered electron density, Fw = 540.81, colorless plate,  $0.24 \times 0.14 \times 0.02 \text{ mm}^3$ , orthorhombic, Pnnm (no. 58),  $a = 7.41601(18)$ ,  $b = 14.0821(3)$ ,  $c = 18.7075(4)$  Å,  $V = 1953.68(7)$  Å $^3$ ,  $Z = 4$ ,  $D_x = 1.839 \text{ g/cm}^3$ ,  $\mu = 6.59 \text{ mm}^{-1}$ . Derived values do not contain the contribution of the disordered electron density. 7962 Reflections were measured on a Bruker Proteum diffractometer with rotating anode and Helios optics ( $\lambda = 1.54184$  Å) at a temperature of 100(2) K up to a resolution of  $(\sin \theta/\lambda)_{\max} = 0.59$  Å $^{-1}$ . The intensities were integrated with the Eval15 software.<sup>[18]</sup> Multi-scan absorption correction and scaling was performed with SADABS<sup>[19]</sup> (correction range 0.25–0.47). 1721 Reflections were unique ( $R_{\text{int}} = 0.047$ ), of which 1717 were observed [ $I > 2\sigma(I)$ ]. Initial atomic coordinates were taken from the literature.<sup>[13]</sup> Least-squares refinement was performed with SHELXL-2014<sup>[20]</sup> against  $F^2$  of all reflections. The crystal structure

Figure 4.2. a) Independent atoms in the framework of sample 1. Displacement ellipsoids are drawn at the 50% probability level. Atoms Si1 and O22 are located on twofold axes, respectively, and O55 is located on a mirror plane. Disordered electron density is omitted in the drawing. b) Packing in the crystal structure of sample 1. View along the b-axis. Disordered electron density is omitted in the drawing. c) Difference electron density map in the a,b,0-plane. Contours are drawn at  $0.25 \text{ e}/\text{\AA}^3$ . Positive contours are drawn in green with a maximum of  $4.25 \text{ e}/\text{\AA}^3$ . Negative contours are drawn in red. The + signs indicate the positions of symmetry equivalent O55 atoms.

Table 4.2. Crystallographic unit cell directions with respect to sample morphology as determined by single crystal X-ray diffraction, allowing the pore orientation to be identified.

| Sample | a (Å) | b (Å) | c (Å) | h  | k  | l  | Distance (mm) | Sample | a (Å) | b (Å) | c (Å) | h  | k  | l  | Distance (mm) |
|--------|-------|-------|-------|----|----|----|---------------|--------|-------|-------|-------|----|----|----|---------------|
| S1     | 7.42  | 14.08 | 18.71 | 0  | 0  | 1  | 0.01          | S3     | 7.39  | 14.02 | 18.57 | 0  | 0  | 1  | 0.02          |
|        |       |       |       | 0  | 0  | -1 | 0.01          |        |       |       |       | 0  | 0  | -1 | 0.02          |
|        |       |       |       | 0  | 1  | 0  | 0.07          |        |       |       |       | 1  | -1 | 0  | 0.08          |
|        |       |       |       | 0  | -1 | 0  | 0.07          |        |       |       |       | 1  | 1  | 0  | 0.08          |
|        |       |       |       | 1  | 0  | 0  | 0.12          |        |       |       |       | -1 | -1 | 0  | 0.06          |
|        |       |       |       | -1 | 0  | 0  | 0.12          |        |       |       |       | -1 | 1  | 0  | 0.06          |
| S2     | 7.42  | 14.05 | 18.80 | 0  | 0  | 1  | 0.02          | S3     | 7.44  | 14.15 | 18.77 | 0  | 1  | 0  | 0.1           |
|        |       |       |       | 0  | 0  | -1 | 0.02          |        |       |       |       | 0  | -1 | 0  | 0.1           |
|        |       |       |       | 0  | 1  | 0  | 0.04          |        |       |       |       | 0  | 0  | -1 | 0.02          |
|        |       |       |       | 0  | -1 | 0  | 0.04          |        |       |       |       | 0  | 1  | 0  | 0.13          |
|        |       |       |       | 1  | 0  | 0  | 0.09          |        |       |       |       | 0  | -1 | 0  | 0.13          |
|        |       |       |       | -1 | 0  | 0  | 0.09          |        |       |       |       | 1  | 0  | 0  | 0.07          |
| S2     | 7.48  | 14.15 | 18.95 | 1  | 0  | 0  | 0.065         | S3     | 7.44  | 14.15 | 18.77 | 0  | 0  | 1  | 0.02          |
|        |       |       |       | -1 | 0  | 0  | 0.065         |        |       |       |       | -1 | 0  | 0  | 0.07          |
|        |       |       |       | 0  | 1  | 0  | 0.03          |        |       |       |       | 1  | 1  | 0  | 0.09          |
|        |       |       |       | 0  | -1 | 0  | 0.03          |        |       |       |       | -1 | 1  | 0  | 0.09          |
|        |       |       |       | 0  | 0  | 1  | 0.015         |        |       |       |       | -1 | -1 | 0  | 0.09          |
|        |       |       |       | 0  | 0  | -1 | 0.015         |        |       |       |       | 1  | -1 | 0  | 0.09          |
| S2     | 7.45  | 14.11 | 18.86 | 0  | 0  | 1  | 0.015         | S3     | 7.44  | 14.15 | 18.77 | 0  | 0  | 1  | 0.02          |
|        |       |       |       | 0  | 0  | -1 | 0.015         |        |       |       |       | -1 | 0  | 0  | 0.07          |
|        |       |       |       | 1  | 0  | 0  | 0.095         |        |       |       |       | 1  | 1  | 0  | 0.09          |
|        |       |       |       | -1 | 0  | 0  | 0.095         |        |       |       |       | -1 | 1  | 0  | 0.09          |
|        |       |       |       | 0  | 1  | 0  | 0.025         |        |       |       |       | -1 | -1 | 0  | 0.09          |
|        |       |       |       | 0  | -1 | 0  | 0.025         |        |       |       |       | 1  | -1 | 0  | 0.09          |

4

contains large voids filled with disordered electron density. The size of the voids and the contribution to the structure factors was determined using the SQUEEZE algorithm<sup>[21]</sup> based on a grid of 0.20 Å and a probe radius of 1.2 Å.<sup>[22]</sup> This resulted in a void size of 596 Å<sup>3</sup> / unit cell and a contribution of 102 electrons / unit cell. The atoms were refined freely with anisotropic displacement parameters. 125 Parameters were refined with no restraints. The disordered density was handled with the SQUEEZE algorithm prior to the final refinements. R<sub>1</sub>/wR<sub>2</sub> [I > 2σ(I)]: 0.0361 / 0.1075. R<sub>1</sub>/wR<sub>2</sub> [all refl.]: 0.0361 / 0.1076. S = 1.136. There is residual electron density between -0.44 and 0.41 e/Å<sup>3</sup>. Geometry calculations and checking for higher symmetry were performed with the PLATON program.<sup>[23]</sup> The results

of the analysis are shown in Figure 4.2.

**Analysis procedure for other samples.** For each of the other zeolite FER crystals,  $3 \times 24$   $\omega$ -scans have been performed (detector distance 60 mm, detector  $2\theta=10^\circ$ , scan width= $0.5^\circ$ ). The Dirax software was used to index the reflections.<sup>[24]</sup> Refinement of the cell parameters was done with the Proteum2 software<sup>[25]</sup> based on 55 and 80 reflections, respectively. Unit cell parameters were constrained to orthorhombic geometry. Results are given in Table 4.2. All calcined samples were reported to be *Pnmm* space group (#58) which has all  $90^\circ$  angles. The 10 MRP lie along the *a* axis and the 8 MRP lie along the *b* axis.

#### 4.2.2 Confocal fluorescence microscopy

Confocal fluorescence microscopy measurements and mapping were performed on a Nikon Eclipse 90i upright microscope using an air objective. The microscope is equipped with a Nikon-Eclipse A1R scan head. Confocal fluorescence microscopy images were recorded using excitation from a Melles Griot argon ion liquid state 488 nm laser (40 Mw) or a Coherent Sapphire solid state 561 nm laser (50 Mw). Emitted fluorescence was detected by either a 32 multiplier spectral detector in the range of 518 to 710 nm (488 nm) or a DU4 detection unit using a 595/50 band pass filter (561 nm). Wide-field microscopy images were recorded on either the Nikon microscope described above, equipped with a scientific metal-oxide-semiconductor (sCMOS) camera (Andor Zyla 5.5), or by an Olympus BX41M upright microscope equipped with a charge-coupled device (CCD) video camera (ColorView IIIu, Soft Imaging System GmbH). For pyrolysis experiments, samples containing template were loaded in a Linkam *in situ* cell (TS1000) positioned on the microscope table. The cell was purged with nitrogen and then heated under nitrogen atmosphere to 873 K at a rate of 25 K/min.

The probe molecule (*trans*-4-(4'-(*N,N*-dimethylamino)styryl)-*N*-methylpyridinium iodide, **1**) was prepared as described in Chapter 2.<sup>[16,26]</sup> The probe molecule has a diameter of 5.8 Å, so it can diffuse into 10-MRPs, but not 8-MRPs. The molecule has an adsorption maximum of  $\lambda_{\text{max}} = 481$  nm. Calcined crystals of each sample were immersed in a 1 µM ethanolic solution of **1** and allowed to stand for at least one week. The crystals were removed from solution, quickly washed once with ethanol to remove any excess dye and then placed on a glass microscope slide and allowed to dry in air.

#### 4.2.3 Scanning electron microscopy

Samples were first mounted on carbon tape and coated with 6 nm of platinum. Scanning electron microscopy (SEM) images were acquired using a Philips XL30 with an accelerating voltage of 5 kV.

#### 4.2.4 Atomic force microscopy

Atomic force microscopy (AFM) was used to characterize the surface structure of FER crystals. The crystals were carefully mounted in super glue such that the surface remained exposed and were then thoroughly rinsed with water to remove surface debris. AFM measurements were conducted using a JPK Nanowizard II using Nanosensors™ PPP-NCHR tips with a Nikon Eclipse Ti-U inverted microscope used to locate the samples. The instrument was mounted on an active vibration isolation table with a Halcyonics Active Vibration Isolation unit, and the entire setup was placed inside an acoustic vibration isolation box.<sup>[27]</sup> AFM data was acquired using the JPK Nanowizard Control software and data were analyzed using Gwyddion data visualization and analysis software (version 2.45). A 20 x 20  $\mu\text{m}$  region of the crystal was selected for measurement. In this region, multiple measurements were made and averaged to get an average terrace height. The terraces exhibit a high degree of uniformity, expected for crystallographic features. However, the terrace width is not necessarily uniform (see Figure 4.4).

### 4.3 Results and discussion

4

#### 4.3.1 Samples and pore orientation determination

Three distinct ferrierite samples were considered, encompassing purely siliceous, aluminosilicate and borosilicate materials, with sample details given in Table 4.1. These crystals exhibited different morphologies and were prepared using different synthetic protocols in two separate laboratories, allowing us to examine a diverse range of materials. Representative images of each sample from both SEM and light microscopy are included in Figure 4.1. The purely siliceous and aluminosilicate materials have a rectangular morphology, though with different aspect ratios, while the borosilicate material has an octagonal morphology.<sup>[2,13]</sup> Furthermore, FER crystals are reported to have a pyramid-shaped extension on the large flat side of the crystal.<sup>[28]</sup> This shape is shown in Figure 4.1b, but the height of this pyramid is negligible, so it cannot be observed by optical microscopy.

The opening of the 10-MRPs in the purely siliceous material is reported to be at either the longest edge<sup>[13]</sup> (length) or second longest edge<sup>[10]</sup> (width) in two separate single crystal studies on different samples of purely siliceous FER. These conflicting observations motivated us to explore the pore orientation with respect to crystal habit in detail.

First, the pore orientation with respect to crystal habit was unambiguously determined in each sample by single crystal X-ray structure analysis and the results are shown in Figure 4.2. The unit cell sizes are given in Table 4.2, and the analysis is in good agreement with previous reports, with small changes in the unit cell size depending on the composition.<sup>[13,29–34]</sup> Herein, we are using the standard space group setting of  $a < b < c$ , and in this description the  $a$ -axis is the direction of the 10-MRPs, the  $b$ -axis

is the direction of the 8-MRPs and the *c*-axis is impermeable.<sup>[13]</sup> The single crystal X-ray studies show that the crystals have a single crystallographic direction. In the purely siliceous S1 and aluminosilicate S2 materials with a rectangular morphology, the 10-MRPs open at the short edge of the crystals, while the 8-MRPs open at the long edge of the crystals. This is in agreement with a recent report by Wiedemann *et al.*,<sup>[9]</sup> who studied pore mouth catalysis occurring only in the 10-MRP openings using sample 1. In octagonal, borosilicate crystals, the orientation is reversed, with the 10-MRPs opening at the long edge of the crystals and the 8-MRPs at the short edge. These results show that crystal morphology alone is not a good indicator of pore orientation, as the locations of the 8- and 10-MRPs with respect to the length and width can indeed be reversed. Therefore, a simple method to determine internal pore orientation would be beneficial and has been developed in this work.

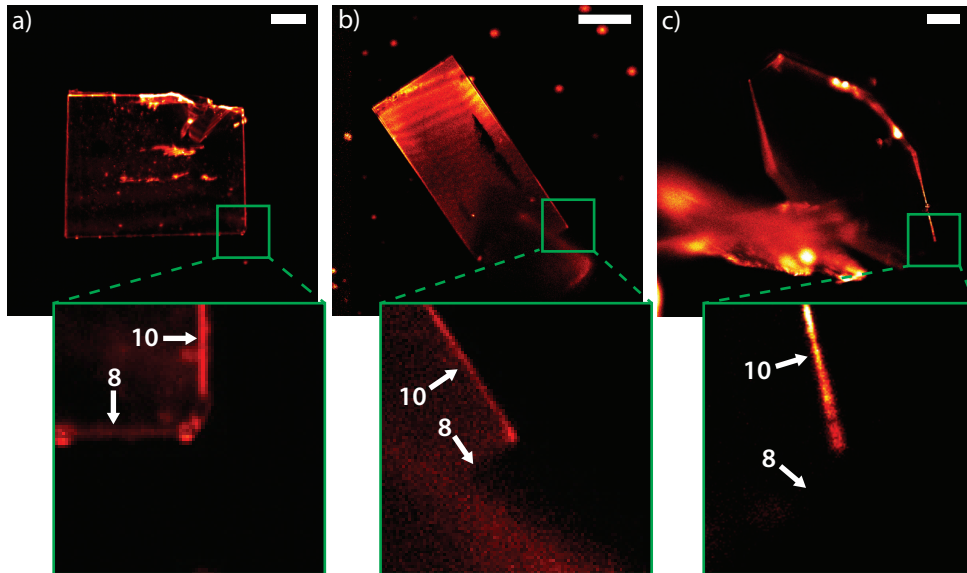


Figure 4.3. Confocal fluorescence microscopy (CFM) images of calcined zeolite (FER) crystals stained with the fluorescent probe molecule 1. No fluorescence at the intensity of that caused by the 1 probe was found in the crystals prior to staining. The direction of the 8- and 10-MRPs is indicated in the zoomed-in images on the right; more probe molecules are at the 10-MRP edge given the higher fluorescence intensity. a) Purely siliceous FER S1 contains obvious mechanical defects that are highlighted by the probe molecule. The complete top edge of the crystal is damaged, explaining the increased fluorescence there. b) Aluminosilicate FER S2, which does not contain any obvious mechanical defects, leading to a uniform background fluorescence across the crystal and highlighting the defect free nature of the growth process. The increased signal at the top of the crystal is caused by scattering, recognizable by the interference pattern. c) Borosilicate FER S3, which does not contain any obvious mechanical defects, leading to a uniform background fluorescence across the crystal and highlighting the defect free nature of the growth process. All scale bars represent 50 µm.

### 4.3.2 Alternative ways to determine pore orientation

From Chapters 2 and 3 it is known that the probe molecule 1 (with a diameter of 5.8 Å) can be selectively inserted into 10-, but not 8-MRPs.<sup>[16,26]</sup> Calcined crystals of all three zeolite FER samples were treated with ethanolic solutions of 1, and then studied using CFM. The results of the CFM study using 1 are shown in Figure 4.3. In all three samples, 1 molecules are found at the opening of the 10-MRPs, demonstrating that from staining FER crystals using this probe the pore orientation can be easily elucidated. Furthermore, the insertion of 1 into the 10-MRPs shows the pores are accessible from the surface and not blocked. However, as observed before with large crystals of MFI, transport of 1 through 10 MRPs is slow, because fluorescence from probe molecules that have entered the pores is observed at the edge of the crystals only.<sup>[16]</sup>

Another benefit of studying the crystals using 1 probe molecules is that these are highly sensitive to any material defects arising from mechanical damage or crystalline intergrowths.<sup>[16]</sup> Further examination of Figure 4.3a shows significant fluorescence in distinct regions of the crystal, which coincide with mechanical damage (optically visible cracks) to the crystal. This demonstrates that 1 molecules accumulate in defects, even in a neutral framework, as is the case with purely siliceous FER crystals of sample 1. The other two zeolite materials did not show any significant internal fluorescence, leading to the conclusion that these have no accessible defects. While this may seem obvious due to the regular nature of these crystals, the MFI crystals studied in Chapter 3 showed that 1 can highlight internal intergrowth structures; the absence of highlighted intergrowth features in these crystals suggests that large FER crystals do not contain these features.<sup>[16]</sup> Thus, the fluorescent probe molecule is able to highlight the location of the 10-MRPs, as well as reveal physical damage to the zeolite crystals. The results show the importance of carefully treating these crystals, as they can be damaged during manual manipulation or calcination (Figure 4.1f, top).

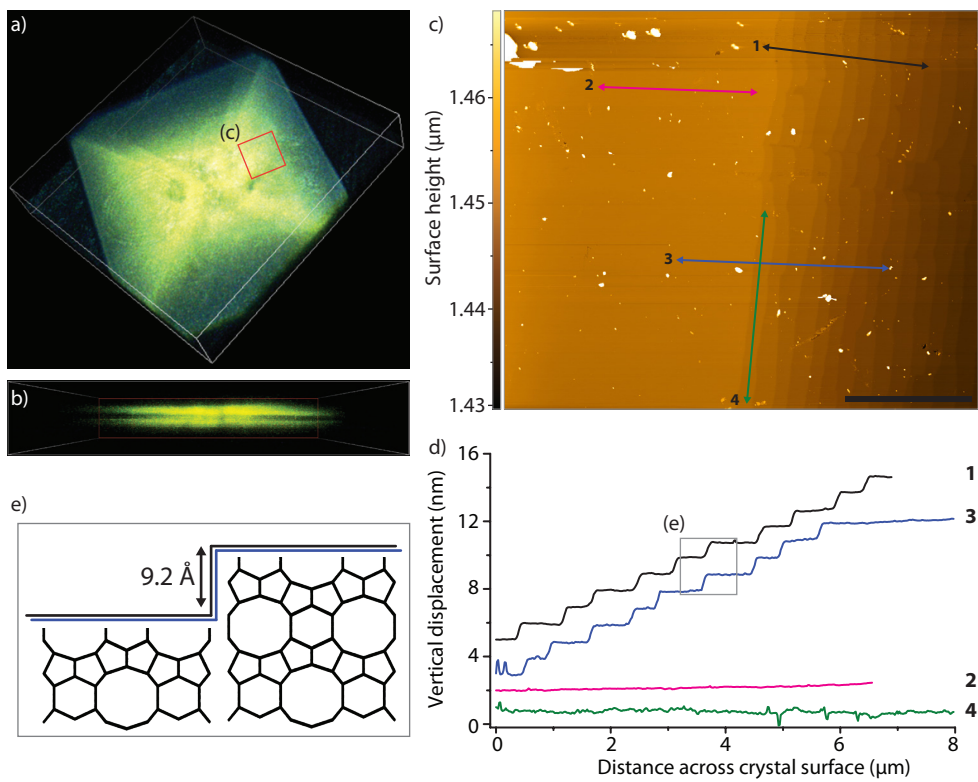
Upon examination of calcined large crystals of aluminosilicate and borosilicate FER (sample S2 and S3) by optical microscopy, it was observed that some crystals contained regular dark patches, with representative images in Figure 4.1e. In the aluminosilicate material 2, with a rectangular morphology, the long edge of these dark triangular regions coincides with the longest crystal edge, which contains the opening of the 8-MRPs as depicted in Figure 4.1c. For the borosilicate material 3, the dark patches lie closest to the short side of the crystal, again coinciding with the side to which the 8-MRPs open. These findings motivated us to understand the origin of the dark patches in the crystals, which were presumably from pyrolyzed organic template molecules that remained occluded due to incomplete calcination of zeolite FER crystals.

The uncalcined sample S1 allowed us to test conditions in which the dark triangular patches, seen in (calcined) crystals of S2 and S3, could be reproduced. A previous thermogravimetric analysis (TGA) study showed that the pyridine template could be easily removed from the 10-MRP channel below 690 K, but that fully removing pyridine from the 8-MRP side-pockets required calcination in dry oxygen at

1073 K for 48 h.<sup>[31]</sup> Crystals of **S1** were heated to 873 K and subsequently cooled down to room temperature, all in N<sub>2</sub> atmosphere, to pyrolyze the organic template molecules inside the crystal. After this procedure, the same distinctive triangular coloration pattern observed in **S2** and **S3** was seen in some of the crystals of **S1** (Figure 4.1e). The long edge of the black triangles points towards the edge of the crystal the 8-MRPs open to, making the location of these black triangles fully consistent with the results from single crystal X-ray diffraction. Thus, pyrolysis leaves dark carbonaceous species that can serve as a marker for the pore direction. The triangular regions that were found in samples **S2** and **S3** likely were the result of incomplete calcination. Incomplete calcination or pyrolysis therefore results in occluded, pyrolyzed carbon deposits caused by organic template molecules that are trapped inside the zeolite framework. These deposits can be used as a marker for 8-MRPs in large FER crystals without having to resort to single crystal diffraction studies.

In our group, CFM has been applied under *in situ* conditions to elucidate the internal crystallographic intergrowth structure of AFI, CHA and MFI frameworks by monitoring fluorescent species during the template removal process at high temperature.<sup>[15,35–37]</sup> Because the dark patches observed in the crystals are most likely aromatic species resembling coke, it is likely they are fluorescent, allowing us to apply CFM to study them. Template-containing crystals of purely siliceous FER (**S1**) were heated to 873 K under a N<sub>2</sub> atmosphere. A CFM image recorded at 773 K is shown in Figure 4.1f. Distinct triangular-shaped fluorescent regions are visible at the same location as the patches observed by optical microscopy. Samples of the aluminosilicate (**S2**) and borosilicate FER (**S3**) containing dark patches were then studied in a similar manner with CFM, with the 2D CFM maps shown in Figure 4.1f. Fluorescence was observed in both samples, suggesting that the dark patches are in all three samples caused by pyrolyzed template molecules. Interestingly, samples **S1** and **S2** only show fluorescence at elevated temperatures, while sample **S3** fluoresces at room temperature. Evidently, removal of the template by calcination in **S3** generates stable fluorescent species not found in the other samples. Furthermore, rapid heating of uncalcined samples caused birefringence, as shown for **S1** in Figure 4.1f. This points towards crystal damage caused by organic template decomposition products that are unable to escape, consistent with the proposed origin of the dark, fluorescent patches.

It has been shown before that the organic template of FER, pyridine, is removed through the 10-MRPs during calcination,<sup>[14]</sup> as pyridine is too large to move through the 8-MRPs. The dark, fluorescent patches are therefore thought to be caused by degradation products of pyridine template molecules that cannot exit through the 10-MRPs. However, in the main body of the crystal, the 8- and 10-MRPs are fully interconnected, so it is unlikely that template molecules are trapped there. To shed more light on the exact location of the carbonaceous species, the CFM results of purely siliceous sample **S1** were examined in 3D, as shown in Figure 4.4a, and it was found that the fluorescent regions were only present in the pyramidal roof section of the crystal (Figure 4.4b). From previous studies it is known that the 8- or 10-MRPs open along the pitch of the roof: using interference microscopy, fast



4

Figure 4.4. a,b) 3D Confocal fluorescence microscopy (CFM) images of template-containing large purely siliceous FER crystals S1 heated in N<sub>2</sub> atmosphere to 873 K in the in situ cell. Image b) reveals that the fluorescent species exist only in the roof sections of the crystal as significantly lower fluorescence is present in the main body of the material. As the 8-MRP openings are along the long edge of the crystal it shows that template molecules are unable to escape the roof portion of the crystal and instead form fluorescent species upon heating. Bounding box dimensions are 255 × 255 × 45 μm. Birefringence (concentric circles) is visible in (a), caused by internal pressure due to occluded organic species that are unable to escape. c) Atomic force microscopy (AFM) image of the surface of purely siliceous FER S1 showing four height traces along the surface. d) Vertical displacement along the four height traces on the surface of FER showing regular terrace heights and flat regions. Notice the difference in units on the x- versus the y-axis. e) Schematic of the FER crystal structure with a step height of 9.2 Å along the c-axis indicated.

diffusion of methanol was observed in the roof as compared with the main body of the crystal (methanol can readily diffuse through both pores).<sup>[5,13,14]</sup> When the results of the 3D CFM study are combined with this view of the crystal roof, a deeper understanding of the interconnectivity of the internal pore system emerges, with distinct regions in the crystal: i) in the main body of the crystal the pore network is fully interconnected, which is why only minimal fluorescence is observed in the center of the crystal as the template molecules can easily diffuse out; ii) in the dome section on top of the crystal, pyridine is not able to easily diffuse out of the side of

the pyramid limited by 8-MRPs, which causes the characteristic black triangular regions. The triangular shape is obviously caused by the shape of the pyramid; the sharp differences in coke and fluorescence between the sides of the pyramids with 8- and 10-MRPs opening to the surface suggests the existence of diffusion barriers. These barriers prevent template molecules from moving between the different parts of the pyramid in the roof sections, similar to what has been observed in large zeolite MFI crystals.<sup>[36]</sup>

### 4.3.3 Evaluating the crystal surface and growth mechanism

The crystal faces of the purely siliceous FER crystals were studied in more detail using AFM; the results are shown in Figure 4.4. We determined that the surface of purely siliceous FER is terraced, with an average terrace step height determined to be  $9.2 \pm 0.6 \text{ \AA}$ ; an AFM view of the terraced crystal surface along with a graph of the vertical displacement across the surface are shown in Figure 4.4. As the terraces are steps along the c-axis of the crystal, which has an experimentally determined unit cell length of  $18.7 \text{ \AA}$  (Table 4.2), they correspond to steps of a half unit cell, which will contain a single layer of intersecting 8- and 10-MRPs (Figure 4.3d). Finding a half unit cell step height makes it likely that these large zeolite FER crystals grow in a layer-by-layer process where pyridine first fits into partial cavities, which then crystallize around it, forming a completed pore. This is equivalent to the step height measured by AFM, and a schematic of this layer-by-layer growth mechanism is shown in Figure 4.4e. Growth in this dimension is much slower than growth in the directions of the 8- and 10-MRPs, which is reflected in the plate-like morphology of the crystals. These regular terraces are consistent with a classical crystal growth mechanism where crystals grow via the addition of monomers in solution. This is an interesting finding as zeolites are known to grow via both classical and non-classical mechanisms.<sup>[38-41]</sup> However, the classical growth mechanism may only apply towards the end of zeolite crystallization as we did not probe the initial stages of crystallization when a non-classical mechanism may apply. Nevertheless, finding a classical growth mechanism, at least at the end of crystallization, is an important observation as these crystals form under seldomly investigated solvothermal conditions. There is a prior AFM study of a siliceous FER sample that reported the surface of the material was covered in ‘nanowires’ that grew parallel to the crystal edges, as if they were on a pyramid, and noted a drop of  $10 \text{ \AA}$  between wires.<sup>[28]</sup> This terrace height is similar to what we observe in the present study, though we did not find any indication of “nanowire” morphology and observed smooth, flat terraced surfaces (see Figure 4.4c).

## 4.4 Conclusions

Large crystals of zeolite FER can serve as model systems for catalysis and diffusion as their size allows spatially resolved studies using various microscopy techniques. We demonstrate a facile method to determine pore orientation with respect to

crystal habit, as this is known to vary between samples, providing researchers with a powerful, yet simple tool to conduct studies where discrimination between 8- and 10-MRPs is critical. The orientation of the 8- and 10-MRPs does not correlate with the length or width of the zeolite crystals, meaning the growth rate in these directions is very similar and can vary from synthesis to synthesis. The ability to screen crystals for defects without using damaging and tedious X-ray or electron diffraction techniques has been shown with pyrolyzed template molecules as well as fluorescent probe molecules using CFM. The occluded template molecules were determined to reside in the roof section of the crystal, and form triangular shaped patches, indicating the direction of the 8- and 10-MRPs. Additionally, the persistence of residual coke molecules even after standard calcination procedures offers a warning to ensure complete template removal in any zeolite study. The roof of the crystals was further investigated using AFM, demonstrating a terraced surface, consistent with a layer-by-layer growth mechanism. When combined, these optical imaging techniques provide a powerful yet facile platform for researchers to continue investigations of large zeolite crystals as they will certainly continue to yield insights into zeolite diffusion and catalysis as well as into their internal architecture.

## Acknowledgements

4

We thank Professor Mark E. Davis (Caltech, Pasadena, USA) for providing the sample of purely siliceous FER and Professor Jens Weitkamp (University of Stuttgart, Stuttgart, Germany) and Professor Jörg Kärger (University of Leipzig, Leipzig, Germany) for providing the aluminosilicate (S2) and borosilicate (S3) samples. We also would like to thank Dr. Ingmar Swart (Utrecht University) for use of the AFM instrument.

## 4.5 References

- [1] W. Vermeiren, J.-P. Gilson, *Top. Catal.* 2009, **52**, 1131–1161.
- [2] A. Kuperman, S. Nadimi, S. Oliver, G. A. Ozin, J. M. Garcés, M. M. Olken, *Nature* 1993, **365**, 239–242.
- [3] J. E. Lewis, G. R. Gavalas, M. E. Davis, *AIChE J.* 1997, **43**, 83–90.
- [4] P. Kortunov, L. Heinke, S. Vasenkov, C. Chmelik, D. B. Shah, J. Kärger, R. A. Rakoczy, Y. Traa, J. Weitkamp, *J. Phys. Chem. B* 2006, **110**, 23821–23828.
- [5] J. Kärger, P. Kortunov, S. Vasenkov, L. Heinke, D. B. Shah, R. A. Rakoczy, Y. Traa, J. Weitkamp, *Angew. Chem. Int. Ed.* 2006, **45**, 7846–7849.
- [6] L. Heinke, C. Chmelik, P. Kortunov, D. M. Ruthven, D. B. Shah, S. Vasenkov, J. Kärger, *Chem. Eng. Technol.* 2007, **30**, 995–1002.
- [7] F. Hibbe, V. R. R. Marthala, C. Chmelik, J. Weitkamp, J. Kärger, *J. Chem. Phys.* 2011, **135**, 184201.
- [8] J. Kärger, T. Binder, C. Chmelik, F. Hibbe, H. Krautscheid, R. Krishna, J. Weitkamp, *Nat. Mater.* 2014, **13**, 333–343.
- [9] S. C. C. Wiedemann, Z. Ristanović, G. T. Whiting, V. R. Reddy Marthala, J. Kärger,

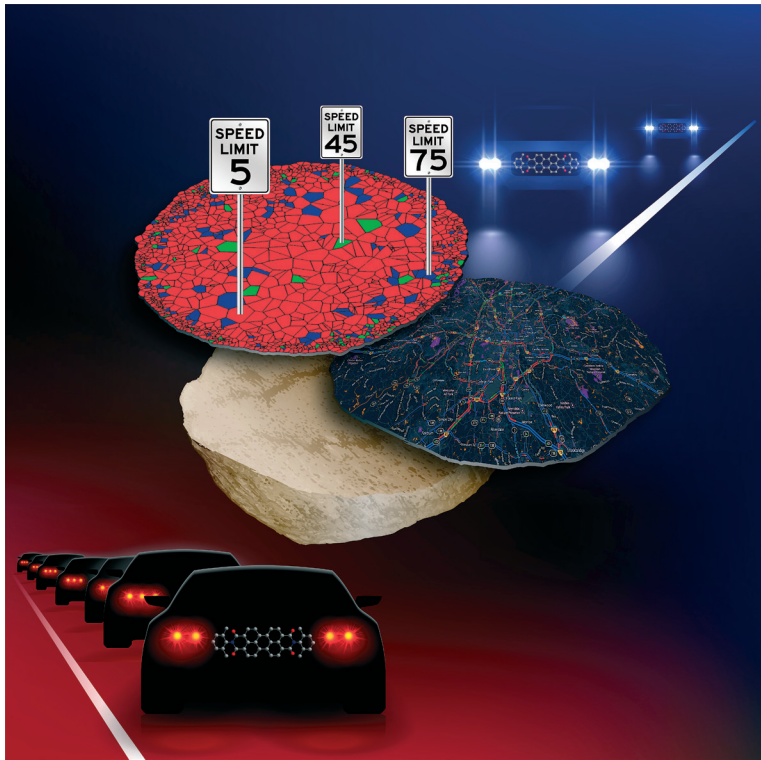
- J. Weitkamp, B. Wels, P. C. A. Bruijnincx, B. M. Weckhuysen, *Chem. Eur. J.* **2016**, *22*, 199–210.
- [10] V. R. R. Marthala, M. Hunger, F. Kettner, H. Krautscheid, C. Chmelik, J. Kärger, J. Weitkamp, *Chem. Mater.* **2011**, *23*, 2521–2528.
- [11] R. A. Rakoczy, Y. Traa, P. Kortunov, S. Vasenkov, J. Kärger, J. Weitkamp, *Microporous Mesoporous Mater.* **2007**, *104*, 179–184.
- [12] Z. Li, M. C. Johnson, M. Sun, E. T. Ryan, D. J. Earl, W. Maichen, J. I. Martin, S. Li, C. M. Lew, J. Wang, M. W. Deem, M. E. Davis, Y. Yan, *Angew. Chem. Int. Ed.* **2006**, *45*, 6329–6332.
- [13] J. E. Lewis, C. C. Freyhardt, M. E. Davis, *J. Phys. Chem.* **1996**, *100*, 5039–5049.
- [14] Z. A. D. Lethbridge, D. S. Keeble, D. Walker, P. A. Thomas, R. I. Walton, *J. Appl. Crystallogr.* **2010**, *43*, 168–175.
- [15] L. Karwacki, E. Stavitski, M. H. F. Kox, J. Kornatowski, B. M. Weckhuysen, *Angew. Chem. Int. Ed.* **2007**, *46*, 7228–7231.
- [16] F. C. Hendriks, J. E. Schmidt, J. A. Rombouts, K. Lammertsma, P. C. A. Bruijnincx, B. M. Weckhuysen, *Chem. Eur. J.* **2017**, *23*, 6305–6314; Chapter 3 of this PhD thesis.
- [17] C. Seebacher, J. Rau, F.-W. Deeg, C. Bräuchle, S. Altmaier, R. Jäger, P. Behrens, *Adv. Mater.* **2001**, *13*, 1374–1377.
- [18] A. M. M. Schreurs, X. Xian, L. M. J. Kroon-Batenburg, *J. Appl. Crystallogr.* **2010**, *43*, 70–82.
- [19] G. M. Sheldrick, SADABS Software, Universität Göttingen, Germany, 2008.
- [20] G. M. Sheldrick, *Acta Crystallogr. Sect. C Struct. Chem.* **2015**, *71*, 3–8.
- [21] A. L. Spek, *Acta Crystallogr. Sect. C Struct. Chem.* **2015**, *71*, 9–18.
- [22] H. Küppers, F. Liebau, A. L. Spek, *J. Appl. Crystallogr.* **2006**, *39*, 338–346.
- [23] A. L. Spek, *Acta Crystallogr. Sect. D Biol. Crystallogr.* **2009**, *65*, 148–155.
- [24] A. J. M. Duisenberg, *J. Appl. Crystallogr.* **1992**, *25*, 92–96.
- [25] Proteum2, v2014.9-0. Bruker AXS Inc. 2014.
- [26] F. C. Hendriks, D. Valencia, P. C. A. Bruijnincx, B. M. Weckhuysen, *Phys. Chem. Chem. Phys.* **2017**, *19*, 1857–1867; Chapter 2 of this PhD thesis.
- [27] L. C. Post, Master Thesis, Utrecht University, The Netherlands, 2015.
- [28] M. W. Anderson, J. R. Agger, N. Pervaiz, S. J. Weigel, A. K. Cheetham, in *12th International Zeolite Conference* (Eds.: M.M.J. Treacy, B.K. Marcus, M.E. Bisher, J.B. Higgins), Materials Research Society, Baltimore, 1999, pp. 1487–1494.
- [29] A. B. Pinar, P. A. Wright, L. Gómez-Hortigüela, J. Pérez-Pariente, *Microporous Mesoporous Mater.* **2010**, *129*, 164–172.
- [30] R. E. Morris, S. J. Weigel, N. J. Henson, L. M. Bull, M. T. Janicke, B. F. Chmelka, A. K. Cheetham, *J. Am. Chem. Soc.* **1994**, *116*, 11849–11855.
- [31] S. J. Weigel, J.-C. Gabriel, E. G. Puebla, a M. Bravo, N. J. Henson, L. M. Bull, A. K. Cheetham, *J. Am. Chem. Soc.* **1996**, *118*, 2427–2435.
- [32] I. Bull, P. Lightfoot, L. A. Villaescusa, L. M. Bull, R. K. B. Gover, J. S. O. Evans, R. E. Morris, *J. Am. Chem. Soc.* **2003**, *125*, 4342–4349.
- [33] R. J. Darton, P. Wormald, R. E. Morris, *J. Mater. Chem.* **2004**, *14*, 2036–2040.
- [34] R. J. Darton, R. E. Morris, *Solid State Sci.* **2006**, *8*, 342–345.
- [35] L. Karwacki, B. M. Weckhuysen, *Phys. Chem. Chem. Phys.* **2011**, *13*, 3681–3685.
- [36] L. Karwacki, M. H. F. Kox, D. A. M. de Winter, M. R. Drury, J. D. Meeldijk, E. Stavitski, W. Schmidt, M. Mertens, P. Cubillas, N. John, A. Chan, N. Kahn, S. R. Bare, M. Anderson, J. Kornatowski, B. M. Weckhuysen, *Nat. Mater.* **2009**, *8*, 959–965.
- [37] L. Karwacki, H. E. Van Der Bij, J. Kornatowski, P. Cubillas, M. R. Drury, D. A. M. de Winter, M. W. Anderson, B. M. Weckhuysen, *Angew. Chem. Int. Ed.* **2010**, *49*, 6790–6794.
- [38] K. N. Olafson, R. Li, B. G. Alamani, J. D. Rimer, *Chem. Mater.* **2016**, *28*, 8453–8465.

- [39] A. I. Lupulescu, J. D. Rimer, *Science* **2014**, *344*, 729–732.
- [40] M. Kumar, H. Luo, Y. Román-Leshkov, J. D. Rimer, *J. Am. Chem. Soc.* **2015**, *137*, 13007–13017.
- [41] M. Kumar, R. Li, J. D. Rimer, *Chem. Mater.* **2016**, *28*, 1714–1727.



# **Part 2**

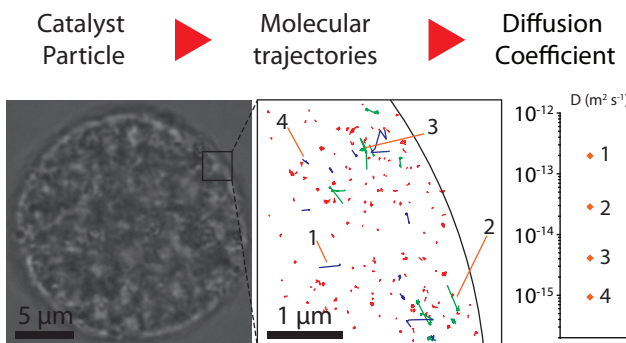
## **Industrial catalysts**



# Chapter 5

## Single-Molecule Fluorescence Microscopy Reveals Local Diffusion Coefficients in the Pore Network of an Individual Fluid Catalytic Cracking Catalyst Particle

Single-molecule fluorescence microscopy was used to study self-diffusion of a feedstock-like probe molecule with nanometer accuracy in the macropores of a micrometer-sized, real-life fluid catalytic cracking (FCC) particle. The observed tracks allowed three different states for the probe molecules to be distinguished. Most probe molecules (88%) were found to be immobile, with these molecules most likely being physisorbed or trapped; the remainder was either mobile (8%), with the molecule moving inside the macropores, or showed hybrid behavior (4%). Mobile tracks had an average diffusion coefficient of  $D = 8 \times 10^{-14} \pm 1 \times 10^{-13} \text{ m}^2 \text{s}^{-1}$ , with the large standard deviation thought to be related to the large range of pore sizes found in FCC particles. The developed methodology can be used to evaluate and map heterogeneities in diffusional properties within complex hierarchically porous materials.



Based on: "Single-Molecule Fluorescence Microscopy Reveals Local Diffusion Coefficients in the Pore Network of an Individual Catalyst Particle", Frank C. Hendriks<sup>1</sup>, Florian Meirer<sup>1</sup>, Alexey Kubarev, Zoran Ristanović, Maarten B. J. Roeffaers, Eelco T. C. Vogt, Pieter C. A. Bruijnincx and Bert M. Weckhuysen, *Journal of the American Chemical Society*, 2017, 139, 13632–13635.

<sup>1</sup> Both authors contributed equally to this manuscript.

## 5.1 Introduction

The accessibility of and mass transport in complex hierarchically porous materials, such as a fluid catalytic cracking (FCC) catalyst, greatly influences the overall catalytic activity and final product composition. Therefore, various bulk methods

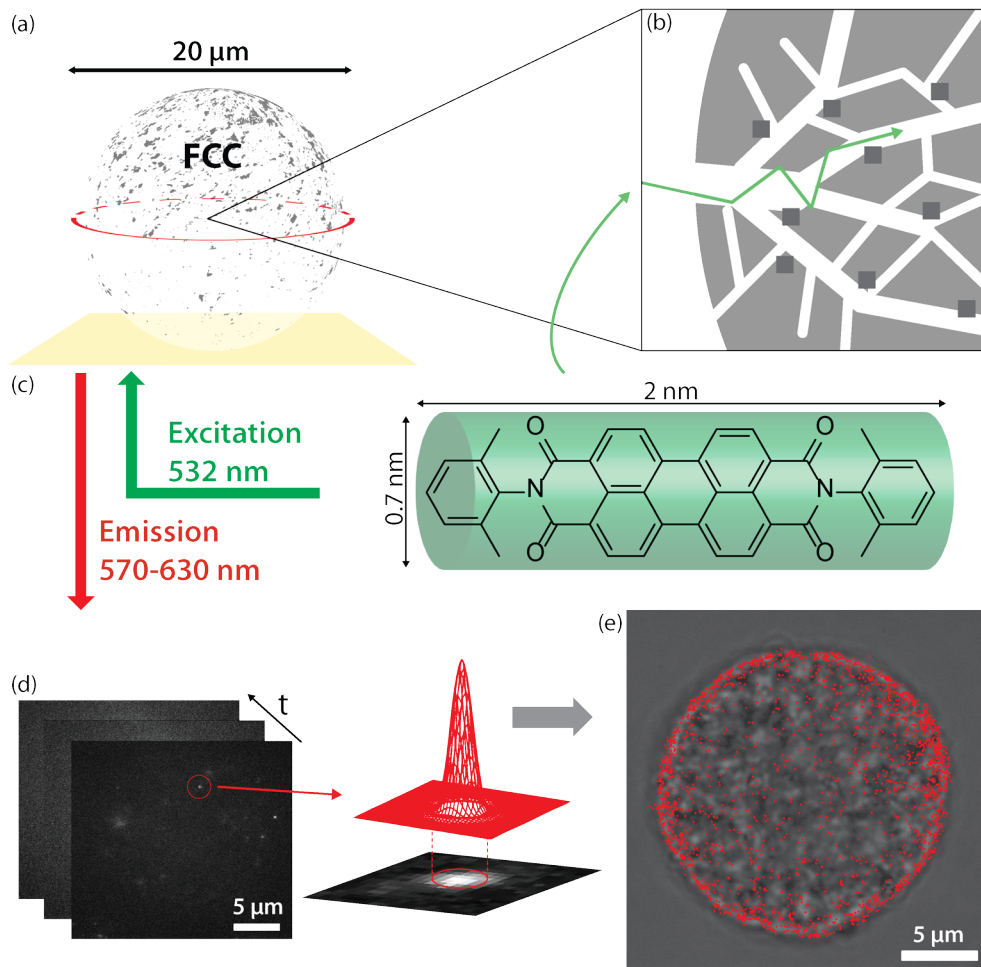


Figure 5.1. Wide-field Single-Molecule Fluorescence (SMF) microscopy was used to determine the location of the feedstock-like probe molecule (PDI) within the pore network of a single Fluid Catalytic Cracking (FCC) particle. (a) The whole FCC particle was submersed in toluene in a custom-made cell. (b) Schematic of the pore network of an FCC particle; light gray represents the matrix while dark gray squares represent the embedded zeolites. (c) The PDI probe molecule, which was added to the cell as a toluene solution. The PDI molecule was excited using 532 nm laser light and its emission was detected using a 600/60 nm band pass filter. (d) A time series of fluorescence images was recorded and processed by fitting the point spread function of each fluorescence event. This resulted in information about the location and movement of single molecules. (e) Map of all detected fluorescence events after trajectory analysis overlaid on the bright field transmission image.

have been developed to determine accessibility and mass transport characteristics, e.g. by water titration<sup>[1]</sup>, physisorption<sup>[2–4]</sup> or determination of the so-called accessibility index.<sup>[5,6]</sup> The latter method evaluates the adsorption of vacuum gas oil (VGO, i.e. the fraction of crude oil with a boiling point range of 340–540 °C)<sup>[7]</sup> dissolved in toluene into the FCC catalyst. These bulk analysis methods have in common that they provide a macroscopic description of the physicochemical diffusion properties, without giving any information about intra- or interparticle heterogeneity. However, recent studies have found that these heterogeneities can play a large role in the functioning of catalysts.<sup>[8]</sup>

In the past decades, novel fluorescence microscopy approaches have been developed to study porous materials, including solid catalysts.<sup>[9–12]</sup> While traditionally diffraction-limited,<sup>[13,14]</sup> several methods, based on the spatial and temporal separation of diffraction-limited fluorescent emitters, now offer spatial resolutions down to 10 nm,<sup>[15]</sup> with temporal resolutions for this type of experiments down to ms.<sup>[16]</sup> This has allowed molecular dynamics to be studied on a nanometer scale, which has led to visualization and analysis of diffusional behavior of molecules in different environments, revealing heterogeneities in diffusion within micro- and mesoporous materials.<sup>[17–20]</sup> Additionally, the high-resolution fluorescence microscopy methods made single-molecule mapping of catalytic reactions possible, which provided insight in diffusion of reactant molecules within catalyst particles.<sup>[21]</sup> These techniques have been applied successfully to model materials, such as thin films,<sup>[17,22]</sup> gels<sup>[23,24]</sup>, and model catalysts,<sup>[25–27]</sup> but the application to real-life catalyst materials has so far been very limited.<sup>[28]</sup>

Here, we present the first study reporting spatially resolved self-diffusion characteristics of feedstock-like molecules moving in the pore network of a single FCC particle mapped with nanometer precision. We employed single-molecule fluorescence (SMF) microscopy to monitor the movement of individual molecules within the catalyst particle, with a spatial resolution of 30 nm and a 20 ms temporal resolution (Figure 5.1). This SMF-based approach mimics the bulk experiments used to determine the accessibility index, but, importantly, can also reveal highly localized differences in diffusional behavior.<sup>[6]</sup>

## 5

## 5.2 Experimental

### 5.2.1 Materials and methods

**Materials.** Toluene (spectroscopic grade) was purchased from Baker. Polystyrene (PS300K,  $M_n = 290,000$ ,  $M_w = 490,000$ ) was purchased from Polymer Source, Inc. *N,N'*-bis-(2,6-dimethylphenyl)-perylene-3,4,9,10-tetracarboxylic diimide (PDI) was purchased from Aldrich. PDI is a highly fluorescent and highly photostable dye that has an absorption maximum at 525 nm.<sup>[29]</sup> The emission spectrum of the probe, excited using a 514 nm laser, is shown in Figure 5.2. The probe molecule was

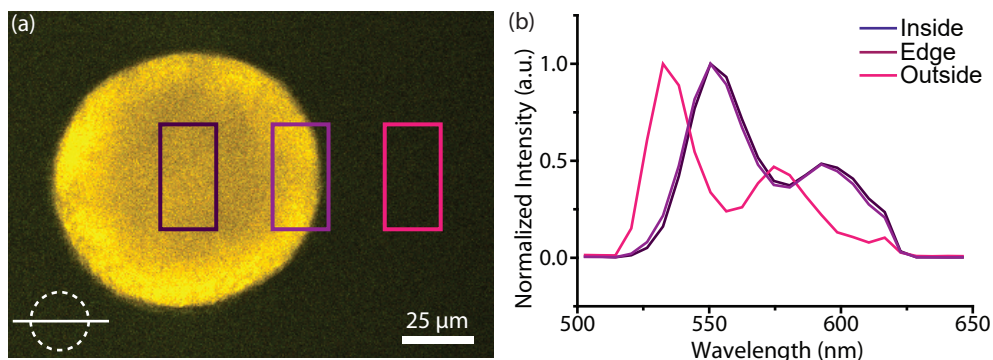


Figure 5.2. a) Confocal fluorescence microscopy image of the probe molecule PDI in an FCC particle, with a region of interest in the middle of the particle (purple), at the edge (violet) and outside of the particle, in the solution (pink). The image was recorded at the center plane of the particle (see scheme) utilizing a confocal fluorescence microscope equipped with a spectral detection unit and using 514 nm laser light for excitation. b) Spectra corresponding to the ROIs in a), with normalized intensity.

diluted to  $3.3 \times 10^{-10}$  M in toluene. For the experiment, 100  $\mu\text{L}$  of this solution were added to FCC particles suspended in 400  $\mu\text{L}$  of toluene, giving a final concentration of  $6.7 \times 10^{-11}$  M.

**Sample preparation.** The FCC catalyst particles, containing ZSM-5 as the active zeolite phase, were provided by Albemarle Catalyst Company B.V. The particles were first calcined at 823 K for 72 h (ramp = 10 K min<sup>-1</sup>) in a static oven to remove residual fluorescent impurities. The particles were suspended in MilliQ water and spin coated onto a glass plate. The glass plate containing the particles was then calcined for 773 K for 48 h (ramp = 1 K min<sup>-1</sup>) in a static oven. For the polystyrene samples, a 1 wt% solution of polystyrene in toluene was added to a probe molecule solution with a concentration of  $1.7 \times 10^{-9}$  M, after which this mixture was spin coated onto a glass plate and allowed to dry in air.

**Experimental setup.** Single molecule tracking experiments were performed using a custom-made setup. An inverted epi-fluorescence wide-field microscope (Olympus IX-71) with a 100 $\times$  oil immersion objective (NA=1.4) was used. A diode-pumped solid-state laser (Excelsior 532 single mode 200 mW, Spectra-Physics) provided 54 mW to the sample. Fluorescence microscopy images were recorded as movies using a Hamamatsu ImagEM X2 C9100-23B EM-CCD camera, after passing through a dichroic mirror, a 3.3 $\times$  camera lens and a 600/60 band pass filter. The resulting field of view was 24.6  $\times$  24.6  $\mu\text{m}^2$  and 48.5  $\times$  48.5 nm<sup>2</sup> per pixel (512  $\times$  512 pixels).

**In situ cell used in single molecule fluorescence experiments.** The *in situ* cell consists of a metal holder in which a glass plate with catalyst particles is placed. The glass plate is lined with a poly(methyl methacrylate) (PMMA) seal and a polytetrafluoroethylene (PTFE) liner making up the walls of the cell; the overall assembly is held in place by two screws (Figure 5.3).

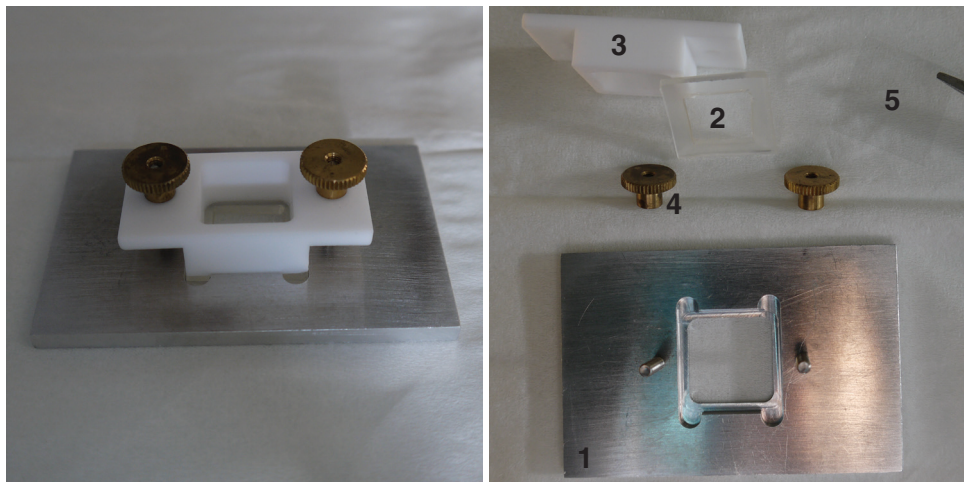


Figure 5.3. In situ cell used in experiments with (1) metal holder; (2) PMMA seal; (3) PTFE liner; (4) screws and (5) glass plate.

**Single molecule fluorescence experiment.** The experiment was performed at room temperature (294 K). A powerful laser is used to illuminate the sample, so some increase in temperature of the toluene suspension cannot be excluded. However, no significant evaporation of the solvent was observed, nor any visual signs of heating of the suspension. After addition of the probe molecule, the system was left to equilibrate for 5 min. In the course of 2 h, 7 movies were recorded with a total of 63,000 frames. There is a slow increase in the number of tracks over time; other than that, the movies show no significant observable differences.

The duration of one frame is set at 20 ms, but deviates from this value because the detector reads out the data from one frame before it can start the next. The frame length for each frame was calculated from the time stamp of the individual frames and is plotted in Figure 5.4. There is a narrow distribution of frame lengths; the observed difference is 0.2 ms. Some outliers are observed but these are likely caused by

5

a delay in writing the time stamp. There is no shift of frame duration over time. Therefore, the average frame duration over the whole movie was used in further calculations, which is 20.3 ms (49 frames/s).

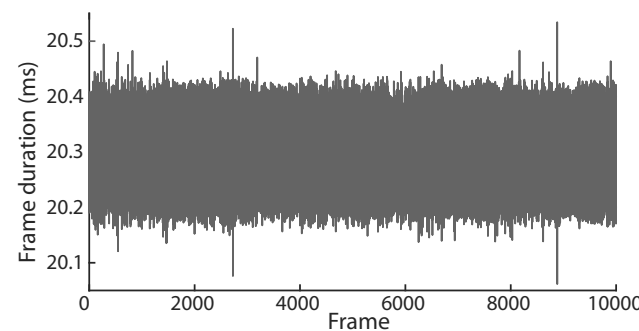


Figure 5.4. Fluctuations in the average frame duration in a movie of 10,000 frames.

**Analysis.** Detection of single molecule events and subsequent track analysis was carried out using the Localizer plug-in of Igor

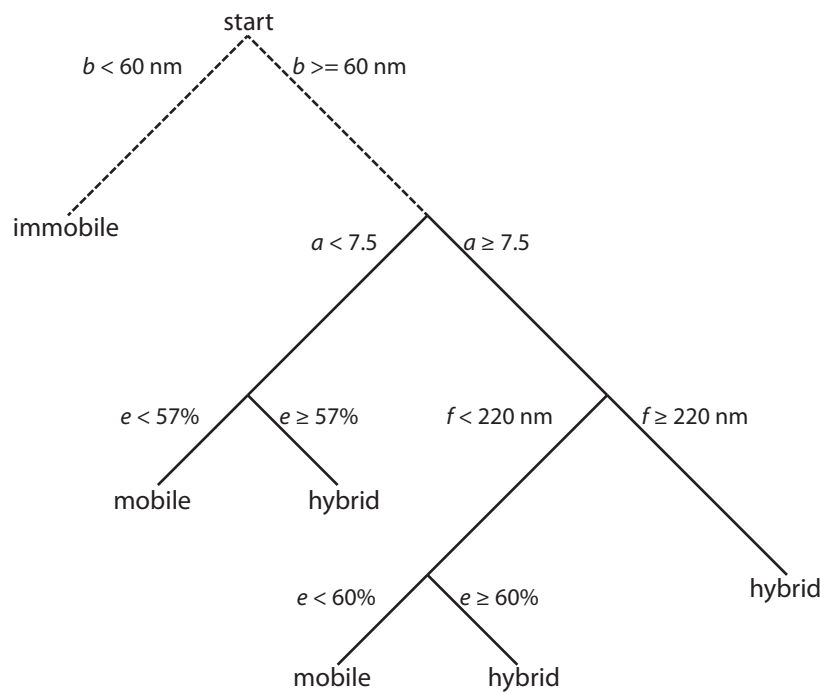


Figure 5.5. A decision tree was used to classify tracks using the machine learning approach. The part of the tree with dashed lines has been added manually (by setting a threshold for the diameter of the minimum enclosing circle based on the localization uncertainty), while the rest of the tree was created automatically by the machine learning algorithm. During classification of all tracks, for each track, the decision tree is followed from top to bottom, weighing one property at each branch, until the track is classified as either mobile, immobile, or hybrid.

Pro.<sup>[30]</sup> For track analysis, molecules were allowed to blink (i.e. the molecule is not fluorescing intermittently) for 1 consecutive frame.<sup>[31]</sup> Only tracks consisting of 4 steps or more were considered. Track classification, analysis and plotting were done using self-developed code in MATLAB. Some of the tracks were found to have a negative diffusion coefficient D; this (physically impossible) result stems from erroneous fitting of the mean square displacement curve and these values were therefore discarded. No tracks are observed outside of the particle, because molecules in solution move too fast to be registered under the experimental conditions applied and analysis parameters used.

**Drift correction.** Some intra- and inter-movie drift was detected. Inter-movie drift (i.e. a shift in the location of the particle between the end of one movie and the start of the next) was corrected for by aligning (rigid shift in x and y) individual movies in a global coordinate system. The shift was determined by comparing the center of the convex hull of the particle (the area including all detected events) in consecutive movies. Intra-movie drift (i.e., drift while the movie is being recorded)

was observed in some movies in the form of a slow, continuous drift. This was difficult to remove, especially because the moving probe molecules inside the catalyst provide no frame of reference for drift. It was estimated that the average error to track analysis introduced by intraparticle drift, in a movie with 10,000 frames, was below 1 nm (i.e. well below the localization uncertainty). Therefore, no correction was made for intraparticle drift.

**Track classification.** Machine learning (using the machine learning toolbox in MATLAB) was applied as a tool for automated track classification. A ‘training set’ of 100 tracks was classified manually. Based on the similarities in track properties in each subgroup, the algorithm is then able to group a large set of tracks following a decision tree built from the training set (Figure 5.5). Table 5.1 show the list of track properties used in the machine learning approach. To filter immobile tracks the decision tree was extended using a condition based on the diameter of the smallest enclosing circle (part of the tree with dashed lines). This condition requires a priori knowledge of the setup (the localization uncertainty) and can therefore not be automated. The total number of tracks is relatively small in this case (1991 tracks) and could have been sorted manually. However, the developed methodology can be applied to datasets of any size. Moreover, if the appropriate properties are chosen, a wide range of possible track types can be identified, not just the track types distinguished here.

Table 5.1. List of track properties used in the machine learning algorithm.

|   | parameter name                                | parameter description  |
|---|---|--|
| a | Number of steps                               | Number of consecutive single molecule emitters detected.   |
| b | Diameter of the smallest enclosing circle     | Diameter of the smallest circle that can be drawn around all the locations in a track.   |
| c | Center of the smallest enclosing circle       | Center of the smallest circle that can be drawn around all the locations in a track.   |
| d | Center of mass based on all points of a track | Location where the weighted relative position of the distributed points equals zero.   |
| e | Distance between c and d                      | The distance between the center of the smallest enclosing circle and the center of mass based on all points gives an indication of how points are distributed spatially. It is calculated as a percentage of the track’s diameter (b). |
| f | Length  | The sum of all the individual steps in a track.  |
| g | Tortuosity                                    | The ratio of the distance between start and end points versus the length of the track.   |
| h | Entropy                                       | A statistical measurement of randomness applied to the distribution of the points within the enclosing square that is defined by the smallest enclosing circle.  |
| i | Diffusion coefficient                         | The diffusion coefficient as calculated from the fit of the mean square displacement graph of the track.   |

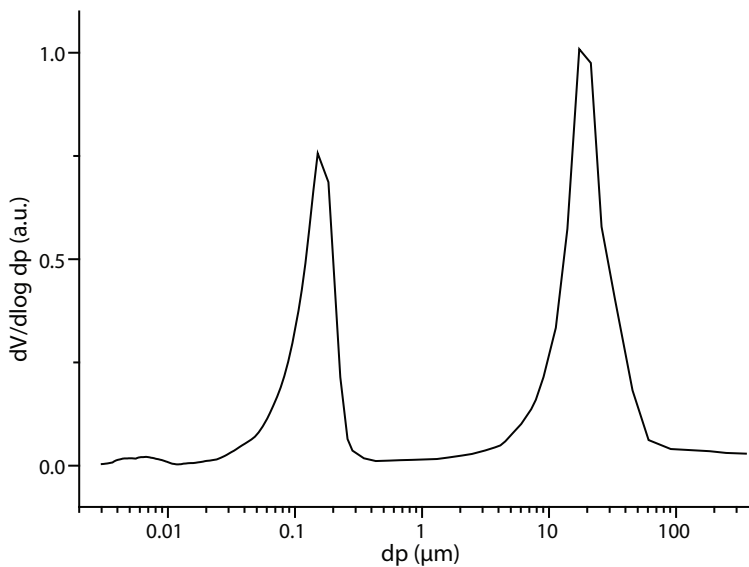


Figure 5.6. Bulk mercury porosimetry results of the FCC catalyst material under study. The peak at 10–50  $\mu\text{m}$  corresponds to the interparticle space.

Although the track types are clearly defined, the differences between tracks are sometimes minimal. For example, as will be shown later in Figure 5.15a, there is no clear distinction between steps that fall within the localization uncertainty and steps associated with actual molecular movement. Therefore, the machine learning algorithm does not perfectly separate tracks. However, from the results obtained in the subsequent analysis of the average properties of the subsets such as the diffusion coefficient D, the obtained classification can be concluded to be of sufficient quality for this study.

## 5.3 Results and discussion

### 5.3.1 Experiment and fluorescence event analysis

The industrially manufactured FCC catalyst sample under study contains zeolite ZSM-5 as the active phase.<sup>[28]</sup> Mercury porosimetry results show that most of the pores range 50–300 nm in size, i.e. are in the macropore regime, but some smaller mesopores are also present (Figure 5.6). The zeolites embedded in the FCC particle contain micropores, but with a pore size of maximum 5.6 Å, these are inaccessible to the probe molecule used (see Figure 5.1c). An intact single fresh FCC particle of about 20  $\mu\text{m}$  in diameter was selected to match the microscope's field of view (25  $\times$  25  $\mu\text{m}^2$ ).

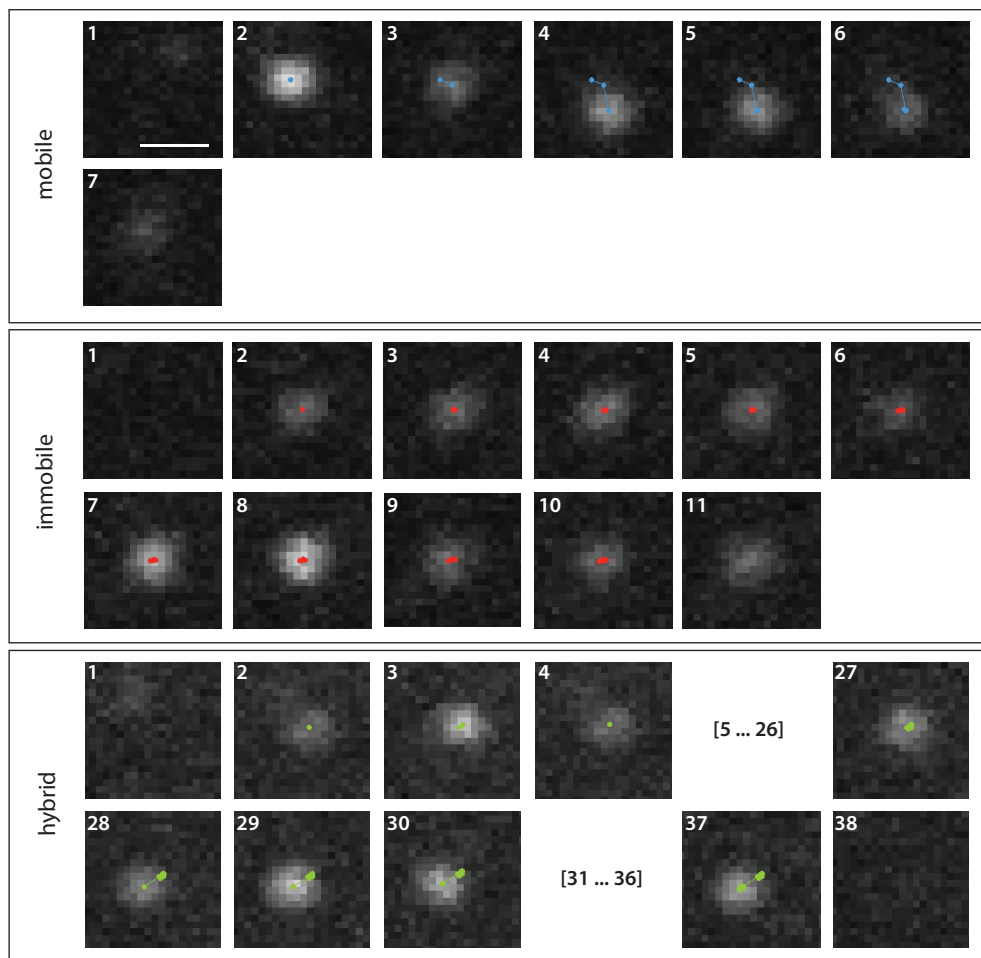


Figure 5.7. Close-up images of each type of track encountered within the recorded movies. Localized positions are denoted by dots, with lines showing the track evolution. The first and last frames in each series show the same area before and after events were detected. The scale bar represents  $0.5\text{ }\mu\text{m}$  and applies to all images. Intensities have arbitrary units and are the same across all images.

The pore network of this catalyst was studied using the *N,N'*-bis(2,6-dimethylphenyl)-perylene-3,4,9,10-tetracarboxylic diimide (PDI, Figure 5.1c) probe molecule. The poly-aromatic nature and dimensions (1–2 nm) of this probe are similar to components of VGO feedstock, although PDI contains more polar functional groups.<sup>[32–34]</sup> It has a high photostability and a fluorescence quantum yield close to unity.<sup>[29]</sup> FCC particles were submerged in this PDI solution in a custom-made cell (Figure 5.3) after which the system was equilibrated for 5 min. By employing an extremely low concentration ( $7 \times 10^{-11}\text{ M}$  in toluene), only a few molecules are present within the field of view at any given time. The movement of individual PDI

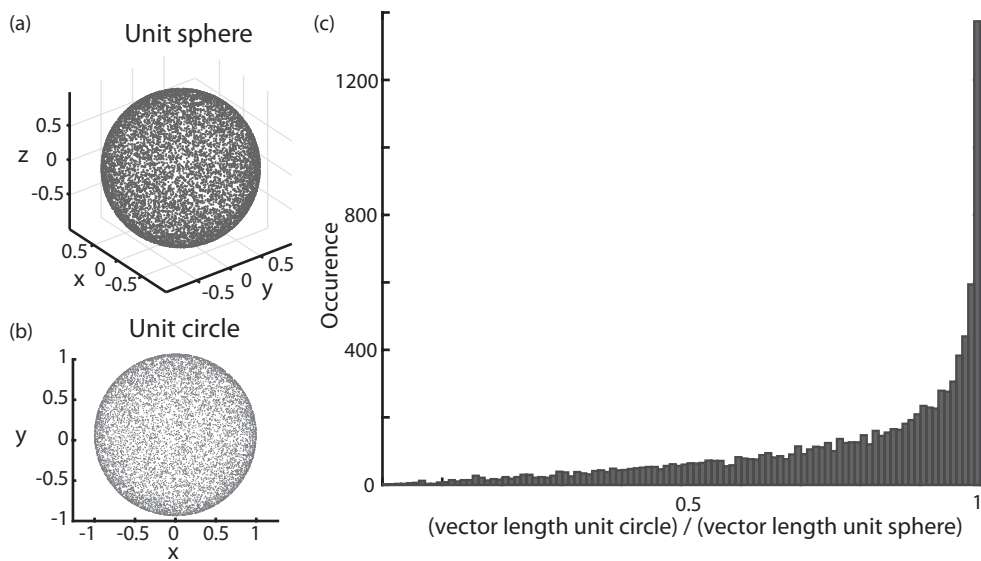


Figure 5.8. (a),(b) A graphical representation of random 3D movement with each point on the surface of the unit sphere signifying the end of a vector pointing from the center of the sphere to that point on the surface (a). The same unit sphere projected onto a 2D surface (b). c) A histogram of the resulting vector lengths measured from the 2D projection.

molecules was monitored with a wide field microscope, focused to the middle of an individual FCC particle to image a complete cross section. Wide field fluorescence microscopy images, showing single molecules as bright fluorescent events (Figure 5.7) were recorded as movies with a frame rate of 49 frames  $s^{-1}$  over a period of 2 h. This SMF method probes self-diffusion rather than diffusion as defined by Fick's law. Both processes are nonetheless governed by the same underlying principle (i.e., random movement of molecules) and ultimately give the same information on macroscopic properties.<sup>[35]</sup> Thus, "diffusion" will be used below to indicate both diffusion and self-diffusion.

The analysis does not consider the position of the emitter in the Z-direction. In the analysis, movement is therefore registered as a projection of a sphere onto a plane, leading to an underestimation of the actual movement.<sup>[9]</sup> To study the influence of this 2D projection, a simulation was carried out in which 10,000 unit vectors from the origin pointing in random directions in 3D were considered. Therefore, all resulting vectors end on the surface of a unit sphere (Figure 5.8a). The vectors were then projected onto 2D space, i.e. a unit circle (Figure 5.8b). A histogram of the resulting vector lengths is reported in Figure 5.8c showing the error introduced by projecting a 3D movement of unit length onto a 2D plane. Considering the average of many movements the error introduced by this projection is relatively small, with the average measured vector length in 2D being  $0.78 (\pm 0.22) \times$  the vector length in 3D.

Figure 5.7 shows zoom-ins of frames containing single molecule events, which

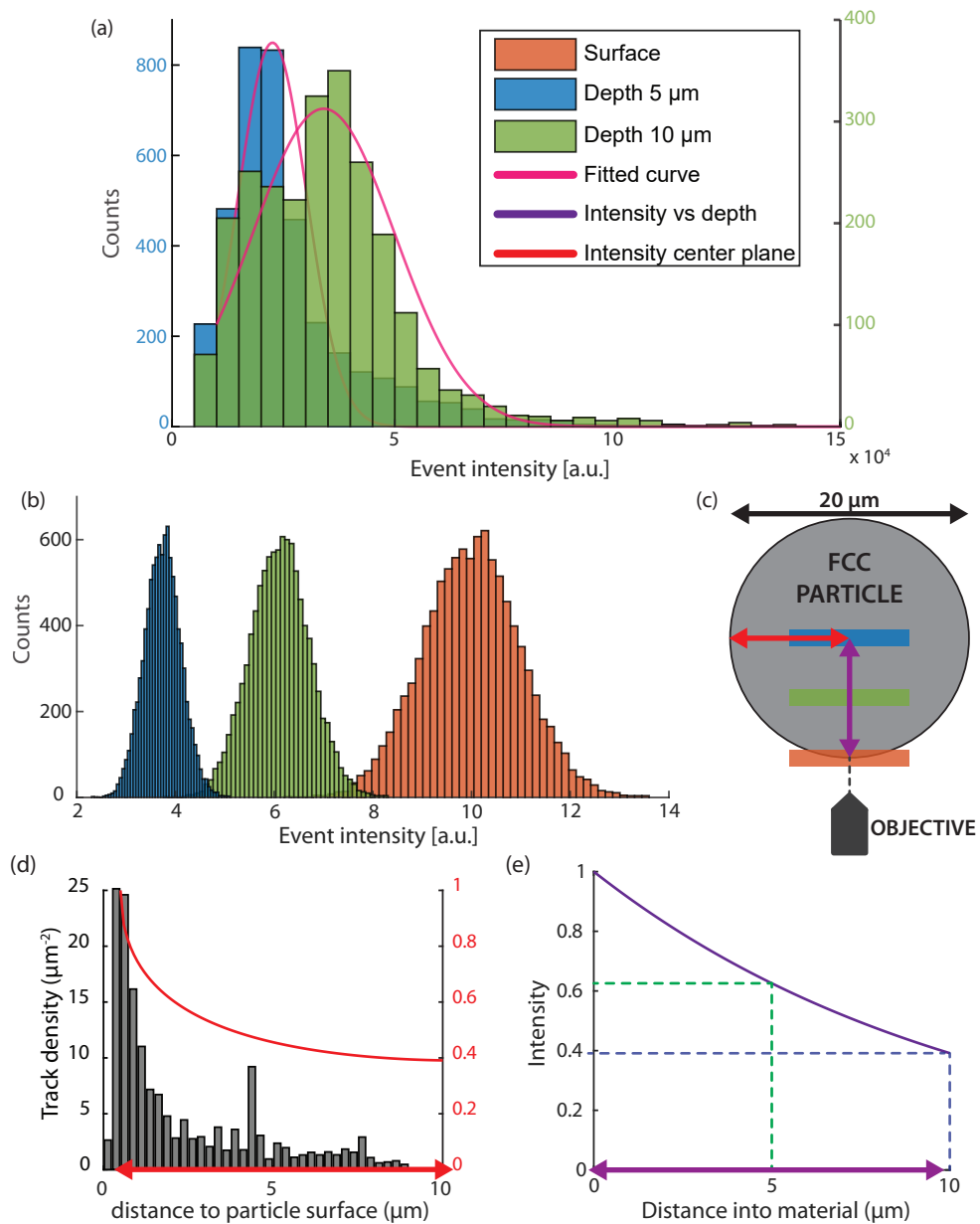


Figure 5.9. An overview of the calculations performed to determine the attenuation of fluorescence intensity by the FCC particle. (a) Histogram of measured intensities of events at 2 different depths (green = 5  $\mu\text{m}$  blue = 10  $\mu\text{m}$  in c), including a Gaussian fit to both histograms. (b) Simulated normal distributions of event intensity at the surface (orange) and at depths of 5 (green) and 10  $\mu\text{m}$  (blue). (c) Scheme showing the locations at which events were recorded within the FCC particle. (d) Track density as a function of distance from the surface of the FCC particle; in red the calculated exponential decay of fluorescence intensity. (e) Intensity as a function of depth into the FCC catalyst material.

are clearly visible as white dots. The location of these single-molecule fluorescent events was extracted from the fluorescence microscopy images using the Localizer<sup>[30]</sup> software. The position of the single molecule causing the fluorescence is determined by fitting a 2D Gaussian to the diffraction-limited spot. In this way, a resolution of 30 nm was achieved (Figure 5.1d).

Because the middle section of a whole, spherical FCC particle is measured, the emitted fluorescence intensity depends on the location at which it is recorded. Due to the spherical shape of the particle, a fluorescence signal must travel through a varying amount of material to reach the detector; the same is true for the incident light (see Figure 5.9c). The material can scatter or absorb the light, leading to lower observed fluorescence intensity. Events toward the middle of the cross section therefore have a lower signal-to-noise ratio, which can cause events to go undetected by the localization algorithm. Because of this, fewer events (and tracks) are observed in the middle of the cross section, as can be seen in Figure 5.1e.

To quantify this fluorescence attenuation effect on the detected event density, the event intensity at different depths within the particle was studied. From these depths, only events within 5  $\mu\text{m}$  from the center were selected to account for the curved surface of the particle and obtain almost constant optical path lengths. The intensity distribution of events at two different depths (5 and 10  $\mu\text{m}$ ) was measured and fitted using a Gaussian function (quality of fit parameter  $R^2 = 0.9647$ ). From the shift and reduced  $\sigma$  observed between the intensity distributions recorded at these two depths, the characteristic fluorescence intensity attenuation coefficient  $\mu$  at the recorded wavelengths ( $\sim 500\text{-}600 \text{ nm}$ ) and for the material (FCC catalyst particle) was calculated using Beer-Lambert's law<sup>[36]</sup>  $I = I_0 \cdot e^{-\mu \cdot x}$ , with  $x$  being the path length through the material, the un-attenuated intensity  $I_0$  and the detected, attenuated intensity  $I$ . To verify this approach of determining  $\mu$ , we simulated the effect of fluorescence intensity attenuation at different depths in a material causing

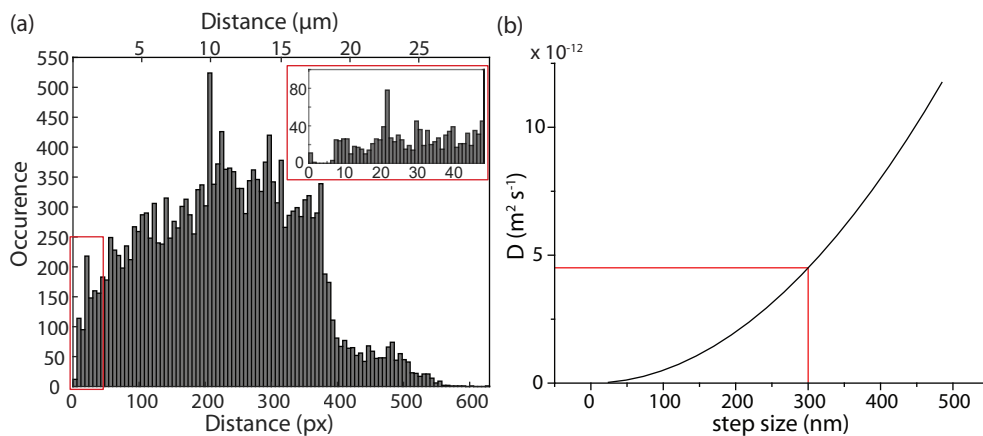


Figure 5.10. (a) Nearest neighbor analysis of events in each frame. (b) The observed diffusion coefficient if a molecule would move with a consistent step size. The red line indicates the allowed maximum chosen in the analysis.

a shift and reduced  $\sigma$  of a normal distribution of fluorescence intensities: a simulated intensity distribution as it would be detected at the surface of the particle (i.e. without any intensity attenuation) can be seen in Figure 5.9b (orange histogram). The green and blue intensity distributions were then calculated being this exact same distribution but with the intensity of each fluorescence event attenuated following Beer-Lambert's law, i.e. as a function of depth  $x$  into the material and an arbitrarily chosen attenuation coefficient  $\mu$ . From the known depths  $x$  and the shift and reduced  $\sigma$  obtained from a fit to the intensity distributions the actual attenuation coefficient  $\mu$  (which is a material constant) can then be recovered and was found to exactly reproduce the arbitrarily chosen value.

Following this approach and using the experimental data, the actual attenuation coefficient  $\mu$  for the FCC catalyst was found to be  $0.094 \text{ } \mu\text{m}^{-1}$ . The data was also fitted using a lognormal function instead of a Gaussian, as this seemed to fit the tail of the distribution better.<sup>[37]</sup> Not surprisingly this gave a very similar result, i.e. an attenuation coefficient  $\mu$  of  $0.085 \text{ } \mu\text{m}^{-1}$  ( $R^2 = 0.9191$ ), because  $\mu$  is determined from the shift between the distribution functions and therefore not directly related to the shape (i.e. nature) of the distribution function. The difference in  $\mu$  obtained from using a Gaussian and lognormal function is only caused by a slightly different shift obtained when using different distribution functions. With this  $\mu$ , the expected decrease in detected light originating from fluorescent events in the middle section of the FCC particle (i.e. the section that was used for the track analysis) was calculated.

The results of this approach are summarized in Figure 5.9d. The red line indicates the expected decrease of events at the center plane of the catalyst particle (i.e., the part studied in our main experiment), estimated from the calculated exponential decay of fluorescence intensity based on the absorption coefficient determined

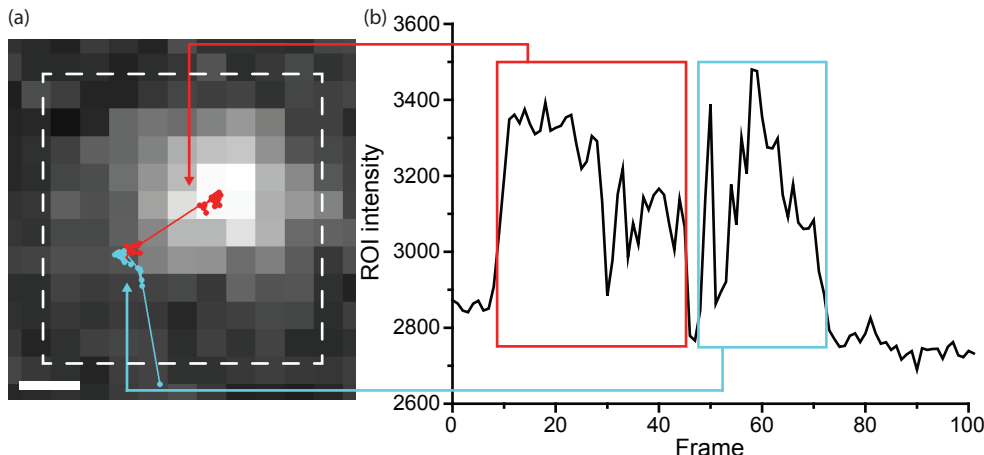


Figure 5.11. Intensity trace of two tracks in the same area. (a) Single molecule event from one of the tracks. The scale bar represents 100 nm. (b) Intensity trace integrated over the complete ROI (indicated by white dashed-line square).

for the material and considering the spherical shape of the particle (i.e. using the non-linear thickness increase of the material with distance from the surface). The histogram shows the actual number of tracks found. Attenuation of fluorescence expectedly accounts for a decrease in tracks towards the middle of the particle. However, this is clearly not the only influence: the edge of the particle shows a much higher density compared to the center than what is expected based on fluorescence attenuation. Additionally, this effect can be explained by the structure of the catalyst particles; FCC particles are known to have a more dense crust to protect them against attrition.<sup>[38,39]</sup> Therefore, molecules may get stuck in the dense crust surrounding the particle, explaining the higher than expected track density there.

### 5.3.2 Track analysis

Before events were linked to each other by a frame-by-frame analysis, the chance of false positives was determined (i.e., the chance of having two molecules in close

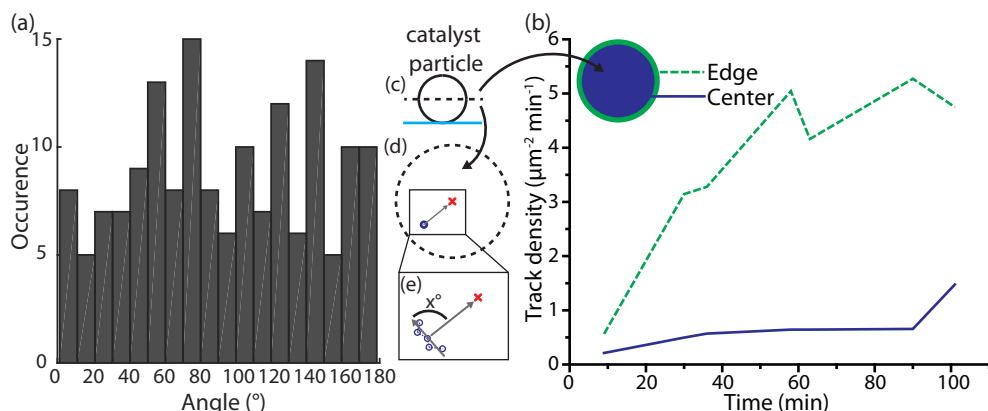
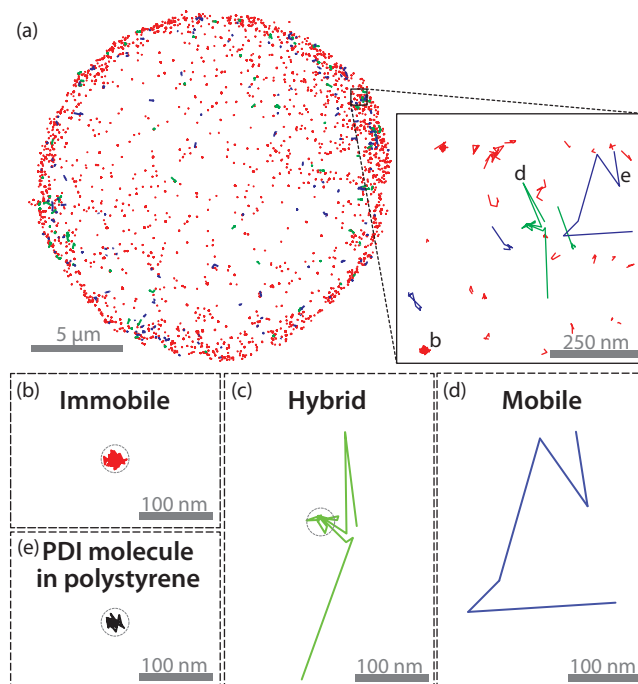


Figure 5.12. (a) Histogram of the angle between the first track Eigenvector and the vector pointing to the particle center calculated for each mobile track (see also (c),(d),(e)). The absence of a preferential angle shows that there was no directed movement of tracks towards the center of the particle, providing evidence that molecule diffusion was not influenced by a concentration gradient. (b) The track density as a function of time. Tracks within  $1/8 \times r$  from the surface were considered to be tracks at the edge of the particle; the rest was considered to be in the center. The discrete times shown are deducted from the time stamp of the individual movies; to obtain track density the number of tracks was divided by the area of the edge/center and divided by the duration of the movie. (c) The FCC catalyst particle used in the experiment; the blue line indicates the glass bottom plate of the in situ cell. The dashed line indicates the center plane at which the main experiment was measured. (d) Schematic of the center plane showing the center of the particle (marked with an  $x$ ) and one track (marked with a circle). (e) a zoom-in of the area, showing the first Eigenvector of the track (which indicates its principal direction) and the vector from the center of mass of the track to the center of the particle, both marked with gray arrows. The angle between these two is shown in the histogram in (a).

proximity that do not belong to the same track). To this end, a nearest neighbor analysis was carried out on all events within each frame (Figure 5.10a). In a single frame, the events are independent (stochastic) and can be used to calculate the probability of two single molecule events in close proximity (events in consecutive frames are themselves not independent as they could be originating from the same molecule). The histogram shows there is a sharp increase in events that are more than 6 pixels (300 nm) apart from each other, which is the reason this step size was chosen as the maximum allowed in track analysis. Figure 5.10b shows that a molecule moving consistently with this maximum step size of 6 pixels would have a diffusion coefficient of  $\sim 5 \times 10^{-12} \text{ m}^2 \text{ s}^{-1}$ ; this then provides an upper limit of the diffusion coefficient that can be observed in this experiment.

A frame-by-frame analysis of the locations of single molecule events, taking into account the maximum step size, yielded trajectories of single PDI molecules. Track analysis showed that some molecules do not emit fluorescence in one of the frames of a trajectory. This phenomenon is called “blinking” and was corrected for in the track analysis in the sense that blinking with a duration of 1 frame was allowed; allowing blinking for more than 1 frame did not alter the results significantly. An example of such behavior is shown in Figure 5.11a. Two single molecule tracks detected in a region are shown in blue and red. The integrated intensity of the region of interest



5

Figure 5.13. (a) Color-coded map of each recorded PDI track within the FCC particle, showing (b) immobile (red), (c) hybrid (green) and d) mobile tracks (blue) and. (e) PDI track immobilized in a polystyrene thin film.

(white dashed-line square) is shown in Figure 5.11b, where the higher intensity caused by the single molecule event can be distinguished for both tracks. Between the higher intensity of the two tracks, two frames with low intensity are observed. Consequently, the algorithm identified two separate tracks. These two tracks may well be from the same PDI probe molecule, which has for example moved out of focus for two frames. However, it can also not be excluded that these tracks are from two different molecules.

Although the system was allowed to equilibrate before the measurement, a slow increase in the number of tracks was observed at the edge of the particle over time. This could imply that a concentration gradient was present within the particle and equilibrium had in fact not been reached. To check for the presence of any directed diffusion that would influence the direction of the tracks, the angle of the first Eigenvector of each track (indicating the principal direction of a track) with respect to the center of the particle was plotted. However, no preferential direction of tracks inside the particle was found (Figure 5.12a), indicating the absence of or only a very weak concentration gradient. Furthermore, an analysis of the location of tracks over time showed that the increase of tracks was mainly located at the edge (surface) of the particle. In the center, the density of tracks was almost constant (Figure 5.12b). This implies molecules had penetrated to the middle of the catalyst particle before the experiment started. We therefore speculate that the increasing number of tracks at the edge of the particle may be partly caused by the dense crust around the FCC catalyst particle (*vide supra*).

Figure 5.13 shows the distribution of the PDI tracks within the central cross section through the FCC particle; a total of 1991 tracks were found. Notably, tracks were found throughout the cross section, showing that PDI probe molecules have access to the particle's complete pore network. Different modes of movement were observed, which is evident from the van Hove graph shown in Figure 5.14. In the distribution of displacements after time lag  $\tau$ , a clear deviation from a normal distribution (red line) is observed.<sup>[40,41]</sup> The exponential tail indicates a subset of molecules showing different diffusion characteristics than the rest of the molecules. This has been observed before in heterogeneous systems, such as quantum dots in polyacrylamide gels.<sup>[23]</sup> These two distinct modes of movement led to the

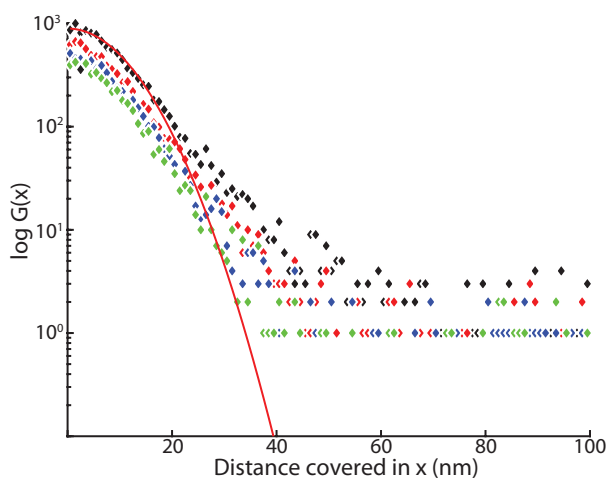


Figure 5.14. Van Hove correlation graph showing the probability of tracks having travelled certain distances after a time lag of 5 (black), 10 (red), 15 (blue) and 20 frames (green). The red line indicates a normal distribution.

identification of 3 different types of tracks (Figure 5.13). These tracks were classified based on a set of track properties using a machine learning approach, allowing tracks to be separated in an automated way. An overview of the step sizes, the number of points and the diameter of the smallest enclosing circle are shown in Figure 5.15 for each track type and are discussed hereafter.

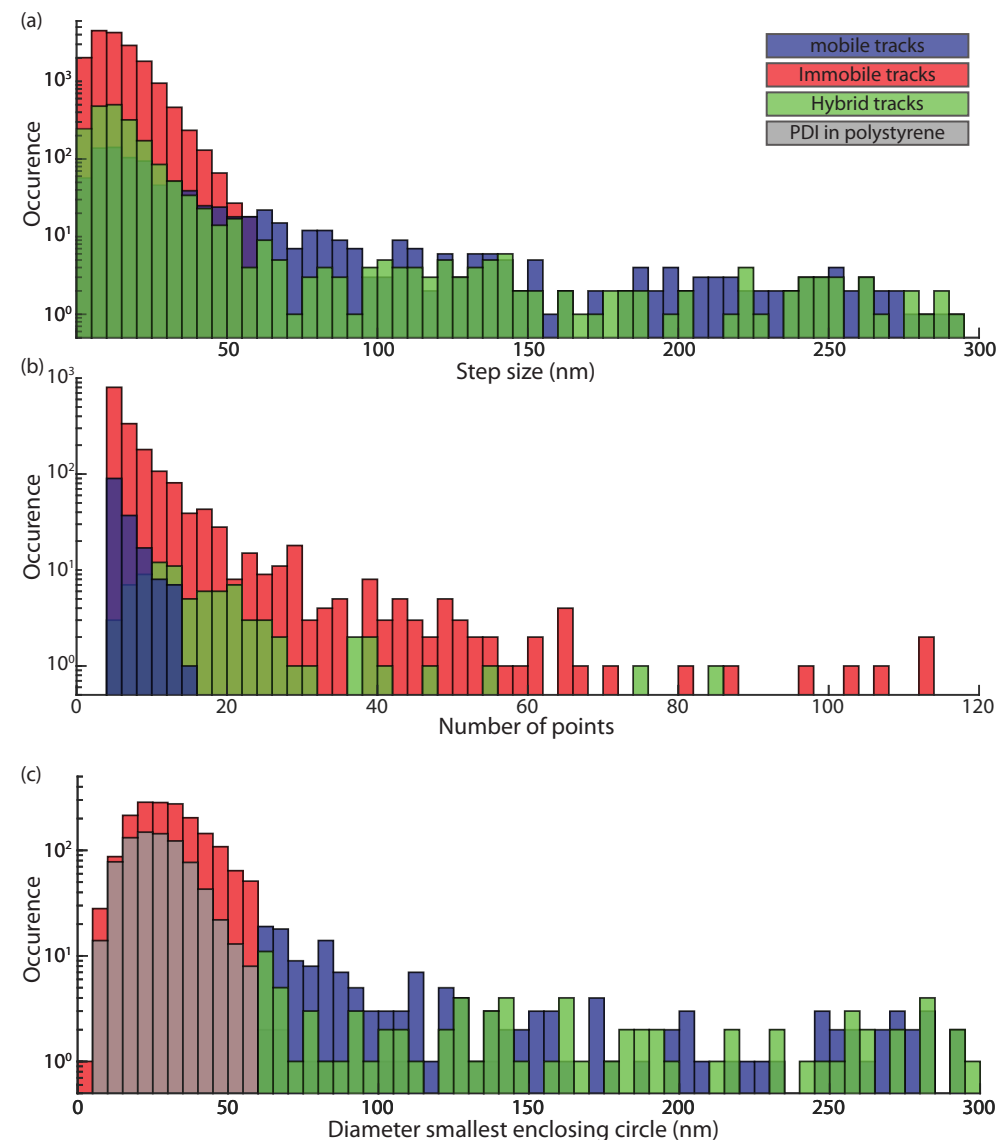


Figure 5.15. Histograms of step sizes (a), the number of points (b) and the diameter of the smallest circle enclosing all points of a track (c). The colors of each type of track are given in the legend; overlapping bars produce different colors (e.g. blue and red combine to purple in (a) and (b)).

The majority of the tracks showed little movement (Figure 5.13b). These tracks were compared to PDI entrapped in a polystyrene film, which are assumed to be non-moving, and measured in the same experimental setup (Figure 5.13e). From the similar shape and corresponding size of their minimum enclosing circle (i.e. the smallest circle encompassing all events of a track, see also Figure 5.15), it can be concluded that the majority of the PDI molecules in the FCC particle is indeed immobile. For these molecules, the apparent observed movement is due to the uncertainty in localization of each point in the track; from the diameter of the enclosing circle, this localization uncertainty (and resolution) was estimated to ~30 nm. This relatively high localization uncertainty reflects the challenging imaging conditions. Because the center plane of a complete catalyst particle is imaged, more light is scattered than with e.g. a thin film sample resulting in a lower signal to noise ratio. This leads to a higher localization uncertainty and hence, a lower effective resolution.

The immobile molecules can either be physically or chemically adsorbed onto the pore wall or be trapped in a small pore. To investigate this, the fluorescence emission spectrum of the probe molecules inside the FCC catalyst particle was measured using confocal fluorescence microscopy. The whole spectrum was red-shifted 18 nm compared to the emission spectrum of molecules in toluene solution, but no change in the relative intensity of the bands was detected (Figure 5.2). Chemisorption (i.e., by protonation) can therefore be excluded as the main reason for immobility.<sup>[42]</sup> Physisorption of the probe molecules onto the pore wall is most likely the main reason for a single molecule's immobility for a certain time period during its movement, explaining the presence of hybrid tracks, for example in the zoomed-in area in Figure 5.13a and in Figure 5.13c. However, some molecules are completely immobile, suggesting that PDI can also be trapped in a small pore or cavity. The tracks belonging to immobile PDI were separated from the other tracks by applying a threshold to the size of the smallest enclosing circle (Figure 5.12). Using a threshold set at a diameter of twice the localization uncertainty (60 nm), it was found that 1743 tracks (88%) were found to belong to the immobile category.

The remaining tracks do show observable movement. Within the subset of moving tracks, a distinction can be made between continuously moving molecules (mobile, Figure 5.13d) and ones that switch between immobile and mobile states within one track (hybrid, Figure 5.13c). Figure 5.13a shows the distribution of each of these track types to be fairly homogeneous. The distance these molecules travel between frames varies from steps as small as the localization uncertainty to the limit imposed by the track analysis (300 nm), with no clear preference for certain distances. While pore size analysis showed that most pores are in the 50–300 nm range (i.e. in the regime of macropores, see Figure 5.6), and because the micropores of the embedded zeolites are inaccessible for PDI molecules due to their size, the observed movement thus originates mainly from molecules present in these macropores. Movement in smaller pores falls within the localization uncertainty of the technique and can therefore not be distinguished from immobility. As mentioned above mobile and hybrid tracks were separated in an automated way using a machine learning algorithm (Figure 5.5) utilizing distinct properties from each type of track and a

training set of 100 manually classified tracks. 160 tracks (8%) were thus classified as mobile, while 88 (4%) belonged to the hybrid type.

The most distinct properties of each track type are shown in Figure 5.15. The histogram of step sizes (Figure 5.15a) shows that while immobile tracks obviously have the smallest steps, hybrid and mobile tracks each also have a significant number of small steps, indicating that most molecules spend at least a short time in the immobile state (or move along the z-axis, see Figure 5.8). Figure 5.15b shows that the number of points for mobile tracks on average is low, which is likely caused by out-of-focus movement of these molecules. The diameter of the smallest enclosing circle of the tracks from the experiment with PDI molecules immobilized in polystyrene is also shown in Figure 5.15c. Strong overlap with the histogram of the immobile tracks provides evidence that the immobile tracks really are immobile.

With an average of 10 steps or 200 ms per track, most of the observed tracks were rather short. This is in sharp contrast to many single particle tracking studies, where it is not uncommon that tracks can be followed for seconds.<sup>[22]</sup> In this case tracks that are longer than one second are present, but these are exclusively caused by molecules in the immobile state. More generally, mobile tracks have on average a shorter duration than hybrid and immobile tracks, which makes it likely that the shortness of the tracks is caused by movement out of the focal plane, terminating the track. The focal plane depth is approximately 500 nm based on the experimental conditions and the used single-molecule tracking parameters, but it may be smaller due to the challenging imaging conditions caused by the scattering catalyst particle

(*vide supra*). The lower signal to noise ratio causes the localization algorithm to reject some slightly out-of-focus events, leading to a reduced effective focal depth compared to the nominal focal plane. As very long ( $> 1$  s) tracks are detected for some immobile molecules, photo-bleaching (irreversible damage to the molecule's conjugated system, making it non-fluorescent) of the PDI probe molecule is unlikely to contribute much to the number of short tracks; in fact, this probe molecule is known to be highly photostable.<sup>[42]</sup>

5

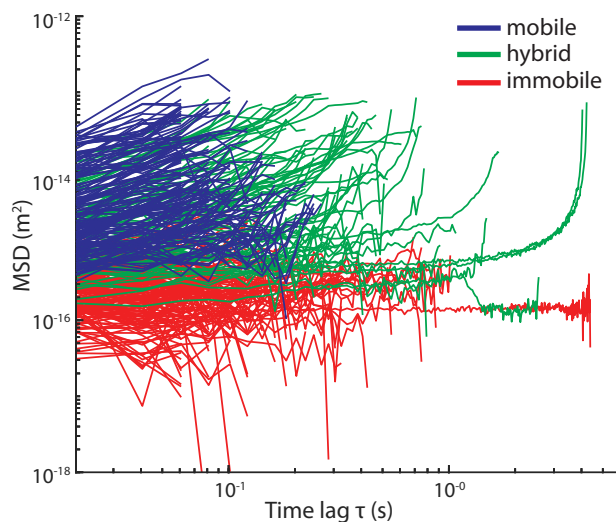


Figure 5.16. The individual mean square displacement (MSD) of each detected track as a function of time lag  $\tau$ , with immobile tracks in red, mobile tracks in blue and hybrid tracks in green. Only 10% of the immobile tracks are shown for clarity.

To quantify the (projected)

2D movement of the PDI probe molecules, the mean square displacement (MSD) as a function of time lag  $\tau$  was calculated for each track (Figure 5.16). In this calculation, each intermediate position of a track is considered a valid starting point for calculating the MSD, rather than looking at each track from start to finish.<sup>[24]</sup> Because of this, higher time lags have an inherently larger error margin, which is evident from the shape of some of the MSD graphs in Figure 5.16. The three track types show clear differences in their MSDs. Clearly the immobile tracks indicate which MSDs can be considered to be within the localization uncertainty. Notably, the mobile and hybrid tracks show a broad distribution in MSD offset values. Mobile tracks are furthermore shorter (with an average number of 8 steps per track) than the other two types, as long tracks are associated with long periods of immobility. With displacement being directly related to a molecule's confinement, this broad MSD distribution can therefore be considered a consequence of the large range of

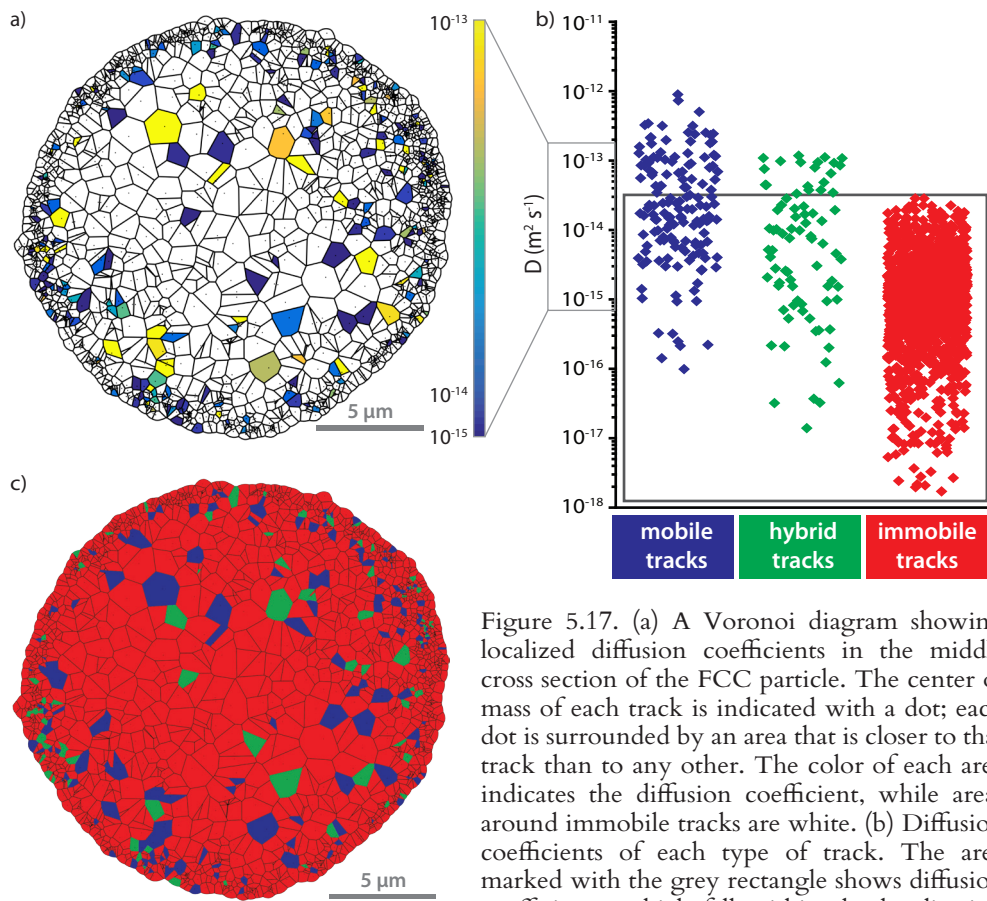


Figure 5.17. (a) A Voronoi diagram showing localized diffusion coefficients in the middle cross section of the FCC particle. The center of mass of each track is indicated with a dot; each dot is surrounded by an area that is closer to that track than to any other. The color of each area indicates the diffusion coefficient, while areas around immobile tracks are white. (b) Diffusion coefficients of each type of track. The area marked with the grey rectangle shows diffusion coefficients, which fall within the localization uncertainty of the single-molecule analysis. (c) A Voronoi diagram, as plotted in (a), showing track type domains in the middle cross section of the FCC particle. The color of each area indicates the type of track found in that area.

pore sizes present within the FCC catalyst particle (Figure 5.6).<sup>[19]</sup>

The diffusion coefficient D can now be obtained by linear fitting of the MSD curve.<sup>[17,24,43]</sup> This bottom-up approach to determine D for a single molecular trajectory provides valuable information about diffusion properties. D gives an indication of mass transfer within the catalyst and is therefore an indication of catalyst performance.<sup>[35,44]</sup> Because we can calculate this for each track, localized information on the diffusion coefficient can be obtained, which is plotted in Figure 5.17a. Local heterogeneity in D is observed, but this heterogeneity is homogeneous over the particle's cross section. These large differences in D are also found between tracks of the same type, as evidenced in Figure 5.17b. It should be noted that for all immobile tracks, the derived values for D are within the localization uncertainty (marked with a grey rectangle in Figure 5.17b). Interestingly, D values for several hybrid tracks also fall within this category, meaning that for those tracks their immobile part dominates their (time-averaged) diffusion coefficient.

To test for a correlation between diffusion coefficient D and the depth into the particle at which a molecule is present, the average diffusion coefficient was plotted for three depths within the particle cross-section (Figure 5.18b). Zone A is  $> 6 \mu\text{m}$ , B is from 3 to  $6 \mu\text{m}$ , while C is  $< 3 \mu\text{m}$  from the surface into the center plane of the particle. The diffusion coefficients of mobile and hybrid tracks were used, as the immobile tracks have diffusion coefficients that cannot be distinguished from the localization uncertainty. Based on a statistical t-test (see Chapter 2 for details), no significant differences were found between the diffusion coefficients in the three

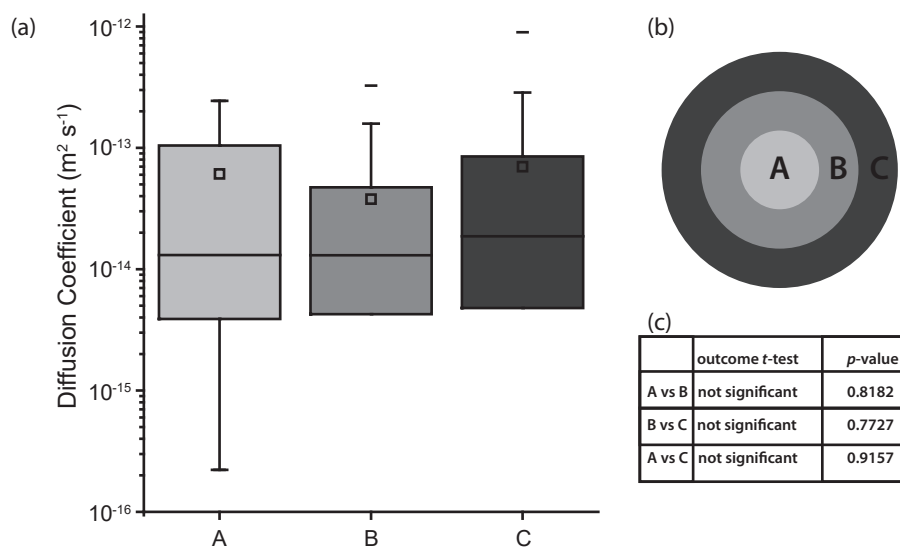


Figure 5.18. a) Box plots of the average diffusion coefficient within three different depths into the particle. The mean value is marked by ‘□’; the maximum value is marked by ‘-’. b) Legend indicating the zones at different depths within the FCC particle cross section. c) Statistical t-tests carried out on the subsets. See Chapter 2 for details on the statistical test.

zones (Figure 5.18c). Therefore, there is no evidence that the diffusion coefficient of a molecule depends on its location in the cross section of the catalyst particle.

A map of the track type distribution is shown in Figure 5.17c. It is clear from this graph and from the large number of immobile tracks (88%) that most PDI probe molecules spent a large amount of time trapped or adsorbed to the pore wall. These relatively strong interactions with the pore walls of the catalyst particle might be the result of the polarity of PDI and its functional groups. While experimental data on the bulk diffusion properties of PDI in FCC are not available, our results thus would predict that low diffusion coefficients would be observed if determined by bulk measurements as those mentioned above. However, considering that PDI is used here to model the diffusion of VGO molecules in a FCC particle, it should be noted that the VGO components are less polar and thus expected to interact less strongly with the pore walls. Apart from the increased physisorption, the similar dimensions of PDI and VGO molecules suggest similar diffusion behavior. Indeed, comparing the bulk diffusion coefficient ( $5 \times 10^{-13} \text{ m}^2 \text{ s}^{-1}$ )<sup>[32]</sup> measured by adsorption for VGO molecules into FCC to our results, we observe this value to be very similar to the average diffusion coefficient of the fraction of mobile molecules ( $8 \times 10^{-14} \pm 1 \times 10^{-13} \text{ m}^2 \text{ s}^{-1}$ ). This result suggests that diffusion of VGO molecules into the catalyst particle is most similar to the mobile tracks seen for PDI.

How efficiently a catalyst particle is used can be estimated based on the relative influence of the intraparticle diffusion and the reaction rate by means of the Thiele modulus  $\phi_2$ , and the related effectiveness factor  $\eta$ .<sup>[45,46]</sup> The Thiele modulus  $\phi_2$  and effectiveness  $\eta$  for a second order reaction can be calculated by the following formula:<sup>[44,47]</sup>

$$\phi_2 = r \cdot \frac{1}{3} \sqrt{\frac{k \cdot C_s}{D}} \quad 5.1$$

$$\eta = \frac{\tanh \phi_2}{\phi_2} \quad 5.2$$

The conversion process for FCC itself was approximated by the cracking of cetane ( $C_{10}$ ) to octane ( $C_8$ ); therefore, one cracking event per feed molecule is assumed as well as 100% conversion.<sup>[48]</sup> For the FCC process,  $40 \times 10^3 \text{ kg}$  catalyst circulates through the reactor per minute.<sup>[49]</sup> Each minute,  $7 \times 10^3 \text{ kg}$  of feedstock is converted. The residence time is 1 second. This leads to a rate  $k$  of  $1.93 \times 10^{-2} \text{ mol L}^{-1} \text{ s}^{-1}$ . The diameter of an FCC catalyst particle was approximated to be  $75 \mu\text{m}$ . For the concentration of feedstock at the catalyst's surface  $C_s$ , a monolayer coverage of reactants (cetane) was used on the outside of the spherical catalyst particle ( $2.57 \times 10^{-4} \text{ mol L}^{-1}$ ). The diffusion coefficient  $D$  for mobile tracks ( $7.73 \times 10^{-14} \text{ m}^2 \text{ s}^{-1}$ ) was used, but a conversion factor ( $5.25 \times 10^3$ ) was used to correct for the difference in temperature between the experiment (294 K) and the real process (800 K).<sup>[48]</sup> The conversion factor used was based on the work by Vasenkov and Kärger.<sup>[50]</sup> Using the experimentally determined, single molecule-based diffusion coefficient of the mobile fraction of molecules and information available on the FCC process, a Thiele modulus  $\phi_2$  of 5.4 was calculated.<sup>[48]</sup> This is in line with what was previously found

for this reaction, which validates our bottom-up approach.<sup>[47,51]</sup> The calculated effectivity was found to be 19%, showing the effect of diffusion limitations on the utilization of the catalyst particle; under reaction conditions, approximately 19% of the catalyst would be available to molecules with a diameter similar to PDI. Here it is important to note that pre-cracking of large molecules, which occurs in the macro- and mesopores of the particle, will increase the diffusion coefficient of the resulting (smaller) products, which are then able to penetrate deeper into the FCC particle.

## 5.4 Conclusions

Single-molecule diffusion inside the pore network of a real-life FCC particle was visualized by recording the movement of individual molecules using SMF microscopy. PDI, a molecule similar in size and structure to actual FCC feedstock, was used as fluorescent probe. Tracks of these single molecules were found throughout the whole cross-section of the FCC catalyst particle. Most PDI probes were found in an immobile, most likely trapped state, with a smaller subset of mobile molecules moving through the pore network of the FCC particle. A large variability of the mean square displacement curves was observed; consistent with the broad range of pore sizes found in FCC catalyst particles. Analysis of the displacement of mobile molecules showed that under reaction conditions, diffusion limitations would limit the part of the catalyst particle that would be used effectively to 19% for molecules of this size. We are now in the unique position to map diffusion properties of different types of molecules in the meso- and macropore network of a single catalyst particle using SMF microscopy. This provides high spatial resolution physicochemical information on a single catalyst particle, which can be related back to macromolecular properties. The combination of this approach with detailed structural information can bring structure-mass-transfer-reactivity relationships down to the level of an individual catalyst particle or any other hierarchically structured material within reach.

5

## Acknowledgments

We would like to thank Albemarle for providing the FCC catalyst particles, Dr. P. Dedecker (KU Leuven) for help with the Localizer software and J. van der Reijen (Utrecht University, UU) and Dr. S. Kalirai (UU) for fruitful discussions.

## 5.5 References

- [1] C. Liu, Z. Tan, W. Ding, S. Zheng, X. Pang, S. Sun, D. Wang, Q. Teng, T. Lu, *Method to Raise the Solid Content of Catalytic Cracking Catalyst Slurry*, 2010, US Patent 7,727,924 B2.

- [2] D. A. M. De Winter, F. Meirer, B. M. Weckhuysen, *ACS Catal.* **2016**, *6*, 3158–3167.
- [3] F. Meirer, S. Kalirai, D. Morris, S. Soparawalla, Y. Liu, G. Mesu, J. C. Andrews, B. M. Weckhuysen, *Sci. Adv.* **2015**, *1*, e1400199.
- [4] S. Mitchell, N.-L. Michels, K. Kunze, J. Pérez-Ramírez, *Nat. Chem.* **2012**, *4*, 825–831.
- [5] S. M. Babitz, *Catalyst, a Process for Its Preparation, and Its Use*, **2017**, US Patent 9534177 B2.
- [6] D. Stamires, P. O'Connor, E. J. Laheij, C. Vadovic, *FCC Catalyst, Its Preparation and Use*, **2016**, US Patent 9381502 B2.
- [7] K. H. Altgelt, M. M. Boduszynski, in *Composition and Analysis of Heavy Petroleum Fractions*, CRC Press, New York, 1993.
- [8] I. L. C. Buurmans, B. M. Weckhuysen, *Nat. Chem.* **2012**, *4*, 873–886.
- [9] A. von Diezmann, Y. Shechtman, W. E. Moerner, *Chem. Rev.* **2017**, *117*, 7244–7275.
- [10] J. Michaelis, C. Bräuchle, *Chem. Soc. Rev.* **2010**, *39*, 4731–4740.
- [11] T. Chen, B. Dong, K. Chen, F. Zhao, X. Cheng, C. Ma, S. Lee, P. Zhang, S. H. Kang, J. W. Ha, W. Xu, N. Fang, *Chem. Rev.* **2017**, *117*, 7510–7537.
- [12] K. P. F. Janssen, G. De Cremer, R. K. Neely, A. V. Kubarev, J. Van Loon, J. A. Martens, D. E. De Vos, M. B. J. Roeffaers, J. Hofkens, *Chem. Soc. Rev.* **2014**, *43*, 990–1006.
- [13] M. B. J. Roeffaers, B. F. Sels, H. Uji-i, F. C. De Schryver, P. A. Jacobs, D. E. De Vos, J. Hofkens, *Nature* **2006**, *439*, 572–575.
- [14] M. B. J. Roeffaers, B. F. Sels, H. Uji-i, B. Blanpain, P. L'hoëst, P. A. Jacobs, F. C. De Schryver, J. Hofkens, D. E. De Vos, *Angew. Chem. Int. Ed.* **2007**, *46*, 1706–1709.
- [15] M. B. J. Roeffaers, G. De Cremer, J. Libeert, R. Ameloot, P. Dedecker, A.-J. Bons, M. Bückins, J. A. Martens, B. F. Sels, D. E. de Vos, J. Hofkens, *Angew. Chem. Int. Ed.* **2009**, *48*, 9285–9289.
- [16] H. Shen, L. J. Tauzin, R. Baiyasi, W. Wang, N. Moringo, B. Shuang, C. F. Landes, *Chem. Rev.* **2017**, *117*, 7331–7376.
- [17] A. Zürner, J. Kirstein, M. Döblinger, C. Bräuchle, T. Bein, *Nature* **2007**, *450*, 705–708.
- [18] M. J. Skaug, L. Wang, Y. Ding, D. K. Schwartz, *ACS Nano* **2015**, *9*, 2148–2156.
- [19] J. Kirstein, B. Platschek, C. Jung, R. Brown, T. Bein, C. Bräuchle, *Nat. Mater.* **2007**, *6*, 303–310.
- [20] C. Jung, J. Kirstein, B. Platschek, T. Bein, M. Budde, I. Frank, K. Müllen, J. Michaelis, C. Bräuchle, *J. Am. Chem. Soc.* **2008**, *130*, 1638–1648.
- [21] G. De Cremer, M. B. J. Roeffaers, E. Bartholomeeusen, K. Lin, P. Dedecker, P. P. Pescarmona, P. A. Jacobs, D. E. De Vos, J. Hofkens, B. F. Sels, *Angew. Chem. Int. Ed.* **2010**, *49*, 908–911.
- [22] B. Rühle, M. Davies, T. Lebold, C. Bräuchle, T. Bein, *ACS Nano* **2012**, *6*, 1948–1960.
- [23] C. H. Lee, A. J. Crosby, T. Emrick, R. C. Hayward, *Macromolecules* **2014**, *47*, 741–749.
- [24] C. Hellriegel, J. Kirstein, C. Bräuchle, V. Latour, T. Pigot, R. Olivier, S. Lacombe, R. Brown, V. Guieu, C. Payrastre, A. Izquierdo, P. Mocho, *J. Phys. Chem. B* **2004**, *108*, 14699–14709.
- [25] K. Liu, A. V Kubarev, J. Van Loon, H. Uji-i, D. E. De Vos, J. Hofkens, M. B. J. Roeffaers, *ACS Nano* **2014**, *8*, 12650–12659.

- [26] K. Kennes, C. Demaret, J. Van Loon, A. V. Kubarev, G. Fleury, M. Sliwa, O. Delpoux, S. Maury, B. Harbuzaru, M. B. J. Roeffaers, *ChemCatChem* 2017, DOI: 10.1002/cctc.201700696.
- [27] J. Van Loon, K. P. F. Janssen, T. Franklin, A. V. Kubarev, J. A. Steele, E. Debroye, E. Breynaert, J. A. Martens, M. B. J. Roeffaers, *ACS Catal.* 2017, 7, 5234–5242.
- [28] Z. Ristanović, M. M. Kerssens, A. V. Kubarev, F. C. Hendriks, P. Dedecker, J. Hofkens, M. B. J. Roeffaers, B. M. Weckhuysen, *Angew. Chem. Int. Ed.* 2015, 54, 1836–1840.
- [29] A. Rademacher, S. Märkle, H. Langhals, *Chem. Ber.* 1982, 115, 2927–2934.
- [30] P. Dedecker, S. Duwé, R. K. Neely, J. Zhang, *J. Biomed. Opt.* 2012, 17, 1–5.
- [31] J. Vogelsang, C. Steinhauer, C. Forthmann, I. H. Stein, B. Person-Skegros, T. Cordes, P. Tinnefeld, *ChemPhysChem* 2010, 11, 2475–2490.
- [32] Z. Liu, S. L. Chen, X. Ge, P. Dong, J. Gao, Z. Xu, *Energy and Fuels* 2010, 24, 2825–2829.
- [33] E. T. C. Vogt, C. T. Kresge, J. C. Vartuli, *Stud. Surf. Sci. Catal.* 2001, 137, 1003–1027.
- [34] J. Fu, S. Kim, R. P. Rodgers, C. L. Hendrickson, A. G. Marshall, K. Qian, *Energy & Fuels* 2006, 20, 661–667.
- [35] F. Feil, S. Naumov, J. Michaelis, R. Valiullin, D. Enke, J. Kärger, C. Bräuchle, *Angew. Chemie* 2012, 124, 1178–1181.
- [36] J. H. Lambert, in *Photometria, Sive de Mensura et Gradibus Luminis Colorum et Umbrae*, Augsburg, 1760.
- [37] L. L. Kish, J. Kameoka, C. G. Granqvist, L. B. Kish, *Appl. Phys. Lett.* 2011, 99, 143121.
- [38] F. Meirer, D. T. Morris, S. Kalirai, Y. Liu, J. C. Andrews, B. M. Weckhuysen, *J. Am. Chem. Soc.* 2015, 137, 102–105.
- [39] S. Kalirai, U. Boesenborg, G. Falkenberg, F. Meirer, B. M. Weckhuysen, *ChemCatChem* 2015, 7, 3674–3682.
- [40] W. K. Kegel, *Science* 2000, 287, 290–293.
- [41] L. Van Hove, *Phys. Rev.* 1954, 95, 249–262.
- [42] S. A. El-Daly, *Spectrochim. Acta Mol. Biomol. Spectrosc.* 1998, 55, 143–152.
- [43] X. Michalet, A. J. Berglund, *Phys. Rev. E* 2012, 85, 61916.
- [44] D. Wallenstein, C. Fougret, S. Brandt, U. Hartmann, *Ind. Eng. Chem. Res.* 2016, 55, 5526–5535.
- [45] J. Pérez-Ramírez, C. H. Christensen, K. Egeblad, C. H. Christensen, J. C. Groen, *Chem. Soc. Rev.* 2008, 37, 2530.
- [46] W. Thiele, *Ind. Eng. Chem.* 1939, 31, 916–920.
- [47] D. M. Stockwell, in *Fluid Catalytic Cracking VII: Materials, Methods and Process Innovations* (Ed.: M.L. Occelli), Elsevier, Amsterdam, 2007, p. 137.
- [48] G. F. Froment, K. B. Bischoff, J. De Wilde, in *Chemical Reactor Analysis and Design*, John Wiley & Sons, New York, 2011, p. 720.
- [49] J. H. Gary, G. E. Handwerk, M. J. Kaiser, in *Petroleum Refining: Technology and Economics*, CRC Press, New York, 2007, p. 115.
- [50] J. Kärger, S. Vasenkov, *Microporous Mesoporous Mater.* 2005, 85, 195–206.
- [51] G. Jiménez-García, R. Aguilar-López, E. León-Becerril, R. Maya-Yescas, *Fuel* 2007, 86, 1278–1281.



# **Chapter 6**

## **Developing Correlative Single Molecule Fluorescence, Electron and X-ray Microscopy as a Tool to Study Structure, Reactivity and Ageing of a Single Catalyst Particle**

Obtaining correlative information about structure, reactivity and ageing is important in understanding the functioning of complex catalytic materials such as fluid catalytic cracking (FCC) catalysts. A new multimodal approach was developed, in which fresh and aged FCC particles are first microtomed into 100 nm thin sections and then analyzed using three complementary analytical techniques. A combination of scanning electron microscopy, super-resolution fluorescence microscopy and X-ray fluorescence microscopy on the same sample gave high-resolution information on structure, reactivity and elemental composition, respectively. Alignment of the resulting three microspectroscopic images was achieved without the need for fiducial markers in the sample.

## 6.1 Introduction

The fluid catalytic cracking (FCC) catalyst is a typical example of a complex, hierarchically structured nanomaterial, consisting of a mixture of zeolite, clay, alumina and other binder materials, which differ in their chemical (e.g., acidity) and structural properties (e.g., porosity).<sup>[1]</sup> High-resolution micro-spectroscopy methods have been developed to study structure and reactivity<sup>[2,3]</sup> as well as deactivation<sup>[4,5]</sup> of these important catalyst particles, revealing considerable intra- and interparticle heterogeneities. Such intraparticle heterogeneities are expected to be exasperated during the FCC process, as the catalyst is exposed to rather harsh conditions. The reaction takes place at elevated temperatures (800–850 K) and the products are separated from the catalyst via steam treatment, which causes dealumination of the zeolite.<sup>[6]</sup> Large amounts of coke are formed as side product of catalytic cracking requiring the catalyst particles to undergo regeneration by coke burn-off, causing further damage. In addition, contaminant metals, present in the crude oil feed, end up deposited onto the catalyst particles, leading to irreversible blockage of the pores. All this results in extensive structural and chemical changes within the catalyst particles. Catalyst deactivation is so severe that new catalyst particles have to be added to the reactor on a daily basis to keep activity at an acceptable level.<sup>[7]</sup> Insight into the various modes of deactivation by detailed analysis of catalyst particles at different stages of its catalytic life has therefore been an important topic of studies dealing with FCC catalyst materials.<sup>[4]</sup>

Due to the complexity of the FCC catalyst material and the different deactivation mechanisms involved, a thorough understanding of its structure–performance relations requires an investigation combining complementary techniques to provide correlated chemical and structural information. Additionally, these correlated techniques should all provide data at high resolution to allow the nanoscale heterogeneities that exist within the material to be examined. Such knowledge can then ultimately serve to guide rational design of FCC catalysts in particular and solid catalysts in general. In this Chapter, a new correlative approach is developed, combining scanning electron microscopy (SEM), single molecule fluorescence (SMF) microscopy and X-ray fluorescence (XRF) microscopy techniques to provide highly complementary information on both fresh and aged zeolite Y-containing FCC catalyst particles. The catalyst particle was first microtomed into 100 nm thin sections for use with these techniques. SMF microscopy measurements were performed on these samples using a thiophene probe reaction to stain the reactive acid sites. Subsequent analysis using super-resolution optical fluctuation imaging (SOFI) provided high-resolution information on the reactivity of the active zeolite phase within the catalyst particle. SEM is used to provide information on the structure of the complete thin section of the FCC catalyst particle, i.e. regardless of reactivity in the probe reaction used for SMF microscopy or the presence of certain (deposited) elements as detected by XRF. Finally, these two data sets are complemented by XRF analysis, offering the possibility to more extensively correlate structure with activity and mode of deactivation by means of elemental mapping. Indeed, XRF allows mapping of elements that are native to the catalyst particle, such as lanthanum, which is indicative of the location of the zeolite. XRF can also identify elements

that originate from the feed, such as metals deposited on aged catalyst particles.<sup>[8,9]</sup> Each technique provides information at sub-micron spatial resolution, making it possible to probe the correlations between the information obtained from the three techniques, such as the reactivity of the zeolite phase and the influence of deposited metals on reactivity.

## 6.2 Experimental

### 6.2.1 Materials

Fresh and aged catalyst particles, containing zeolite Y as the active phase, were supplied by Albemarle. The aged catalyst particles have been taken from an industrial FCC reactor. Because new catalyst particles are continuously added to the reactor during FCC operation, the catalyst mixture present in the reactor has an age distribution and is called equilibrium catalyst (ECat). Older ECat particles have a higher density because more contaminant metals, present in the reactant feed, have been deposited onto them. The ECat used in this Chapter has been density separated, using a sink-or-float method, to separate the particle based on their age.<sup>[4]</sup> The ECat was thus separated into 5 samples and the one used here has the second highest density; this means that the ECat used here has been severely deactivated based on its metal loading.

Thiophene (99%) was purchased from Aldrich and used as received. Silicon nitride (SiN) membranes were purchased from Silson Ltd. and had a frame size of  $3\times 3\text{ mm}^2$ , a membrane size of  $0.5\times 0.5\text{ mm}^2$ , a frame thickness of  $200\text{ }\mu\text{m}$  and a membrane thickness of  $50\text{ nm}$ .

6

### 6.2.2 Sample preparation

The FCC catalyst samples were first calcined in a static oven at  $823\text{ K}$  ( $1\text{ K min}^{-1}$ ) for 48 h. Subsequently, the catalyst particles were embedded in Epofix, a two-component epoxy resin by mixing the resin and the hardener in a weight ratio of 25:3 and adding this mixture to the catalyst at  $294\text{ K}$  and atmospheric conditions in a small polyethylene vial. The samples were cured overnight at  $333\text{ K}$ . Sectioning was performed using a Reichert-Jung Ultracut E microtome and a diamond knife (Diatome Ultra 35°, 4 mm size) under a 6 degrees' clearance angle with a cutting speed of  $2\text{ mm s}^{-1}$ . Using a droplet of milliQ water, the sections were then placed on a SiN membrane. The SiN membrane containing the FCC particles was calcined in a static oven at  $873\text{ K}$  (ramp  $1\text{ K min}^{-1}$ ) for 48 h to remove the epoxy resin, which is fluorescent, and any organic impurities.

The samples were first measured using SMF microscopy. The addition of thiophene for the fluorogenic probe reaction was performed immediately prior to the experiment;  $10\text{ }\mu\text{L}$  of pure thiophene was placed on top of the membrane

containing the particles and allowed to dry for 5 min after which the SiN membrane was immediately placed in the vacuum chamber for the fluorescence microscopy experiments (see Section 6.2.3). The staining reaction and all experiments were carried out at 294 K. Next, the sample was measured using XRF; no additional sample preparation was needed. Prior to the SEM measurements, the samples were placed on an SEM stub and coated with Pt in a Cressington 208 HR sputter coater using a Pt target. Sputtering was performed at 0.08 mbar Ar atmosphere with an applied current of 40 mA. The samples were rotated at a slight tilt to obtain a homogeneous layer of Pt. The coating was done for 200 s resulting in a layer of circa 10 nm.

### 6.2.3 Single molecule fluorescence microscopy

SMF microscopy images were recorded using an epifluorescence wide-field microscope (Nikon) with a 25 $\times$  air objective (NA = 0.55). The fluorescence microscope is part of an integrated SMF-TEM setup; therefore, the fluorescence experiment is carried out in the vacuum chamber of this integrated setup. The sample was illuminated with a Cobolt 532 nm laser operating at 5%, providing 175 W cm<sup>-2</sup> to the sample. The emitted fluorescence was passed through a dichroic mirror and a 585/65 band pass filter and recorded using a PCO 4.2 Edge (s)CMOS camera. This field of view was cropped to 107 $\times$ 107  $\mu\text{m}$  (400 $\times$ 400 pixels) with a pixel size of 268 $\times$ 268 nm<sup>2</sup>. Movies of the fluorescence microscopy maps were recorded with an exposure time of 0.3 s. The optimum exposure time was determined experimentally. For each sample, a movie of 600 images was recorded. Analysis of the fluorescence movies was carried out using the SOFI algorithm implemented in the Localizer software, a plug-in of the Igor Pro software.<sup>[10]</sup> Second order SOFI was used; the resolution is slightly below the diffraction-limited resolution of fluorescence microscopy (i.e.  $\sim$  300 nm).<sup>[11]</sup>

### 6.2.4 X-ray fluorescence microscopy

2D X-ray fluorescence (XRF) mapping was performed at the P06 beamline at the PETRA III synchrotron, DESY, Hamburg (Germany).<sup>[12]</sup> A monochromatic X-ray beam of 10.5 keV was focused to a 0.5 $\times$ 0.5  $\mu\text{m}^2$  spot using KB-mirror optics. The sample was placed in the focal spot and raster scanned continuously. Full XRF spectra were collected for pixels 0.1 $\times$ 0.1  $\mu\text{m}$  in size with a dwell time of 0.1 s. The energy-dispersed fluorescent signal was detected using a 384-element Maia detector array.<sup>[13]</sup>

The spectra shown in Figure 6.1 are a summation over the whole FCC thin section for each sample. The spectra were fitted using a model including the elements Ar, Cr, Cu, Fe, K, La, Ni, Si, Ti and Zn for the fresh sample; for the ECat sample, V was additionally included because it is known to deposit onto the catalyst during the FCC process.<sup>[4,9,14]</sup> Each of these elements was found to be present, although some in small amounts. Data analysis and spectral deconvolution were performed using

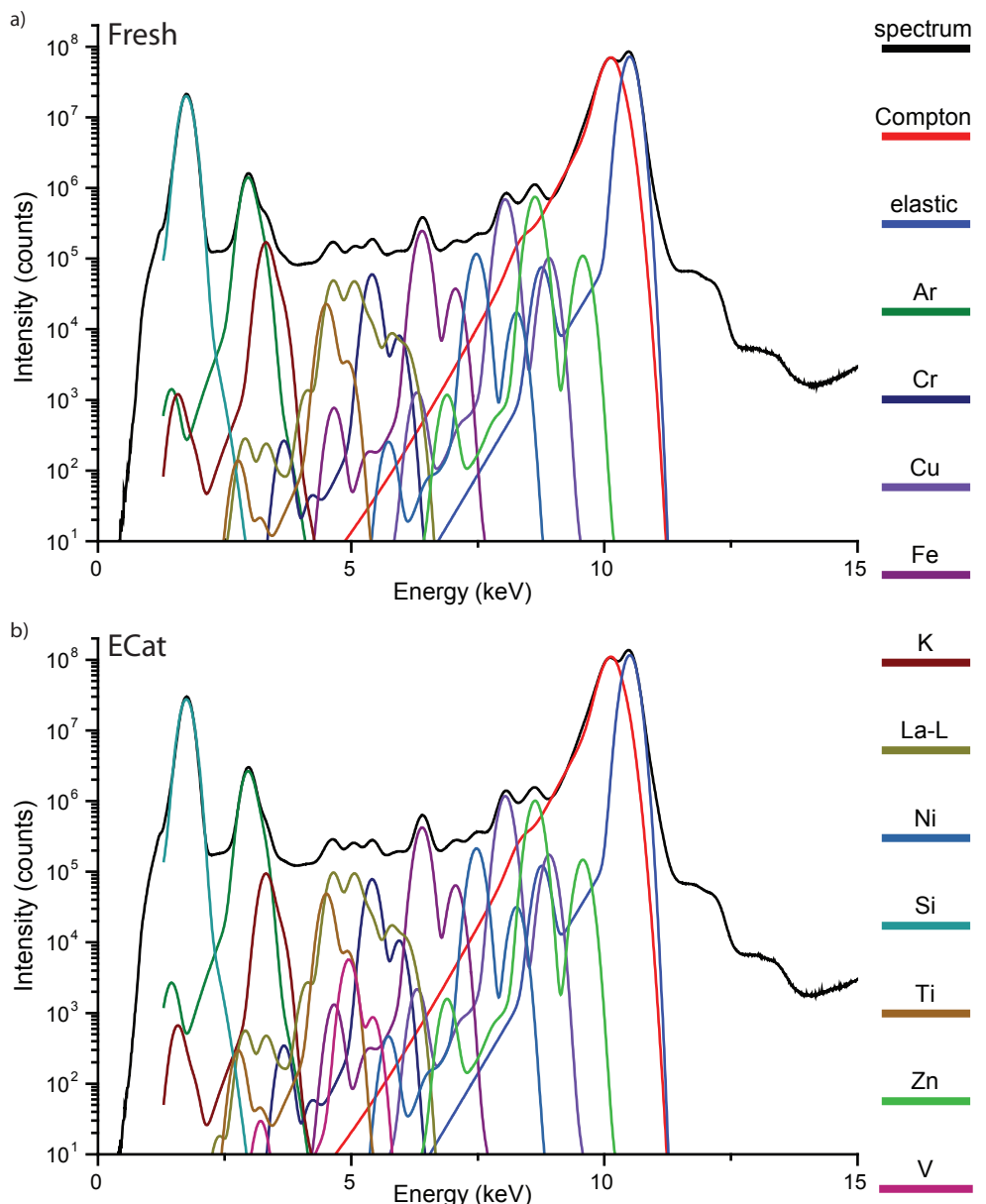


Figure 6.1. XRF spectrum and its deconvolution of the FCC thin section of a fresh (a) and ECat sample (b). The spectra are summed over the complete section at a single projection image.

the GeoPIXE<sup>[15]</sup> software suite providing elemental distribution maps for the FCC particles. A 4×4 binning of pixels was applied during analysis to improve the signal-to-noise ratio, leading to a resolution of 400×400 nm<sup>2</sup>. Background subtraction was carried out for each element, with the maximum intensity of an area outside

of the thin section taken as a threshold. Furthermore, a circular crop was applied to remove everything but the thin section of interest.

### 6.2.5 Scanning electron microscopy

Prior to the scanning electron microscopy (SEM) measurements, the SiN membranes were placed on a SEM stub and sputter coated with Pt (section 6.2.2) to avoid charging of the sample. SEM measurements were performed on a FEI Helios Nanolab 600 DualBeam microscope. The electron beam was operated at both 2 and 10 kV at a current of 0.20 nA. The SEM images were obtained from the secondary electrons with a dwell time of 1  $\mu$ s. Although SEM has a resolution down to 1 nm, in practice, the structural features of the catalyst that can be distinguished are approximately 500 nm in size.

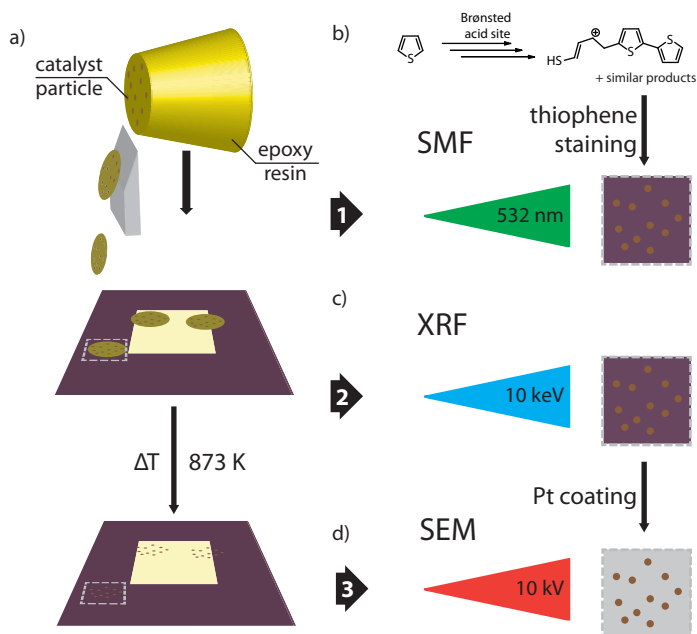


Figure 6.2. Overview of the approach developed to analyze an individual catalyst particle using three complementary high-resolution techniques. a) FCC catalyst particles embedded in epoxy resin (yellow) are microtomed into 100 nm thin sections and deposited onto a SiN membrane. b) calcination of the SiN membranes at 873 K removes the resin and leaves just the catalyst thin sections. b) First, the reactive sites of the catalyst are stained using the thiophene oligomerization reaction. The fluorescent products are excited using a 532 nm laser and fluorescence movies are recorded for SOFI analysis. c) X-ray fluorescence spectra are recorded for each pixel using a 10 keV X-ray beam with a spot size of 500 nm. Deconvolution of the spectra gives the elemental concentration in each pixel. d) The sample is first coated with a 10 nm Pt layer, after which SEM images are recorded using a 10 kV acceleration voltage.

### 6.2.6 Image alignment

The SEM and XRF images were aligned to the SMF images. From the SEM images, the background was removed first by applying a threshold and Gaussian smoothing. The XRF images were cropped to remove everything but the particle of interest. For XRF, the combined channels of elements Ca, Fe, K, La, Si and Ti were used for alignment of the fresh particle, while for the ECat particle, the sum image was used. All images were rotated and scaled manually before applying the overlay algorithm. The correlation coefficient between SOFI and XRF images was calculated using MATLAB. The aligned images were compared pixel-to-pixel, omitting any pixels for which the value of one of the images was 0.

## 6.3 Results and discussion

### 6.3.1 Sample preparation and analysis using the three techniques

To probe complete cross sections of the catalyst with electron and fluorescence microscopy, the fresh and ECat FCC particles were embedded in an epoxy resin and microtomed to 100 nm thin sections (Figure 6.2a), which were subsequently placed on a silicon nitride (SiN) membrane. These membranes were chosen as sample holders because of their unique heat resistance, allowing calcination of the sample at temperatures as high as 873 K. Preliminary experiments, however, showed that catalyst thin sections on the SiN membrane emit a broad fluorescent signal from 550–750 nm (Figure 6.3). This fluorescence background signal was found to be too high in comparison to the signal generated by the thiophene probe reaction (see below) on the acid sites of the active zeolite Y phase. The background fluorescence intensity thus precluded the intended, single-molecule fluorescence experiment. This effect has not been described previously, but it may be caused by dangling SiN bonds on the window.<sup>[16,17]</sup> That the fluorescence background is prohibitively high also results from the choice to study H-Y-containing FCC particles, as the

6

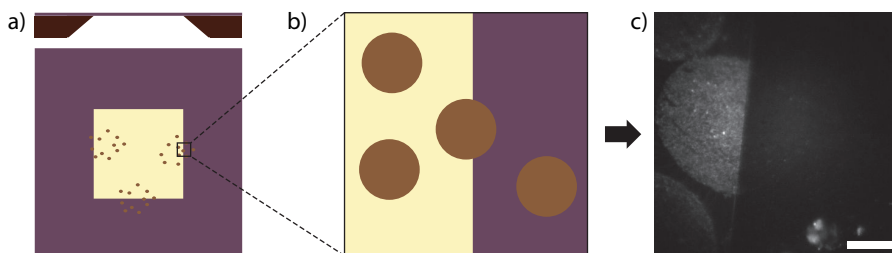


Figure 6.3. Example of the fluorescent background signal observed with non-stained thin sections lying on top of the SiN membrane. a) side (top) and top (bottom) view of a SiN membrane. b) Zoomed-in area of a catalyst thin section on the edge of the membrane. c) Fluorescent signal, without application of a fluorogenic reaction, of the catalyst thin section. The scale bar represents 20  $\mu$ m.

fluorescence signal generated by this particular zeolite upon thiophene staining is weaker than with, e.g., ZSM-5. Surprisingly, this background fluorescence signal was not observed on the frame of the membrane, i.e., the part of the SiN membrane that has a silicon wafer beneath it. Therefore, for both the fresh and the ECat FCC catalyst samples, those thin sections were selected for analysis that were located on the frame of the SiN membrane (Figure 6.2a). Unfortunately, this precluded the use of TEM for these samples (see Chapter 7 for an alternative approach to correlating SMF and TEM).

First, fluorescence microscopy was used to evaluate the reactivity of the FCC catalyst thin section, using thiophene oligomerization as the probe reaction, which forms fluorescent products on Brønsted acid sites. Indeed, this probe has been used effectively before to study reactivity of fresh and deactivated FCC catalysts containing zeolite Y as the active phase.<sup>[18]</sup> Most of the fluorescence intensity after staining the FCC particle is associated with the active zeolite phase, with a minor contribution from the non-zeolitic matrix. Pure thiophene was deposited onto the sample, after which fluorescence intensity was studied in the vacuum chamber of an integrated light and electron microscope. Excitation of the fluorescent thiophene oligomerization products was accomplished by illumination with a 532 nm laser. This laser most effectively excites higher oligomerization products (i.e. trimers and higher).<sup>[19]</sup> Fluorescence microscopy images were recorded with a wide-field microscope as movies of 600 frames. Products of single molecule catalytic turnovers were observed as bright fluorescent events, but such events were few and observed only for the fresh catalyst particle. These events were in fact too few to allow for a NASCA analysis, which is typically used in super resolution fluorescence studies to localize the reactive components with high resolution. Such a high-resolution map of the reactivity of the catalyst thin sections could therefore not be reconstructed. This is most likely because the low acid strength of the zeolite Y component in the FCC material induces only limited oligomerization, in combination with less effective stabilization of the fluorescent carbocation in the large cages of this zeolite.<sup>[20]</sup> Additionally, the reactants of the fluorogenic reaction may not be sufficiently adsorbed into zeolite Y under high vacuum conditions.

However, fluctuations in fluorescence intensity were observed, which prompted us to analyze the SMF movies using the SOFI algorithm.<sup>[11]</sup> Fortunately, SOFI analysis of the recorded movies was possible, as it requires stochastic, reversible fluctuations in fluorescence and can analyze images with a low signal-to-noise ratio. Background fluorescence, which was observed on the complete thin section, was effectively suppressed by the SOFI algorithm, which enabled us to distinguish areas of higher reactivity and greatly improve fluorescence image resolution.<sup>[11]</sup> The results are shown in Figure 6.4. Both the SOFI analysis as well as the underlying fluorescence movies show higher intensity for the ECat particle than for the fresh particle, although the intensity difference is much higher in the SOFI images. As the fresh catalyst particle is expected to be more active for thiophene oligomerization and thus more fluorescent than the ECat particle, this finding is counterintuitive. Possibly, the experimental conditions in this type of staining experiments (i.e., using pure thiophene and measuring in high vacuum conditions) are hard to reproduce

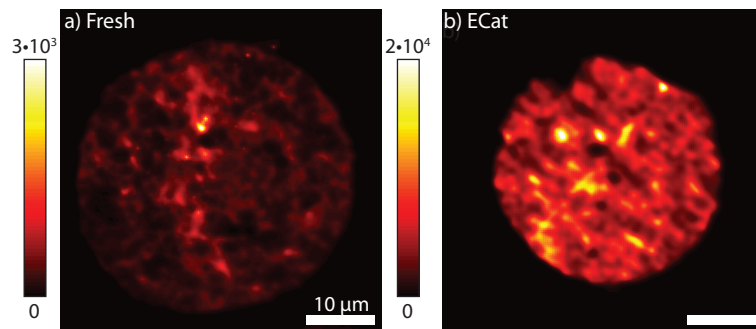


Figure 6.4. SOFI intensity maps showing reactivity of the catalyst thin section of the fresh catalyst particle (a) and the ECat particle (b). Intensities of these images cannot be directly compared. Both scale bars represent 10 µm.

exactly, leading to fluctuations in the fluorescence intensity between experiments. Furthermore, differences in thin sections between batches may also play a role (*vide infra*). The distribution of SOFI intensity within one catalyst thin section can still be evaluated, however. Looking at the complete thin section, the ECat particle seems to have a more evenly distributed SOFI intensity, with the fresh particle showing more fluorescence intensity in a narrow region running from the top to the bottom of the particle. For both particle thin sections, there is significant heterogeneity of intensity, which is expected as the active zeolite material is dispersed within a matrix of less active elements.

Second, elemental maps of the same FCC thin sections were recorded using XRF

Table 7.1. Correlation coefficients for fluorescence intensity and XRF element concentrations, for the fresh and the ECat thin sections.

| Fresh | Ti    | La    | K     | Fe    |       |
|-------|-------|-------|-------|-------|-------|
| SOFI  | 0.00  | -0.22 | 0.21  | 0.05  |       |
| Fe    | 0.37  | -0.06 | 0.24  |       |       |
| K     | -0.05 | 0.43  |       |       |       |
| La    | -0.09 |       |       |       |       |
| ECat  | V     | Ni    | Ti    | La    | K     |
| SOFI  | 0.10  | -0.18 | 0.10  | 0.13  | 0.26  |
| Fe    | 0.03  | 0.94  | 0.01  | -0.22 | -0.02 |
| K     | -0.13 | 0.01  | 0.07  | 0.45  |       |
| La    | -0.25 | -0.13 | -0.12 |       |       |
| Ti    | 0.75  | 0.03  |       |       |       |
| Ni    | 0.10  |       |       |       |       |

microscopy. The most significant elements are La, as this rare earth element is present only in zeolite component and can therefore be used to locate it,<sup>[6,21,22]</sup> and the feed-derived catalyst poisons Fe, Ni, known to block entrance to the pore network when deposited and V, which damages the active zeolite phase.<sup>[4,8,9,14,23]</sup> Because the catalysts are microtomed into very thin slices (100 nm), only a limited amount of material is available to obtain an elemental analysis from any position within the cross section of the particle. Fitting of the XRF spectrum to obtain elemental concentrations therefore proved challenging, also because the background level of each element was found to shift within the dataset of one catalyst particle thin section. This shift in background could be corrected for each element, but some inaccuracy is introduced in this step. Table 7.1 provides the quantification of the (lack of) correlation between the concentrations of the various metals as measured using XRF, as well with SOFI intensity. Most of these do not show a high correlation coefficient, with a few notable exceptions (in *italics*), which are discussed below.

The background-corrected elemental distributions are shown in Figure 6.5. Surprisingly, the fresh catalyst particle does not seem to contain much lanthanum and thus not much active zeolite phase, compared to the ECat particle. This would explain the higher observed fluorescence for the ECat compared to the fresh particle. It also suggests that an anomalous fresh particle containing little zeolite was measured. Particles with no zeolite (so-called metal traps) are sometimes used in the FCC process, designed to combat the negative effects of contaminant metals; it is possible this is such a particle.<sup>[24]</sup> Although the composition of such particles is not known, it may also provide an explanation of the high K concentration in the fresh particle, again compared to the ECat. Fe and Ti are both observed in the fresh particle, mostly in several concentrated regions, some of which are overlapping. Both iron and titania are associated with the clay (kaolin) added to FCC particles, thus suggesting that clay *is* present in the fresh particle. However, the weak correlation coefficient between Fe and Ti indicates both of these elements are not omnipresent in the clay.

In contrast to the fresh particle, La is found in the ECat particle in concrete domains, homogeneously distributed in the thin section, which are presumably the zeolite domains. The homogeneous distribution of these domains resembles those found in complete ECat FCC particles using XRF, as well as thin sections using scanning transmission x-ray microscopy.<sup>[6,14]</sup> This provides further proof that the La concentration found in the ECat is as expected, while the La concentration in the fresh is not. Both Ni and Fe are clearly localized at the rim of the particle, in line with previous observations, and their locations show a strong correlation (Table 7.1).<sup>[4,14]</sup> Both Ni and Fe are present as a contaminant metal in the feedstock and, because of their limited mobility inside the catalyst particle, are deposited at the edge of the particle during the FCC reaction. V is also known to be deposited during the reaction, but being more mobile it indeed shows a more homogeneous distribution throughout the thin section. Furthermore, the distribution of Ti in the ECat particle is very similar to the fresh, suggesting the distribution of clay in the particles is comparable. Finally, an apparent correlation between Ti and V is

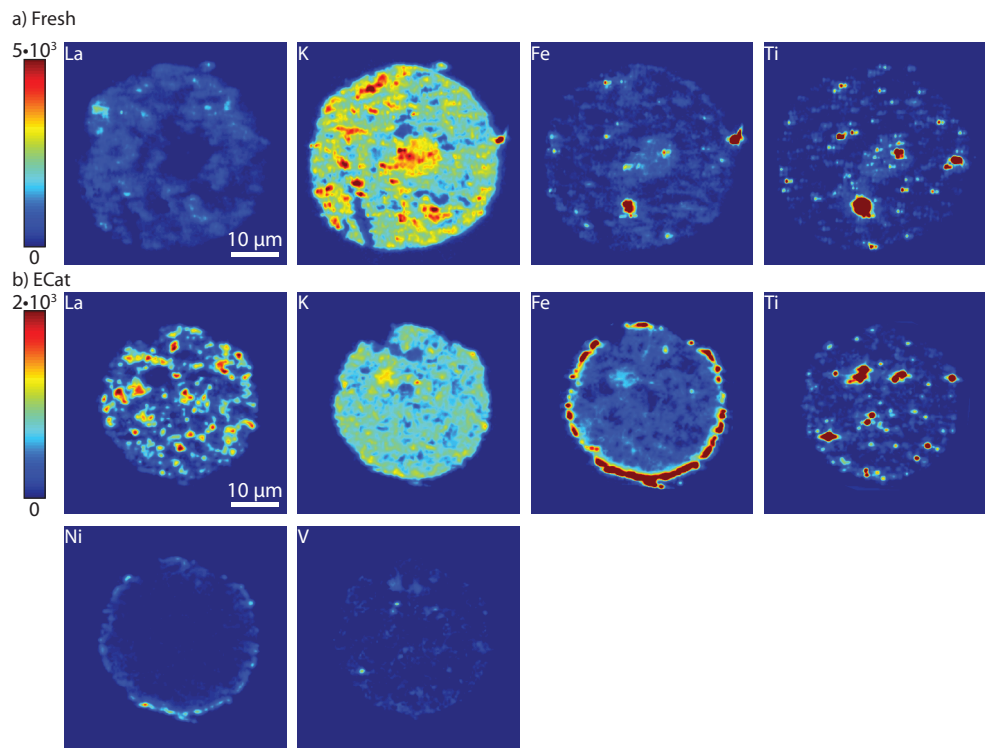


Figure 6.5. XRF results for the fresh (a) and the ECat (b) particle, for selected elements. Intensities of different catalyst particles cannot be directly compared. All images have the same magnification; the scale bar is 10 µm.

observed in the ECat particle, with a corresponding high correlation coefficient. However, this is most likely artificial as these lines overlap in the XRF spectrum (Figure 6.1).

Third, SEM images of the fresh and the ECat samples were recorded, as shown in Figure 6.6a and b. Marked differences can be observed in the structure of the two particles. In the ECat sample, the cutting direction (from bottom left to top right) is clearly visible from the folds in the thin section. Furthermore, it seems some hard material has ‘ploughed’ through the thin section leaving a long mark, and judging from the dented, non-spherical circumference, some parts of the outside of the particle are missing. The fresh particle is better preserved: it is still spherical and only misses an area at the bottom left. Furthermore, the ECat particle seems to have a smoother structure in which less details can be discerned than in the fresh particle. For example, no differences in structure (e.g. as marked by the arrow and zoom-in for the fresh thin slice) can be distinguished in the ECat particle.

The fresh and the ECat sample used in this study were embedded and thin sectioned in different batches; most likely, subtle and unintentional differences in embedding and microtoming have caused these thin sections to look different. For comparison,

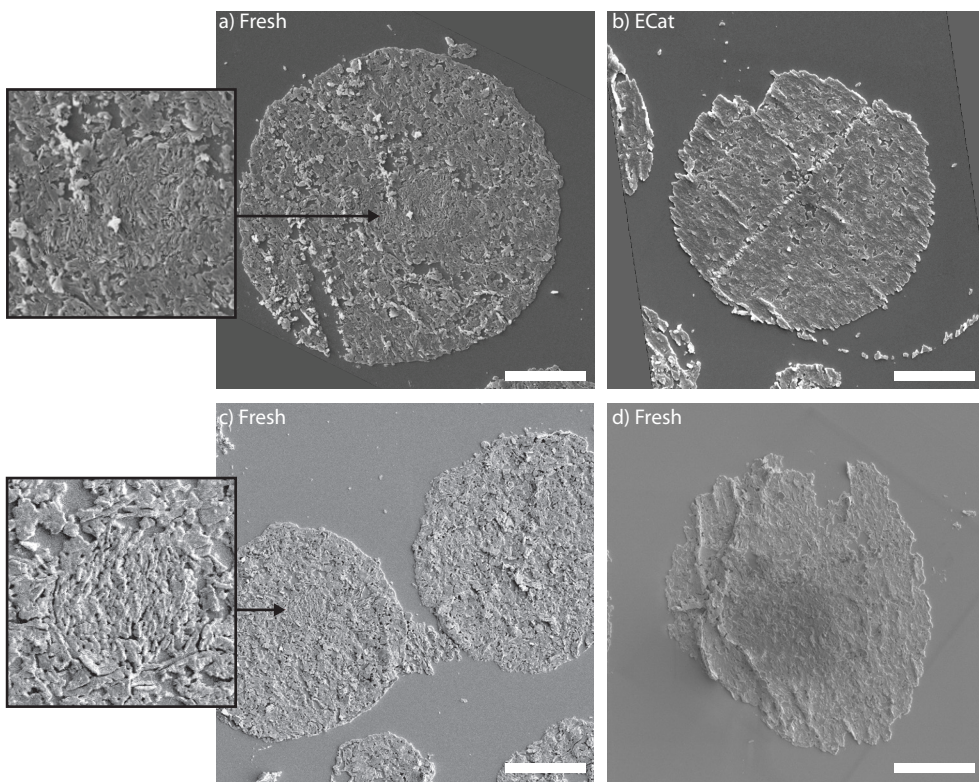
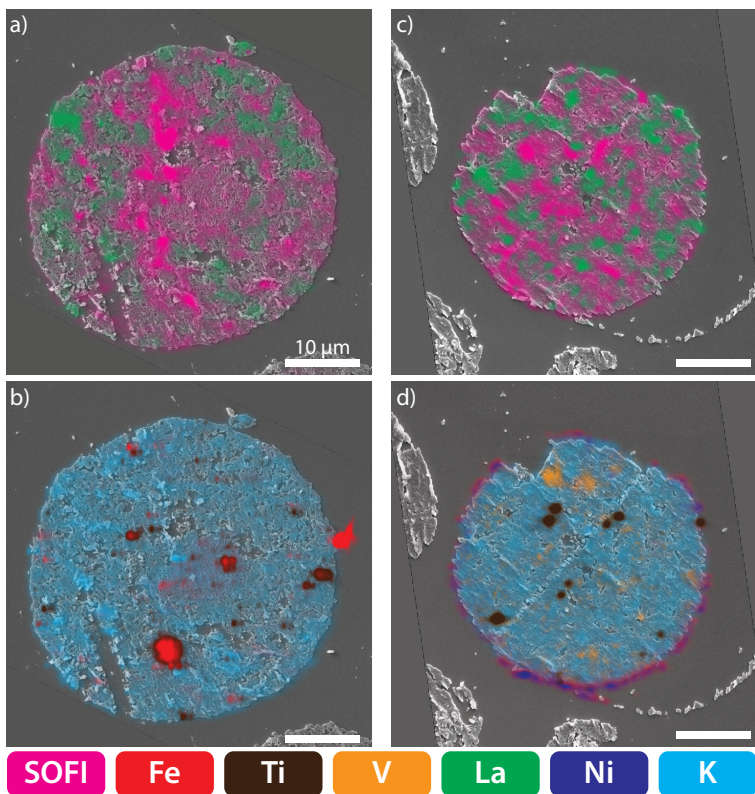


Figure 6.6. SEM images of the thin sections of the FCC particles previously studied with SMF and XRF, as well as some other, representative slices for comparison. a) and b): fresh and ECat thin sections used in the correlative study. c) Sections of the fresh catalyst particles microtomed in the same batch as the fresh particles in a. d) Sections of the same fresh catalyst particles microtomed in the same batch as the thin sections from the ECat particles in b. All scale bars represent 10 µm. All image settings were kept constant except the accelerating voltage of the electron beam: 10 kV for a, b and 2 kV for c, d. The red arrows and zoom-ins in a and c indicate an area with different morphology.

Figure 6.6c shows thin sections of the same type of fresh FCC particles, embedded and thin sectioned at the same time as a, showing a very similar structure, including the subtle differences in morphology not visible in b. In contrast, Figure 6.6d shows another thin section from particles of the same type of fresh FCC particle, however, this one is embedded and thin sectioned at the same time as b, showing again the smoother, less detailed structure. This last image thus suggests that the differences seen between the structures in a and b are not caused by whether the particle is fresh or ECat, but rather the sensitivity to the sample preparation stages of embedding and sectioning procedure.

### 6.3.2 Correlative analysis

The three recorded data sets obtained on the same thin slice were then overlaid semi-automatically using an iterative algorithm based on the Enhanced Correlation Coefficient (ECC) method,<sup>[25]</sup> which does not require (fiducial) markers to be added to the sample. Although the shape of the particle is visible in each of the separate maps, the SEM images were vital to properly overlaying the different data sets; the shape of the particle derived from the SEM images most accurately defined the particle's boundaries. In addition to providing structural information, the SEM images can thus also serve as a control for the alignment and correlation of the XRF and SMF data sets, something which otherwise would be challenging. The SEM and SMF images could be overlaid by scaling and rotating, with the XRF images also required warping (i.e. distorting) to be overlaid. The results of the image alignment are shown in Figure 6.7. Visual inspection shows that the



6

Figure 6.7. An overlay of all correlated techniques. a) SOFI intensity and La distribution overlaid on the SEM image of the fresh catalyst thin section. b) K, Fe and Ti overlaid on the SEM image of the fresh catalyst thin section. c) SOFI intensity and La distribution overlaid on the SEM image of the ECat catalyst thin section. d) K, Fe, Ni, V and Ti overlaid on the SEM image of the Ecat catalyst thin section. The color intensities have been adjusted for maximum visibility, and therefore the intensities of elements in these images cannot be directly compared. The scale bars are 10  $\mu\text{m}$ .

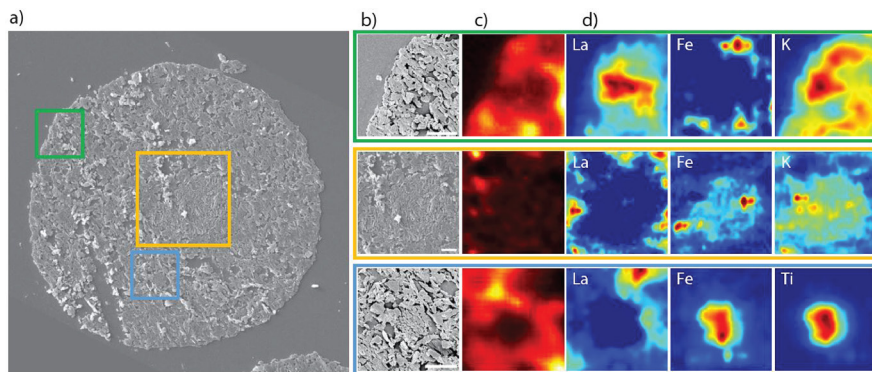


Figure 6.8. Regions of interest within the fresh catalyst particle thin section. a) regions of interest are shown in the SEM image. b,c,d) The regions of interest shown in a, marked with the same color and highlighting SEM (b) features, SOFI (c) intensity and selected elemental concentrations by XRF (d). The XRF intensity maps are not directly comparable.

structural features visible in SEM are well matched with the SOFI and XRF results. An example of the accuracy of the overlay is given by the deposited Fe and Ni at the edge of the ECat particle, which closely follows the edge of the SEM structure.

Figure 6.7a and c show an overlay of the SOFI intensity with the La elemental map. Surprisingly, no correlation between La and SOFI intensity is detected in neither the fresh or ECat particle thin slice. This is counter to expectation, as the La-containing zeolites are associated with the strongest acidic sites in the catalyst particle, which should be most effective in converting thiophene to fluorescent products.<sup>[18]</sup> However, the results show that apparent zeolite location and fluorescence intensity do not coincide; the correlation coefficient for La and SOFI, shown in Table 7.1, is even slightly negative. Given the low SOFI intensity in both particles, as observed before, the SOFI results should be treated with some serious caution as they may not accurately represent zeolite Y reactivity under these reaction conditions.

Figure 6.8 shows selected regions of interest (ROIs) of the fresh catalyst thin section for each technique. The green ROI indicates one of the few areas in the fresh particle with a higher La concentration. The low SOFI intensity in the same region again demonstrates that high La is not associated with high SOFI intensity. The yellow ROI highlights a region with a different morphology compared to the rest of the catalyst thin section. The finer structure in this area suggests that this area is amorphous, which would be in line with the area being low in La (indicating no zeolite is present), and high in Fe (associated with the clay). A different morphology is also observed in the blue ROI, suggesting another clay particle, as it also has high Ti and Fe concentrations.

Figure 6.9 shows the combination of techniques for the ECat particle thin section. A high concentration of deposited V is found in the green ROI. It has been suggested that V preferably deposits on zeolite crystals in a destructive manner, however, a recent study has found no evidence for this.<sup>[14]</sup> The La concentration in this area

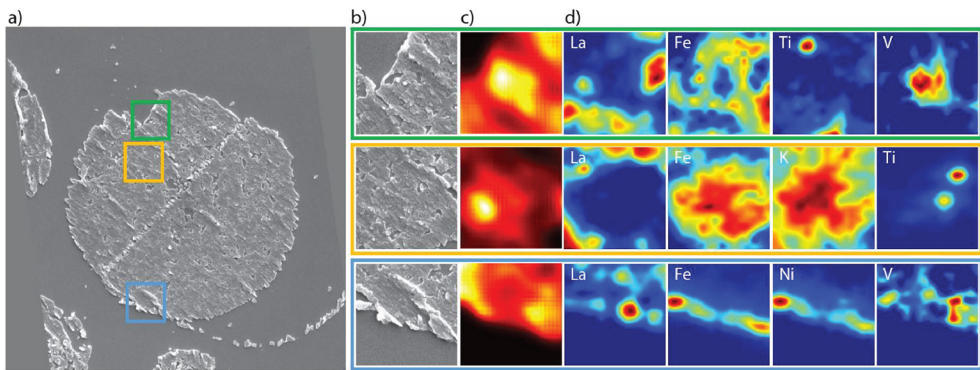


Figure 6.9. Regions of interest within the ECat particle thin section. a) regions of interest are shown in the SEM image. b,c,d) The regions of interest shown in a, marked with the same color and highlighting SEM (b) features, SOFI (c) intensity and selected elemental concentrations by XRF (d). The XRF intensity maps are not directly comparable.

is low, suggesting V indeed does not deposit preferably on the zeolite crystals. The yellow region shows an amorphous area with a high Fe concentration, similar to the yellow region in Figure 6.8, although the differences in structure are difficult to see in the ECat thin section. Finally, the blue area shows a section at the edge of the particle, with the contaminant metals Fe, Ni and V clearly present close to the edge of the catalyst thin section.

## 6.4 Conclusions

A method has been developed that allows three complementary high-resolution techniques to be applied to one and the same sample of fluid catalytic cracking (FCC) catalyst material in a correlative manner. A new sample preparation method allows calcination of the finished sample, essential to remove organic impurities and the resin used for microtomting. The combination of SEM, XRF and SMF now offers new possibilities to study structure-reactivity-ageing relationships in FCC particles, or in complex catalyst materials in general. Correlation of these techniques with different fields of view and resolutions was achieved with sub-micron precision, showing that correlation does not require the use of integrated setups or fiducial markers.

Structural analysis using SEM is a feasible method to identify large structural features of the catalyst thin section down to 1  $\mu\text{m}$ . X-ray fluorescence gives an overview of key elements needed to assess the extent of metal deposition of aged FCC catalyst particles and can locate the rare-earth exchanged active zeolite phase. It was found that the fresh catalyst particle shows a lower than expected concentration of La, suggesting this is an anomalous particle with little active zeolite phase. This is in line with the observed SOFI intensity, which is lower in the fresh than in the ECat particle. Furthermore, SOFI intensity is low for both particles; the zeolite Y in

the FCC particle may not be efficient in producing fluorescent species under the applied reaction conditions.

Using the correlated results of the three techniques, several areas with different morphology and chemical composition were identified within the FCC catalyst particle. No correlation between the La and the SOFI intensity was found, casting serious doubt on the credibility of the SOFI results. Thus, the correlative approach between SEM, XRF and SMF shows promise in studying structure-ageing relationships in FCC catalyst thin sections, but optimization of the experimental method to study reactivity is needed. It is a positive development, however, that the anomalous behavior of a catalyst particle can be recognized more readily using such complementary correlated techniques.

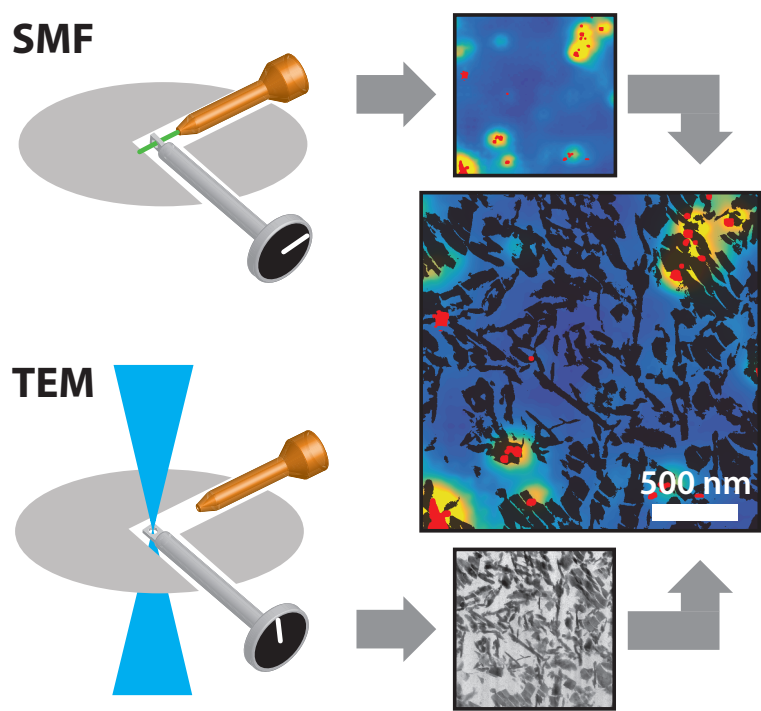
## Acknowledgments

We would like to thank Albemarle for providing the FCC particles, Hans Meeldijk (Utrecht University, UU) for preparing the sectioned catalysts, Jochem Wijten (UU) for SEM imaging and Ulrike Boesenberg (PO6) for useful discussions on XRF. Parts of this research were carried out at beamline P06 at PETRA III at DESY, a member of the Helmholtz Association (HGF).

## 6.5 References

- [1] C. Perego, R. Millini, *Chem. Soc. Rev.* **2013**, *42*, 3956–3976.
- [2] Z. Ristanović, M. M. Kerssens, A. V. Kubarev, F. C. Hendriks, P. Dedecker, J. Hofkens, M. B. J. Roeffaers, B. M. Weckhuysen, *Angew. Chem. Int. Ed.* **2015**, *54*, 1836–1840.
- [3] J. C. da Silva, K. Mader, M. Holler, D. Haberthür, A. Diaz, M. Guizar-Sicairos, W.-C. Cheng, Y. Shu, J. Raabe, A. Menzel, J. A. van Bokhoven, *ChemCatChem* **2015**, *7*, 413–416.
- [4] F. Meirer, S. Kalirai, D. Morris, S. Soparawalla, Y. Liu, G. Mesu, J. C. Andrews, B. M. Weckhuysen, *Sci. Adv.* **2015**, *1*, e1400199.
- [5] Á. Ibarra, A. Veloso, J. Bilbao, J. M. Arandes, P. Castaño, *Appl. Catal. B Environ.* **2016**, *182*, 336–346.
- [6] S. Kalirai, P. P. Paalanen, J. Wang, F. Meirer, B. M. Weckhuysen, *Angew. Chem. Int. Ed.* **2016**, *55*, 11134–11138.
- [7] H. S. Cerqueira, G. Caeiro, L. Costa, F. Ramôa Ribeiro, *J. Mol. Catal. A Chem.* **2008**, *292*, 1–13.
- [8] A. M. Wise, J. N. Weker, S. Kalirai, M. Farmand, D. A. Shapiro, F. Meirer, B. M. Weckhuysen, *ACS Catal.* **2016**, *6*, 2178–2181.
- [9] Y. Liu, F. Meirer, C. M. Krest, S. Webb, B. M. Weckhuysen, *Nat. Commun.* **2016**, *7*, 12634.
- [10] P. Dedecker, S. Duwé, R. K. Neely, J. Zhang, *J. Biomed. Opt.* **2012**, *17*, 1–5.
- [11] T. Dertinger, R. Colyer, G. Iyer, S. Weiss, J. Enderlein, *Proc. Natl. Acad. Sci.* **2009**, *106*, 22287–22292.
- [12] C. G. Schroer, P. Boye, J. M. Feldkamp, J. Patommel, D. Samberg, A. Schropp, A.

- Schwab, S. Stephan, G. Falkenberg, G. Wellenreuther, N. Reimers, *Nucl. Instr. Meth. Phys. Res. A* 2010, **616**, 93–97.
- [13] U. Boesenberg, C. G. Ryan, R. Kirkham, D. P. Siddons, M. Alfeld, J. Garrevoet, T. Núñez, T. Claussen, T. Kracht, G. Falkenberg, *J. Synchrotron Radiat.* 2016, **23**, 1550–1560.
- [14] S. Kalirai, U. Boesenberg, G. Falkenberg, F. Meirer, B. M. Weckhuysen, *ChemCatChem* 2015, **7**, 3674–3682.
- [15] C. G. Ryan, D. R. Cousens, S. H. Sie, W. L. Griffin, *Nucl. Instr. Meth. Phys. Res. B* 1990, **49**, 271–276.
- [16] S. V. Deshpande, E. Gulari, S. W. Brown, S. C. Rand, *J. Appl. Phys.* 1995, **77**, 6534–6541.
- [17] M. Wang, D. Li, Z. Yuan, D. Yang, D. Que, *Appl. Phys. Lett.* 2007, **90**, 2005–2008.
- [18] I. L. C. Buurmans, J. Ruiz-Martínez, W. V. Knowles, D. van der Beek, J. A. Bergwerff, E. T. C. Vogt, B. M. Weckhuysen, *Nat. Chem.* 2011, **3**, 862–867.
- [19] G. T. Whiting, F. Meirer, D. Valencia, M. M. Mertens, A. Bons, B. M. Weiss, P. A. Stevens, E. De Smit, B. M. Weckhuysen, *Phys. Chem. Chem. Phys.* 2014, **16**, 21531–21542.
- [20] A. Corma, H. García, *Top. Catal.* 1998, **6**, 127–140.
- [21] E. F. Sousa-Aguiar, F. E. Trigueiro, F. M. Z. Zotin, *Catal. Today* 2013, **218–219**, 115–122.
- [22] R. Carvajal, P. J. Chu, J. H. Lunsford, *J. Catal.* 1990, **125**, 123–131.
- [23] C. A. Trujillo, U. N. Uribe, P.-P. Knops-Gerrits, L. A. Oviedo A, P. A. Jacobs, *J. Catal.* 1997, **168**, 1–15.
- [24] P. O'Connor, J. P. J. Verlaan, S. J. Yanik, *Catal. Today* 1998, **43**, 305–313.
- [25] G. D. Evangelidis, E. Z. Psarakis, *Int. J. Artif. Intell. Tools* 2009, **18**, 121–139.



# Chapter 7

## Integrated Transmission Electron and Single Molecule Fluorescence Microscopy Correlates Reactivity with Ultrastructure in a Single Catalyst Particle

Establishing structure–activity relationships in complex, hierarchically structured nanomaterials, such as fluid catalytic cracking (FCC) catalysts, requires characterization with complementary, correlated analysis techniques. An integrated setup has been developed to perform transmission electron microscopy (TEM) and single molecule fluorescence (SMF) microscopy on such nanostructured samples, from which correlated structure–reactivity information was obtained on thin sections of a single FCC catalyst particle. High reactivity in a thiophene oligomerization probe reaction correlated well with TEM–derived zeolite locations, while matrix components, such as clay and amorphous binder material, were found not to display activity. Differences in fluorescence intensity were also observed within and between distinct zeolite aggregate domains, indicating that not all zeolite domains are equally active.

Based on: “Integrated Transmission Electron and Single-Molecule Fluorescence Microscopy Correlates Reactivity with Ultrastructure in a Single Catalyst Particle”, Frank C. Hendriks,<sup>1</sup> Sajjad Mohammadian,<sup>1</sup> Zoran Ristanović, Sam Kalirai, Florian Meirer, Eelco T. C. Vogt, Pieter C. A. Bruijnincx, Hans C. Gerritsen and Bert M. Weckhuysen, *Angewandte Chemie International Edition*, 2017, DOI: 10.1002/anie.201709723.

<sup>1</sup> Both authors contributed equally to this manuscript.

## 7.1 Introduction

The fluid catalytic cracking (FCC) catalyst is a typical example of a complex, hierarchically structured nanomaterial, consisting of a mixture of zeolite, clay, alumina and other binder materials, which differ in their chemical (e.g., acidity) and structural properties (e.g., porosity).<sup>[1,2]</sup> High-resolution micro-spectroscopy methods have been developed to study structure and activity<sup>[3,4]</sup> as well as deactivation<sup>[5–7]</sup> of such industrially relevant catalyst particles, providing insight into intra- and interparticle heterogeneities. For example, the ratio of tetrahedral versus octahedral Al in the active zeolite components of FCC catalyst particles was found to vary, suggesting a heterogeneity in Brønsted acidity within such individual catalyst particles.<sup>[8]</sup> Furthermore, deactivation mechanisms, such as dealumination and lattice destruction of the zeolite phase by steaming<sup>[8–10]</sup> and pore blockage by metal deposition<sup>[4,7,11]</sup>, occur simultaneously, bringing about structural as well as chemical changes within the catalyst material during operation. Given the complexity of both the material and its deactivation mechanisms, FCC particle studies, or in general any complex functional material, require a combination of techniques, preferably correlated, to provide a thorough understanding of structure–performance relations. Additionally, these correlated techniques should both have high resolution, as any heterogeneities are structured at the nanoscale in the material. Such knowledge can then ultimately serve to guide rational design of solid catalysts.

In Chapter 6, scanning electron microscopy (SEM), to study structure; single molecule fluorescence (SMF) microscopy, to study reactivity; and X-ray fluorescence microscopy, to study elemental composition were applied FCC catalyst particle thin sections. The maps and images obtained from these techniques showed differences in resolution, tilt and field of view, and were subsequently overlaid using an algorithm. The resulting overlay was sufficient for the level of detail provided by these techniques, but obtaining an overlay of higher precision would have been very challenging. Integration of different techniques in one instrument can facilitate this. The combination of fluorescence and electron microscopy is a well-known example; originally pioneered in the life sciences,<sup>[12]</sup> this technique has recently also made its way into materials science.<sup>[13,14]</sup> Indeed, fluorescence microscopy (FM) is an effective tool to study reactivity and diffusion in catalytic materials,<sup>[15–18]</sup> while electron microscopy (EM) can visualize the different ultrastructures present. For example, confocal FM of whole FCC catalyst particles after Brønsted acid sites staining by styrene or thiophene oligomerization<sup>[19,20]</sup> has been combined Transmission Electron Microscopy (TEM) to correlate structure degradation with reactivity loss.<sup>[13,14]</sup> Excitingly, FM has now improved beyond the traditionally diffraction-limited resolution of light microscopy, bringing sensitivity and resolution to the level of individual molecules.<sup>[21,22]</sup> SMF microscopy has indeed been used to study catalytic turnover on individual active sites of catalyst particles.<sup>[3,23]</sup> Very recently, SMF was combined with scanning electron microscopy (SEM) to study photocatalysis over ZnO crystals, photoluminescence of perovskite nanorods and the acidity of mordenite crystals.<sup>[24–26]</sup>

In this Chapter, we for the first time demonstrate such a correlative SMF-TEM analysis to identify and correlate reactivity and ultrastructure within an individual

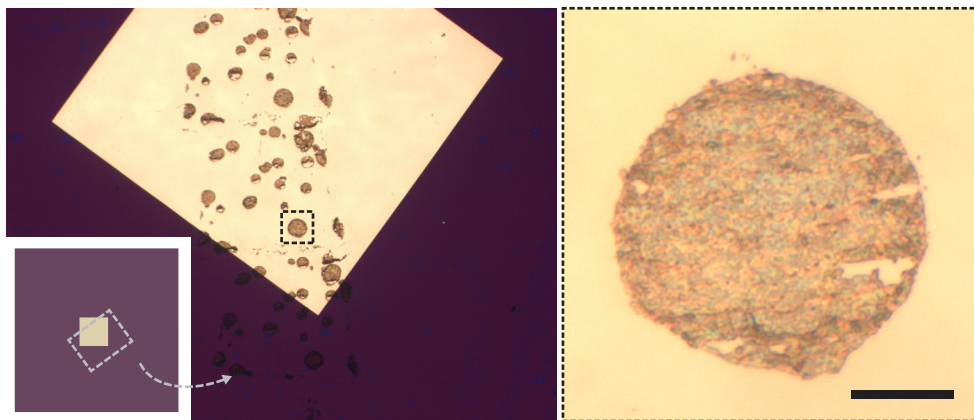


Figure 7.1. The silicon nitride (SiN) membrane used as sample support, after deposition of the thin section and subsequent calcination at 873 K. A silicon nitride membrane of  $3 \times 3 \text{ mm}^2$  was used, with a membrane of  $0.5 \times 0.5 \text{ mm}^2$ . The scale bar is  $20 \mu\text{m}$ .

ZSM-5-containing FCC particle. An integrated setup, with a FM module built into a TEM machine, allowed both techniques to be applied in a single experiment on one and the same sample.

## 7.2 Experimental

### 7.2.1 Materials

Fresh fluid catalytic cracking (FCC) particles, containing zeolite ZSM-5 as the active phase, were supplied by Albemarle. Thiophene (99%) was purchased from Aldrich and used as received. Silicon nitride membranes were purchased from Silson Ltd. and had the following specifications: frame size  $3 \times 3 \text{ mm}^2$ , membrane size  $0.5 \times 0.5 \text{ mm}^2$ , frame thickness  $200 \mu\text{m}$ , membrane thickness  $50 \text{ nm}$ .

### 7.2.2 Sample Preparation

The FCC catalyst samples were first calcined in a static oven at 823 K (ramp  $1 \text{ K min}^{-1}$ ) for 48 h. Subsequently, the catalyst particles were embedded in Epofix, a two-component epoxy resin by mixing the resin and the hardener in a weight ratio of 25:3 and adding this mixture to  $<0.1 \text{ mg}$  of catalyst powder at 294 K and atmospheric conditions in a small polyethylene vial. The samples were cured overnight at 333 K. Sectioning was performed using a Reichert-Jung Ultracut E microtome and a diamond knife (Diatome Ultra 35°, 4 mm size) under a 6° clearance angle with a cutting speed of  $2 \text{ mm s}^{-1}$ . Using a droplet of milliQ water, the sections were then placed on a silicon nitride (SiN) membrane (Figure 7.1). The SiN membrane

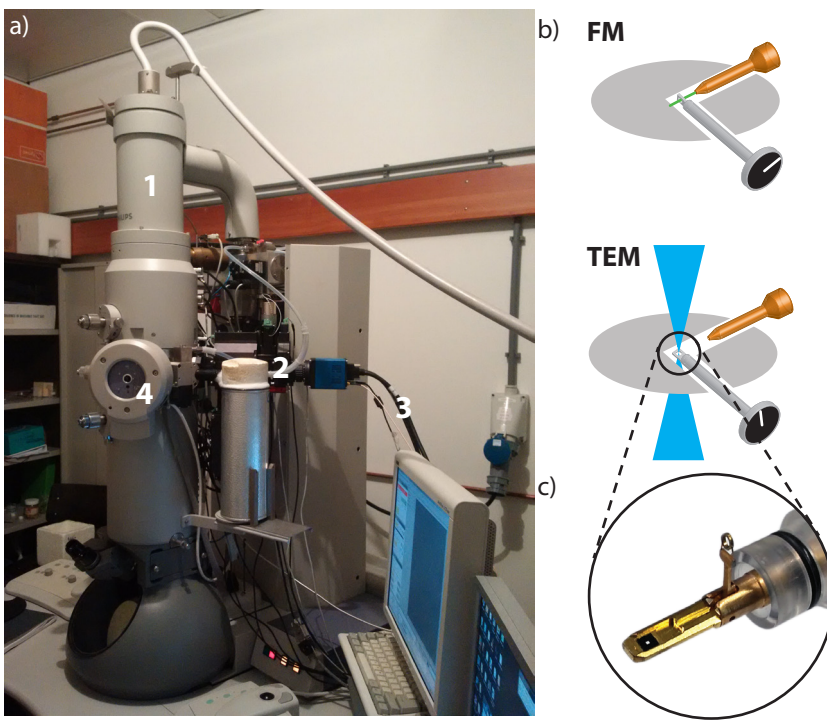


Figure 7.2. Overview of the integrated SMF-TEM setup enabling to measure single molecule fluorescence (SMF) microscopy and transmission electron microscopy (TEM). a) A photo of the set-up showing the TEM column (1), the fluorescence detector (2), the fiber-optic cable through which laser light is transmitted (3) and the sample port (4). b) The sample can be rotated inside the setup to accommodate the two techniques. For fluorescence microscopy measurements, the sample is vertical; for TEM measurements, it is horizontal. c) A close-up of the standard TEM sample holder in which the silicon nitride membrane is placed.

containing the FCC particles was calcined in a static oven at 873 K (ramp 1 K min<sup>-1</sup>) for 48 h to remove the epoxy resin, which is fluorescent, and any organic impurities. The addition of thiophene for the fluorogenic probe reaction was performed immediately prior to the experiment; 10 µL of pure thiophene was placed on top of the membrane containing the particles and allowed to dry for 5 min after which the SiN membrane was placed in the vacuum chamber of the integrated setup. Both the staining reaction and the integrated SMF-TEM experiment were carried out at 294 K.

### 7.2.3 Methods

Prior to depositing the FCC thin sections, the SiN membranes were coated with a titanium oxide ( $TiO_2$ ) layer using atomic layer deposition (ALD). Plasma-assisted ALD was carried out on a Flexal 2 (Oxford Instruments) with a separate load lock accessory. A cyclic deposition process was used with titanium isopropoxide and

water as reactants, resulting in a 5 nm layer of  $\text{TiO}_2$  on the complete surface of the SiN membrane (i.e. on the top and bottom).

Both transmission electron microscopy (TEM) and single molecule fluorescence (SMF) microscopy were carried out in a customized iCorr setup (FEI). This setup is modeled after the integrated setup used in the work by Karreman et al., however, instead of a confocal fluorescence microscope, a wide-field fluorescence microscope is now used to enable SMF microscopy capabilities.<sup>[13,14]</sup> A photograph of the setup is shown in Figure 7.2. The schematic in this figure shows that the sample, held in a (standard) TEM holder, can be rotated 90° to enable both the TEM and SMF measurements.

Fluorescence microscopy images were recorded using an epifluorescence wide-field microscope with a 25× air objective ( $\text{NA} = 0.55$ ). The sample was illuminated with a Cobolt 532 nm laser providing  $3.5 \text{ kW cm}^{-2}$  to the sample. The emitted fluorescence was passed through a dichroic mirror and an ET585/65 band pass filter (Chroma Technology Corporation) and recorded using a PCO 4.2 Edge (PCO-Tech) sCMOS camera. This field of view was cropped to  $107 \times 107 \mu\text{m}^2$  ( $400 \times 400$  pixels) with a pixel size of  $268 \times 268 \text{ nm}^2$ . The exposure time was experimentally determined to be optimal at 300 ms. TEM measurements were performed on a Tecnai 12 TEM (FEI) instrument. An 80 kV acceleration voltage was applied and images were taken using a 2K x 2K TEMCAM F214 (TVIPS).

#### 7.2.4 Image analysis

Single molecule fluorescence microscopy analysis was carried out using the Localizer plugin of Igor Pro,<sup>[27]</sup> using the “SmoothSigma” segmentation algorithm and Gaussian fitting to localize single molecule events. Particles were found using 8-way adjacency; the standard deviation of the point spread function was 1 pixel.

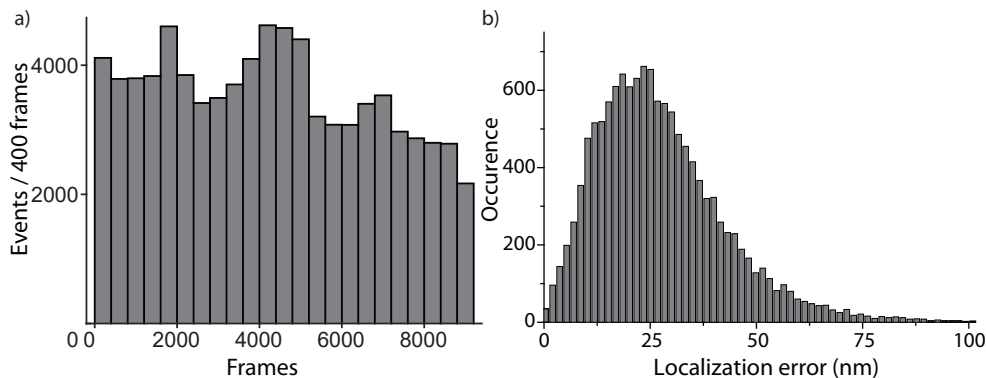


Figure 7.3. a) A histogram of the number of detected single molecule events over time. Each bar represents the sum of events detected in a subset of 400 frames. b) The localization error of detected single molecule events as calculated by the Localizer software, estimated by comparing localized emitters appearing in consecutive frames.

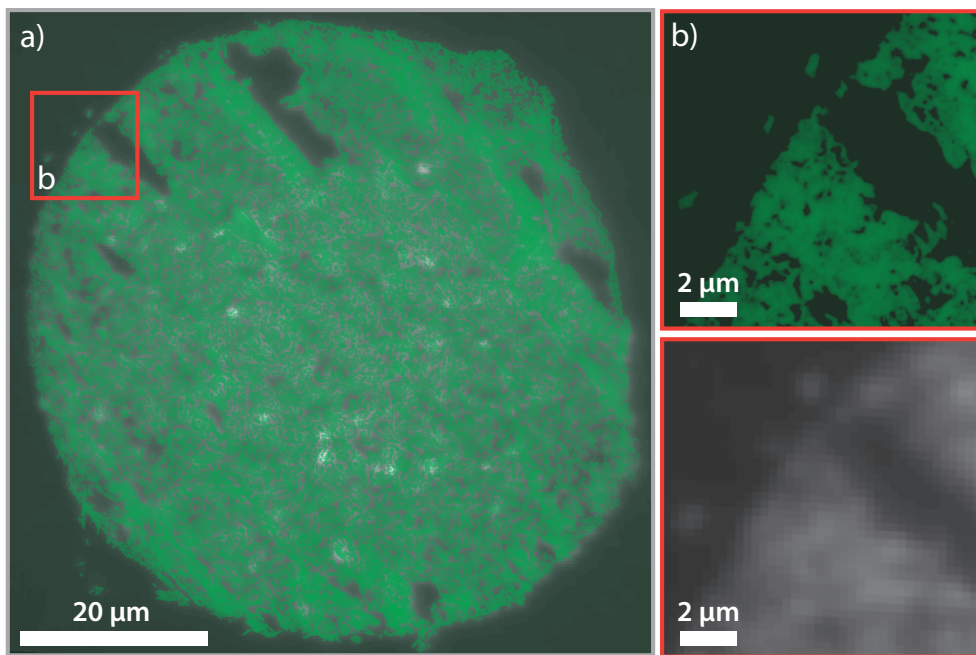


Figure 7.4. Details of the overlay of SMF and TEM. The TEM structure is shown in green for clarity; the average fluorescence is shown in gray scale. a) This image provides an overview of the overlay. b) This image shows an example of the visual marker at the edge of the thin section used to fine-tune the overlay, showing TEM (top) and average fluorescence image (bottom).

A “SmoothSigma” factor of 4.5 was experimentally determined to be optimal for detecting events, based on visual inspection of localized events in selected frames at different times in the movie. The localization error was calculated from the location of recurring events, and was estimated by Localizer to be 25 nm (Figure 7.3b). Drift correction was performed based on the localized events, using 82 sub-images with a pixel size 4× the original. This drift correction was then applied to each individual fluorescence microscopy image in order to apply this correction to both the average image and the SOFI analysis. A second order SOFI analysis was subsequently carried out at “maximum” quality; frames with saturated pixels (spikes) were removed from SOFI analysis.

The classification of structural features observed in TEM was done manually. A region of interest within the catalyst particle thin section of  $20 \times 20 \mu\text{m}^2$  was first divided into 1600 ( $40 \times 40$ ) segments of  $0.5 \times 0.5 \mu\text{m}^2$  each, with the size of these segments based on the size of the structural features observed as well as the feasibility of manual classification. Each segment was then classified as either zeolite material, matrix material or no material present. The classification was made solely based on structure, i.e. without taking into account the SOFI intensity of the areas. The SOFI intensity within each square was then summed and analyzed separately for each structure type.

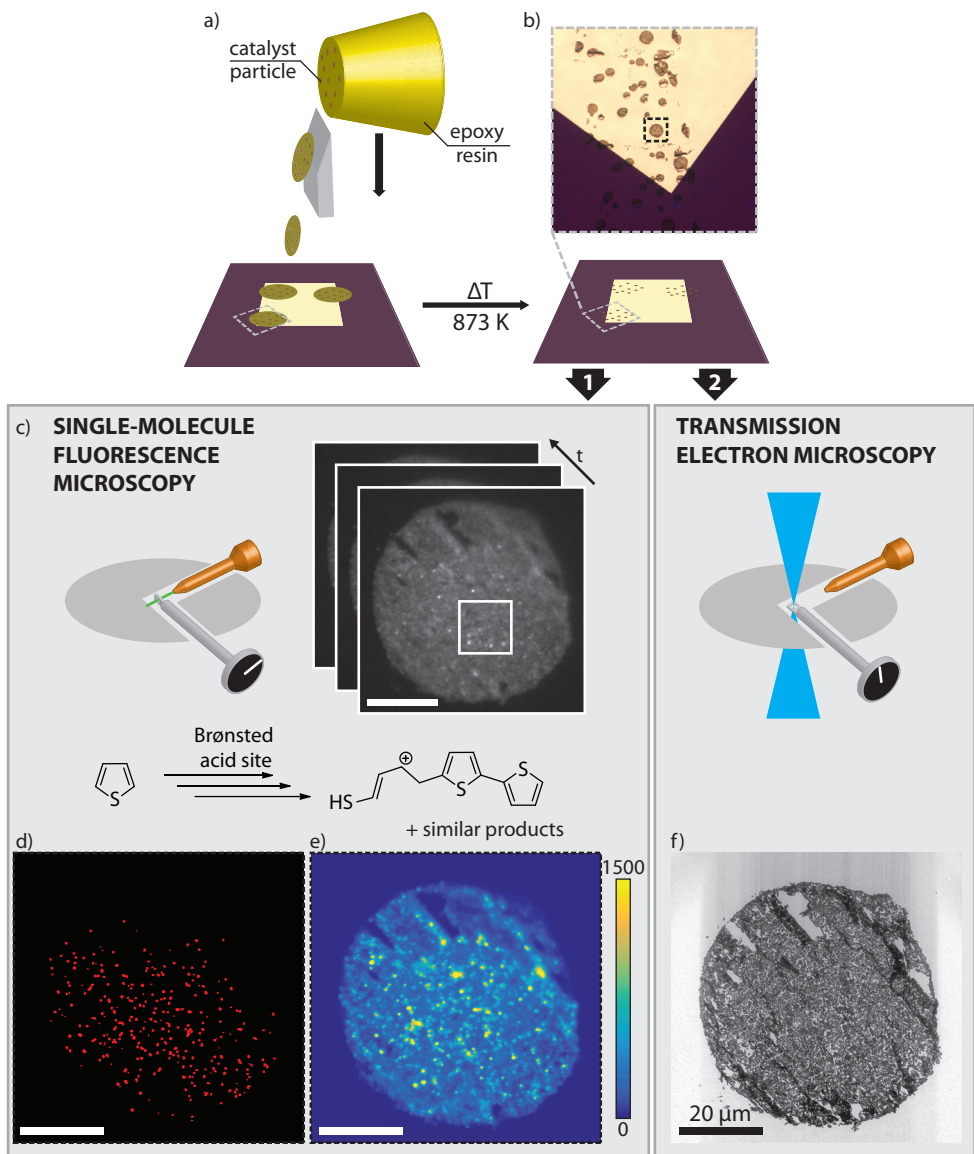


Figure 7.5. Integrated single molecule fluorescence (SMF) microscopy and transmission electron microscopy (TEM) of a single catalyst particle. a) Fluid catalytic cracking (FCC) particles embedded in epoxy resin (yellow) are microtomed into thin sections and deposited onto a SiN membrane. b) Calcination of the SiN membrane removes the resin and leaves just the catalyst thin sections. c) Sample reactivity is evaluated using SMF using the thiophene oligomerization as probe reaction; a movie with 9200 frames is recorded, showing the emitted fluorescence as bright, diffraction-limited spots. The movie is analyzed by NASCA (d) and SOFI (e). d) Map of detected single molecule events by NASCA. For clarity, the detected events have been enlarged. Fewer events are observed in the top right area because it is slightly out of focus. e) Map of the SOFI intensity. f) TEM image of the thin section. The scale bars represent  $20\text{ }\mu\text{m}$ .

Alignment of the results for both techniques was carried out using the cross-correlation algorithm “imregform” (multimodal method) in MATLAB (Figure 7.3). The overlay was then refined, based on structural features visible in both TEM and SMF: e.g., the area in Figure 7.3b. It must be noted here that in this type of correlated experiments, it is highly desirable to use fiducial markers (i.e. markers that are visible in both fluorescence microscopy and TEM) to fully automate the overlaying procedure and overlay with high accuracy. However, fiducial markers were not used in these experiments.

### 7.3 Results and discussion

An integrated setup, with a FM module built into a TEM machine, allowed both techniques to be applied in a single experiment on one and the same sample (Figure 7.2). An overview of the developed approach is shown in Figure 7.5. As TEM measurements demand a very thin sample on an electron-transparent substrate and SMF requires an extremely low fluorescent background, a fresh FCC catalyst particle was microtomed into 100 nm thin sections after being embedded in an epoxy resin matching the hardness of the catalyst particles (Figure 7.5a). The thin sections were placed on heat-resistant silicon nitride (SiN) membranes coated with  $\text{TiO}_2$  to prevent any interaction of the catalyst with the SiN membrane. Calcination at high temperature removed the resin and any organic impurities, leaving just the catalyst thin sections on the coated SiN (Figure 7.5b). The TEM image of the thin section shows the catalyst to be in good shape after this procedure, even though few cutting artifacts perpendicular to the cutting direction (from top right to bottom left) do exist (Figure 7.5f).

Thiophene oligomerization was used as a sensitive single molecule probe reaction, generating fluorescent species that allow the active acid sites in the catalyst thin section to be visualized (Figure 7.5c).<sup>[19,28]</sup> Both SMF and TEM measurements were carried out in the vacuum chamber of the integrated setup; to this end, thiophene was deposited directly onto the sample prior to the insertion. A 46 min long movie was recorded (Figure 7.5c) and fluorescence can be observed as bright, high-intensity events for the full duration of the experiment. The average number of events per frame is approximately 10 in the beginning, after which there is a gradual decrease to 5–6 events per frame. This still significant number of events shows that over the course of the experiment, enough reactants are available for the fluorogenic probe reaction, even though the experiment is carried out in a vacuum chamber (Figure 7.3a). This suggests that adsorption of reactants and subsequent product formation, most probably in the micropores of zeolite ZSM-5, was sufficient to observe catalytic events, even under the high vacuum conditions. Notably, a 532 nm laser was used as it most effectively excites higher, less volatile oligomer products, i.e. mostly trimeric species or larger.<sup>[29]</sup> Thus, a pool of dimerized and adsorbed thiophene species may form, which further oligomerize to species that can be excited by the laser.

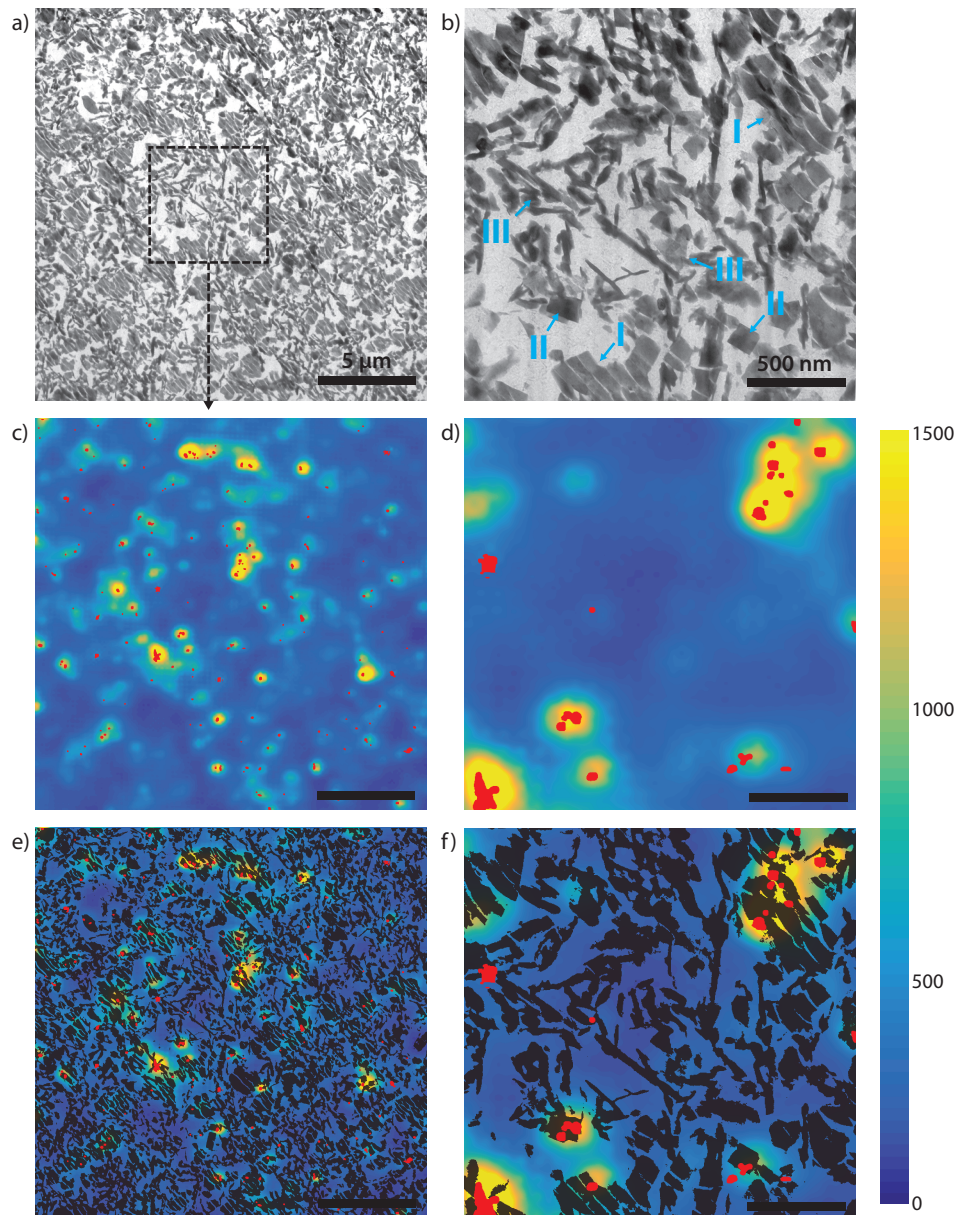
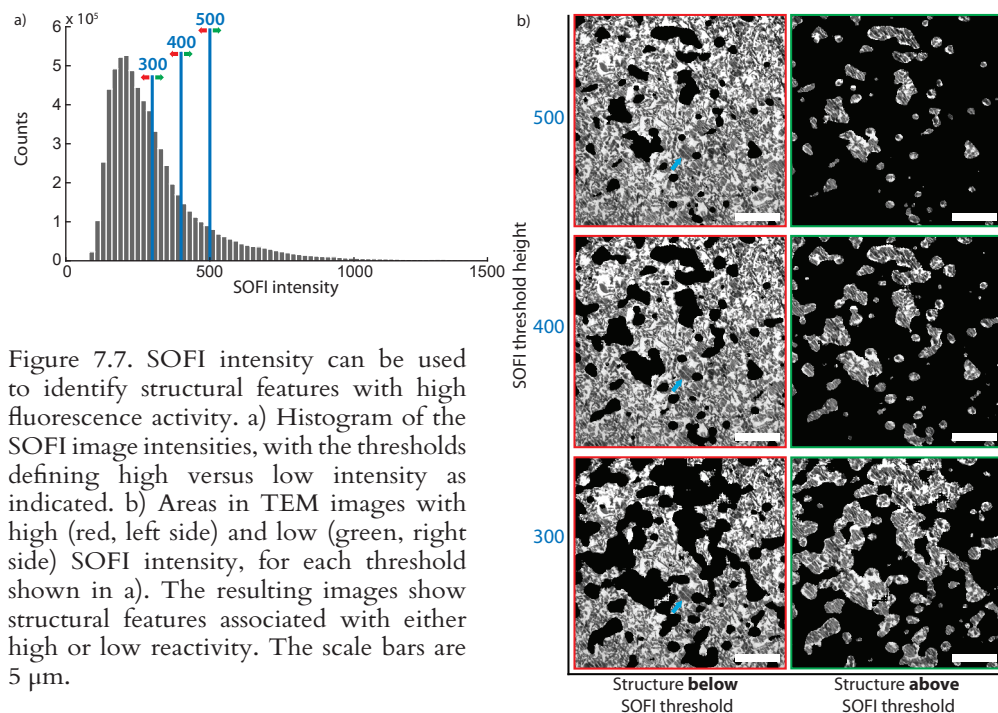


Figure 7.6. Analysis of SMF and TEM and overlays of an intermediate zoom level (a, c, e, all showing the same area) and high zoom level (b, d, f, all showing the same area) of the thin section. The intermediate zoom level is marked by a white square in Figure 7.5c. The high zoom level area is marked in a. a, b) TEM of the catalyst thin section. In b), different types of ultrastructure are marked: fragmented zeolites (I); intact zeolite crystals (II); non-zeolitic matrix material (III). c,d) Combined maps of NASCA and SOFI intensity (NASCA events in red and SOFI intensity corresponding to the scale bar). e,f) thresholded TEM images (a and b), showing the structure, overlaid on the NASCA/SOFI images from c) and d). Scale bars represent 5  $\mu\text{m}$  (a, c, e) or 500 nm (b, d, f).

Fluorescence intensity was evaluated using two complementary super-resolution techniques: Nanometer Accuracy by Stochastic Chemical reactions (NASCA)<sup>[27,30]</sup> and Super-resolution Optical Fluctuation Imaging (SOFI).<sup>[31]</sup> Both techniques rely on stochastic and reversible fluorescent fluctuations, here caused by excitation and immediate photobleaching of fluorescent molecules being continuously formed on the Brønsted acid sites in the FCC particle.<sup>[3]</sup> NASCA detects high intensity, single catalytic turnovers, such as seen in Figure 7.5c, locating these events by fitting a 2D Gaussian to the fluorescence intensity to give a resolution of 25 nm (Figure 7.3b). NASCA analysis requires a high signal-to-noise ratio (SNR), as well as a sufficiently long experiment duration, so that enough single catalytic turnovers are recorded. A map of all the events detected by NASCA is shown in Figure 7.5d. Conversely, SOFI analyzes temporal fluctuations in fluorescence in each pixel separately using higher-order statistics. This way, SOFI analysis can increase the resolution, while simultaneously eliminating (non-fluctuating) background fluorescence. Indeed, the ample background fluorescence (see e.g. the wide-field movie frames in Figure 7.5c, showing a low, static fluorescence signal over the complete thin section) observed in the movie is effectively suppressed by SOFI. The resulting SOFI intensity image for the complete thin section is shown in Figure 7.5e. To correlate reactivity with (ultra)structure, the NASCA, SOFI and TEM results were overlaid based on features visible in both FM and TEM, using a combination of automatic and manual correlation (Figure 7.4).

Secondly, catalyst structure was studied at high resolution using TEM (Figure 7.6a and 2b). TEM images at intermediate and high magnification show the structural features of the FCC catalyst. Zeolite crystals fragmented by the cutting procedure (I), relatively intact zeolite crystals (II) and non-zeolitic matrix elements (III) are highlighted in Figure 7.6b, in line with previous studies.<sup>[13,14,32,33]</sup> The clay, silica and alumina matrix elements could not be separately identified. Next, these zoomed-in TEM images were compared to co-localized fluorescence intensity events. A combination of NASCA events and SOFI intensity at the same locations as the intermediate and high magnification TEM images (Figure 7.6a and 7.6b) is shown in Figure 7.6c and 7.6d. Both NASCA and SOFI images show highly localized regions of fluorescence. Furthermore, the overlay of NASCA events and SOFI intensity shows that the two fluorescence analysis methods are highly correlated. A few areas with many NASCA events show no SOFI intensity; these areas show no fluctuation in fluorescence, and are therefore most likely caused by a contamination rather than the thiophene oligomerization reaction. SOFI does not show these areas, because they do not fluctuate. An example of this behavior can be observed in Figure 7.6d, in the middle-left of the image. The combination of NASCA and SOFI allows detection of these species and therefore shows the value of employing both types of analysis.<sup>[3]</sup> Conversely, areas are found with only SOFI intensity and no NASCA events. The intrinsic requirements needed by the NASCA method to successfully localize events (i.e., a high SNR ratio), cause only highly active regions to be detected using NASCA. The obtained SOFI intensity maps show more subtle differences in reactivity, albeit with a lower spatial resolution than NASCA. In fact, SOFI results show that an absence of detected fluorescence by NASCA does not



necessarily mean there is no activity in a region.

The power of the TEM-SMF approach is demonstrated by a combination of the NASCA, SOFI and TEM results (Figure 7.6e and 7.6f). The TEM images are thresholded and overlaid on the SOFI images, with NASCA on top of both of these images. Areas with high NASCA and SOFI intensity clearly coincide with the areas in TEM containing structural features I and II. This correlation of fluorescence activity with the active phase of the catalyst validates both our staining procedure as well as the image correlation. However, the correlation of NASCA and SOFI with TEM also shows that certain zeolite domains do not seem to show any activity, even though the underlying TEM structures look similar to domains that do show intensity. For NASCA it can be argued only the most active zeolite domains show single catalytic turnovers. However, SOFI should be sensitive even to low amounts of fluorescence. Thus, the correlative analysis of NASCA, SOFI and TEM indicates that intrinsic differences in reactivity exist among zeolite aggregates of seemingly identical structure. Additionally, Figure 7.6f shows differences in reactivity even within one zeolite domain. These differences in reactivity have been observed before in similar fluorescence staining experiments of FCC particles, but the unique correlative approach presented here allows us now to unambiguously link reactivity to ultrastructure.<sup>[3,19]</sup> The differences seen in reactivity may be explained by differences in the distribution of Al coordination in the zeolite particles, which has been shown to vary within ZSM-5 particles<sup>[34]</sup> as well as in zeolite Y embedded in FCC catalysts.<sup>[8]</sup> Furthermore, previous research has shown polarization

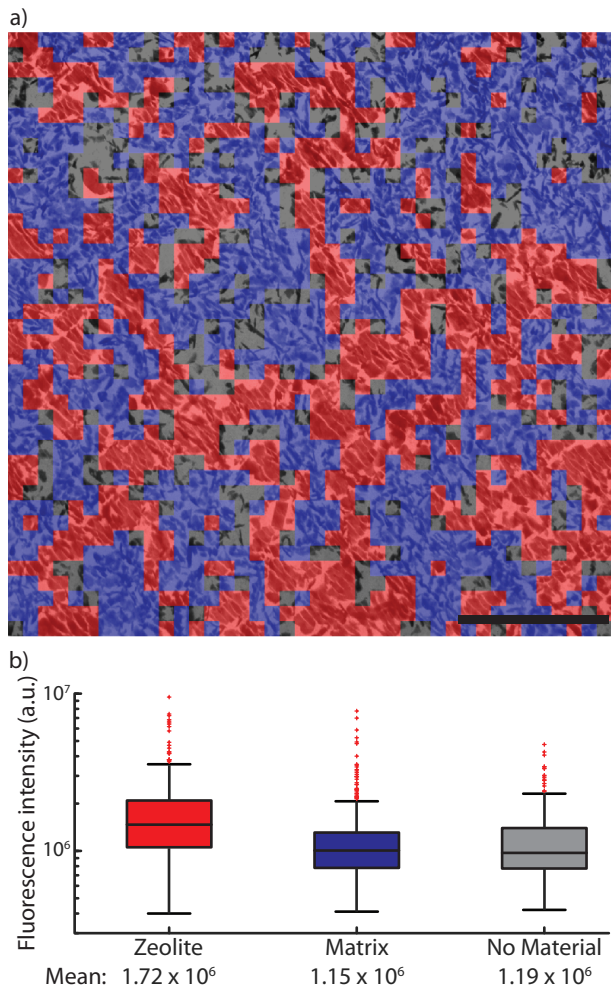


Figure 7.8. a) A zoomed-in area of the TEM image (same image as Figure 7.6a), with each structural element classified as either zeolite (604 squares, 38%), matrix (739 squares, 46%) or with no material present (260 squares, 16%). Each square represents an area of  $0.5 \times 0.5 \mu\text{m}^2$ ; the scale bar represents 5  $\mu\text{m}$ . b) Box plots of the SOFI intensity in the areas of each type of material classified. The whiskers represent the data within  $2.7\sigma$ ; other points are considered outliers (red squares), but are still used to calculate the mean.

right set of images (boxed green) shows features corresponding to high reactivity in the thiophene oligomerization reaction. Structures identified as zeolite crystals are mostly visible in the right set of images. Upon increase of the threshold, the remaining areas in the image are seen to be ‘closing-in’ on these zeolite

dependence of the fluorescent products can also play a role in ZSM-5 containing FCC particles, although this does not play a role in reactivity differences within one zeolite domain.<sup>[35]</sup> Differences in accessibility between these zeolite components can be excluded, as the thiophene reaction is carried out after microtomizing, eliminating accessibility gradients within the catalyst particle.

The correlation between SOFI intensity and structural features was explored using a threshold to segment the TEM images based on the corresponding SOFI intensity. Although the SOFI method is able to remove most of the background, because it is not fluctuating, low levels of background fluorescence remain. Therefore, the efficiency of removing this background by thresholding the TEM image at different intensity levels were assessed. Figure 7.9a shows the histogram of SOFI intensity with the chosen thresholds. The SOFI image above and below this threshold was then used as a mask for the TEM image. The left set of images (boxed red) in Figure 7.9b shows structural features corresponding to low reactivity, while the

ultrastructures. Additionally, apparently unreactive zeolite ultrastructures can be identified in the left set of images (indicated with a blue arrow in Figure 7.9b). The thresholding approach shows the correlation between certain structural features and fluorescence intensity, and therefore provides a facile, qualitative method to probe structure–activity relationships.

To study the correlation between SOFI intensity and TEM in a quantitative way, a classification of the structural features visible in the TEM image was carried out. To this end, a region of interest (ROI) within a catalyst thin section of  $20 \times 20 \mu\text{m}^2$  was divided into section of  $0.5 \times 0.5 \mu\text{m}^2$  (Figure 7.8a). The dominant structural feature of each square was then manually classified into zeolite material (type I and II in Figure 7.6b) and non-zeolitic matrix material (type III in Figure 7.6b). It must be emphasized here that this classification was made based solely on structural information in the TEM, i.e. not on the corresponding SOFI intensity of these squares. The zeolite material was found to be homogeneously distributed in this ROI, covering 38% of the surface of the thin section. A further 46% was covered by matrix material, while 16% contained no material. Consequently, the SOFI intensity of each of these types was evaluated as a measure of reactivity (Figure 7.8b). A significantly higher reactivity was found for the zeolite compared to the matrix material, showing that the probe reaction used most effectively stains zeolite material with strong Brønsted acid sites within the catalyst. Furthermore, the majority of matrix material showed similar reactivity to areas with no material present, suggesting this is mostly background fluorescence. The observed heterogeneity in fluorescence intensity for each type is partly caused by the resolution of the classification map, as the squares in Figure 7.8a can contain more than 1 type of material. However, as observed in Figure 7.6, the observed heterogeneity in fluorescence intensity for zeolite material again shows differences in activity for zeolite particles with identical structural features.

## 7.4 Conclusions

In conclusion, a generally applicable, correlated micro-spectroscopy approach with nanoscale spatial resolution is presented, which combines transmission electron microscopy (TEM) and single molecule fluorescence (SMF) microscopy. The utility of this integrated SMF-TEM approach has been demonstrated by its application to a single fluid catalytic cracking (FCC) particle, correlating for the first time ultrastructures, such as zeolite, clay and binder with (lack of) reactivity. Clear differences in reactivity were observed between the active zeolite phase and the non-zeolitic matrix components. It is shown that among the zeolite aggregate domains with seemingly identical structural features significant differences in reactivity exist. It is our opinion that the developed SMF-TEM combination can aid in elucidating structure–performance relationships for a wide range of functional materials, such as other solid catalysts, batteries, adsorbents and fuel cells.

## Acknowledgments

Albemarle is acknowledged for providing the FCC catalyst particles, Jeroen van Gerwen (Eindhoven University of Technology) for performing ALD on the SiN membranes and Hans Meeldijk (Utrecht University) for preparing the FCC thin sections.

## 7.5 References

- [1] C. Perego, R. Millini, *Chem. Soc. Rev.* **2013**, *42*, 3956–3976.
- [2] C. Martínez, A. Corma, *Coord. Chem. Rev.* **2011**, *255*, 1558–1580.
- [3] Z. Ristanović, M. M. Kerssens, A. V. Kubarev, F. C. Hendriks, P. Dedecker, J. Hofkens, M. B. J. Roeffaers, B. M. Weckhuysen, *Angew. Chemie Int. Ed.* **2015**, *54*, 1836–1840.
- [4] J. C. da Silva, K. Mader, M. Holler, D. Haberthür, A. Diaz, M. Guizar-Sicairos, W.-C. Cheng, Y. Shu, J. Raabe, A. Menzel, J. A. van Bokhoven, *ChemCatChem* **2015**, *7*, 413–416.
- [5] F. Meirer, S. Kalirai, D. Morris, S. Soparawalla, Y. Liu, G. Mesu, J. C. Andrews, B. M. Weckhuysen, *Sci. Adv.* **2015**, *1*, e1400199.
- [6] Á. Ibarra, A. Veloso, J. Bilbao, J. M. Arandes, P. Castaño, *Appl. Catal. B Environ.* **2016**, *182*, 336–346.
- [7] Y. Liu, F. Meirer, C. M. Krest, S. Webb, B. M. Weckhuysen, *Nat. Commun.* **2016**, *7*, 12634.
- [8] S. Kalirai, P. P. Paalanen, J. Wang, F. Meirer, B. M. Weckhuysen, *Angew. Chemie Int. Ed.* **2016**, *55*, 11134–11138.
- [9] G. Agostini, C. Lamberti, L. Palin, M. Milanesio, N. Danilina, B. Xu, M. Janousch, J. A. van Bokhoven, *J. Am. Chem. Soc.* **2010**, *132*, 667–678.
- [10] A. C. Psarras, E. F. Iliopoulos, K. Kostaras, A. A. Lappas, C. Pouwels, *Microporous Mesoporous Mater.* **2009**, *120*, 141–146.
- [11] F. Meirer, D. T. Morris, S. Kalirai, Y. Liu, J. C. Andrews, B. M. Weckhuysen, *J. Am. Chem. Soc.* **2015**, *137*, 102–105.
- [12] A. V. Agronskaia, J. A. Valentijn, L. F. van Driel, C. T. W. M. Schneijdenberg, B. M. Humber, P. M. P. van Bergen en Henegouwen, A. J. Verkleij, A. J. Koster, H. C. Gerritsen, *J. Struct. Biol.* **2008**, *164*, 183–189.
- [13] M. A. Karreman, I. L. C. Buurmans, J. W. Geus, A. V. Agronskaia, J. Ruiz-Martínez, H. C. Gerritsen, B. M. Weckhuysen, *Angew. Chemie - Int. Ed.* **2012**, *51*, 1428–1431.
- [14] M. A. Karreman, I. L. C. Buurmans, A. V. Agronskaia, J. W. Geus, H. C. Gerritsen, B. M. Weckhuysen, *Chem. - A Eur. J.* **2013**, *19*, 3846–3859.
- [15] J. Michaelis, C. Bräuchle, *Chem. Soc. Rev.* **2010**, *39*, 4731–4740.

- [16] P. Chen, X. Zhou, N. M. Andoy, K.-S. Han, E. Choudhary, N. Zou, G. Chen, H. Shen, *Chem. Soc. Rev.* **2014**, *43*, 1107–17.
- [17] K. P. F. Janssen, G. De Cremer, R. K. Neely, A. V. Kubarev, J. Van Loon, J. A. Martens, D. E. De Vos, M. B. J. Roeffaers, J. Hofkens, *Chem. Soc. Rev.* **2014**, *43*, 990–1006.
- [18] K. Kitagawa, S. A. Blum, *ACS Catal.* **2017**, *7*, 3786–3791.
- [19] I. L. C. Buurmans, J. Ruiz-Martínez, W. V. Knowles, D. van der Beek, J. A. Bergwerff, E. T. C. Vogt, B. M. Weckhuysen, *Nat. Chem.* **2011**, *3*, 862–867.
- [20] I. L. C. Buurmans, J. Ruiz-Martínez, S. L. van Leeuwen, D. van der Beek, J. A. Bergwerff, W. V. Knowles, E. T. C. Vogt, B. M. Weckhuysen, *Chem. - A Eur. J.* **2012**, *18*, 1094–1101.
- [21] F. C. Hendriks, F. Meirer, A. V. Kubarev, Z. Ristanović, M. B. J. Roeffaers, E. T. C. Vogt, P. C. A. Bruijnincx, B. M. Weckhuysen, *J. Am. Chem. Soc.* **2017**, DOI: 10.1021/jacs.7b07139.
- [22] A. Zürner, J. Kirstein, M. Döblinger, C. Bräuchle, T. Bein, *Nature* **2007**, *450*, 705–708.
- [23] N. M. Andoy, X. Zhou, E. Choudhary, H. Shen, G. Liu, P. Chen, *J. Am. Chem. Soc.* **2013**, *135*, 1845–1852.
- [24] E. Debroye, J. Van Loon, X. Gu, T. Franklin, J. Hofkens, K. P. F. Janssen, M. B. J. Roeffaers, *Part. Part. Syst. Charact.* **2016**, *33*, 412–418.
- [25] H. Yuan, E. Debroye, G. Caliandro, K. P. F. Janssen, J. van Loon, C. E. A. Kirschhock, J. A. Martens, J. Hofkens, M. B. J. Roeffaers, *ACS Omega* **2016**, *1*, 148–159.
- [26] J. Van Loon, K. P. F. Janssen, T. Franklin, A. V. Kubarev, J. A. Steele, E. Debroye, E. Breynaert, J. A. Martens, M. B. J. Roeffaers, *ACS Catal.* **2017**, *7*, 5234–5242.
- [27] P. Dedecker, S. Duwé, R. K. Neely, J. Zhang, *J. Biomed. Opt.* **2012**, *17*, 1–5.
- [28] M. H. F. Kox, A. Mijovilovich, J. J. H. B. Sättler, E. Stavitski, B. M. Weckhuysen, *ChemCatChem* **2010**, *2*, 564–571.
- [29] G. T. Whiting, F. Meirer, D. Valencia, M. M. Mertens, A. Bons, B. M. Weiss, P. A. Stevens, E. De Smit, B. M. Weckhuysen, *Phys. Chem. Chem. Phys.* **2014**, *16*, 21531–21542.
- [30] M. B. J. Roeffaers, G. De Cremer, J. Libeert, R. Ameloot, P. Dedecker, A.-J. Bons, M. Bückins, J. A. Martens, B. F. Sels, D. E. de Vos, J. Hofkens, *Angew. Chemie Int. Ed.* **2009**, *48*, 9285–9289.
- [31] T. Dertinger, R. Colyer, G. Iyer, S. Weiss, J. Enderlein, *Proc. Natl. Acad. Sci.* **2009**, *106*, 22287–22292.
- [32] R. A. Beyerlein, C. Choi-feng, J. B. Hall, B. J. Huggins, G. J. Ray, *Top. Catal.* **1997**, *4*, 27–42.
- [33] C. Choifeng, J. B. Hall, B. J. Huggins, R. A. Beyerlein, *J. Catal.* **1993**, *140*, 395–405.
- [34] L. R. Aramburo, Y. Liu, T. Tyliszczak, F. M. F. De Groot, J. C. Andrews, B. M. Weckhuysen, *ChemPhysChem* **2013**, *14*, 496–499.
- [35] C. Sprung, B. M. Weckhuysen, *Chem. - A Eur. J.* **2014**, *20*, 3667–3677.



# **Chapter 8**

## **A Summary, Conclusions and Future Perspectives**

## 8.1 Summary

The main subject of this thesis is the study of the accessibility, structure and reactivity of zeolite-based catalysts. We have focused both on model zeolite crystals and real-life, fluid catalytic cracking (FCC) particles, using fluorescence microscopy as the main analytical technique. The thesis is divided into two parts.

Part 1 is focused on the development and application of a series of organic probe molecules of tunable size, and the application of this probe series to study the accessibility of zeolites and zeolite crystals. The fluorescence (micro-)spectroscopy studies are complemented with additional, advanced characterization techniques to explore and elucidate the internal zeolite crystal architecture.

In Chapter 2, a series of four fluorescent probe molecules based on the commercially available *trans*-4-(4'-(*N,N*-diethylamino)styryl)-*N*-methylpyridinium iodide (2) scaffold was designed and synthesized. The dynamic radii of these DAMPI-type probes range from 5.8 to 10.1 Å, as a result of the variation in the alkyl substituents on the amine donor group. Importantly, this synthetic handle to control the probe radius had limited effect on the electronic properties, making a direct comparison of the probes by electronic spectroscopies possible. These probe molecules allowed for the direct evaluation of the molecular accessibility into confined spaces, i.e. the micropore architecture of selected zeolite materials. Evaluation of industrially relevant powdered zeolite materials with 8- (CHA), 10- (MFI) and 12-membered ring (FAU) pores showed that steric bulk indeed influences 1) the rate of adsorption, 2) the amount of probe molecule taken up by the zeolite and 3) the interaction of the probe molecule with the zeolite material. For example, the total amount of probe taken up by the zeolite was found to correlate linearly with the pore-probe size difference. The absorption spectra of each probe molecule within the zeolites furthermore showed the DAMPI-type probes to be chemically bound to the zeolite's acid sites. Thus, the general strategy of studying size-dependent accessibility and mass transfer in microporous solids with a series of fluorescent probes of systematically tunable size was demonstrated, an approach that can be extended to other porous systems and probe series.

In Chapter 3, this series of fluorescent DAMPI-type probes of increasing molecular size was used to probe the accessibility of large zeolite model crystals. Staining of zeolite crystals with MFI topology and subsequent mapping of the resulting fluorescence using confocal fluorescence microscopy revealed intra- and inter-crystal differences in structural integrity. The large MFI crystals used consist of six subunits of which two have a crystallographic orientation that is rotated by 90°. The differently oriented subunits were often found to have structural imperfections acting as entrance routes for the probe molecules during uptake into the zeolite crystal. Exploiting the anisotropic shape and resulting electronic properties of the probes, polarization-dependent fluorescence measurements provided evidence for the probe molecule's alignment within the MFI zeolite pore system. The developed method was extended to the much less studied BEA crystals, showing that a previously observed hourglass pattern is in fact a general feature of BEA crystals

with this morphology. Furthermore, the probes provided detailed insight on pore orientation within the BEA crystal, identifying at which crystal faces straight or sinusoidal pores open to the surface. The results showed that this method can spatially resolve the architecture-dependent internal pore structure of microporous materials, which is difficult to assess using other characterization techniques such as X-ray diffraction. In analogy to the adsorption of the probe series into zeolite powders, the uptake of each probe into both types of zeolite crystals; the uptake was found to decrease significantly with increased probe diameter. Additionally, a comparison of the location of probe molecules visualized by 3D confocal fluorescence microscopy (CFM) shows that defects larger than 1 nm exist in both types of crystals, allowing the entrance of the largest probe molecule.

In Chapter 4, a combination of single crystal X-ray diffraction, high-temperature *in situ* CFM and CFM after probe molecule staining, wide-field microscopy and atomic force microscopy (AFM) was employed to unravel the internal architecture of three distinct Ferrierite (FER) zeolite crystal types. FER crystals often exist as large, plate-like single crystals, with a well-defined pore orientation. The 8- or 10-membered ring pores (MRPs) of FER run perpendicular with respect to each other and parallel to the longest dimensions of the crystal, allowing e.g. differences in diffusion between these pores size to be studied. However, the exact pore orientation, i.e. which pores open to which side of the crystal, cannot directly be derived from the shape of the crystals. While pore orientation is normally determined by single crystal X-ray diffraction techniques, several different approaches are demonstrated in this Chapter. It is shown that pyrolyzed template species, remaining in the pores after incomplete calcination of the templated zeolites, are trapped in the terraced roof of the FER crystals on the side where the 8-MRPs surface. These can be used as markers to determine the pore orientation of the crystal, as they are visible by optical microscopy. Additionally, the methyl-substituted DAMPI-analogue probe molecule 1 is shown to selectively stain the 10-MRPs' entrance, providing an additional method to reveal the exact pore orientation in FER crystals. Finally, a study into the growth mechanism of these crystals using AFM revealed that, at least at the end of the synthesis, they grow in a layer-by-layer, defect-free manner normal to the large crystal surface.

**Part 2** of this thesis concerned fluorescence microscopy studies of diffusion in and reactivity of industrially used heterogeneous zeolite-based catalysts. The accessibility, reactivity and structure of a FCC catalyst was studied at the single molecule, single catalyst particle level. Super-resolution fluorescence microscopy techniques, correlated with other microscopies, namely scanning electron microscopy (SEM), transmission electron microscopy (TEM) and X-ray (XRF) fluorescence microscopy were used.

In Chapter 5, single-molecule fluorescence (SMF) microscopy was used to study self-diffusion of a feedstock-like probe molecule with nanometer accuracy in the (macro)pores of an FCC particle. Movies of the fluorescence events, caused by these molecules emitting light, allowed the movement of individual molecules through

the pore network to be reconstructed in the center plane of an intact catalyst particle. These tracks showed the probe molecules to be mainly found in two states: most (88%) were immobile, with the molecule was most likely being physisorbed to the macropore wall or trapped in a mesopore or cavity; the rest was mobile (8%), with the molecule moving inside the macropores. The molecules were also found to switch between these two states, as hybrid tracks (showing both movement and immobility) were observed in 4% of the cases. Classification of the tracks into subsets by a machine-learning algorithm allowed each type of track to be analyzed separately. Mobile tracks had an average diffusion coefficient of  $D = 8 \times 10^{-14} \pm 1 \times 10^{-13} \text{ m}^2 \text{s}^{-1}$ , in agreement with values found for similar systems using bulk methods. The large standard deviation in the average D highlighted the large variation in the detected diffusion coefficients of the individual molecules, which is thought to be related to the large range of pore sizes found in the FCC catalyst particle. Finally, mapping of the spatial distribution of molecular tracks over a cross-section of the catalyst particle demonstrated that all types of tracks were rather homogeneously distributed over the entire particle. The developed methodology can be applied more generally to evaluate and map heterogeneities in diffusional properties within complex hierarchically porous materials.

Obtaining correlative information about structure, reactivity and ageing is important in understanding the performance of complex catalytic materials, such as FCC catalysts. In Chapter 6, we focus on the development of a multimodal, correlative approach as a tool to study such structure–performance relationships. Fresh and aged FCC particles were first embedded in an extremely hard resin, needed to preserve the structure during microtoming of the catalyst particles in 100 nm thin sections. The application of heat-resistant sample holders allowed calcination of the complete sample and removal of the resin, which otherwise emits a strong fluorescent signal. The samples thus obtained were then analyzed with three complementary analytical techniques. SEM revealed the structure of the catalyst material, which proved essential in overlaying the techniques. The reactivity of the zeolite Y-containing FCC particle was probed using the thiophene oligomerization reaction, which produces fluorescent species on Brønsted acid sites. The fluorescence was recorded as movies and analyzed using the super-resolution optical fluctuation imaging (SOFI) method. Finally, X-ray fluorescence (XRF) microscopy gave high-resolution information on the elemental composition. Alignment of the resulting images was achieved using a cross correlation algorithm, without the need for fiducial markers in the sample, and showed the feasibility of overlaying the results of multiple techniques with different resolutions and field-of-views.

Building on the multimodal approach of Chapter 6, in Chapter 7, a modified sample preparation step allowed the use of TEM rather than SEM, which could visualize the ultrastructure of the catalyst in much more detail. An integrated approach was developed that enabled TEM and SMF microscopy to be measured in one setup and on the same single catalyst particle. With this novel approach, high-resolution correlated structure–reactivity information could be obtained for a fresh FCC particle, which was first microtomed into 100 nm thin sections. The reactivity of

the zeolite phase of the ZSM-5 containing catalyst particle was probed using the thiophene oligomerization reaction, and the resulting fluorescence was recorded as movies and analyzed using two analysis techniques, namely, nanometer accuracy by stochastic chemical reactions (NASCA) and SOFI. High reactivity in the thiophene oligomerization reaction correlated with zeolite structural features observed using TEM, while matrix components, such as clay and amorphous binder material, were not associated with reactivity. Differences in reactivity were also observed between zeolite aggregate domains with identical structural features, indicating that not all zeolite domains are equally reactive. The developed approach can be widely applied to study structure-activity relationships in hierarchically structured nanomaterials, including but not limited to solid catalysts.

## 8.2 Concluding remarks and future perspectives

An important component of the research described in this PhD thesis has been the development and application of fluorescent probe molecules and probe reactions to study the accessibility, structure and reactivity of zeolites and zeolite-based catalyst materials. Fluorescent probe molecules offer some distinct advantages over other types of molecular probes. Most importantly, their location can be determined with high-resolution techniques such as confocal fluorescence microscopy (CFM), offering the opportunity to map the distribution, movement and/or conversion of the probe in 3D, and more recently single molecule fluorescence (SMF) microscopy, providing nanometer resolution. Such high resolution is essential for detailed understanding of the materials studied in this thesis, which often show heterogeneities at the nanoscale. Secondly, organic fluorescent probe molecules can be modified by the tools provided by synthetic organic chemistry; the resulting probes allow studying a wide range of properties of the environment in the inorganic host to be probed, such as pH, acidity or confinement.<sup>[1,2]</sup> Indeed, the UV-Vis absorption and fluorescence properties are highly sensitive to, and can be used as reporters of the molecule's local environment. Both the DAMPI-type molecules from Chapter 2-4 as well as perylene-type probe molecule in Chapter 5 offer this sensitivity, which has been exploited to determine the uptake and interaction of the probe molecules with the host materials. In addition, steric bulk can be tailored, as applied in the series of DAMPI-type molecules used in Chapter 2-4, to assess the accessibility of porous hosts, for example.

The concept of control over the molecular size of a probe molecule by changing the surrounding steric bulk, as done with the DAMPI probe series, is a powerful tool to study accessibility. After having first established with powdered samples that pore entrance size of microporous materials can indeed be probed with this series, it was applied to study accessibility of zeolite crystals, model systems that have been highly rewarding in the past in terms of insights gained in zeolite structure and accessibility. Added benefits were i) the inherent fluorescence of the probes, i.e. they require no external activation using a fluorogenic reaction, as it made the series broadly applicable to all types of zeolite crystals; ii) the absorption anisotropy

of the probe molecules, making polarization-dependent measurements possible that proved to be very valuable in the determination of pore orientation. It is perhaps most surprising that these crystals seemingly have many defects in their crystalline structure, as evidenced by 3D mapping of the probes inside the crystals with CFM. Even supposedly defect-free crystals such as the BEA crystals used in Chapter 3 showed many small defects. Furthermore, the size of these defects could be estimated by studying the accessibility using probes of different diameters; most of these defects had sizes of approximately 1 nm. The versatility of the approach can be seen in its recent extension to estimate the size of intentionally created mesopores in crystals with the chabazite (CHA) framework.<sup>[3]</sup> Possibilities for further application of this size approximation strategy include the study of specific defects, such as screw dislocations, in zeolite crystals.<sup>[4]</sup> Indeed, the ease with which DAMPI-type probes can be applied should be encouraging to researchers to use them as a standard tool for crystal analysis.

The diameter of the DAMPI series ranges from the smallest possible size (i.e. for this type of molecule) to larger than 1 nm. While this range is sufficient to study zeolites and most microporous materials, materials with larger pores may need different substituents. Bulky substituents can be introduced to the aniline and pyridinium precursors before the final, base-catalyzed synthesis of DAMPI. The size of these precursors can thus be tuned, i.e., by changing the alkyl groups on the aniline moiety or the methyl on the pyridinium moiety. The facile modular synthesis of the probe molecule opens up possibilities for further exploration of micro- and mesoporous materials, for example by substituting larger or tethered alkyl groups, or even labile groups that allow reactivity of the probe towards catalytic sites. Alternatively, the final base-catalyzed step could also be used to probe basic reactivity in solid catalytic materials, as the base-catalyzed synthesis of the probe molecule itself can act as a probe reaction. Preliminary experiments, not described in this thesis, showed that basic zeolites can catalyze DAMPI synthesis, providing a simple probe reaction with a single, highly fluorescent product, in contrast to oligomerization-type reactions used in probing acidity, which typically have many different types of products. Together with the tunable size of the reactants, the base-catalyzed synthesis leads to a compact and highly adaptable probe system. Furthermore, the strategy of step-wise variation of the size of the probe is not limited to the DAMPI-type series, but can be extended to other fluorescent probes amenable to organic modification. For example, the addition of steric bulk to reactants could be used in fluorogenic reactions, such as styrene oligomerization. Oligomerization of bulky styrenes would lead to large fluorescent products that would selectively stain Brønsted acid sites in large cavities or on the zeolite surface only.

Fluid catalytic cracking (FCC) catalysts receive considerable interest in zeolite research, both as an archetypal example of a complex and hierarchically structured catalytic material as well as an industrially very relevant catalyst material. The catalyst particles are composed of an active zeolite phase within a matrix of clay and binder materials such as silica and alumina. These materials form a hierarchically porous network that provides the reagents access to the active acid sites, and as such has a large influence on product composition and overall efficiency of conversion

of the FCC process. This pore network was explored in Chapter 5, by studying the diffusion of individual feedstock-like probe molecules inside a whole, single FCC catalyst particle. Importantly, this study shows that attenuation of fluorescence light by the catalyst particle, which has previously hampered studying reactivity in these particles at more than a few microns below the surface, can be overcome using a highly fluorescent probe molecule. The results show heterogeneous diffusion behavior at the nanoscale, thought to be caused by the large range of pore sizes within the catalyst particle. The characteristics of the pore network thus dictate molecular dynamics through the catalyst particle, emphasizing the importance of the pore network in the outcome of a catalytic process. The pressing question that then remains is to directly correlate the observed molecular dynamics to the underlying pore structure, highlighting the need for complementary correlated information on the inorganic structure. Such a correlated structure-diffusivity approach has shown its validity in the study of model porous materials, and can now be explored as a next step to study diffusion in complex catalytic materials, such as those included in this thesis.<sup>[5]</sup>

The complexity of the pore network of FCC, as studied by single molecule spectroscopy in Chapter 5, is compounded by the chemical complexity of the materials that make up the catalyst. While the zeolite phase supplies most of the Brønsted acidity, acid sites are also found on the matrix materials, which function as pre-cracking sites for molecules too large to enter the zeolite. An extra level of complexity is added by the rather harsh conditions to which the catalyst is subjected, causing profound changes in terms of structure and chemical composition. To capture the resulting, structural heterogeneities required the application of complementary and correlated analysis techniques. Chapter 6 and 7 are devoted to developing methods to perform such correlated measurements on FCC particles, e.g. to study structure-activity-ageing relationships. While the highly fluorescent probe molecule used in Chapter 5 allowed imaging of intact catalyst particles, the fluorescent products of oligomerization reactions used to study reactivity usually have a low fluorescence quantum yield, and can therefore probe just a few microns below the surface of the catalyst particle due to fluorescence attenuation.<sup>[6,7]</sup> In Chapter 6 and 7, an approach involving microtoming and subsequent calcination of the catalyst particles was developed, allowing the evaluation of reactivity by SMF of thin sections of the catalyst. These 100 nm thick slices could additionally be studied using electron microscopy to study the structure of the catalyst thin section, as well as XRF microscopy to determine the catalyst's elemental composition.

The thiophene probe reaction applied to stain the Brønsted acid sites within of an FCC catalyst thin section containing ZSM-5 worked surprisingly well under the high vacuum conditions of the integrated setup used in Chapter 7. With SMF microscopy, single molecule events were observed over the whole duration of the experiment. Subsequent analysis using NASCA demonstrated the acidity of the catalyst could be mapped with extremely high resolution (25 nm). Normally, this method relies on constant supply of reactants from a solution; evidently, reactants for the fluorogenic reaction are stored within the zeolite pores or adsorbed to the acid sites. However, the reaction did not work well on FCC containing zeolite Y under

these conditions, described in Chapter 6, which suggests this zeolite's acid sites are too weak or its pores do not retain reactants. Both SEM and TEM were applied to study the structure of the FCC catalyst thin sections. While SEM is sufficient as a technique to get the shape and overall structure of thin sections, TEM is far superior in the structural detail that can be obtained. Structural analysis using electron microscopy, however, is essential when multiple techniques are overlaid, as these techniques show the complete particle thin section, in contrast to SMF and XRF. Of course, the combination of these high-resolution techniques has one important requirement: the possibility to accurately overlay the separate images. Using an integrated setup, overlaying the images usually only needs translation, rotation and scaling, which can be done by cross correlation or even manually. However, if the sample is also tilted (such as the XRF results in Chapter 6) and sheared, overlaying with nanometer precision can quickly become very challenging. In these cases, the use of fiducial markers may be the best solution, provided they don't disturb the experiment.

Finally, the developed probe molecule approach, analysis methods and correlative technique combinations developed in this thesis have provided the fields of zeolite science and, more in general, materials science with new insights and novel tools. Fluorescence microscopy, on which most of these advances were based, is again demonstrated to be a powerful and diverse tool to study these materials, especially if it is combined with complementary structural techniques. The next step in studying catalytic solids using these techniques would have to include further integration of the techniques described in this thesis, to the point that the complete diffusion and conversion pathways of a molecule by a catalyst can be followed. This would mean that a fluorescent probe molecule's diffusion path towards the active site in a catalyst can be mapped, after which conversion at a catalytic site can be detected by a change in the fluorescent properties of the molecule. This approach would require fitting the probe molecule of Chapter 5, for example, with a labile, acid-sensitive group. The outgoing, modified molecule could then be distinguished from the molecules entering the catalyst and followed on its way out of the catalyst particle. A look at the current state of art in the field shows that these types of experiments could soon become reality.

### 8.3 References

- [1] A. Corma, H. García, *J. Chem. Soc. Dalton Trans.* **2000**, 1381–1394.
- [2] E. Reddington, A. Sapienza, B. Gurau, R. Viswanathan, S. Sarangapani, E. S. Smotkin, T. E. Mallouk, *Science* **1998**, *280*, 1735–1737.
- [3] R. Oord, I. C. ten Have, J. M. Arends, F. C. Hendriks, J. E. Schmidt, I. Lezcano-Gonzalez, B. M. Weckhuysen, *Catal. Sci. Technol.* **2017**, DOI: 10.1039/c7cy00798a.
- [4] A. M. Walker, B. Slater, J. D. Gale, K. Wright, *Nat. Mater.* **2004**, *3*, 715–720.
- [5] A. Zürner, J. Kirstein, M. Döblinger, C. Bräuchle, T. Bein, *Nature* **2007**, *450*, 705–708.
- [6] Z. Ristanović, M. M. Kerssens, A. V. Kubarev, F. C. Hendriks, P. Dedecker, J. Hofkens, M. B. Roeffaers, B. M. Weckhuysen, *Angew. Chem. Int. Ed.* **2015**, *54*, 1836–1840.

- [7] I. L. C. Buurmans, J. Ruiz-Martínez, W. V. Knowles, D. van der Beek, J. A. Bergwerff, E. T. C. Vogt, B. M. Weckhuysen, *Nat. Chem.* 2011, 3, 862–867.



# **Chapter 8**

## **B Nederlandse samenvatting**

## Dutch summary

Het hoofdonderwerp van dit proefschrift is het bestuderen van de toegankelijkheid, structuur en reactiviteit van model- en industriële katalysatoren. We hebben ons gericht op zeolietmodelsystemen en vloeibaar katalytisch kraken (fluid catalytic cracking, FCC) katalysatordeeltjes die worden gebruikt in de industrie. Deze systemen werden voornamelijk bestudeerd met fluorescentiemicroscopie. Het proefschrift is in twee delen verdeeld.

Deel 1 is gericht op de ontwikkeling en toepassing van een reeks organische probemoleculen met verschillende diameters en de toepassing van deze serie om de toegankelijkheid van zeoliëten en zeolietkristallen te onderzoeken. De fluorescentie-(micro)spectroscopische studies zijn aangevuld met complementaire, geavanceerde karakterisatietechnieken om de interne structuur van zeoliëten te bestuderen en te ontrafelen.

In Hoofdstuk 2 wordt het ontwerp en de synthese van een reeks van vier fluorescerende probemoleculen op basis van het commercieel verkrijgbare *trans*-4-(4'-(*N,N*-diethylamino)styryl)-*N*-methylpyridiniumjodide (DAMPI-2) beschreven. De diameter van deze DAMPI-type probe moleculen kan gevareerd worden van 5,8 tot 10,1 Å door verandering van de alkylsubstituenten op de aminegroep. Deze verandering heeft een beperkte invloed op de elektronische eigenschappen, wat het mogelijk maakt deze probes direct te vergelijken met elektronische spectroscopie. De toegankelijkheid van moleculen in poriën, in het bijzonder de microporiën van zeoliëten, kan zo direct bepaald worden. De industrieel relevante poedervormige zeolietmaterialen met poriën met 8- (CHA, 3.8 Å), 10- (MFI, 5.6 Å) en 12-ringen (FAU, 7.4 Å) werden onderzocht. Hieruit werd duidelijk dat de effectieve diameter invloed heeft op 1) de snelheid van de moleculaire adsorptie, 2) de totale hoeveelheid probemolecuul dat door de zeoliet wordt opgenomen en 3) de interactie van het probemolecuul met de zeoliet. Er is bijvoorbeeld een positieve lineaire correlatie tussen het grootteverschil van probe en porie versus totale opname van de probe door de zeoliet. De absorptiespectra van ieder probemolecuul binnen de zeoliet laten zien dat deze DAMPI-type probe moleculen chemisch gebonden zijn aan de Brønsted zure plaatsen van de zeoliet. Deze aanpak demonstreert een algemene strategie voor het bestuderen van de grootte-toegankelijkheidsrelaties in microporeuze vaste stoffen met een reeks fluorescerende probes met een systematisch aangepaste grootte.

In Hoofdstuk 3 wordt deze serie fluorescerende DAMPI-probemoleculen met toenemende moleculaire diameter gebruikt om de toegankelijkheid van zeolietkristallen te onderzoeken. Grote zeolietkristallen met MFI topologie werden in contact gebracht met oplossingen van deze probe moleculen, waarbij de probe moleculen achterblijven op plaatsen waar ze toegang tot hebben. Dit werd vervolgens in kaart gebracht met behulp van confocale fluorescentiemicroscopie (CFM), waarbij verschillen in structurele integriteit op intra- en inter-kristalniveau worden onthuld. De gebruikte grote MFI-kristallen bestaan niet uit één deel, maar zijn onderverdeeld in 6 in elkaar passende delen, waarvan er 2 een kristallografische oriëntatie hebben die 90° gedraaid is. In de delen met een gedraaide oriëntatie

zitten vaak structurele imperfecties, die als toegangsweg naar de binnenkant van het kristal kunnen dienen voor probe moleculen. Polarisatieafhankelijke metingen toonden aan dat de probe moleculen uitgelijnd zijn met de poriën binnen het MFI-poriesysteem. De ontwikkelde markeringsmethode werd daarna ook toegepast op kristallen met de BEA topologie, waarnaar veel minder studies gedaan zijn. Het zandloperpatroon dat hierbij geobserveerd werd in de gemarkerde kristallen was al eerder gezien in grote BEA-kristallen; het blijkt dus een algemeen kenmerk van BEA-kristallen met deze morfologie te zijn. Daarnaast kunnen de probes de porie-oriëntatie binnen het kristal identificeren en aan welke zijden van het BEA kristal rechte of sinusvormige poriën aan de oppervlakte komen. De resultaten tonen aan dat deze methode geschikt is om de interne poriestructuur van microporeuze materialen te bepalen. De techniek kan dus als aantrekkelijk alternatief voor karakteriseringstechnieken zoals röntgendiffractie gebruikt worden, aangezien deze soms in de praktijk moeilijk uit te voeren zijn. De verschillen in toegankelijkheid van DAMPI probe moleculen werd nu ook bestudeerd voor de MFI- en BEA-kristallen, in een experiment dat overeenkomt met het experiment gedaan op poeders in Hoofdstuk 2. Wederom werd aangetoond dat de hoeveelheid probe die opgenomen wordt door de zeolietkristallen afneemt, naarmate de probe groter is. Daarnaast bleek uit een vergelijking van de locatie van de opgenomen probe moleculen, gevisualiseerd met behulp van 3D CFM, dat beide typen kristallen defecten groter dan 1 nm hebben, waardoor het grootste probemolecuul het kristal kan binnendringen.

In Hoofdstuk 4 wordt een combinatie van röntgendiffractie van individuele kristallen, *in situ* CFM bij hoge temperatuur, fluorescerende probemoleculen, optische microscopie en atomaire-krachtmicroscopie (atomic force microscopy, AFM) gebruikt om de interne architectuur van drie typen Ferrieriet (FER) zeolietkristallen te ontrafelen. FER-kristallen worden vaak gesynthetiseerd als grote, plaatvormige kristallen met een goed gedefinieerde poriestructuur in 2D. Ze hebben een gekruist poriesysteem, waarbij 8-ringporiën aan de oppervlakte komen aan twee overstaande zijden, en 10-ringporiën aan de andere twee zijden. Welke poriën openen aan welke zijde wordt normaal gesproken bepaald door röntgendiffractietechnieken op individuele kristallen, maar we laten in dit Hoofdstuk zien dat het ook anders kan. Deze kristallen bevatten soms gepyroliseerde organische moleculen die gebruikt zijn als mal tijdens de kristalsynthese en achtergebleven in de poriën. Deze moleculen zitten gevangen in het bovenste deel van het kristallen aan de zijde van de 8-ringporiën. Ze kunnen als markers gebruikt worden om de oriëntatie van het porienetwerk in het kristal vast te stellen, omdat ze zichtbaar zijn met een optische microscoop. Daarnaast kan DAMPI probe-molecuul 1 de ingang van 10-ringporiën selectief markeren, en zo ook de oriëntatie van het porienetwerk onthullen. Aldus worden verschillende eenvoudige methodes voor het vaststellen van het poriesysteem gepresenteerd, waarbij röntgendiffractie-experimenten worden vermeden. Tenslotte werd met behulp van AFM vastgesteld dat, in ieder geval aan het eind van de synthese, de kristallen laag-voor-laag en vrij van defecten groeien, haaks op de twee langste zijden van het kristal.

Deel 2 van dit proefschrift betreft fluorescentiemicroscopiestudies van diffusie in en

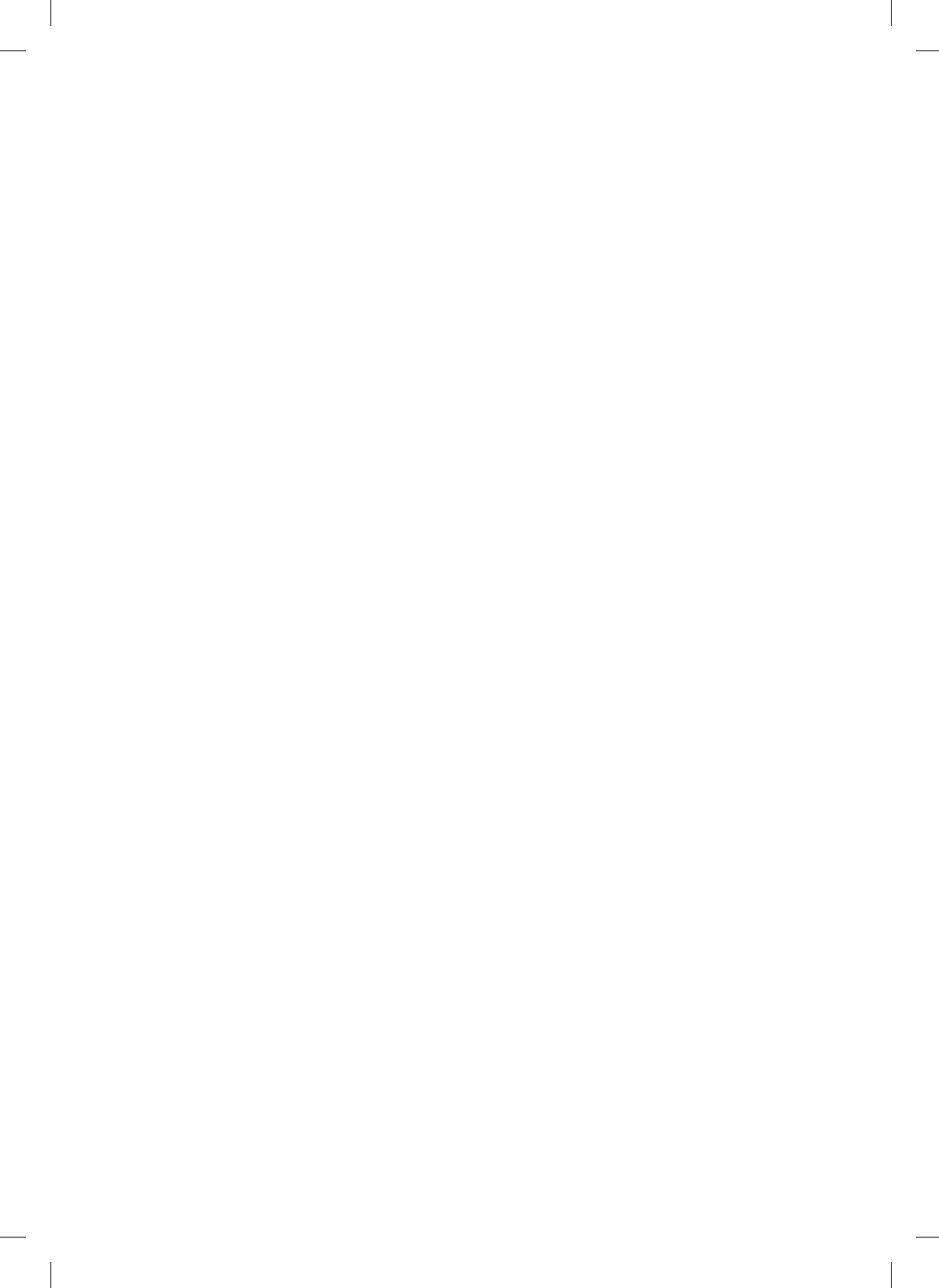
reactiviteit van industrieel gebruikte heterogene katalysatoren. De toegankelijkheid, reactiviteit en structuur van een FCC katalysator wordt onderzocht op het niveau van individuele moleculen en individuele katalysatordeeltjes. Hiervoor werden super-resolutie fluorescentiemicroscopiemethoden gebruikt, gecorreleerd met andere methoden, namelijk scannende elektronenmicroscopie (SEM), transmissie-elektronenmicroscopie (TEM) en Röntgenstraal-fluorescentiemicroscopie (X-ray fluroescence, XRF).

In Hoofdstuk 5 wordt enkel-molecuul-fluorescentiemicroscopie gebruikt om zelfdiffusie van een probemolecuul op de nanometer nauwkeurig te bestuderen in de macroporiën van een FCC deeltje. Het gebruikte probemolecuul heeft een soortgelijke samenstelling en grootte als de reactanten in de FCC-reactie. Bij deze methode worden films van individuele fluorescerende gebeurtenissen opgenomen, die te zien zijn als heldere lichtpuntjes in de film. Deze worden veroorzaakt door emissie van deze moleculen en maken het mogelijk om hun beweging door het porienetwerk te reconstrueren in een doorsnede in het midden van een heel katalysatordeeltje. De geanalyseerde routes laten zien dat de probe-moleculen hoofdzakelijk in twee staten verkeren: de meeste (88%) zijn immobiel, waarbij het molecuul waarschijnlijk aan de wand van een macroporie geadsorbeerd is, of opgesloten in een holte. De rest is mobiel (8%), waarbij het molecuul binnen de macroporiën beweegt; of hybride, waarbij een route zowel mobiliteit als stilstand laat zien (4%). De moleculen werden verdeeld in subsets door een automatisch lerend algoritme, waardoor elk type route afzonderlijk kan worden geanalyseerd. Mobiele moleculen hebben een gemiddelde diffusiecoëfficiënt van  $D = 8 \times 10^{-14} \pm 1 \times 10^{-13} \text{ m}^2 \text{ s}^{-1}$ , die overeenkomt met waarden die zijn gevonden voor soortgelijke systemen met behulp van bulkanalysemethoden. De grote standaardafwijking in D benadrukt de grote variatie van gedetecteerde diffusiecoëfficiënten en houdt waarschijnlijk verband met het grote bereik van poriegroottes die in het FCC-katalysatordeeltjes voorkomen. Tenslotte wordt de ruimtelijke verdeling van moleculaire routes in een doorsnede van het katalysatordeeltje vastgelegd; de soorten routes blijken redelijk homogeen verdeeld over het gehele deeltje. De ontwikkelde methodologie kan worden gebruikt om heterogeniteit in diffusie-eigenschappen in vaste katalysatoren, maar ook andere complexe hiërarchisch poreuze materialen te evalueren.

Het verkrijgen van gecorreleerde informatie over de structuur, reactiviteit en veroudering is belangrijk voor een goed begrip van de werking van complexe katalytische materialen, zoals FCC katalysatoren. In Hoofdstuk 6 richten we ons op het ontwikkelen van een multimodale, correlatieve aanpak als hulpmiddel om structuur-activiteitsmechanismen te bestuderen. Verse en verouderde (zogenaamde ECat) FCC katalysatordeeltjes werden eerst in een zeer harde hars gegoten, die nodig is om de structuur te behouden wanneer de deeltjes in 100 nm dunne secties gesneden worden. Hitteresistente staalhouders werden gebruikt om calcinatie van de stalen bij hoge temperatuur mogelijk te maken. De calcinatiestap is nodig om de hars te verwijderen, omdat deze anders een fluorescent achtergrondsignaal geeft. De stalen werden na deze procedure geanalyseerd met behulp van drie complementaire technieken. SEM toonde de structuur van het katalysatormateriaal,

en bleek essentieel in het overleggen van de technieken. De reactiviteit van het zeoliet Y-bevattende FCC katalysatordeeltje werd gemarkeerd met de thiofeen oligomerisatiereactie, dat fluorescente moleculen produceert op Brønsted zure plaatsen. De fluorescentie werd opgenomen als een film en vervolgens geanalyseerd met behulp van de super-resolutie optische fluctuatie beeldvorming (super-resolution optical fluctuation imaging, SOFI) methode. Als laatste werd XRF microscopie gebruikt om informatie over elementdistributie te verkrijgen met hoge resolutie. De verschillende technieken werden over elkaar gelegd met behulp van een kruis-correlatie algoritme, en de resultaten laten zien dat dit mogelijk is voor deze technieken zonder gebruik te maken van locatiemarkeringen. De resultaten laten echter zien dat er ook nadelen kleven aan het onderzoeken van enkele katalysatordeeltjes; de gecorreleerde resultaten stroken niet met de verwachtingen en eerder bevonden resultaten.

Voortbouwend op de multimodale aanpak van Hoofdstuk 6 werd in Hoofdstuk 7 een aangepaste staalpreparatie gebruikt om het mogelijk te maken de samples met TEM te meten in plaats van SEM. Dit maakte het mogelijk de ultrastructuur van de katalysatordeeltjes in meer detail weer te geven. Een geïntegreerde aanpak werd ontwikkeld, die het mogelijk maakte SMF en TEM in dezelfde meetopstelling toe te passen, en op hetzelfde katalysatordeeltje. Gecorreleerde structuur-activiteit informatie met een hoge resolutie kon verkregen worden met behulp van deze nieuwe aanpak. De reactiviteit van het ZSM-5 bevattende katalysatordeeltje werd gemarkeerd met behulp van de thiofeen oligomerisatiereactie; de resulterende fluorescentie werd opgenomen als films en geanalyseerd met behulp van twee analysetechnieken, namelijk nanometer nauwkeurigheid door stochastische chemische reacties (nanometer accuracy by stochastic chemical reactions, NASCA) en SOFI. Hoge reactiviteit in de thiofeen oligomerisatiereactie kon gecorreleerd worden met de structuur van zeolietmateriaal, in beeld gebracht met TEM. Matrix-componenten in de zeoliet, zoals klei en amorf bindermateriaal, werden niet geassocieerd met reactiviteit. Daarnaast werden zeolitedomeinen gevonden met een identieke structuur, maar met grote verschillen in reactiviteit, wat aangeeft dat niet alle zeolitedomeinen even reactief zijn. De hier ontwikkelde aanpak kan breed toepassing vinden in het bestuderen van structuur-activiteitrelaties in hiërarchisch gestructureerde nanomaterialen, inclusief maar niet gelimiteerd tot heterogene katalysatoren.



# **Back matter**

## Abbreviations

|         |   |
|---------|---|
| AFM     | atomic force microscopy                             |
| ALD     | atomic layer deposition                             |
| CFM     | confocal fluorescence microscopy                    |
| CMOS    | complementary metal oxide semiconductor             |
| DFT     | density functional theory                           |
| ECat    | equilibrium catalyst                                |
| ECC     | enhanced correlation coefficient                    |
| EM      | electron microscopy                                 |
| EM-CCD  | electron multiplying charge coupled device          |
| ESI-TOF | electron spray injection – time of flight           |
| FCC     | fluid catalytic cracking                            |
| HOMO    | highest occupied molecular orbital                  |
| IDM     | intraparticle diffusion model                       |
| LUMO    | lowest unoccupied molecular orbital                 |
| x-MRP   | x-membered ring pore                                |
| MSD     | mean square displacement                            |
| NA      | numerical aperture                                  |
| NASCA   | nanometer accuracy by stochastic chemical reactions |
| NMR     | nuclear magnetic resonance                          |
| OFM     | optical fluorescence microscopy                     |
| PFOE    | pseudo-first order equation                         |
| PPSD    | probe diameter versus pore size difference          |
| PSOE    | pseudo-second order equation                        |
| SEM     | scanning electron microscopy                        |
| SiN     | silicon nitride                                     |
| SMF     | single molecule fluorescence                        |
| SNR     | signal-to-noise ratio                               |
| SOFI    | super-resolution optical fluctuation imaging        |
| TEM     | transmission electron microscopy                    |
| TGA     | thermogravimetric analysis                          |
| TPD     | temperature programmed desorption                   |
| XRD     | X-ray diffraction                                   |
| XRF     | X-ray fluorescence                                  |

## **Zeolites**

|     |                |
|-----|----------------|
| AFI | AlPO-5         |
| BEA | beta           |
| CHA | chabazite      |
| MFI | ZSM-5          |
| FAU | zeolite Y      |
| FER | ferrierite     |
| MOR | mordenite      |
| USY | ultra-stable Y |

## **Chemical compounds**

|      |   |
|------|---|
| 1    | trans-4-(4'-(N,N-dimethylamino)styryl)-N-methylpyridinium iodide; DAMPI-1     |
| 2    | trans-4-(4'-(N,N-diethylamino)styryl)-N-methylpyridinium iodide; DAMPI-2      |
| 3    | trans-4-(4'-(N,N-diisopropylamino)styryl)-N-methylpyridinium iodide; DAMPI-3  |
| 4    | trans-4-(4'-(N,N-dicyclohexylamino)styryl)-N-methylpyridinium iodide; DAMPI-4 |
| DCM  | dichloromethane   |
| DMF  | dimethylformamide   |
| DMSO | dimethylsulfoxide   |
| PMMA | poly(methyl methacrylate)   |
| PTFE | polytetrafluoroethylene   |
| TPA  | tetrapropyl ammonium  |
| VGO  | vacuum gas oil  |

## List of publications

F. C. Hendriks, S. Mohammadian, S. Kalirai, Z. Ristanović, F. Meirer, E. T. C. Vogt, P. C. A. Bruijnincx, H. C. Gerritsen and B. M. Weckhuysen, “Integrated Transmission Electron and Super-Resolution Fluorescence Microscopy Connects Reactivity and Ultrastructure within a Single Catalyst Particle”, *Angew. Chem. Int. Ed.*, 2017, DOI: 10.1002/anie.201709723.

*Featured as a very important paper in Angewandte Chemie International Edition.*

J. E. Schmidt, F. C. Hendriks, M. Lutz, L. C. Post, D. Fu, and B. M. Weckhuysen, “Diagnosing the Internal Architecture of Zeolite Ferrierite”, *ChemPhysChem*, 2017, DOI: 10.1002/cphc.201700583.

*Featured as a very important paper in ChemPhysChem*

F. C. Hendriks, F. Meirer, A. V. Kubarev, Z. Ristanović, M. B. J. Roeffaers, P. C. A. Bruijnincx, and B. M. Weckhuysen, “Single Molecule Fluorescence Microscopy Reveals Molecular Mobility and Local Diffusion Coefficients within the Pore Network of an Individual Catalyst Particle”, *J. Am. Chem. Soc.*, 2017, 139, 13632–13635.

R. Oord, I. C. ten Have, J. M. Arends, F. C. Hendriks, J. E. Schmidt, I. Lezcano-Gonzalez and B. M. Weckhuysen, “Enhanced Activity for the Selective Catalytic Reduction of NO<sub>x</sub> by Desilicated Cu-SSZ-13, and its Comparison to Steaming”, *Catal. Sci. Tech.*, 2017, 7, 3851–3862.

F. C. Hendriks, J. E. Schmidt, J. A. Rombouts, K. Lammertsma, P. C. A. Bruijnincx, and B. M. Weckhuysen, “Probing Zeolite Crystal Architecture and Structural Imperfections Using Differently Sized Fluorescent Organic Probe Molecules”, *Chem. Eur. J.*, 2017, 23, 6305–6314.

*Featured as a hot paper and on the front cover of Chemistry: a European Journal*

F. C. Hendriks, D. Valencia, P. C. A. Bruijnincx and B. M. Weckhuysen, “Zeolite molecular accessibility and host–guest interactions studied by adsorption of organic probes of tunable size”, *Phys. Chem. Chem. Phys.*, 2017, 19, 1857–1867.

Z. Ristanović, M. M. Kerssens, A. V. Kubarev, F. C. Hendriks, P. Dedecker, J. Hofkens, M. B. J. Roeffaers, and B. M. Weckhuysen, “High-Resolution Single-Molecule Fluorescence Imaging of Zeolite Aggregates within Real-Life Fluid Catalytic Cracking Particles”, *Angew. Chem. Int. Ed.*, 2015, 54, 1836–1840.

## **Selected attended conferences**

**Europacat conference, Florence, Italy, 2017**

Oral presentation: “Single-Molecule Fluorescence Microscopy Reveals Local Diffusion Coefficients in the Pore Network of an Individual Catalyst Particle”.

**18th NCCC conference, Noordwijkerhout, The Netherlands, 2017**

Oral presentation: “Probing Structure- Activity Relationships in a Real-life Catalytic Cracking Catalyst”.

**17th NCCC conference, Noordwijkerhout, The Netherlands, 2016**

Oral presentation: “Probing the Porous Network of a Real-life FCC Catalyst Using Single Molecule Fluorescence”.

**CHAINS conference, Veldhoven, The Netherlands, 2015**

Oral presentation: “Zeolite shape selectivity studied by adsorption of differently sized fluorescent organic probes”.

**16th NCCC conference, Noordwijkerhout, The Netherlands, 2015**

Oral presentation: “Micro-spectroscopy of Zeolite Crystals: Shape Selectivity Effects”.

**2nd European Zeolite Conference, Nice, France, 2015**

Oral and poster presentation: “Nano- and Microscopy of Zeolite Crystals: Shape Selectivity Effects”.

**15th NCCC conference, Noordwijkerhout, The Netherlands, 2014**

Poster presentation: “Shape selectivity in zeolites: Accessibility of zeolite pores by fluorescent organic probes”.

**23rd North American Meeting, Louisville, KY, United States, 2013**

Oral presentation: “A Phosphine-Based Covalent Organic Framework for the Pd-Catalyzed Telomerization of 1,3-Butadiene”.

## Acknowledgments

*“But we are strong, each in our purpose, and we are all more strong together.”*

- Bram Stoker

What a ride! It's been a great five years, and I've met some wonderful people on the way, without whom I could not imagine how my PhD would have looked like. I will take the time to thank them here and apologize if I have forgotten someone in the text below.

Ten eerste, **Bert**, je hebt mij uitgedaagd om meer uit mezelf te halen dan ik voor mogelijk hield, en daarin ben je zeker geslaagd. Bedankt ook voor je vertrouwen in mij. Met je blik op het grotere plaatje heb je op de goede momenten bijgestuurd en me bovendien geïntroduceerd met een breed scala aan geavanceerde meetmethoden, die bijgedragen hebben dit proefschrift te maken tot wat het is. Je hebt me op cruciale momenten advies gegeven, maar me ook de ruimte gegeven fouten te maken en daarvan te leren. Naast het wetenschappelijke advies heb je mij, richting het einde, ook persoonlijke inzichten gegeven waar ik je erg dankbaar voor ben. Ik ben blij dat ik mijn professionele carrière onder jouw toezicht gestart ben. **Pieter**, bedankt voor je intensieve begeleiding, vooral in het begin. Hoewel het onderwerp van dit proefschrift grotendeels afwijkt van jouw eigen expertise, voelde het eigenlijk nooit zo. Ik ken niemand anders die zo snel tot de kern van een probleem kan komen. Waar ik ook mee binnen liep, meestal stond ik binnen een kwartier weer buiten met nieuwe ideeën en invalshoeken voor mijn onderzoek. Jouw oog voor detail is het niveau van mijn werk ten goede gekomen, wat denk ik terug te zien is in hoe de artikelen ontvangen zijn. **Florian**, master of Matlab, with your guidance I've learned most of my skills in advanced data analysis, which became more and more important as the data kept pouring in. The ability to analyze and visualize any type of data is a liberating experience. Your look on things was often refreshing, which lead to very long, rich and sometimes off-topic discussions. Furthermore, your enthusiasm for science is contagious, which I have found highly inspiring. If I was stuck or otherwise demoralized, you always said the right things to get me back on track.

I would like to thank my colleagues and collaborators who have helped making the scientific articles what they are now. **Javi**, thank you for your help and guidance on confocal fluorescence microscopy when I just started my PhD research work. **Zoran**, you were always ready to discuss single molecule fluorescence microscopy with me, and your advice inside and outside the lab has been essential in my research. **Joel**, thank you for the fruitful cooperation, I think we've got the best out of the fluorescent probes and zeolite crystals. **Diego, Katarina, Rosa, Jelle and Jeroen**, thanks for the computational insights on the DAMPI probe molecules. **Pasi**, your determination in getting physisorption data for the zeolites got us the results in the end. **Sajjad**, we've spent a lot of time holed up in the iLEM room, I'm glad we managed to measure what we needed in the end. Thanks also to, **Eelco Vogt, Hans Meeldijk, Henk Kleijn, Koop Lammertsma, Maarten Roeffaers, Alexey Kubarev**,

**Christiaan Post, Martin Lütz, Peter Hausoul and Peter Dedecker.** I would also like to thank the reading and defense committee.

I would like to thank the **Inorganic Chemistry and Catalysis** group for the great time and atmosphere, for such a large group there is a surprising amount of cohesion and order. **Sam**, you were a large contribution to keeping me mentally stable and we've shared some priceless moments. Thank you for being my paranimf and for being my friend. **Arjan**, thanks for the great time when we ran the borrel committee and when we were living together in Lunetten. **Ramon**, thanks as well for the borrel collaboration and for drinking all those beers together. **Annelie, Robin, Ilona, Carolien, Fang, Antonio**, thanks for the great times and music in the biomass lab. On the other side of the corridor, **Qingyun, Suzanne, Marjolein, Beatriz, Anne-Eva, Özgün, Abhishek, Rogier**, sitting in front of a microscope in a very hot room would not have been the same without you. In the hood on the fourth floor balcony, **Nazila, Nynke, Robin, Gang, Peter, Guusje, Laurens, Koen, Jochem, Jogchum, Zafer, Jeroen**, thank you for the serene atmosphere and all the cookies. **Katinka**, thanks for the nice time in Nice. **Jan**, thanks for the bouldering and yoga sessions. A further thanks to **Charlotte, Ilse, Iván, Donglong, Ara, Jeroen, JX, Roy, Carlo, Wenhao, Arjan Mank, Matthijs de Winter** and everybody else from the group I have not mentioned but deserves to be. **Laurens and Sanne**, I had fun supervising you and I wish you all the best in the rest of your studies and career. I would also like to thank those who keep the ICC group running smoothly: **Dymph, Iris, Monique, Fouad, Ad M., Ad vdE** and the other technical staff.

**Jeroen**, bedankt dat je mijn paranimf wilt zijn, waarvoor je uitermate geschikt bent, zeker na onze collectieve ervaring bij de VU. Ik ben trots dat jij je PhD ook bijna afgerond hebt. **Maarten**, ik vind het erg bijzonder hoe onze vriendschap is geëvolueerd over de jaren, van de scouting tot motorrijden en zelfs bier brouwen. Over het brouwen van bier gesproken: **Joost**, wij zijn daar ook echt goed in. Bedankt dat je je door mijn tenenkommende eerste versies van artikelen hebt geworsteld. **Mignon**, bedankt dat je altijd beschikbaar was aan de andere kant van de straat als de zaken niet liepen zoals ik wilde, of als er koffie gedronken moest worden. **Joep vdW**, bedankt voor (vierdaagse)feesten en voor de heldere inzichten op de goede momenten. **Alen**, without you I would probably have not returned from some parties, thanks for the navigation! I'm glad you chose me as your paranimf. **Joep adB**, wij hebben samen een aantal van de diepste discussies gevoerd die ik me zou kunnen voorstellen, het heeft me veel inzichten gegeven. **Peter**, ook al woon je nu in een ander land met **Nikki**, ik denk dat we kunnen vaststellen dat het eigenlijk niet zo ver weg is. **Tim**, bedankt voor de vele avondjes bier drinken en voetbal kijken of gamen. **Janne-Mieke**, ik vond het leuk om samen met je te dansen, misschien dat we het later nog een keer op kunnen pakken. **Ivo**, onze avondjes flossen in de clubs in Wenen zijn nog steeds ongeëvenaard. **Paul, Peter, Joost**, bedankt voor de uitdagende en soms gevaarlijke squashochtenden. **Stephan**, ik heb veel geleerd van onze gezamenlijke DJ-sessies. **Nico**, bedankt voor de gezellige avonden in Lunetten, toen we huisgenoten waren.

## Acknowledgments

---

Er gaat niets boven een biertje in café Jan Primus op vrijdagmiddag, om tot rust te komen na een week werken, gevolgd door een vette versnapering in de Reiger. **Timo, Arjan, Bieneke, René, Paul, Christine, Els, Laurens, Lilian, Marjon, Tiemen en Winnie**, bedankt voor de goede tijden die in de toekomst ongetwijfeld zo door gaan. Op de vele feesten die ik over de jaren bezocht heb, werd ik niet alleen bijgestaan door pompende technomuziek, maar ook door een *die hard party crew*: voornamelijk **Maarten, Sam, Alen, Anne-Marie, Joost, Jeroen, Peter, Nikki, Leon, Tim, Joep, Joep, Tim, Ramon, Stephan, Timo, Bieneke, René, Pasi, Floor, Pieter, Michaël, Robbert, Sjoerd, Rik, Rick, Liselot, Bram, Thijs**. Jullie zijn geweldig!

**Pap en mam**, bedankt dat jullie me altijd de vrijheid hebben gegeven mijn eigen weg te vinden, en daarnaast bij te sturen wanneer het nodig was. Het heeft me erg geholpen op eigen benen te kunnen staan, en ik denk dat dit proefschrift daar een mooi bewijs van is. Dank ook aan mijn broer **Guido** en mijn zus **Hilde** voor de altijd gezellige tijd als we elkaar zien. **Mariet en Gerard**, bedankt voor de gezellige etentjes en interesse in mijn onderzoek. **Brian**, thank you for arranging my internship and for looking out for job opportunities.

De persoon die ik het meest dank verschuldigd ben is **Anne-Marie**. Schatje, jij hebt mij bijna vier jaar lang door dik en dun gesteund, terwijl ik zelf niet altijd even leuk was. Ondertussen heb je ook nog een fantastische nieuwe baan gescoord, en daar ben ik ontzettend trots op. Ik hou van je en wil de rest van mijn leven met je delen.

## About the author

Frank Hendriks was born in 1985 in Waalre, the Netherlands. He attended Were Di college in Valkenswaard where he obtained his high school diploma in 2004. He then moved to Utrecht to study chemistry at the University of Utrecht. After completing his Bachelor's degree, he moved his studies to Amsterdam for the Master Molecular Design, Synthesis and Catalysis. During his Master's, he spent six months in Austria to do an internship at the polymer manufacturer Borealis.

In 2012 Frank started his PhD research project at the Inorganic Chemistry and Catalysis group at Utrecht University, under the supervision of Bert Weckhuysen, Pieter Bruijnincx and Florian Meirer. The most important results of his work are described in this thesis, have been published in peer-reviewed journals and have been presented at (inter)national conferences. During his PhD, he supervised one Master's student and two Bachelor's students. Furthermore, as an elected member of the University Council of the University of Utrecht, he represented PhD candidates and checked the university's finances, housing and ICT.

In real life, Frank lives in Utrecht with his fiancée and two cats. If he has any spare time, he likes to spend it in the bar, at festivals, on a motorcycle or in the gym.

## About the cover

The design of the cover (i.e., the objects, their distribution and the landscape) is done by the author. An algorithm using a neural network (available at [www.deeppart.io](http://www.deeppart.io)) in combination with a work of art with a clear style is then used.<sup>[1]</sup> Application of this algorithm results in an image resembling the work of art. Editing color values and noise reduction in Photoshop produced the final image. The painting used here was “L’Usine, Horta de Ebro” (“*Brick Factory at Tortosa*”), created by Picasso in 1909.

[1] L. Gatys, A. Ecker, M. Bethge, J. Vis. 2016, 16, 326.